Optimised Polyolefin Branch Quantification by ^{13}C NMR Spectroscopy

Dissertation
zur Erlangung des Grades

„Doktor der Naturwissenschaften“

am Fachbereich Chemie, Pharmazie und Geowissenschaften
der Johannes Gutenberg-Universität Mainz

Katja Klimke

geboren in Mainz

Mainz, 2006

Die vorliegende Arbeit wurde in der Zeit von September 2001 bis April 2006 am Max-Planck-Institut für Polymerforschung in Mainz angefertigt.

Tag der mündlichen Prüfung: 07.07.2006

Abstract

Quantitative branch determination in polyolefins by solid- and melt-state ^{13}C NMR has been investigated. Both methods were optimised toward sensitivity per unit time. While solid-state NMR was shown to give quick albeit only qualitative results, melt-state NMR allowed highly time efficient accurate branch quantification. Comparison of spectra obtained using spectrometers operating at 300, 500 and 700 MHz ^{1}H Larmor frequency, with 4 and 7 mm MAS probeheads, showed that the best sensitivity was achieved at 500 MHz using a 7 mm ^{13}C–^{1}H optimised high temperature probehead. For materials available in large quantities, static melt-state NMR, using large diameter detection coils and high coil filling at 300 MHz, was shown to produce comparable results to melt-state MAS measurements in less time. While the use of J-coupling mediated polarisation transfer techniques was shown to be possible, direct polarisation via single-pulse excitation proved to be more suitable for branch quantification in the melt-state. Artificial line broadening, introduced by FID truncation, was able to be reduced by the use of π pulse-train heteronuclear dipolar decoupling. This decoupling method, when combined with an extended duty-cycle, allowed for significant improvement in resolution. Standard setup, processing and analysis techniques were developed to minimise systematic errors contributing to the measured branch contents. The final optimised melt-state MAS NMR method was shown to allow time efficient quantification of comonomer content and distribution in both polyethylene- and polypropylene-co-α-olefins. The sensitivity of the technique was demonstrated by quantifying branch concentrations of 8 branches per 100,000 CH_2 for an industrial linear polyethylene in only 13 hours. Even lower degrees of 3–8 long-chain branches per 100,000 carbons were able to be estimated in just 24 hours for a series of γ-irradiated polypropylene homopolymers.

Contents

Chapter 1

Introduction

Polyethylene (PE) and polypropylene (PP), as well as their respective copolymers with other olefins, make up over 50% of all plastics produced worldwide (Figure 1.1). These systems are commonly collectively termed polyolefins and constitute an important sector of the polymer family.

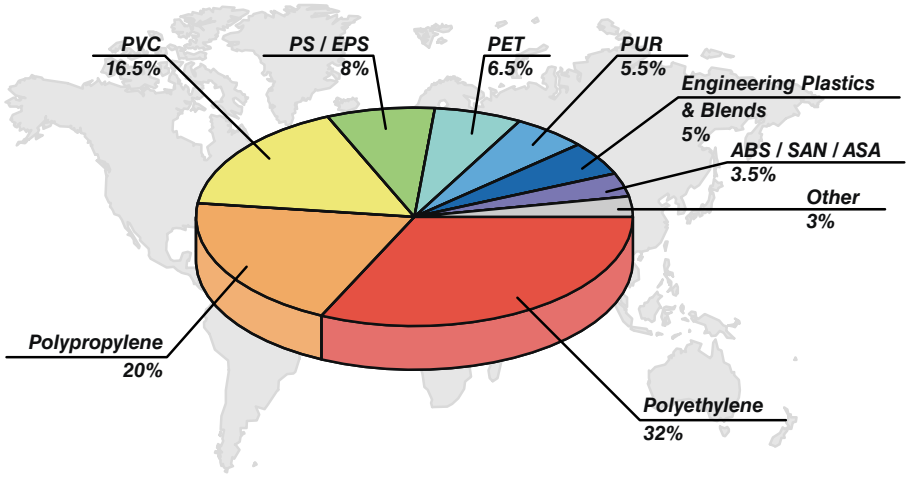

***Figure 1.1**: Relative worldwide production of plastics in 2004 [PlasticsEurop 05], accounting for a total production of 250 million tons [Frey 06].*

Due to their low density, form stability, non-toxicity and corrosion resistance they are used for a wide range of applications such as packaging materials, pipes, films, fibres and car interiors (Figure 1.2) [Kaminsky 01].

The macroscopic properties of polyolefins are determined by their molecular weight (MW), molecular weight distribution (MWD) and chain microstructure. The microstructure being characterised by type, amount and distribution of comonomer and branching. The importance of comonomers and branches is due to the advantageous properties their presence imparts on the bulk polymers. In polyolefins, the physical properties of both the solid and the melt can be tuned by the presence of

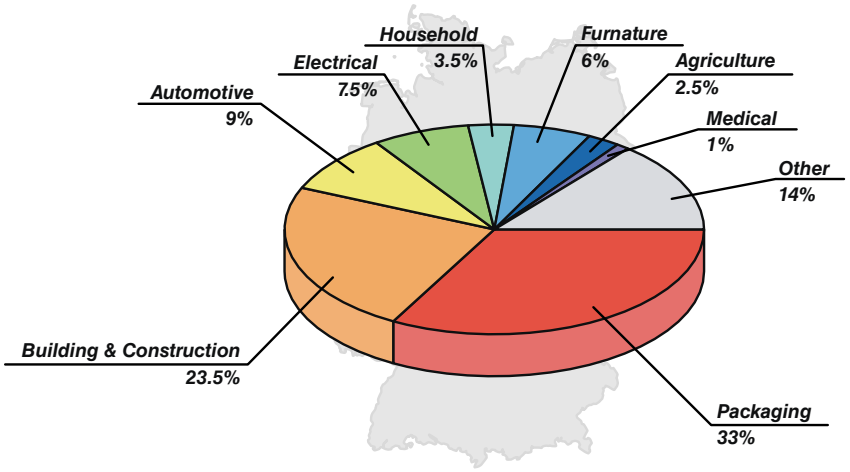

***Figure 1.2**: Fields of use for plastics in Germany in 2003 [PlasticsEurop 04].*

branches of various lengths in the polymer backbone. Long chain branches (LCB), which are generally considered to be longer than the entanglement molecular weight, are rheologically active and mainly affect the melt-state properties such as flow behaviour and processing characteristics [Wang 04]. In contrast, short chain branches (SCB) influence the solid-state properties by lowering the melting point (T_m), degree of crystallinity and the density, thus synthetic control of the chain microstructure is essential for tailoring the material properties.

The first synthetic strategy for polyolefins was based on free radical polymerisation of ethylene at extremely high pressures [Fawcett 37]. This produced low density polyethylene (LDPE) with a broad MWD and a highly branched structure including SCB, LCB and branches on branches (Figure 1.3). Ziegler-Natta (Z-N) [Ziegler 55, Natta 56] and Phillips catalysts [Clark 56] allowed the synthesis of linear high density polyethylene (HDPE) and stereo-regular polypropylene. These catalysts were also used for the copolymerisation of ethylene with α-olefins to produce linear low density polyethylene (LLDPE). However, due to their multiple reaction sites these catalysts produced polymers with a broad MWD and copolymers with a heterogeneous distribution of comonomers. In recent years catalysts with a single reaction site have thus become the focus of research. Metallocenes (m) [Andresen 76, Kaminsky 83] and constrained-geometry catalysts (CGC) [Lai 93, Brant 93] have enabled the production of polymers with much narrower MWDs and copolymers with homogeneous comonomer distribution. The precise control of the polymer structure has made the synthesis of polyolefins with improved or even completely new properties possible.

Despite their desirable bulk properties, polyolefins with a narrow MWD are difficult to process. However melt processability can be considerably improved by the incorporation of LCB into the polymer backbone. It has been found that even very low amounts of LCB can have large effects on the melt properties of the polymers. In

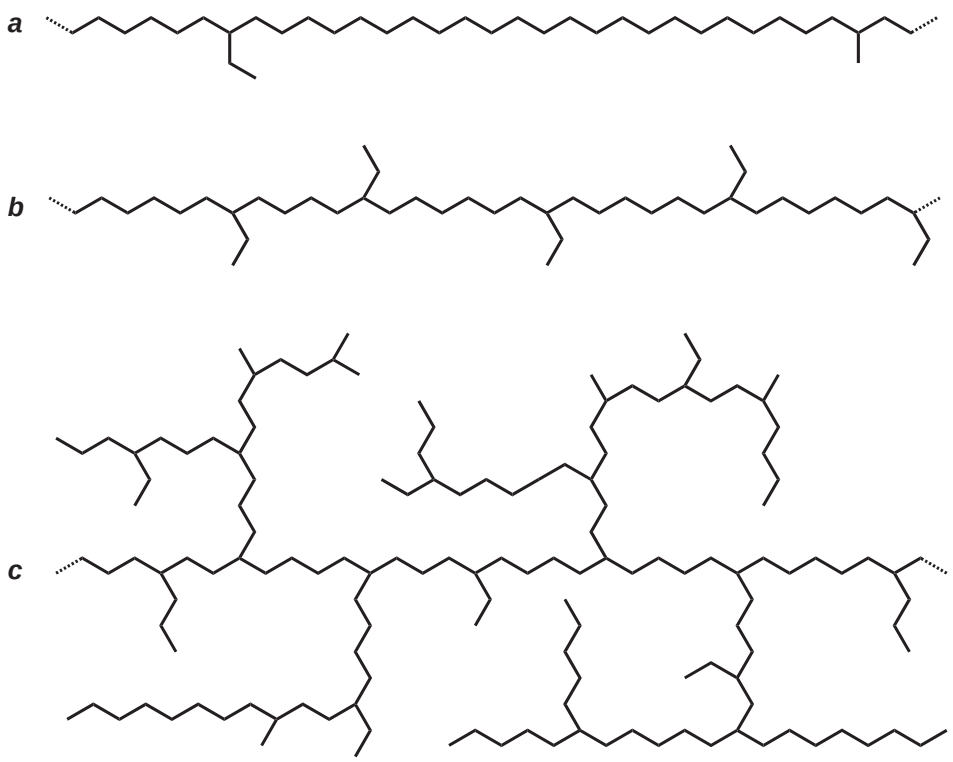

***Figure 1.3**: Types of polyethylenes: (a) high density, (b) linear low density and (c) low density.*

fact, the concentration of LCB for which these effects are observed is often at the very limit of the currently available detection methods. Thus increasing the sensitivity of existing methods and finding new ways to detect and quantify very low levels of branching has become an important field of research.

The well-established polymer characterisation methods fourier-transform infrared spectroscopy (FTIR) [Dorman 72], temperature rising elution fractionation (TREF) [Zhang 03], differential scanning calorimetry (DSC) [Shroff 96, Zhang 03], multi-detector size exclusion chromatography (SEC) [Bovey 76, Bugada 87, Striegel 00] and rheology [Gabriel 98, Vega 98, Shroff 99, Wood-Adams 00, Wood-Adams 01, Lohse 02, Gabriel 02, Crosby 02, Trinkle 02] can all be used for branch detection.

Although these techniques may be very sensitive to the presence of branching, without some form of external calibration they only provide qualitative insight into the degree and type of branching. Alternatively, ^{13}C nuclear magnetic resonance (NMR) spectroscopy is one of the few methods capable of providing quantitative, albeit sample average, values of the branch content without the need for calibration [Wood-Adams 00, Shroff 01].

The typical implementation of NMR undertakes analysis of the sample in the solution-state due to the high resolution spectra obtained. However when applied to polyethylene a number of problems arise [Bovey 96, Morris 86, Shroff 01]. The most important being the low solubility of polyethylene, even at high temperatures

[Liu 99, Seger 04]. The resulting low concentration of ^{13}C nuclei requires extended measurement times, especially for the quantification of very low levels of branching (Figure 1.4). Furthermore, solution-state NMR does not allow access to crosslinked and other non-soluble polyolefin fractions.

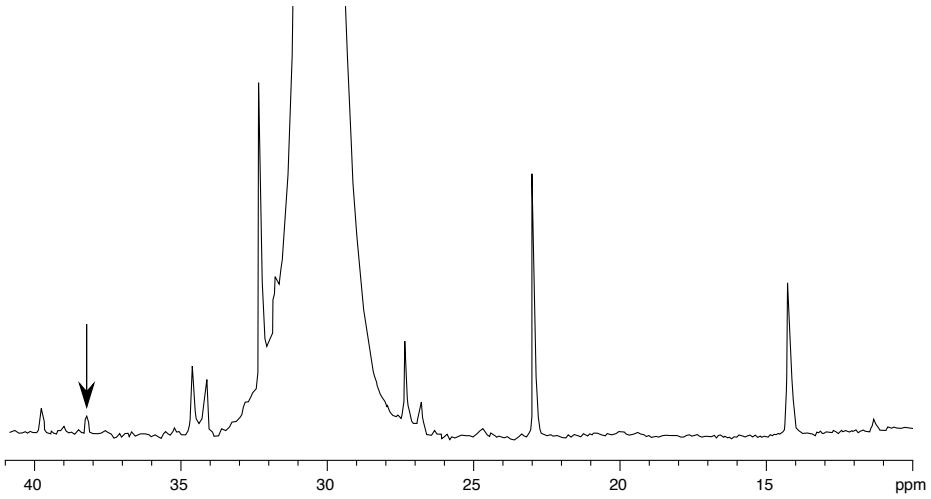

***Figure 1.4**: Example solution-state NMR spectrum of a polyethylene with very low amounts of LCB (2–3 branches per 100,000 CH_2) requiring long measurement times (up to 2,000,000 transients) at high field (600 MHz). Reproduced from [Wood-Adams 00].*

Solid-state NMR, under magic angle spinning (MAS), has previously been shown to overcome some of the limitations of solution-state NMR [Zeigler 94, Guo 00]. Due to the higher density of ^{13}C nuclei in the bulk state higher sensitivity can be obtained. The signal from the ^{13}C nuclei can be further enhanced by transferring magnetisation from the more abundant protons with techniques such as cross-polarisation (CP) [Pines 72, Axelson 86]. However, in the solid-state the lack of isotropic motion leads to severe line broadening in the polymer spectra due to strong heteronuclear ^{13}C–^{1}H dipolar coupling, large distribution of isotropic chemical shift and chemical shift anisotropy [Dechter 81].

Melt-state NMR of polyolefins under static conditions has also been investigated, but was found to not provide enough resolution for quantitative NMR [Zeigler 94]. Melt-state NMR under MAS, however, has been found to be a suitable compromise between solution-state and solid-state NMR for polyethylene branch quantification. This method combines high nuclear spin concentration and motional averaging of line broadening interactions [Dechter 81, Zeigler 94, Hatfield 95, Guo 00, Litvinov 02, Thakur 03]. With the effects of dipolar coupling greatly reduced, the line widths obtained by melt-state MAS NMR come close to those in the solution-state. The main drawback of this method however is the long recycle delays needed between consecutive scans. For quantitative measurements the observed nuclei must be allowed to fully relax back to their thermal equilibrium state, resulting in long measurement times.

1.1 Outline

A more detailed description of the importance of SCB and LCB in polyolefins is given in Chapter 2. The synthetic strategies for branched polyolefins are introduced as well as the current methods for branch detection and quantification. The physical properties of the polyolefin systems studied for this body of work are given in Section 2.5.

With branch quantification by NMR the focus of this body of work, a description of the underlying principles of NMR and discussion of the methods used is given in Chapter 3.

The potential of solid-state NMR for the quantification of branching is described in Chapter 4. The use of low temperatures to 'freeze out' dynamic heterogeneities is described and shown to enable a semi-quantitative estimate of the amount of branching from solid-state NMR spectra.

In Chapter 5 measurement of melt-state NMR under static conditions is discussed. The size of both the detection coil and sample were investigated regarding a decrease in measurement time.

Melt-state MAS NMR is established as a viable alternative to branch quantification via solution-state NMR in Chapter 6. Optimisation of the hardware setup and the experimental conditions allowed a further increase in sensitivity of this method. It is shown that, contrary to expectation, shortening of the recycle delay to less than $5 \times T_1^C$ still led to quantitative spectra, resulting in much shorter measurement times. The importance of the decoupling scheme is also discussed in this section.

With an optimised measurement method established, standard processing and analysis techniques are discussed in Chapter 7, with the aim of reducing user-dependent errors. General sources of error are identified by statistical analysis and the reliability of the obtained branch contents estimated.

The general applicability of the optimised melt-state MAS NMR method towards common characterisation problems encountered in polyolefins is shown in Chapter 8. Rapid quantification of comonomer contents and sequences up to the tetrad level are shown to be possible. The measurement times required for the quantification of very low concentrations of functional groups are also shown to be strongly reduced, as compared to solution-state NMR characterisation. The quantification of LCB in polypropylene is also shown.

A summary of all results is presented in Chapter 9.

Chapter 2

Branching in Polyolefins

The chain microstructure of polyolefins strongly determines the macroscopic behaviour. Short (SCB) and long (LCB) chain branches can be used to control the solid-state and melt-state properties respectively. Short chain branches are either produced by isomerisation reactions during homopolymerisation [Prosenc 97, Thorshaug 98, Izzo 99, Lehmus 00] or by copolymerisation of relatively short alkenes [Halász 05]. Long chain branches are formed *in situ* by macromonomer incorporation during polymerisation [Malmberg 98]. An overview of synthetic strategies for controlling SCB and LCB in polyethylene and polypropylene is given in Section 2.1 and Section 2.2 respectively.

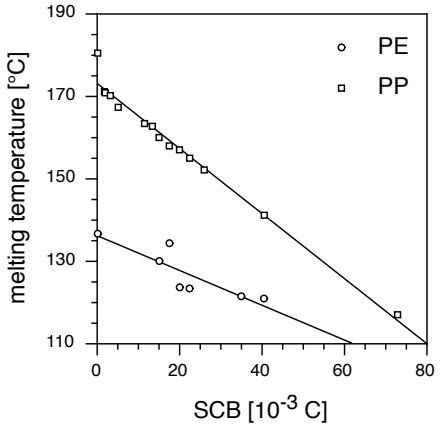

***Figure 2.1**: Dependence of melting point on SCB content in polyethylene- and polypropylene-co-α-olefins. Reproduced from [Halász 05].*

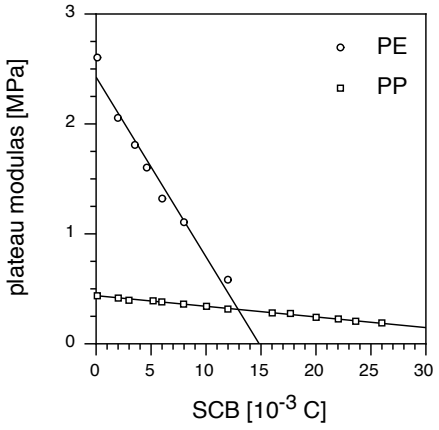

***Figure 2.2**: Dependence of plateau modulus on SCB content in polyethylene- and polypropylene-co-α-olefins. Reproduced from [Halász 05].*

Since SCB forms structural defects during crystallisation, their presence affects the crystallisation rate and lowers the overall degree of crystallinity. Hence, an increase in SCB content leads to a decrease of several thermal and rheological properties such as density, glass transition temperature (T_g), melting point

(T_m), (Figure 2.1), zero shear viscosity η_0 and plateau modulus (Figure 2.2) [Kaminsky 01, Zhang 03, Halász 05]. Generally, SCB affects mostly solid-state properties such as stiffness, rigidity, hardness, permeability and stress-crack resistance [Blitz 94, Knuuttila 04].

In contrast, LCB mostly affect the melt properties such as flow behaviour and processing characteristics [Wang 04]. Long chain branching leads to a broadening of the mechanical relaxation time distribution, resulting in an increase of the zero shear viscosity and viscous relaxation times [Rohlfing 00]. The viscosity of a polyolefin with LCB is also more sensitive to temperature, as shown by higher flow-activiation energies [Janzen 99]. Long chain branched polyolefins also show higher degrees of shear thinning (Figure 2.3), the onset of which occurring at lower shear rates, thus improving processibility [Hatzikiriakos 00, Wood-Adams 00]. Furthermore, when subjected to extensional deformation, polyolefins exhibit non-linear strain-hardening (Figure 2.4). Flow instabilities, such as the sharkskin effect, tend to occur at much higher shear rates than for systems not containing LCB [Wang 04].

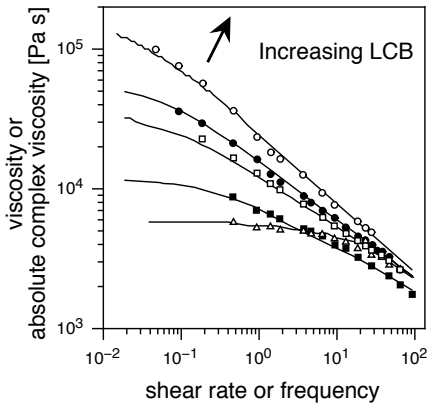

***Figure 2.3**: The effect of long-chain branching on polyethylene shear thinning behaviour. Reproduced from [Wood-Adams 00].*

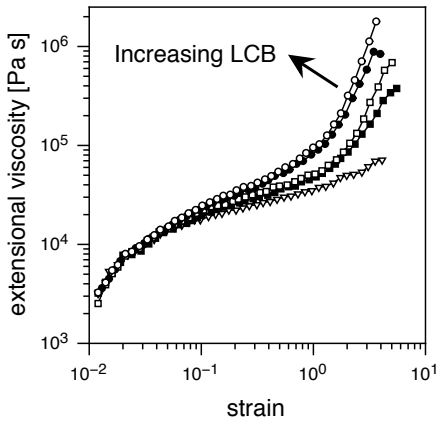

***Figure 2.4**: The effect of long-chain branching on polypropylene strain hardening behaviour. Reproduced from [Lagendijk 01].*

It is important to note that even very low degrees of LCB can have large effects on the melt properties of the polyolefins. Indeed, the concentration of LCB for which these effects are observed is often at the very limit of detection for currently available analytical methods. In a recent study, LCB has been shown to influence the zero shear viscosity even at concentrations of 2–3 long chain branches per 100,000 CH_2, as characterised by ^{13}C NMR [Wood-Adams 00, Shroff 01]. Thus, the development of new techniques, as well as the improvement of sensitivity for existing techniques, has become an important field of research for polyolefins.

The catalyst and polymerisation conditions play an important role for SCB and LCB incorporation. It is thus important for the synthetic chemist to have access to analytical techniques sensitive to both SCB and LCB. With access to such techniques, links between the physical properties of the polyolefin, the macromolecular structure and

the method of synthesis can be made. With such information polyolefins with highly tuned physical properties can be produced.

2.1 Polyethylene synthesis

With the bulk properties of polyethylenes strongly determined by their chain microstructure, one of the most important areas of polyethylene production has always been the synthetic control of branching. Due to the importance of polyethylene synthesis and the various classes of polyethylenes produced by the different synthetic routes, a brief outline of polyethylene synthesis will be given in order of historical development.

2.1.1 1930s: Low-density polyethylene (LDPE)

The first polyethylenes to be commercially produced were low-density polyethylenes (LDPE). These were first produced in the 1930s using free-radical initiators. The high temperatures (140–300°C) and high pressures (1100–3000 bar) used for such free-radical polymerisation of ethylene allow multiple side-reactions to take place. Such intermolecular and intramolecular chain-transfer reactions (Figure 2.5) result in characteristic broad MWDs as well as high degrees of LCB and SCB. The SCB produced also have a distribution of chain lengths. Due to the unregulated nature of the free-radical process, the branch topology obtained is one of branches upon branches (Figure 2.6). Such branch topologies are difficult to control, reproduce and characterise.

The high concentration of LCB in LDPEs provides good rheological properties, such as flexibility at low temperatures. Low density polyethylenes are also ideal for wire and cable insulation, as no metal-based catalysts are used during their production and hence no residual catalyst particles are incorporated into the polymer. Due to their good processability LDPEs are also commonly used for film formation and extrusion coating.

There are two main types of reactors available for the production of LDPE, the continuous-flow autoclave and the tubular reactor. The continuous-flow autoclave is mechanically stirred and results in LDPEs with high concentrations of LCB, and thus produces LDPEs ideal for extrusion coating. In contrast, the tubular reactor leads to polymers with a much lower degree of LCB, and thus produces LDPEs ideal of insulation and packaging purposes [Knuuttila 04].

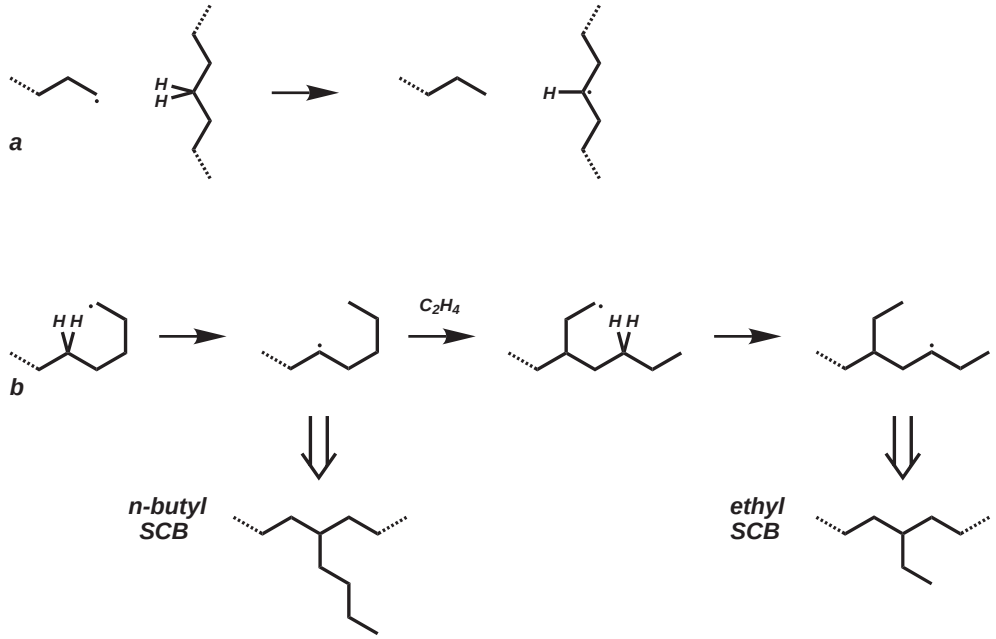

***Figure 2.5**: The (a) intermolecular and (b) intramolecular H-transfer free-radical side reactions present during the free radical polymerisation of ethylene used for LDPE production [Young 91].*

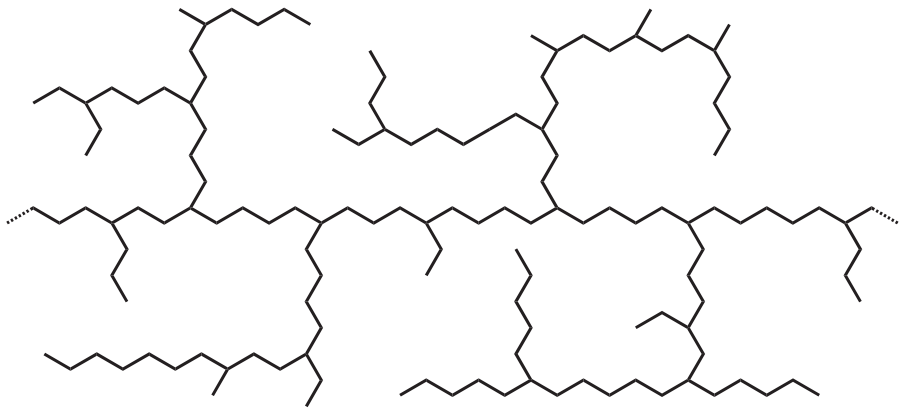

***Figure 2.6**: Illustration of the chemical structure of a low density polyethylene (LDPE).*

2.1.2 1950s: High-density polyethylene (HDPE)

In the 1950s the discovery of the Ziegler-Natta (Z-N) [Ziegler 55, Natta 56] and Phillips [Banks 51, Hogan 58] catalysts enabled the production of polyethylenes with very few or no branches for the first time (Figure 2.7). These high density polyethylenes (HDPE) have the advantageous properties of high stiffness, temperature resistance and mechanical stress resistance. However, due to their high density, HDPEs suffer from poor optical properties and low impact strengths. These properties result in HDPEs used predominantly as bottles, containers, pipes, wires, cable jacketing and as stiff films. Through the use of a catalyst, the polymerisation reaction was able to be carried out under low pressures in either a suspension (slurry), solution or the gas-phase.

In the slurry process the monomers and catalyst are dissolved in short hydrocarbons, such as hexane or heptane, at temperatures between 70–100°C and pressures of 5–40 bar. With the reaction temperature below the melting point of PE (140°C), the product precipitates as it is formed. Using the slurry process an ethylene conversion of over 95% is achieved after about one hour.

In the solution process the polymerisation is carried out in hydrocarbons at temperatures above the melting point of PE, between 160–300°C, and under pressures of 25–100 bar. Using this process a conversion of 95% is reached after only 1–5 minutes. However the maximum MW of the polyethylene produced with this method is limited due to the high viscosity of the solution.

Both the slurry and solution process consume large amounts of energy, with the removal of the hydrocarbon solvents occurring in post-production. Due to these limitations the gas-phase process was developed in the 1970s. In this process gaseous monomers are brought in contact with a solid catalyst at 75–110°C and pressures of 20–25 bar. A 95% conversion is only obtained after 3–4 hours with the gas phase process however.

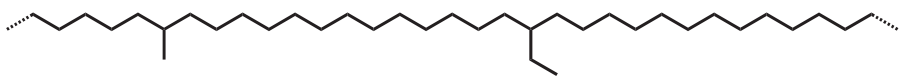

***Figure 2.7**: Illustration of the chemical structure of a high-density polyethylene (HDPE).*

2.1.3 1970s: linear low-density polyethylene (LLDPE)

During the 1970s the gas phase process was used to produce copolymers of ethylene with α-olefins (Figure 2.8). The resulting linear low-density polyethylenes (LLDPE) showed increased impact strength and toughness as well as improved clarity and elasticity [Kaminsky 05]. Their low stiffness and melting point made them ideal for use in packaging films and sealing layers in multilayer films [Knuuttila 04].

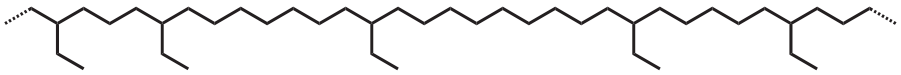

***Figure 2.8**: Illustration of the chemical structure of a linear low-density polyethylene (LLDPE).*

2.1.4 1980s: ultra-high molecular weight polyethylene (UHMWPE)

In the 1980s a new class of HDPEs, with molecular weights of over 1,000,000 g mol^{-1}, were developed (Figure 2.9). These ultra-high molecular weight polyethylenes (UHMWPE) are characterised by high abrasion resistance, high impact toughness, good corrosion and chemical resistance as well as resistance to cyclic fatigue and radiation. With these favourable properties UHMWPE can thus be used in highly demanding applications such as artificial implant materials. However for the same reasons, UHMWPE also has poor processability. For example compression moulding and ram-extrusion often show fusion defects or grain boundaries, both resulting in poor mechanical performance of the finished product [Sharma 05]. Alternatively UHMWPE may be dissolved in a suitable solvent followed by ultra-drawing (solution-spinning). This results in very strong fibres which can be woven into high-performance materials, such as those used in bullet-proof vests. Although commonly thought to contain no branching, NMR investigations of a range of commercial UHMWPEs have shown the presence of both SCB and LCB [Kaji 91].

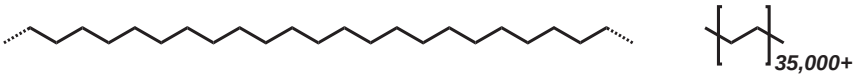

***Figure 2.9**: Illustration of the chemical structure of an ultra-high molecular weight polyethylene (UHMWPE).*

2.2 Polypropylene synthesis

Besides the molecular weight distribution and type and degree of branching, the stereo-regularity of the polymer backbone strongly determines the macroscopic properties of polypropylenes. Depending on whether neighbouring monomer units have the same (*meso*), opposite (*racemic*), semi-random or random configuration relative to the backbone, isotactic, syndiotactic, hemiisotactic or atactic PP is obtained respectively (Figure 2.10). The stereo-irregular atactic PP is a highly viscous liquid, while both isotactic and syndiotactic PP are semi-crystalline solids with relatively high melting points [Kaminsky 01]. Compared to PE, stereo-regular PP has the advantage of higher melting points and high tensile moduli combined with lower densities and low production costs [Gotsis 04]. Stereo-regular PP also has excellent chemical resistance, making it suitable for a wide range of applications.

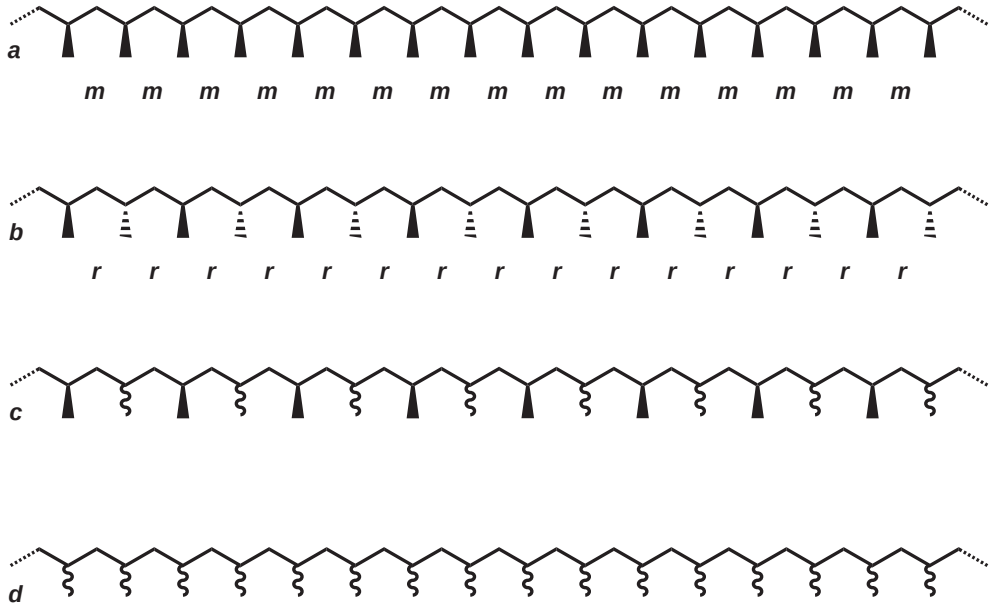

***Figure 2.10**: Microstructure and stereochemistry of (a) isotactic, (b) syndiotactic, (c) hemiisotactic and (d) atactic polypropylenes [Vandeveer 04].*

2.2.1 Stereo-regular polypropylene (iPP/sPP)

The synthesis of stereo-regular PP only became possible in the 1950s with the discovery of Ziegler-Natta catalysts (Section 2.3.1), allowing the production of isotactic and syndiotactic polypropylene. With the discovery of metallocene based catalysts (Section 2.3.2) in the 1970s even greater control of PP properties became possible. Polypropylenes produced by metallocene catalysts have characteristically narrow MWDs and no LCB. Thus such polypropylenes have poor processability, especially for extensional flow processes. For this reason several strategies have been devised to produce LCB in PP.

2.2.2 High melt strength polypropylene (HMS-PP)

Branched polypropylenes are generally called high melt-strength polypropylenes (HMS-PP), due to their advantageous physical properties. Such HMS-PPs can be produced via post-processing by electron beam irradiation, γ-irradiation or reactive extrusion with peroxides [Gotsis 04]. For all these post-processing methods, branches are formed by random chain scission followed by radical recombination. Thus, as with LDPEs, complex branching topologies my be formed (Figure 2.11), as well as changes in stereochemistry [Busfield 87, Busfield 91]. Recently, LCB in PP has been achieved synthetically by either copolymerisation with prefabricated PP macromonomers [Shiono 99] or by in-situ macromonomer incorporation [Weng 02, Ye 03, Ye 04].

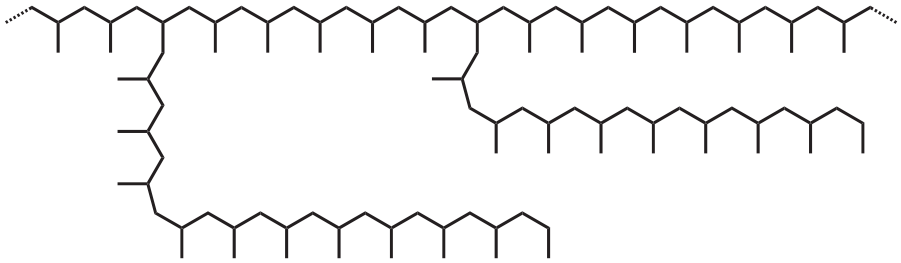

***Figure 2.11**: Illustration of the chemical structure of a high melt strength polypropylene (HMS-PP).*

2.2.3 Polypropylene-co-α-olefins

Alternatively, the copolymerisation of PP with α-olefins (Figure 2.12) can be used to obtain materials with novel properties. For copolymers of propylene and 1-octadecene, significant changes in crystal structure have been observed, leading to changes in mechanical behaviour. Increasing the comonomer content was found to decrease the rigidity and increase the impact strength [Palza 05].

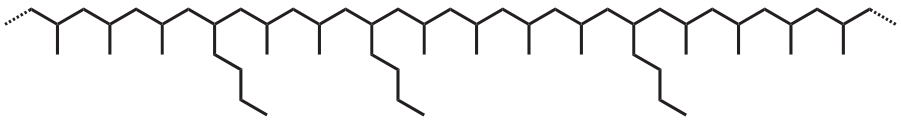

***Figure 2.12**: Illustration of the chemical structure of a polypropylene-co-α-olefin.*

2.3 Catalysts for polyolefin synthesis

The properties of polyolefins can be controlled to a large extent by the catalyst geometry. Two main classes of catalysts are used for the synthesis of polyolefins based on the number of available reaction sites per catalyst. The Ziegler-Natta and Phillips class of catalysts have multiple reaction sites per catalyst molecule, whereas the metallocene based constrained geometry class of catalysts have only a single reaction site per catalyst molecule. Due to the different properties of each class of catalysts, and the related polyolefin macrostructures produced, each will be discussed separately.

2.3.1 Multiple-site catalysts: Ziegler-Natta/Phillips

Ziegler-Natta catalysts [Ziegler 55, Natta 56] consist of a catalyst and a cocatalyst (Figure 2.13). The catalyst is usually a complex of a group IV–VIII transition metal, usually a halide, alkoxide, alkyl or aryl derivative. The cocatalyst, which is also known as an activator, is commonly a group I–III metal alkyl halide. Such catalysts can either be used in homogeneous, heterogeneous or colloidal form. The control of the polymer molecular weight is achieved by using hydrogen gas as a chain transfer agent, thus stopping chain growth.

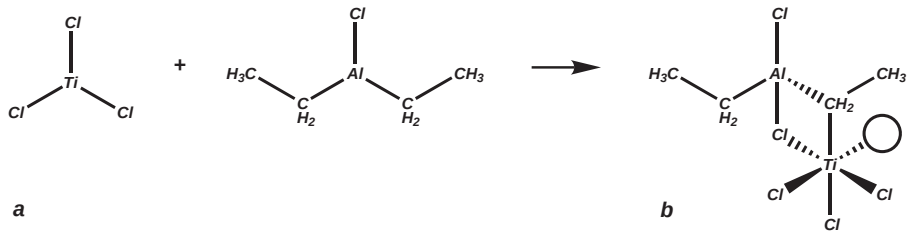

***Figure 2.13**: The most common Ziegler-Natta (a) catalyst ($TiCl_3$) and cocatalyst ($AlEt_2Cl$) and (b) illustration of the active site [Carney 05a, Michalovic 05].*

In contrast, the Phillips catalysts [Banks 51, Hogan 58] are based on chromium-(VI)-oxide supported on silica or aluminosilicate (Figure 2.14). Such catalysts need to be activated by temperature, with regulation of the temperature also allowing to control the polymer molecular weight.

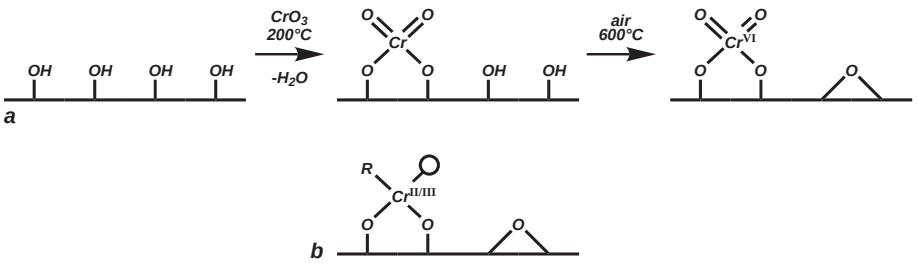

***Figure 2.14**: The (a) formation and activation of a Phillips catalyst and (b) illustration of the active site [Kaminsky 01, Carney 05b].*

Both Ziegler-Natta and Phillips catalysts have been shown to contain multiple reaction sites per catalyst molecule. These multiple reaction sites result in the production of polyolefin homopolymers and copolymers with broad molecular weight distributions. Polydispersity indices (PDIs) of 4–6 and > 7 are seen for Ziegler-Natter and Phillips catalysts respectively (Figure 2.15). The multiple reaction sites also result in a non-random distribution of SCB within the polymer, with comonomers more likely to be found in shorter chains and at the ends of chains in general.

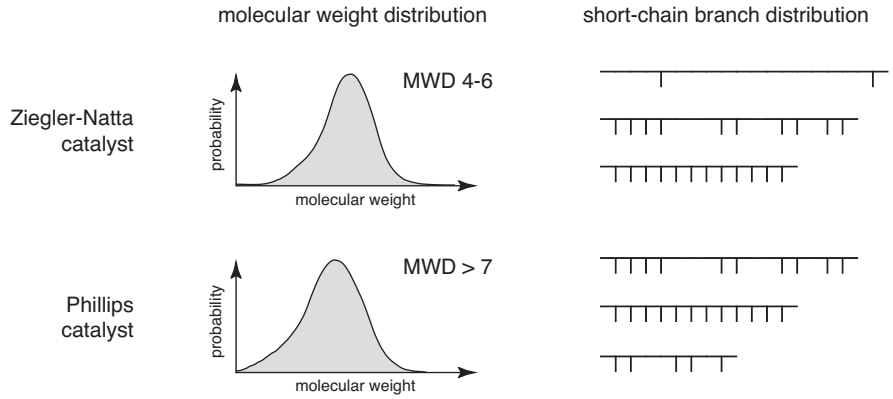

***Figure 2.15**: Comparison of the molecular weight and SCB distribution obtained with Ziegler-Natta and Phillips catalysts. Reproduced from [Knuuttila 04].*

2.3.2 Single-site catalysts: Metallocenes

Although single reaction site catalysts were originally discovered at the same time as multiple reaction site catalysts, their potential for commercial polyethylene production only became clear when their activation with alumoxane was discovered in the 1970s [Andresen 76].

The first single-site catalysts consisted of a metallocene metal complex, usually Zr with two cyclopentadienyl ligands (Figure 2.16a). These metallocene complexes were then activated by methylaluminoxane acting as a cocatalyst (Figure 2.16b) [Kaminsky 83]. Since this discovery a wide range of metallocenes, with varying metal centres and modified ligands, have been developed to accommodate the need for tailored polymer properties. Initially only metallocenes of early transition metals such as Ti, Zr and Hf were investigated. Recently however, the potential of late transition metals, such as Ni, Pd, Co and Fe, has been recognised [Löfgren 04].

In the 1990s another form of single site catalyst based on half-metallocenes were discovered [Stevens 93], these being known as constrained-geometry catalysts (CGC) (Figure 2.16c). Such catalysts were found to be especially useful for the copolymerisation of ethylene with long-chain α-olefins.

Single site catalysts allow unprecedented control over the bulk polymer properties, such as temperature resistance, hardness, impact strength and transparency

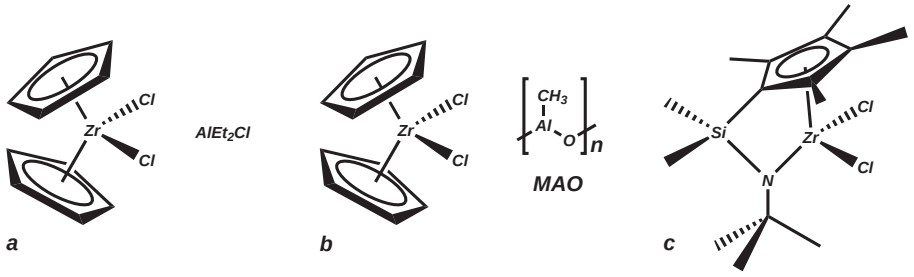

***Figure 2.16**: Chemical structures of (a) the first example of a metallocene based catalyst, (b) Kaminsky type catalyst with methylaluminoxane cocatalyst and (c) constrained geometry catalyst [Piel 05, Löfgren 04].*

[Kaminsky 01, Halász 05]. In contrast to multiple site catalysts, narrow molecular weight distributions of PDI = 2 are possible with a homogeneous distribution of comonomers (Figure 2.17).

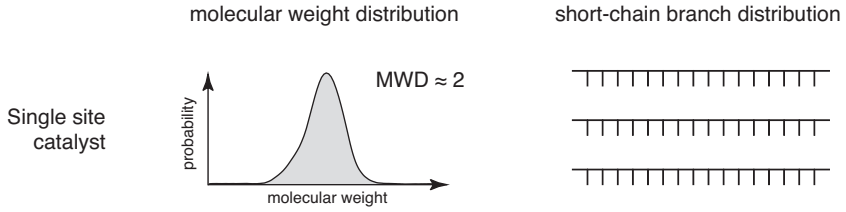

***Figure 2.17**: Comparison of the molecular weight and SCB distribution obtained with single site catalysts. Reproduced from [Knuuttila 04].*

The uniform comonomer distribution results in lower melting and sealing temperatures as compared to polymers with the same comonomer content produced using Ziegler-Natta or Phillips catalysts. Similarly, the narrow molecular weight distributions result in higher zero-shear-rate viscosities and mechanical relaxation times. However, although this improves the toughness of the material it also reduces melt processability.

Catalytic incorporation of LCB

With the melt processing properties able to be improved by the incorporation of small amounts of LCB, recent research has focused on the development of single-site catalysts capable of introducing LCB into the polymer chain. The first catalysts found to produce LCB were based on constrained geometry catalysts [Lai 93, Wang 98b, Yan 99, Wood-Adams 00]. Subsequently, several conventional metallocene catalysts were also shown to incorporate low amounts of LCB [Malmberg 98, Kokko 00b, Kokko 01, Gabriel 02].

The formation of LCB is thought to occur via copolymerisation of vinyl-terminated polyethylene chains produced *in situ* by β-hydrogen transfer (Figure 2.18). It has been found that both the catalyst structure and the polymerisation conditions determine if, and to what extent, LCB is incorporated [Kaminsky 01, Löfgren 04].

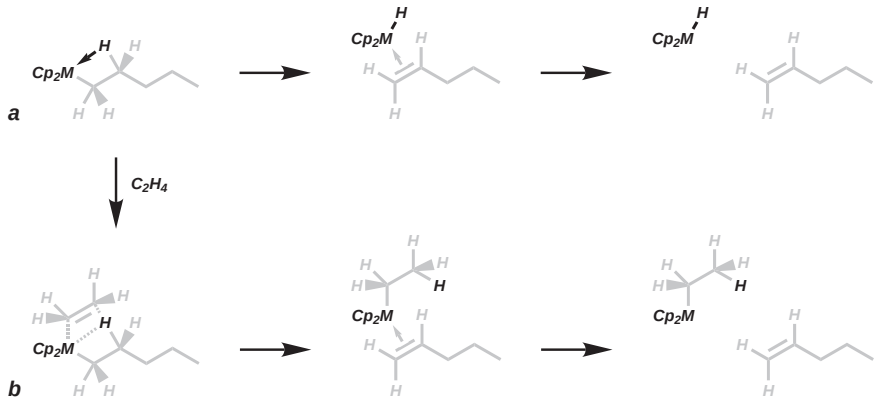

***Figure 2.18**: Termination reactions via β-H transfer to (a) catalyst and (b) monomer [Piel 05].*

The main characteristics found to increase the tendency of a catalyst to form LCB are good polymerisation ability and high vinyl selectivity. Catalysts based on ethylene-bridged bis(indenyl) ansa-metallocenes (Figure 2.19a) were found to be especially suitable for LCB incorporation [Malmberg 98, Kokko 00b]. Substitution of the bis(indenyl) ligands with tert-butyldimethylsiloxyl groups has been seen to have a strong influence on the catalysts ability to incorporate LCB [Lehmus 99, Malmberg 99, Kokko 00a]. Decreasing the concentration of ethylene was found to increase the degree of LCB, whereas the presence of hydrogen gas lowered LCB [Kokko 00b]. Recently a new class of bis(phenolate) titanium complexes has also been found to produce LCB in PE (Figure 2.19c) [Capacchione 04]. For a diphenyl-carbon bridged catalyst containing a fluorenyl ligand (Figure 2.19b) [Kaminsky 05] it was shown that the presence of α-olefin comonomers decreased the LCB concentration [Stadler 05].

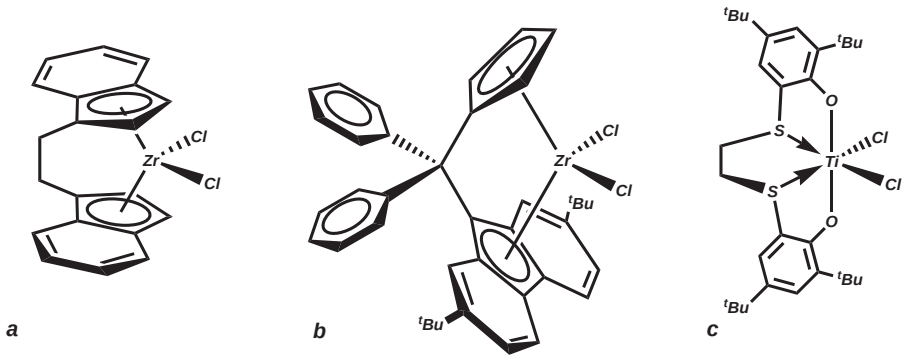

***Figure 2.19**: Single site catalysts shown to incorporate LCB. (a) Et[Ind]$_2$ZrCl$_2$, (b) [Ph$_2$C(2,7-di-^{t}Bu-Flu)(Cp)]ZrCl$_2$ and (c) di-chloro[1,4-dithiabutanediyl-2,2-bis(4,6-di-tert-butyl-phenoxy]titanium [Piel 05, Capacchione 04].*

Catalysts for stereo-regular polypropylenes

The symmetry of metallocene catalysts about the single reactive site plays a pivotal role in their stereo-specificity [Resconi 00]. Thus such catalysts play a major role in the production of stereo-regular polymers such as isotactic and syndiotactic PP (Figure 2.10). Generally, metallocene complexes with ansa-C_2-, nonbridged pseudo-C_2- and ansa-C_1-symmetry produce isotactic PP, whereas catalysts with a C_s-symmetry result in syndiotactic PP (Figure 2.20).

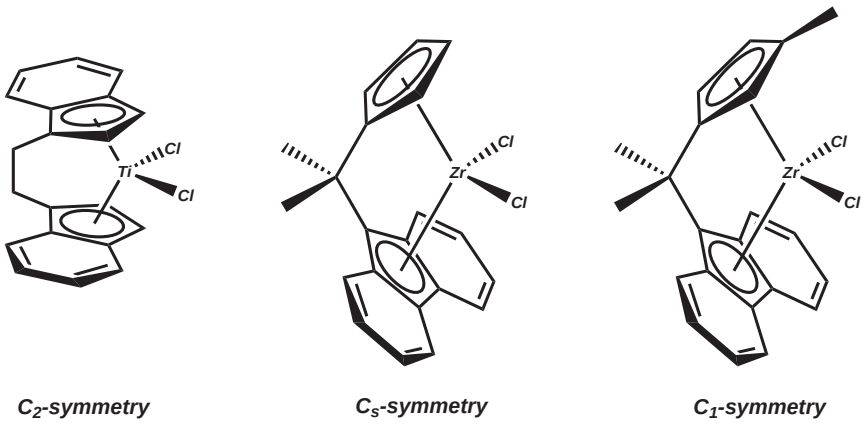

***Figure* 2.20**: *Stereo-specific catalysts for production of stereo-regular PP [Vandeveer 04].*

Similarly, bridged asymmetric catalysts may be used to produce elastomeric PP, with isotactic-atactic or isotactic-hemiisotactic stereoblocks. The resulting polypropylenes having a rubbery consistency at room temperature due to the amorphous atactic/hemiisotactic blocks being connected to crystalline isotactic blocks [Vandeveer 04].

2.4 Polyolefin branch determination

With new catalysts allowing greater control over the chain microstructure accurate characterisation of polyolefins becomes essential. While MW and MWD of soluble fractions can be determined reliably by gel permeation chromatography (GPC), accurate quantification of branching, especially sparse branching, remains problematic. Although several analytical methods have been developed for either sensitive branch detection or accurate branch quantification, generally speaking, no single method is good at both. Commonly the methods which are sensitive to branching require external calibration by the methods of accurate branch quantification. For this reason polyolefin branch quantification is inherently a multidisciplinary research field. Due to the variety of analytical techniques used for polyolefin branch quantification it is important to understand the basis behind each of the commonly applied analytical methods. For this reason a brief outline of each of the analytical techniques is given in this section.

2.4.1 Transmission infrared spectroscopy

Transmission fourier-transform infrared spectroscopy (FTIR) is used for both qualitative and quantitative SCB determination. It is widely used due to its simplicity, speed and low equipment cost.

Traditionally the methyl deformation band at 1378 cm^{-1} has been used for qualitative and quantitative analyses. However it has since been recognised that the use of this band cannot differentiate between SCB and end groups, thus resulting in correction factors needing to be used at low branching levels. Additionally, the molar absorptivity of the methyl deformation band depends on the short-chain branch length. The methyl and methylene rocking bands have been found to be more characteristic of short chain branch type. For example, using the characteristic absorbance bands of methyl (935 cm^{-1}), ethyl (770 cm^{-1}), butyl (893 cm^{-1}), isobutyl (920 cm^{-1}), and hexyl (888 cm^{-1}) branches (Figure 2.21) the degree of branching in LLDPE copolymers, LLDPE terpolymers and LDPEs have been qualitatively and quantitatively characterised [Blitz 94]. However, in order to resolve the overlapping bands for ethyl, butyl, and isobutyl branches Fourier self-deconvolution[†] was needed.

Although FTIR is less costly and faster for quantitative results, calibration curves relating absorbance to degree of branching are required. Such calibration curves need to be determined, for the type and degree of branching in question using materials of known degrees of branching, by ^{13}C NMR (Figure 2.22). Furthermore, the differentiation of butyl and hexyl branches within the same polymer by IR spectroscopy is not possible, wheras such a distinction remains possible by ^{13}C NMR.

[†]The application of an exponential window function to the FT of an FTIR spectrum followed by inverse FT, resulting in the artificial narrowing of the spectral lines.

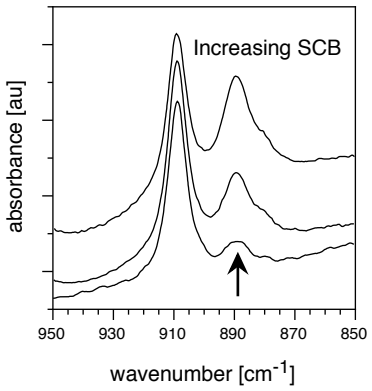

***Figure 2.21**: FTIR spectra showing the methyl rocking mode of a hexyl branch (890 cm^{-1}) for a series of PE-co-octenes with increasing co-octene content. Reproduced from [Blitz 94].*

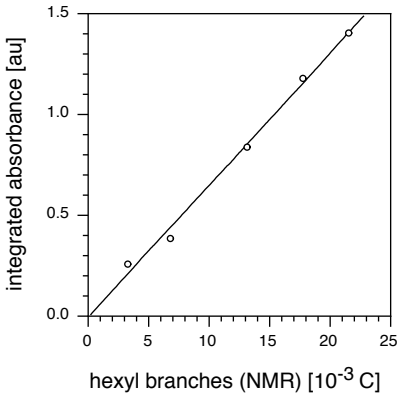

***Figure 2.22**: The derived calibration curve relating integrated absorbance with degree of short-chain branching, as determined via ^{13}C NMR. Reproduced from [Blitz 94].*

2.4.2 Thermal fractionation methods

Two methods based on thermal fractionation may also be used to detect short-chain branching in polyolefins; temperature rising elution fractionation (TREF) and thermally fractionated differential scanning calorimetry (TF-DSC).

Temperature rising elution fractionation (TREF)

Temperature rising elution fractionation involves a polymer being heated to 125°C in the presence of a solvent and a support material, these typically being o-xylene and glass beads respectively. After 4 hours at high temperature the system is cooled to -8°C at a constant rate of 1.5°C per hour [Zhang 03]. During this controlled cooling process polymers are separated depending on their ability to crystallise, i.e. with less branched fractions crystallising at higher temperatures and higher branched fractions at lower temperatures (Figure 2.23).

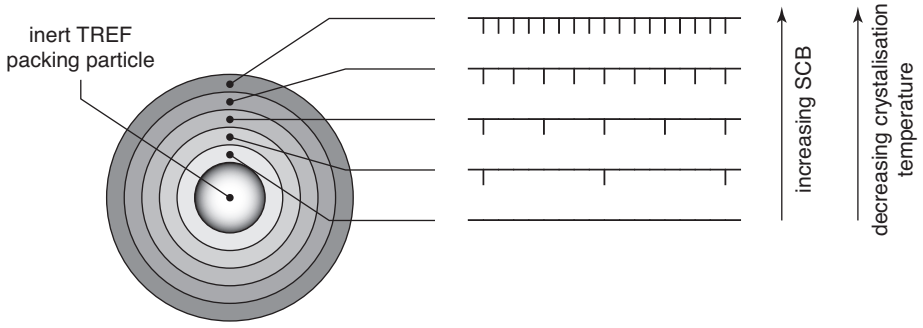

***Figure 2.23**: Illustration of the crystallisation stage of a TREF experiment. Layer formation on the inert support material as a function of SCB content and crystallisation temperature. Adapted from [Yau 01].*

Following the crystallisation stage, the crystallised sample is eluted under heating of 1°C per min in a TREF apparatus. The signal from an IR detector monitoring the eluted volume is then correlated against the elution temperature (Figure 2.24). By this process differences in SCB content, and their distribution, can be determined.

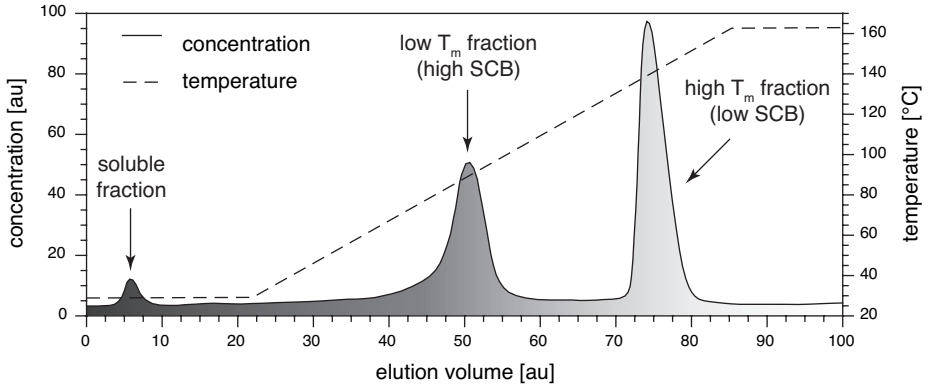

***Figure 2.24**: Illustration of the elution stage of a TREF experiment showing layer-wise elution of polyolefin as a function of temperature. Adapted from [Yau 01].*

A qualitative comparison of the TREF profiles of polyethylenes indicates that metallocene catalysts produce a more uniform distribution of SCB than Ziegler-Natta catalysts (Figure 2.25). However for quantitative analysis a calibration curve is required, relating the elution temperature to the actual degree of SCB. Such calibration curves can be obtained by fractionating a polymer via preparative TREF and then determining the SCB contents for each fraction, and its specific elution temperature, via FTIR or ^{13}C NMR.

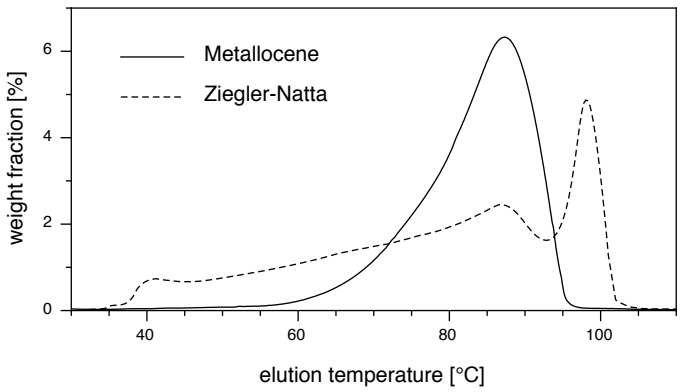

***Figure 2.25**: Comparison of the TREF elution profiles for a Ziegler-Natta and metallocene polyethylene. [Kristen 99]*

It should be noted that the elution temperature of a semicrystalline polymer, such as polyethylene, is determined by a wide range of material properties. These include parameters such as the molecular weight as well as the content, length and distribution of the branches [Pigeon 94]. For example, by increasing the branch length from methyl to hexyl a shift of the calibration curve to lower TREF elution temperatures

occurs [Savitski 03]. Thus in order to obtain correct SCB contents and distributions with TREF the type of branching present needs to be known beforehand.

In general, each set of polymerisation conditions will produce polymers with a unique relation of SCB branch content and TREF elution temperatures. Thus a specific calibration curve is required for each set of polymerisation conditions, resulting in a higher degree of uncertainty for the determined properties.

Thermally fractionated differential scanning calorimetry (TF-DSC)

A solvent-free and faster alternative to temperature rising elution fractionation is thermally fractionated differential scanning calorimetery (TF-DSC). This technique is based on thermal fractionation of the polymer chains according to methylene sequence lengths (MSL). After successive nucleation and annealing (SNA), DSC allows distinction between the different MSLs according to their respective melting points [Zhang 03].

More specifically, the sample is heated to 135°C, annealed for 10 min and then cooled to 25°Cwith a 5°C min^{-1} cooling rate. For consecutive heating cycles the annealing temperate is reduced by 5°C until an annealing temperature of 30°C is reached. During the successive nucleation and annealing cycles chain reorganisation occurs resulting in crystals of different sizes depending on the methylene sequence length. With such crystals melting at different temperatures their distribution can then be detected by DSC after all annealing cycles have been completed.

The DSC endotherms obtained after SNA treatment for a series of commercial metallocene polyethylenes show how different distributions of methyl sequence lengths may be observed (Figure 2.26a) [Zhang 03].

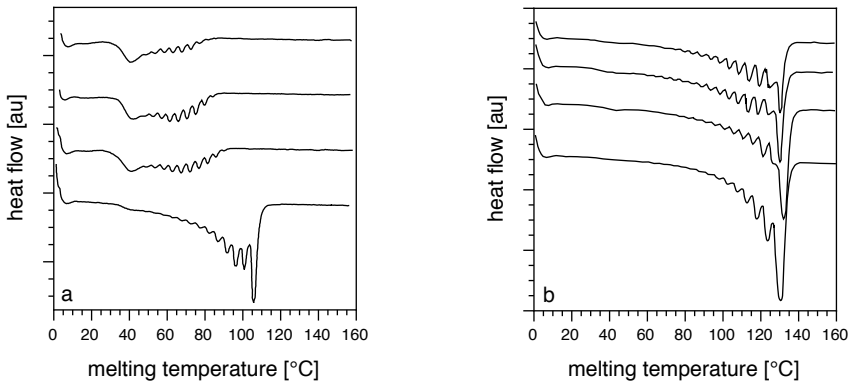

***Figure 2.26**: Example DSC endotherms of (a) four commercial metallocene and (b) four commercial Ziegler-Natta PEs after SNA treatment. Reproduced from [Zhang 03].*

For quantitative analysis of the SNA-DSC endotherms a calibration curve relating melting temperature to MSL is required. Such a relation is commonly obtained by

SNA-DSC of a series of linear hydrocarbons (Figure 2.27) [Zhang 01]. If the polyethylene in question contains only one type of SCB, and their length i is known, the MSL can be used to calculate the number of SCB per 1000 carbons using:

$$B = \frac{1000}{MSL + i + 1} \tag{2.1}$$

Thus, for each short-chain branch length a separate calibration curve is obtained directly relating DSC determined melting temperatures with degree of SCB (Figure 2.28). Using the calibration curves the degree of SCB can then be determined for each peak in the SNA-DSC endotherm.

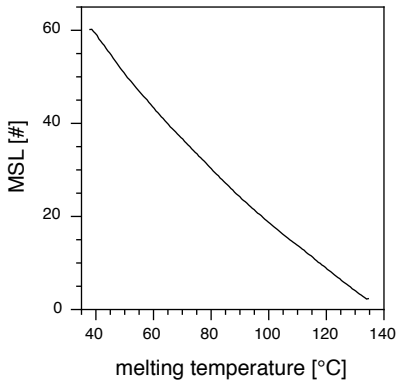

***Figure 2.27**: SNA-DSC calibration curve relating methylene sequence length (MSL) with determined melting temperatures. Reproduced from [Zhang 01, Zhang 03].*

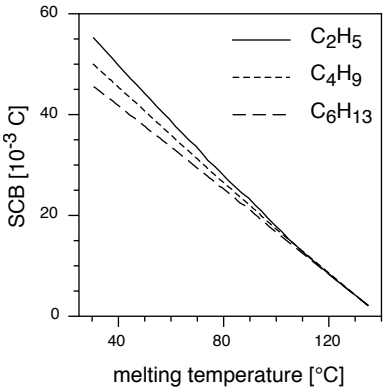

***Figure 2.28**: SNA-DSC calibration curves relating degree of SCB with melting temperatures for three types of branching. Reproduced from [Zhang 03].*

For determination of the overall distribution of SCB, the mass fraction of each peak has to be measured by deconvolution. From the first and second moments of the distribution of SCB the average degrees of SCB for the whole sample, similar to M_n and M_w, can be obtained (Figure 2.29).

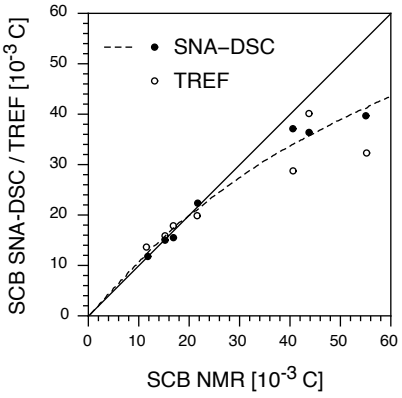

***Figure 2.29**: Comparison of SCB contents obtained with ^{13}C-NMR, SNA-DSC and TREF [Zhang 03].*

For branch contents $>$ 30 branches per 1000 carbons a discrepancy in degree of SCB is observed for both TREF and SNA-DSC as compared to ^{13}C NMR. At high SCB contents the average MSL is less than 25 carbons long, with a significant amount being even shorter. Since polyethylenes with MSL $<$ 10 carbons in length do not crystallise during TREF or SNA-DSC a systematic underestimation of the degree of SCB for such systems is observed.

2.4.3 Multiple detection size exclusion chromatography (SEC)

The use of multiple detectors with size exclusion chromatography (SEC) has been found to be a very sensitive method for the detection of LCB in polyolefins. Through the use of Zimm-Stockmayer theory the degree of LCB may also be quantified, however, a number of assumptions also have to be made by this approach. Using this method multiple detection SEC has been shown to enable the quantification of 1 long-chain branch per 10,000 carbons [Wood-Adams 00]. However multi-detection SEC is not sensitive to the degree or type of SCB, unless it has a direct effect upon the degree LCB.

Detectors and their related properties

Triple detection SEC combines the use of differential refractive index (DRI) or infrared (IR) concentration detectors with a capillary viscometer (CV) and light scattering (LS) apparatus. Recently the combination of SEC with multi-angle laser light scattering (SEC-MALLS) has been shown to be even more powerful [Yu 05, Stadler 06].

With this setup not only can the concentration of each fraction be determined but also its molecular weight and intrinsic viscosity (Figure 2.30). The determination of molecular weight being extremely important as the commonly used calibration curves, relating retention volume to molecular weight, are not valid. This is due to these having been constructed using standards without LCB. The measurement of the intrinsic viscosity [η] allows the distinction of samples with and without LCB to be achieved. By monitoring light scattering intensity at several angles for each sample fraction insight into the degree of LCB is provided. Analysis of the light scattering data via the Zimm method [Zimm 49] provides both the absolute molecular weight (MW) and mean square radius of gyration (R_g) for each fraction (Figure 2.31).

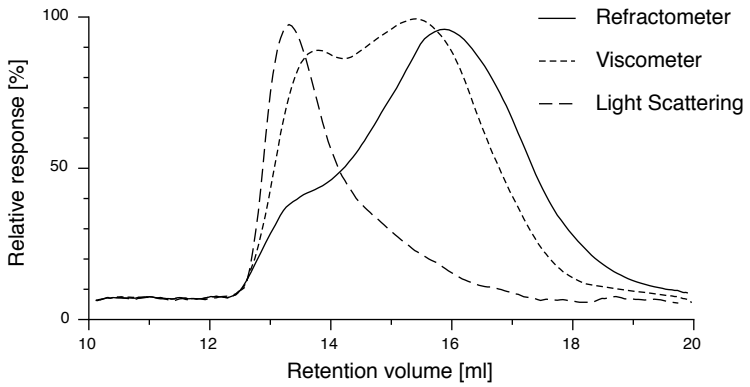

Figure 2.30: *Comparison of the detector signals as a function of retention volume obtained with triple detection SEC for a LDPE sample [Yau 01].*

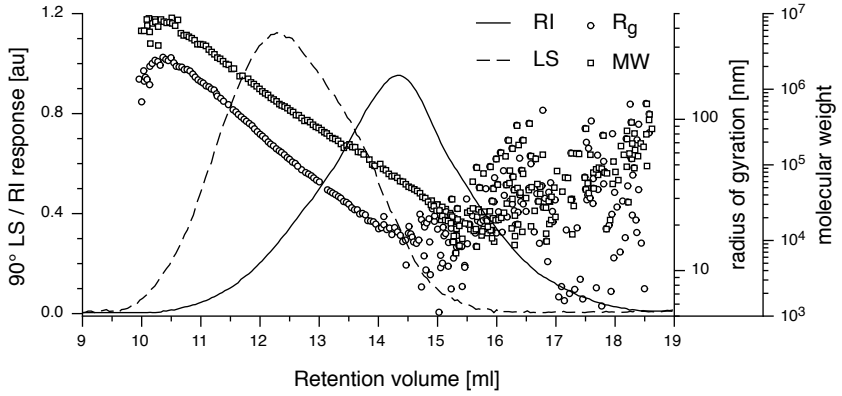

Figure 2.31: *Example of the detector signals as a function of retention volume obtained with SEC-MALLS. For clarity only the light scattering signal from one angle is shown (LS). Zimm-analysis of the signals from all light scattering angles is used to determine both molecular weight and mean square radius of gyration for each sample fraction.*

Detection of LCB

Polyolefins containing LCB have lower intrinsic viscosities and smaller mean square radii of gyration, as compared to polyolefins of the same total molecular weight without LCB. This being caused by the contraction of the polymer coils in the branched samples. It should also be noted that the radius of gyration may also be decreased if SCB is present at greater than 20 wt-% [Sun 01]. Thus, for such systems a SCB correction factor is needed, with this having been separately determined for each type of comonomer [Yu 05].

The influence of LCB may be illustrated using a double logarithmic plot of either $[\eta]$ or $\langle {R_g}^2 \rangle$ versus molecular weight. This method of analysis being know as the Mark-Houwink plot (Figure 2.32). This shows that LCB mainly occurs in the higher molecular weight fractions of polyolefins.

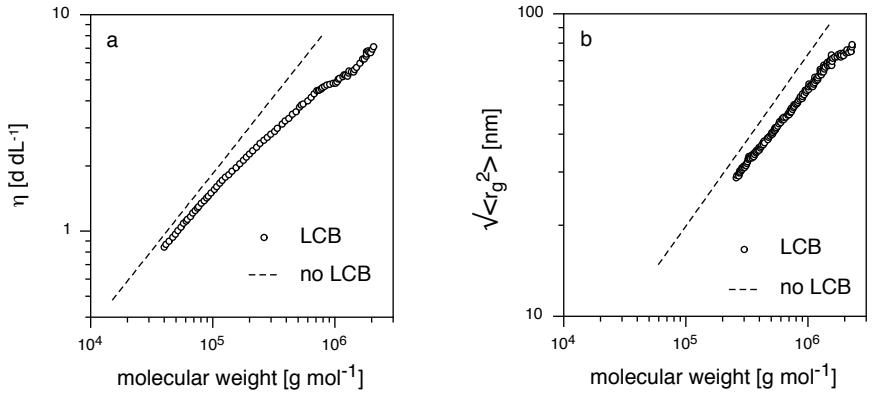

***Figure 2.32**: Mark-Houwink plots of the (a) intrinsic viscosity [η] (from triple detection SEC) and (b) root mean square radius of gyration $\langle {R_g}^2 \rangle$ (from SEC-MALLS) as a function of molecular weight for polyethylene samples with and without LCB. Adapted from [Wang 04].*

The greater the deviation of intrinsic viscosity or mean square radius of gyration from those of a linear sample, the higher the degree of LCB. The extent of this deviation may be quantified by calculating a viscosity branching index factor g' (Equation 2.2) or a branching index factor g (Equation 2.3) for standard triple detection SEC or SEC-MALLS respectively [Yu 05].

$$g' = \frac{[\eta]_b}{[\eta]_l} \tag{2.2}$$

$$g = \frac{\langle {R_g}^2 \rangle_b}{\langle {R_g}^2 \rangle_l} \tag{2.3}$$

where $[\eta]_b$ and $\langle {R_g}^2 \rangle_b$ relate to the system with LCB and $[\eta]_l$ and $\langle {R_g}^2 \rangle_l$ to the reference material without LCB. Branching index factors < 1 thus indicate the presence of LCB. Furthermore, the lower the value of the branching index factors the higher the degree of LCB (Figure 2.33).

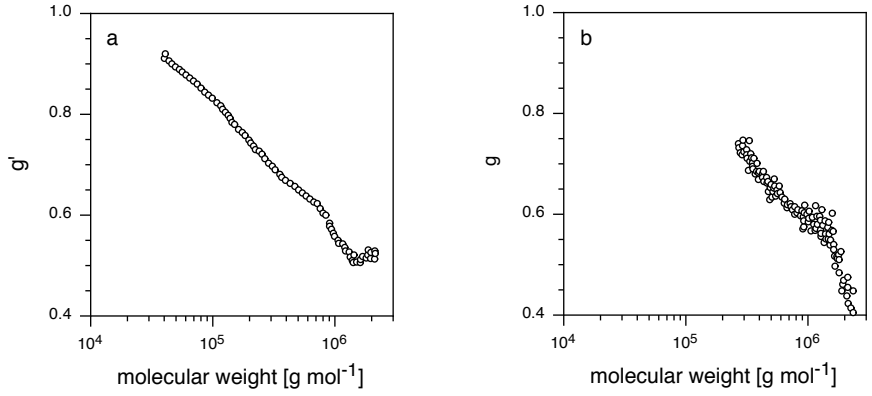

***Figure 2.33**: Comparison of the (a) viscosity branching factor g' (from triple detection SEC) and (b) branching factor g (from SEC-MALLS) as a function of molecular weight. The lower the values of the branching factors, the higher the degree of LCB per molecular weight fraction. Adapted from [Wang 04].*

Quantification of LCB

For each molecular weight fraction the average number of long-chain branches per molecule, or LCB frequency F_i, is related to the branching index factor g_i according to Equation 2.4. This is achieved by the use of Zimm-Stockmayer theory, which assumes a random distribution of tri-functional long-chain branches [Zimm 49].

$$g_i = \left\{ \left(1 + \frac{F_i}{7}\right)^{1/2} + \frac{4 \cdot F_i}{9\pi} \right\}^{-1/2} \tag{2.4}$$

From the LCB frequency the LCB density for each fraction D_i may be calculated as the number of branches per 1000 carbons using the molecular weight of each fraction M_i (Equation 2.5). The LCB density for the whole system may then be calculated using the weight fraction w_i of each molecular weight fraction i (Equation 2.6).

$$D_i = \frac{F_i}{M_i} \cdot 14 \times 10^3 \quad [10^{-3}\text{C}] \tag{2.5}$$

$$D = \sum_i w_i \cdot D_i \quad [10^{-3}\text{C}] \tag{2.6}$$

An example of the distribution of LCB frequency and density with molecular weight is shown in Figure 2.34. This illustrates that LCB is more likely for high molecular weight fractions. From Equation 2.4 it can be seen that only the branching index factor g (based on $\langle {R_g}^2 \rangle$) is directly related to the degree of LCB.

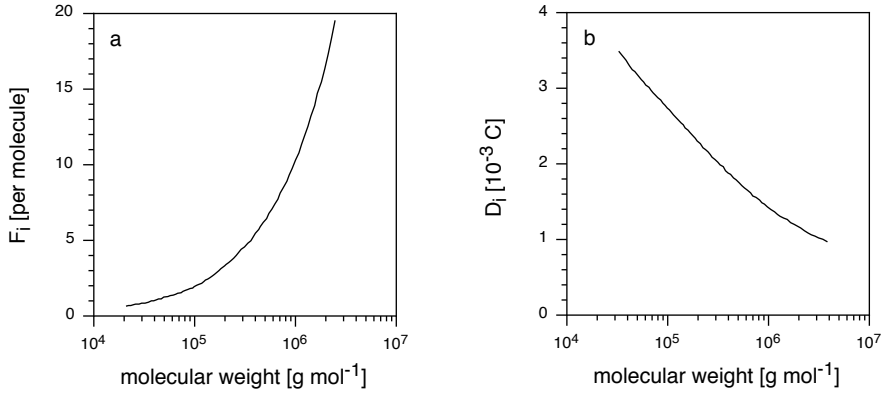

***Figure 2.34**: An example of LCB (a) frequency F_i and (b) density D_i as a function of molecular weight determined from the branching index factor g using the Zimm-Stockmayer theory. Adapted from [Wang 04]*

However the viscosity branching index factor g' (based on $[\eta]$) obtained from standard triple detection SEC may also be used as this is related to g according to: $g' = g^{\epsilon}$. Unfortunately, the relationship between intrinsic viscosity and radius of gyration is not trivial, due to the 'shielding' effects in polymer solutions [Yu 05]. The parameter ϵ depends on not only the type of LCB and solvent quality, but more importantly, is often also found to be molecular weight dependent. Thus the number of assumptions needed when choosing the value of ϵ may lead to inaccuracy in the final quantified degree of LCB by standard triple detection SEC. Typically ϵ ranges between 0.5–2.0 [Yu 05]. It should also be considered that the Zimm-Stockmayer itself is derived assuming a random distribution of LCB and the use of θ-solvents. In practice these conditions are rarely met. When combined with the assumption of tri-functional branch points the values determined using multiple detection SEC can only be regarded as estimates, albeit very good estimates, of the true degree of LCB [Bugada 87]. Despite these limitations multiple detection SEC is the only method currently able to provide insight into the distribution of LCB as a function of MW.

2.4.4 Rheology

Several linear and non-linear rheological properties can be used to detect the presence of LCB, even at very low levels, in polyolefins. Although rheology is very sensitive to LCB it is much less sensitive to SCB. However, when the degree of SCB affects the degree of LCB, qualitative results regarding SCB may be obtained.

Distinct differences between systems with and without LCB may be seen with the dependence of zero shear-rate viscosity η_0 on weight-average molecular weight M_w, the viscosity function, the steady-state creep recovery compliance J_e^0 and the dependence of phase angle δ on complex modulus $|G^*|$. Recently the potential of FT-rheology to distinguish between branched and linear systems has also been shown [Fleury 04, Vitorias 06]. It should also be noted that due to the length of the rheology experiments, especially creep measurements, stabilisation with antioxidants is essential to prevent sample degradation.

Zero shear-rate viscosity

Above a given molecular weight, the critical molecular weight M_c, polyolefins without LCB show a well established correlation between zero shear-rate viscosity (η_0) in Pa s and weight-average molecular weight (M_w) in g mol^{-1} (Equation 2.7). This correlation has been found to be independent of polydispersity between a PDI of 2–16 and M_w of 0.4–923 kg mol^{-1} for polyethylenes at 150°C [Stadler 05]. However, deviation from this trend occurs with the presence of LCB.

$$\eta_0 = 9 \times 10^{-15} \cdot M_w^{3.6} \tag{2.7}$$

In the case of sparse LCB, η_0 increases with LCB content, while for high degrees of LCB found in LDPEs η_0 decreases with LCB content. This behaviour relates to whether the separation between the individual long-chain branches along the backbone is longer or shorter than the entanglement molecular weight M_e respectively [Janzen 99, Wood-Adams 00, Gabriel 02].

Although the degree of SCB can not be directly detected, SCB content has been shown to play an important role on the degree of LCB for some polyethylenes-co-α-olefins [Stadler 05]. The LCB content as detected by η_0 was found to be dependent on the amount and type of SCB (Figure 2.35), the latter having been determined by ^{13}C NMR (Section 8.1). The normalised viscosity functions also showed a clear trend of increasing LCB with decreasing SCB content (Figure 2.36).

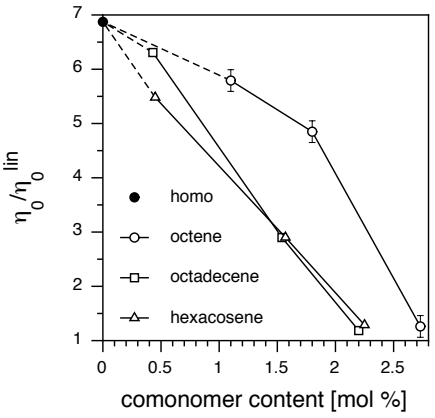

***Figure 2.35**: Enhancement of η_0 as a function of SCB concentration and type. Adapted from [Stadler 05].*

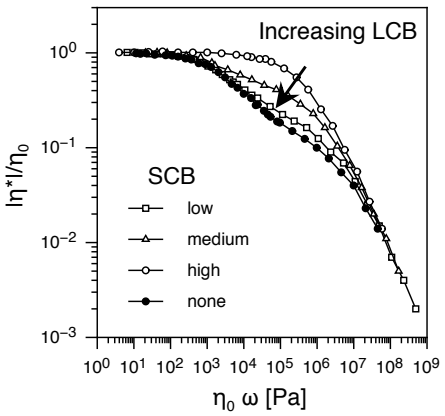

***Figure 2.36**: Change in the shape of the normalised viscosity function with increasing LCB [Stadler 05].*

Steady-state creep recoverable compliance

Rheological creep experiments are also sensitive to LCB in polyolefins. In these experiments a constant shear stress is applied to a sample during a given time. During this so called 'creep time' the shear deformation is measured as a function of time and normalised to the creep stress. The resulting characteristic property is known as the creep compliance $J(t')$ (Figure 2.37a). When the stress is removed the recoverable part of the shear deformation is recorded as a function of recovery time, and again normalised to the creep stress. This being known as the creep recovery compliance $J_R(t)$ (Figure 2.37b). After very long creep and creep recovery times the steady-state recoverable compliance J_e^0 is reached (Figure 2.37c). With this property being a measure of the elasticity of the sample it may then be correlated to molecular structure such as the degree of LCB [Gabriel 98, Gabriel 99, Gabriel 02]. Generally J_e^0 increases with LCB content (Figure 2.38).

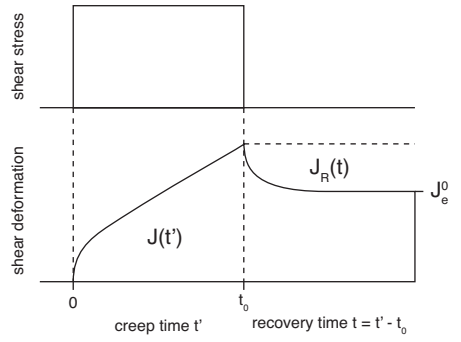

Figure 2.37: Principle of creep and creep recovery experiment.

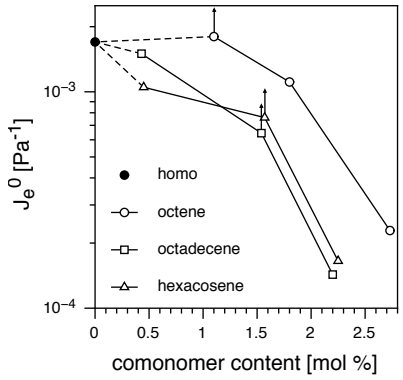

Figure 2.38: Dependence of J_e^0 on SCB for a set of polyethylene-co-α-olefins produced using the same catalyst. Data shows that for this catalyst increased SCB suppressed LCB. Adapted from [Stadler 05].

Correlation of phase angle with complex modulus

One of the most sensitive ways of detecting the presence of LCB by rheology is based on the dependence of the phase angle δ on the complex modulus $|G^*|$. This representation being also known as the 'van Gurp-Palmen plot' [Gurp 98, Trinkle 01].

For polyolefins without LCB δ increases sharply with decreasing $|G^*|$ and reaches a plateau at 90°. However for polyolefins with LCB a second plateau in δ is observed, the depth of which depends on the degree of LCB [Wood-Adams 00, Hatzikiriakos 00]. The degree of LCB can be more accurately described by defining a characteristic phase angle (δ_c) and modulus (G_c) which lie at the intersection of the two tangents through the neighbouring inflection points [Trinkle 01, Trinkle 02]. This analysis method is advantageous as normalisation to MW is not necessary, since only the shape of the MWD and degree of LCB affect the curve's form. The detection of LCB is however restricted to polymers with narrow monomodal MWDs, as bimodal and very broad MWDs result in similar deviations as seen for LCB.

The sensitivity of this analytical method can be clearly seen when the series of polyethylene-co-α-olefins was compared to a related homopolymer and reference polyethylene without LCB (Figure 2.39). The homopolymer can be seen to contain most LCB, with LCB decreasing with increasing comonomer content. It should be noted that the copolymers with the highest degree of SCB behaved like the reference material, suggesting no LCB was present. The extracted characteristic phase angle δ_c may then be used to relate the degree of LCB between systems (Figure 2.40). For example showing that longer co-α-olefins are more effective at suppressing LCB [Stadler 05].

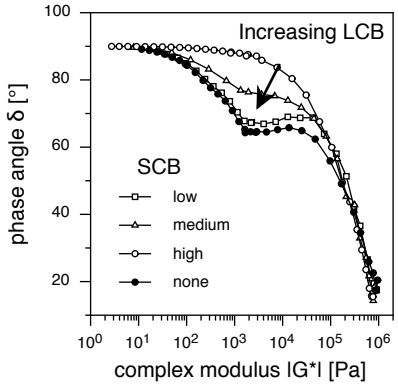

Figure 2.39: *δ-|G*|-plot for a series of PE-co-α-hexacosenes with increasing SCB showing a decrease in LCB. Adapted from [Stadler 05].*

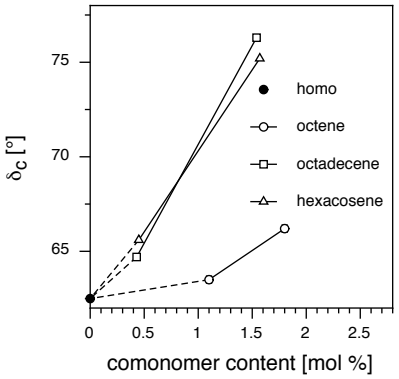

Figure 2.40: *Correlation of δ_c, from the δ-|G*|-plot, with the comonomer type and content. Adapted from [Stadler 05].*

Fourier-transform rheology

Fourier-transformation of the torque signals obtained during large angle oscillatory shear (LAOS) result in a mechanical frequency spectrum. This being analysed with respect to the relative intensities of the third and fifth harmonics to that of the fundamental as a function of strain amplitude. Recently the distinction by Fourier-transform rheology of branched polyethylenes that showed no difference in δ-$|G^*|$-plots has been shown [Fleury 04]. While the third harmonic was only able to distinguish between polethylenes with and without LCB, the fifth harmonic showed differences between LCB systems (Figure 2.41).

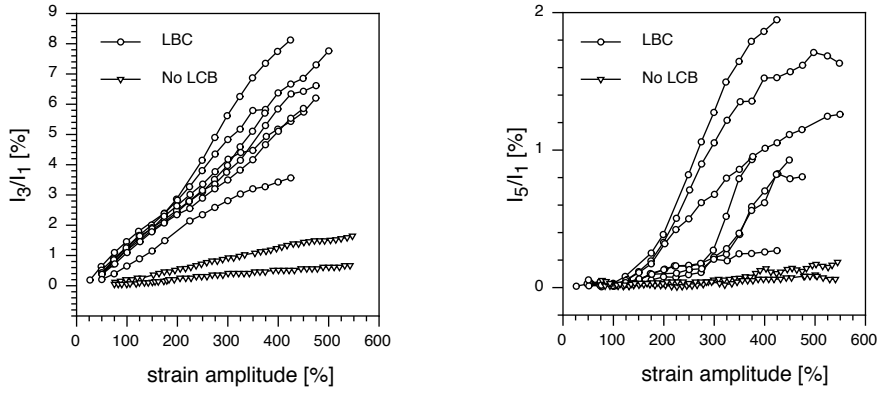

Figure 2.41: *Differentiation between commercial PEs using the relative intensity of the third harmonic (I_3/I_1) and fifth harmonic (I_5/I_1) as a function of strain amplitude. Adapted from [Fleury 04].*

2.4.5 Nuclear magnetic resonance (NMR)

It has been shown that the relatively inexpensive and reliable methods of FTIR, TREF and FT-DSC provide only qualitative results for the determination of SCB contents and distributions. In order for these techniques to provide quantitative results the construction of calibration curves relating to the absolute SCB contents is needed. Similary, although multi-detection SEC and rheology are very sensitive to LCB again only qualitative results may be achieved without external calibration.

In contrast to all the other analytical methods discussed nuclear magnetic resonance (NMR), and in particular ^{13}C NMR, can provide quantitative results regarding branch contents without external calibration. This is due to the area of the observed peak being directly proportional to the number of nuclear spins contributing to that peak. More importantly, through the use of the bulk CH_2 peak as an internal standard, absolute degrees of branching can be determined by simple spectral integration. For these reasons ^{13}C NMR, with its large chemical shift range, has become the standard method for comonomer content and sequence determination in polyolefins (Figures 2.42 and 2.43, Table 2.1) [Randall 89, De Pooter 91, Hansen 97, Liu 99, Seger 04].

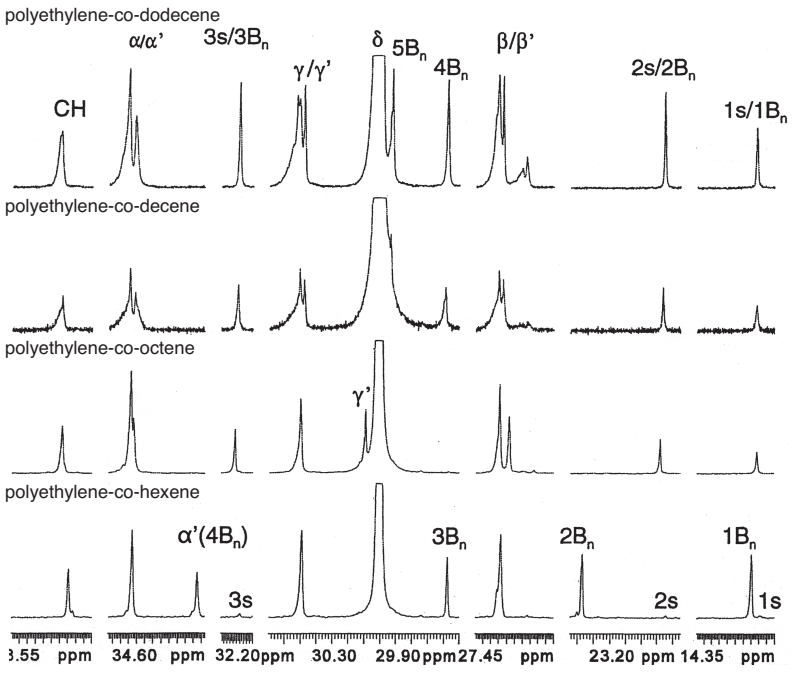

***Figure 2.42**: Solution-state ^{13}C NMR spectra of a series of polyethylene-co-α-olefins. For polyethylene ^{13}C NMR assignment nomenclature see Figure 2.43. Adapted from [Liu 99].*

High-field solution-state NMR at ν_{1_H} = 600 MHz has been shown to provide sufficient resolution to expand the configurational analysis from the pentad to the heptad level [Busico 02]. Recently, multidimensional pulsed field gradient (PFG) NMR methods, at 750 MHz and high temperature, have been shown to allow access to unambiguous resonance assignments of higher orders of comonomer sequences [Liu 01, Sahoo 03].

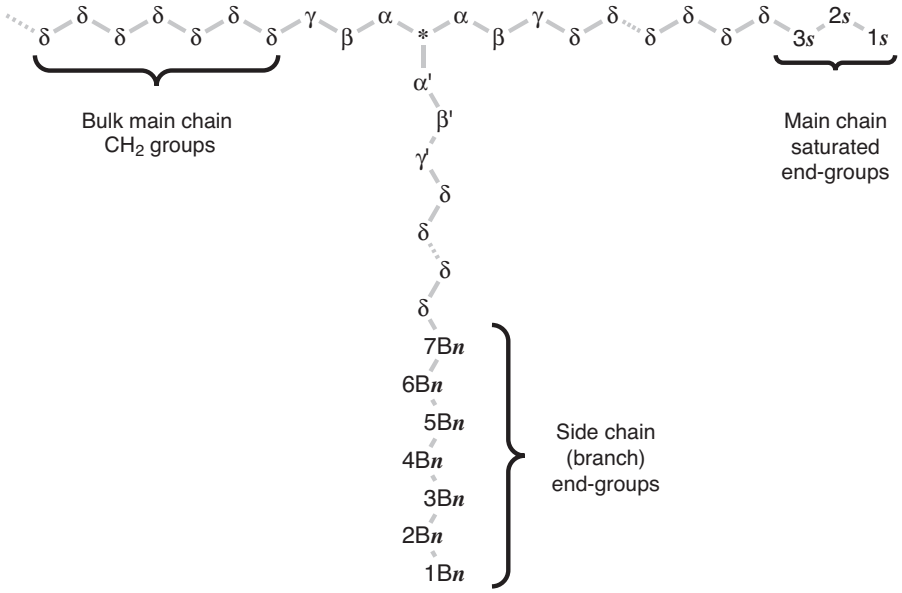

***Figure 2.43**: Carbon assignment of polyethylene-co-α-olefins [Liu 99].*

***Table 2.1**: Polyethylene-co-α-olefins ^{13}C chemical shift assignments as determined by solution-state NMR for varying SCB branch length (n). Adapted from [Liu 99].*

		branch length (n)				
		10	8	6	4	2
Main chain	1s	-	-	-	13.992	-
	2s	-	-	22.846	22.846	-
	3s	-	-	32.182	32.182	-
	δ	30.000	30.000	30.000	30.000	30.000
	γ	30.508	30.505	30.500	30.491	30.491
	β	27.355	27.351	27.343	27.334	27.357
	α	34.653	34.646	34.639	34.626	34.145
	$\star$	38.293	38.286	38.283	38.243	39.790
Side chain	nBn (α')	34.612	34.615	34.623	34.226	26.797
	[$n-1$]Bn (β')	27.326	27.325	27.286	29.573	-
	[$n-2$]Bn (γ')	30.479	30.478	30.093	23.367	-
	6Bn / 7Bn	30.016	-	-	-	-
	6Bn / 7Bn	29.985	-	-	-	-
	5Bn	29.925	29.935	-	-	-
	4Bn	29.574	29.591	-	-	-
	3Bn	32.184	32.195	32.213	-	-
	2Bn	22.852	22.864	22.881	-	-
	1Bn	14.015	14.018	14.020	14.046	11.158

Solution-state NMR has also been used to estimate LCB content in homopolymers [Malmberg 98, Yan 99, Wood-Adams 00, Shroff 01]. It was shown that very low levels of LCB were still able to be determined using extended measurement time. However, it should be noted that all LCB contents determined by NMR can only be regarded as upper limits of the LCB content. This is due to the peaks that are used for quantification not solely representing long-chain branches, but all branches containing 4 or more carbons. Unfortunately peaks resulting from longer branches in LCB containing polyethylenes are usually not resolved due to their low intensity and position close to the bulk CH_2 peak (Figure 2.44).

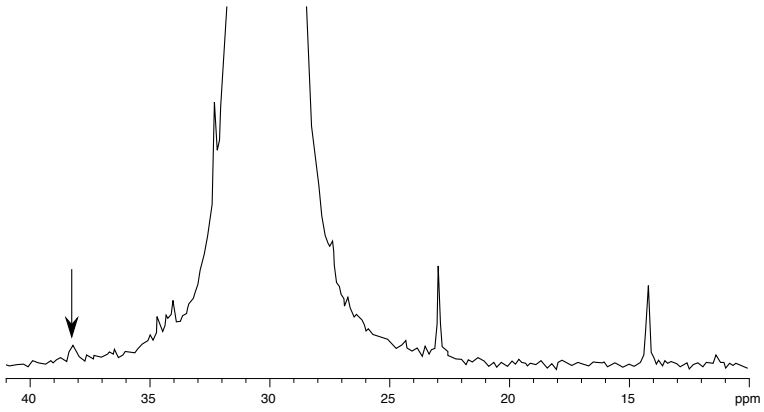

***Figure 2.44**: An example solution-state NMR spectrum of a polyethylene containing LCB indicating the resolved LCB site used for quantification. Reproduced from [Wang 98a].*

However, solution-state NMR measurements of polyolefins are hampered by their limited solubility. Generally polyolefins need to be heated to above their melting point in order to dissolve, thus requiring chlorinated solvents such as trichlorobenxene (TCB). Prolonged preparation times of up to 12 hours are also needed in order to generate the sufficiently homogeneous solutions required for NMR [Sahoo 03, Seger 04]. More importantly, the low solubility also results in low sample concentrations, thus leading to reduced NMR sensitivity as less NMR active ^{13}C nuclie are present. Thus, in order to achieve signal-to-noise ratios allowing reliable integration of low branch contents, extremely long measurement times of up to several weeks are needed [Wood-Adams 00].

NMR analysis of bulk polyolefins

Alternative NMR implementations to solution-state NMR without the need for solvents, such as solid-state NMR and melt-state NMR, have also been investigated for branch quantification [Dechter 81, Zeigler 94, Hatfield 95, Guo 00, Litvinov 02, Thakur 03]. However, due to the lack of isotropic motion, as found in the solution-state, these methods are not commonly implemented due to various resolution limitations.

Another problem related to bulk NMR analysis of polyolefins is the common use of additives for polymer stabilisation. Commonly, commercial polyolefins always contain anitoxidants (Figure 2.45), albeit at low concentrations of 0.01–1 wt-% [Koerner 02, Tice 03, Stadler 06].

The use of antioxidants becomes problematic when the quantification of sparse branching is considered. Although only small amounts of antioxidants are used they are present in the bulk sample at the same, or greater, concentration as the sparse branching itself. Thus, the peaks related to the antioxident are of similar

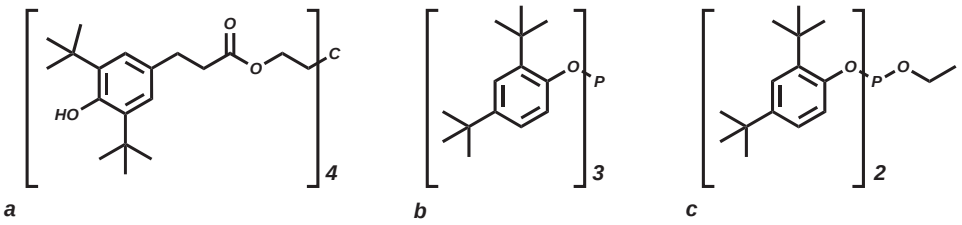

***Figure 2.45**: The chemical structures of the main commercial antioxidants used for polyethylene stabilisation: (a) Irganox 1010, (b) Irgafos 168 and (c) Irgafos 38.*

or greater intensity to that of the branching in question. Furthermore, some of the peaks from the antioxidents lie within the spectral region of interest hampering quantification, or in the worst-case-scenario rendering branch quantification impossible. Such problems may be alleviated by comparison of ^{13}C NMR spectra of common antioxidents. From the ^{13}C NMR spectra of Irgafos 168 and Irgafos 38 it can be seen that the latter is better suited for NMR based branch quantification, with less signals in the relevant spectral region (Figure 2.46). Even when considering the inherent resolution limitations, and problems related to measurement of unstabilised systems, bulk-state NMR analysis of polyolefins show promise for rapid branch quantification.

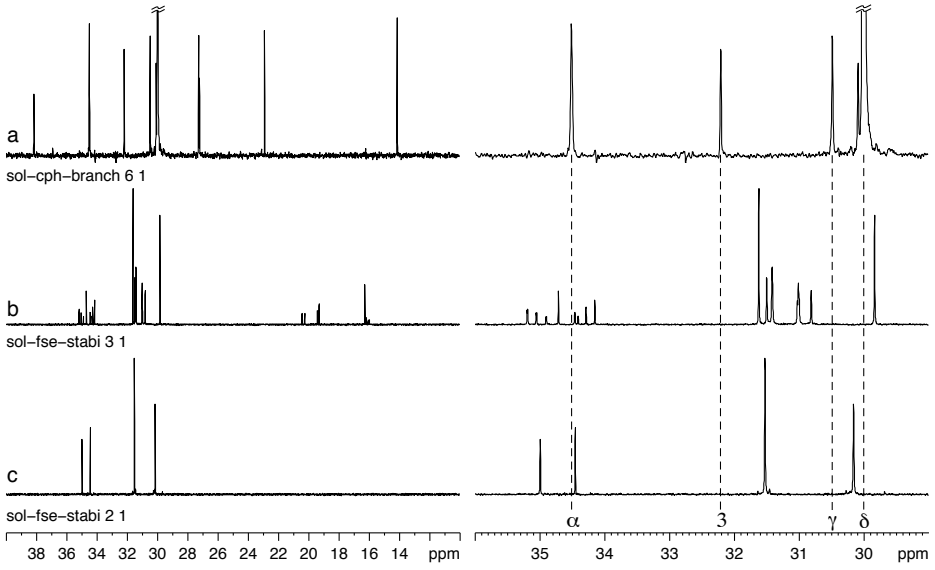

***Figure 2.46**: Solution-state ^{13}C NMR spectra of (a) polyethylene, (b) Irgafos 38 and (c) Irgafos 168 showing less peaks in the relevant spectral region for Irgafos 168.*

2.5 Polyolefins studied

In the following section the origin and physical properties (Table 2.2) of the polyolefins used throughout this body of work are given.

***Table 2.2**: Polyolefin materials investigated.*

Label	Comonomer		T_m	M_n	M_w	PDI
	C_nH_{2n}	mol-%	°C	kg mol^{-1}		
PE-O	-	-	140	0.6	0.6	1.0
PE0a	-	-	140	114	181	1.6
PE0b	-	-	141	23	117	5.1
PE0c	-	-	133	66	33	2.0
PE4a	4	6.5	90	48	96	2.0
PE4b	4	9.1	70	108	54	2.0
PE8	8	17.6	108	31	71	2.3
PE8a-A	8	1.0	125	95	179	1.9
PE8a-B	8	1.7	119	67	126	1.9
PE8a-C	8	2.0	116	57	100	1.8
PE8b-A	8	1.1	120	112	240	2.2
PE8b-B	8	1.8	116	92	190	2.1
PE8b-C	8	2.7	112	76	152	2.0
PE10	10	1.7	116	84	177	2.1
PE12	12	1.7	116	81	161	2.0
PE18-A	18	0.4	128	80	183	2.3
PE18-B	18	1.5	117	84	167	2.0
PE18-C	18	2.2	116	79	159	2.0
PE26-A	26	0.5	129	89	185	2.1
PE26-B	26	1.6	116	82	194	2.4
PE26-C	26	2.3	113	78	175	2.3
PP6-A	6	1.7	131	108	215	2.0
PP6-B	6	10.3	74	92	183	2.0
PP-γ-0	-	-	163	159	669	4.2
PP-γ-60	-	-	164	85	263	3.1
PP-γ-100	-	-	161	66	272	4.1
PP-γ-150	-	-	158	67	411	6.1

The polyethylenes and polypropylenes investigated here were obtained from several sources. A series of model polyethylene-co-α-olefins, of varying comonomer length and incorporation, were synthesised in the group of Prof. Kaminsky, Hamburg using the metallocene [Ph_2C(2,7-di-^{t}Bu-Flu)(Cp)]$ZrCl_2$ catalyst (Figure 2.19b) with methylaluminoxane (MAO) as cocatalyst [Kaminsky 05, Stadler 05]. The nomenclature of the polymers reflects the comonomer length and relative degree of incorporation, i.e. PE18-A and PE18-C represent two PE-co-octadecenes with the lowest and highest comonomer incorporation respectively. The two series PE8a and PE8b belong to different batches made with the same catalyst. A model temperature sensitive HDPE PE0c was synthesised using the metallocene rac-[Et$(Ind)_2$]$ZrCl_2$ catalyst (Figure 2.19a) and MAO as cocatalyst.

The samples PE-O and PE0b were obtained as linear standards from PSS, Mainz. The polyethylenes PE0b and PE8 were non-commercial industrial polyethylenes provided by Total SA, Feluy, Belgium. The polyethylenes PE4a, and PE4b were commercial industrial samples sold as Exxon Exact 3027 and Exact 4011 respectively.

Isotactic polypropylene-co-hexenes with low, PP6-A, and high, PP6-B, comonomer content were synthesised in the group of Prof. Quijada, Santiago Chile, via the metallocene rac-[Me_2Si(2-Me-Ind)$_2$]$ZrCl_2$ catalyst and MAO cocatalyst combination [Quijada 99].

To investigate the possible detection of LCB in PP an industrial polypropylene (Novolen PPH2150), here designated PP-γ-0, was subjected to increasing doses of γ-irradiation in the group of Prof. Münstedt, Erlangen. The particular dose is given in the nomenclature, i.e. PP-γ-150 indicates a dose of 150 kiloGray.

Chapter 3

General NMR Theory

In this chapter the basic NMR interactions are introduced and their averaging by motional processes discussed. A introduction to nuclear relaxation phenomena is given and their influence on both the measurement conditions and final spectra presented. Finally, an overview of the basic NMR techniques and data processing methods used for this body of work will be given.

3.1 NMR interactions

The quantum state of a sample is fully described by a wavefunction $|\psi_{\text{full}}\rangle$, which contains position, velocity, and spin information of all electrons and nuclei. The wavefunction obeys the time-dependent Schrödinger equation:

$$\frac{\mathrm{d}}{\mathrm{d}t}|\psi_{\text{full}}(t)\rangle = -i\hat{\mathcal{H}}_{\text{full}}|\psi_{\text{full}}(t)\rangle \tag{3.1}$$

where the Hamiltonian $\hat{\mathcal{H}}_{\text{full}}$ contains all the interactions present in the system. Although complete, it is useless, as it can never be solved for a realistic situation. However, a simplified form can be used where only the nuclear spin states are considered:

$$\frac{\mathrm{d}}{\mathrm{d}t}|\psi_{\text{spin}}(t)\rangle = -i\hat{\mathcal{H}}_{\text{spin}}|\psi_{\text{spin}}(t)\rangle \tag{3.2}$$

where $|\psi_{\text{spin}}\rangle$ is the spin state of the nuclei and $\hat{\mathcal{H}}_{\text{spin}}$ is the nuclear spin Hamiltonian. The latter only contains information about the direction of the nuclear spin polarisation. By doing so it is assumed that the rapid motion of the electrons can be regarded as an average, with these average interactions taken into account by the spin Hamiltonian $\hat{\mathcal{H}}_{\text{spin}}$. This massive simplification is known as the spin Hamiltonian hypothesis and holds for almost all systems at ordinary temperatures. From this point on the operator $\hat{\mathcal{H}}$ will be assumed to be the nuclear spin Hamiltonian $\hat{\mathcal{H}}_{\text{spin}}$

and the quantum state $|\psi\rangle$ to imply the nuclear spin state $|\psi_{\text{spin}}\rangle$.

The NMR interactions contributing to the spin Hamiltonian may originate from the external apparatus or from the sample itself and are classified as *external spin interactions* or *internal spin interactions*. The nuclear spin Hamiltonian can thus be written:

$$\hat{\mathcal{H}} = \hat{\mathcal{H}}_{\text{ext}} + \hat{\mathcal{H}}_{\text{int}} \tag{3.3}$$

External spin interactions are purely magnetic in origin and hence magnetic fields can be used to manipulate nuclear spins. The external spin Hamiltonian $\hat{\mathcal{H}}_{\text{ext}}$ contains the following terms:

Zeeman Interaction: $\hat{\mathcal{H}}_{\text{Z}}$
: these represent the direct magnetic interaction of a static external magnetic field and nuclear spins.

RF Interaction: $\hat{\mathcal{H}}_{\text{RF}}$
: these represent the direct magnetic interaction of a transverse-oscillating external magnetic field and nuclear spins

In contrast, the internal interactions originate from the sample itself and thus carry information regarding the nuclear environment. The internal spin Hamaltonian $\hat{\mathcal{H}}_{\text{int}}$ contains the following terms:

Quadrupolar Couplings: $\hat{\mathcal{H}}_{\text{Q}}$
: these represent the electronic interaction of spin $I > \frac{1}{2}$ nuclei with the surrounding electric fields.

Chemical Shift: $\hat{\mathcal{H}}_{\text{CS}}$
: these represent the indirect magnetic interaction of the static external magnetic field and the nuclear spins, through the involvement of the electrons.

Dipole-Dipole Couplings: $\hat{\mathcal{H}}_{\text{D}}$
: these represent the direct magnetic interactions of nuclear spins with each other.

J-Coupling: $\hat{\mathcal{H}}_{\text{J}}$
: these represent the indirect magnetic interaction of nuclear spins with each other, through the involvement of electrons.

The most important interactions influencing the spin Hamiltonian $\hat{\mathcal{H}}$ are, in order of typical strength: the Zeeman-interaction, quadrupolar coupling, interaction with RF pulses, chemical shift, dipole-dipole coupling and J-coupling:

$$\hat{\mathcal{H}} = \hat{\mathcal{H}}_{\mathrm{Z}} + \hat{\mathcal{H}}_{\mathrm{Q}} + \hat{\mathcal{H}}_{\mathrm{RF}} + \hat{\mathcal{H}}_{\mathrm{CS}} + \hat{\mathcal{H}}_{\mathrm{D}} + \hat{\mathcal{H}}_{\mathrm{J}} \tag{3.4}$$

The mathematical forms of the nuclear spin Hamiltonians can be complicated, however simplification can occur due to the secular approximation and by considering motional averaging. The secular approximation arises due to the interactions being dominated by the largest interaction with the static external magnetic field. In the secular approximation some components of the internal spin interaction $\hat{\mathcal{H}}_{\mathrm{int}}$ can be replaced by a simplified form, $\hat{\mathcal{H}}^0_{\mathrm{int}}$. If the molecules undergo rapid molecular motion, then the interaction terms fluctuate with time. If the molecular motion is sufficiently fast, the fluctuating interaction Hamiltonian $\hat{\mathcal{H}}^0_{\mathrm{int}}$ may be replaced by a motional averaged value $\overline{\hat{\mathcal{H}}}^0_{\mathrm{int}}$. The parts of $\hat{\mathcal{H}}^0_{\mathrm{int}}$ which have a zero time-average can then also be discarded. The motionally averaged spin Hamiltonian is usually a good approximation in gases and liquids, unless the molecular motion is slow. The discarded parts of the internal spin Hamiltonian terms then become partially responsible for the relaxation of the nuclear spin system:

$$\hat{\mathcal{H}}_{\mathrm{int}} \xrightarrow[\textit{relaxation}]{} \hat{\mathcal{H}}^0_{\mathrm{int}} \xrightarrow[\textit{relaxation}]{} \overline{\hat{\mathcal{H}}}^0_{\mathrm{int}} \tag{3.5}$$

Interaction representations

In general, the NMR interactions exhibit an orientation dependence with respect to the external static magnetic field $\boldsymbol{B}_0$, and are thus anisotropic. The part of an interaction Hamiltonian $\hat{\mathcal{H}}_\lambda$ that describes this orientation dependence can thus be represented as a second-rank tensor $\underline{A}_\lambda$, allowing $\hat{\mathcal{H}}_\lambda$ to be represented as a bilinear product [Mehring 83]:

$$\hat{\mathcal{H}}_\lambda = \hat{\boldsymbol{I}}_j \cdot \underline{A}_\lambda \cdot \hat{\boldsymbol{S}}_k \tag{3.6}$$

The spin angular momentum vector operators $\hat{\boldsymbol{I}}$ and $\hat{\boldsymbol{S}}$ can belong to: like spins (homonuclear dipolar coupling), unlike spins (heteronuclear dipolar coupling), the same spin (quadrupolar coupling) or one can represent a spin and the other a Cartesian vector of the $\boldsymbol{B}_0$ field (chemical shift). The most intuitive representation of the interaction tensor $\underline{A}$ is as a (3×3) spatial Cartesian matrix:

$$\underline{A} = \begin{pmatrix} A_{xx} & A_{xy} & A_{xz} \\ A_{yx} & A_{yy} & A_{yz} \\ A_{zx} & A_{zy} & A_{zz} \end{pmatrix} \tag{3.7}$$

Such a matrix can always be decomposed into three contributions:

$$\underline{A} = a + \begin{pmatrix} 0 & b & c \\ -b & 0 & d \\ -c & -d & 0 \end{pmatrix} + \begin{pmatrix} e & g & h \\ g & f & i \\ h & i & (-e-f) \end{pmatrix} \tag{3.8}$$

where the first term a denotes the isotropic part, this being one third the trace of the tensor:

$$a = \frac{1}{3}\mathsf{Tr}\{\underline{A}\} = \frac{1}{3}\{A_{xx} - A_{yy} - A_{zz}\} \tag{3.9}$$

The second term of Equation 3.8 being a traceless antisymmetric matrix of three components, and the third term a traceless symmetric matrix of five components. Alternatively the interaction tensor $\underline{A}$ can be described by the irreducible spherical tensor representation, consisting of a scalar, and two vectors of dimension (1×3) and (1×5):

$$\underline{A} = A_0 + \Big(A_{1-1}, A_{10}, A_{11}\Big) + \Big(A_{2-2}, A_{2-1}, A_{20}, A_{21}, A_{22}\Big) \tag{3.10}$$

The reason for using the irreducible spherical tensor representation lies in the favourable transformation behaviour of the spherical tensor components, which transform identically to the spherical harmonics Y_{Lm}, with familiar multiplicity of $2L+1$ and $m = -L, -L+1 \ldots + L$. This greatly simplifies the mathematical description of rotations, inevitable in solid-state NMR, since only linear combinations need to be performed instead of costly matrix multiplication. The interaction Hamiltonian in the spherical tensor representation reads:

$$\mathfrak{H}_\lambda = \sum_{k=0}^{2} \sum_{q=-k}^{k} (-1)^q \mathcal{A}_{kq}\, \hat{\mathfrak{T}}_{k-q} \tag{3.11}$$

where $\hat{\mathfrak{T}}_{k-q}$ are the irreducible spherical spin tensor operators of rank k and order $-q$. Another advantage of this mathematical description arises from the separation of rotations in *real-space* caused by physical motion, and those of the spins in *spin-space* caused by RF-pulses. Thus separating the space part $\mathcal{A}$ and spin part $\hat{\mathfrak{T}}$ of the interaction Hamiltonian:

$$\mathfrak{H}_\lambda = \mathcal{A} \cdot \hat{\mathfrak{T}} \tag{3.12}$$

3.1.1 Zeeman-interaction

The strongest interaction, and inherently most important to NMR, is the Zeeman interaction, the interaction of a nuclear spin I with an external static magnetic field $\boldsymbol{B}$ for nuclei with spin quantum number $I \geq \frac{1}{2}$. In the presence of a magnetic field, this interaction causes the normally degenerate $2I + 1$ nuclear spin energy levels, defined by the magnetic nuclear spin quantum number $m_I = -I, -I + 1, \ldots + I$, to have different energies. The breakdown of this degeneracy enables the absorption and emission of energy in the form of electromagnetic radiation (Figure 3.1).

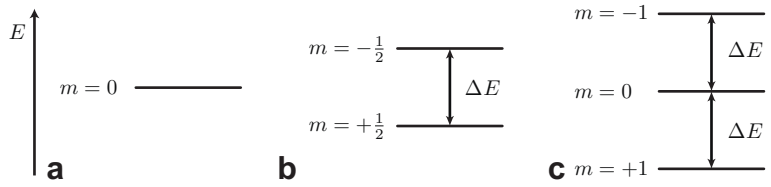

***Figure 3.1**: Energy level diagram illustrating the breakdown of nuclear spin degeneracy upon the application of a magnetic field for (a) $I = 0$, (b) $I = \frac{1}{2}$ and (c) $I = 1$. $\Delta E = \hbar\omega_L = \hbar\gamma_j B$*

The individual energies of the Zeeman levels are given by:

$$E_m = -m\gamma_j \hbar B \tag{3.13}$$

For nuclei with $I = \frac{1}{2}$, the energy difference between the two Zeeman levels is $\Delta E = -\gamma\hbar B = \hbar\omega_L$, where ω_L is the so-called Larmor frequency. This means that each isotope can have different Larmor frequencies depending on the magnet used for NMR. For example, a proton in a 7 T magnetic field has a Larmor frequency of $\approx$ 300 MHz, whereas in a 11.7 T magnet it has a Larmor frequency of $\approx$ 500 MHz.

If the external magnetic field is oriented along the z-axis, the corresponding Hamiltonian $\hat{\mathcal{H}}_Z$ is:

$$\hat{\mathcal{H}}_Z = -\gamma_j \hbar \boldsymbol{B} \hat{I}_z \tag{3.14}$$

Secular approximation

For strong external magnetic fields the influence of the B_x and B_y components of $\boldsymbol{B}$ can be considered to be negligible as compared to the B_z-component. The magnetic field vector can thus be approximated to:

$$\boldsymbol{B} \approx \begin{pmatrix} 0 & 0 & B_z \end{pmatrix} = \boldsymbol{B}_0 \tag{3.15}$$

Under such conditions the Zeeman interaction exceeds all other interactions by a large degree. This allows the weaker interactions to be treated as perturbations of

the Zeeman interaction in the z direction. The secular approximation leads to some components of the internal spin interactions being masked by the strong Zeeman interaction, thus simplifying the internal interaction Hamiltonians $\hat{\mathcal{H}}_{int}$. This can be understood by considering the energy-level diagram for systems where all interactions are considered. In the secular approximation some near-degenerate energy levels are considered to be fully degenerate, and thus simplify the energy level diagram. The interaction Hamiltonian may now be divided into a *secular* and *non-secular* part, depending if their components commute with I_z or not. Only the secular Hamiltonians $\hat{\mathcal{H}}_0$ are now considered to contribute to the observable spectrum:

$$\hat{\mathcal{H}} = \hat{\mathcal{H}}_0 + \hat{\mathcal{H}}' \approx \hat{\mathcal{H}}_0 \tag{3.16}$$

The secular, or high-field approximation, is valid for all cases presented in this body of work.

3.1.2 The effect of radio frequency pulses

The application of a radio frequency (RF) pulse does not merely excite the spin system, it does so in a well-defined manner. Understanding this interaction allows detailed manipulation of the spin system, and facilitates access to much more information than the chemical shift of the nuclei and their relative abundance alone. This has lead to a huge number of 'pulse-sequences' being developed, and the continued interest in Fourier-transform (FT) NMR spectroscopy.

The RF coil generates a magnetic field along the x-axis of the laboratory reference frame. During a pulse the magnitude of the field oscillates at the Larmor frequency ω_L, and between pulses the field is equal to zero:

$$\boldsymbol{B}^{\mathrm{RF}}_{on}(t) = B_{\mathrm{RF}} \cos(\omega_L t + \phi_p)\boldsymbol{e}_x \tag{3.17}$$

$$\boldsymbol{B}^{\mathrm{RF}}_{off}(t) = 0 \tag{3.18}$$

where $\boldsymbol{e}_x$ is a unit vector along the x-axis and B_{RF} the maximum amplitude of the transverse magnetic field during the pulse. It is convenient to visualise this oscillating field as two counter rotating vectors representing the resonant and non-resonant components. The resonant component rotates with the Larmor precession and the non-resonant component in the opposite direction:

$$\boldsymbol{B}_{\mathrm{RF}}(t) = \boldsymbol{B}^{\mathrm{RF}}_{res}(t) + \boldsymbol{B}^{\mathrm{RF}}_{non\text{-}res}(t) \tag{3.19}$$

where:

$$\boldsymbol{B}^{\mathrm{RF}}_{res}(t) = -\frac{1}{2}\gamma_j B_{\mathrm{RF}}\{\cos(\omega_L t+\phi_p)\boldsymbol{e}_x + \sin(\omega_L t+\phi_p)\boldsymbol{e}_y\} \tag{3.20}$$

$$\boldsymbol{B}^{\mathrm{RF}}_{non\text{-}res}(t) = -\frac{1}{2}\gamma_j B_{\mathrm{RF}}\{\cos(\omega_L t+\phi_p)\boldsymbol{e}_x - \sin(\omega_L t+\phi_p)\boldsymbol{e}_y\} \tag{3.21}$$

The non-resonant component has almost no influence on the spins, and may be neglected. The corresponding Hamiltonian for the effect of an RF pulse is therefore:

$$\hat{\mathcal{H}}_{\mathrm{RF}}(t) \approx -\frac{1}{2}\gamma_j B_{\mathrm{RF}}\{\cos(\omega_L t+\phi_p)\hat{I}_x + \sin(\omega_L t+\phi_p)\hat{I}_y\} \tag{3.22}$$

The quantity $|\frac{1}{2}\gamma_j B_{\mathrm{RF}}|$ is proportional to the maximum RF field created by the coil. This is called the nutation frequency ω^j_{nut} and is a measure of how strong the RF field influences the spins. Typically the nutation frequency is in the range 1–200 kHz, even under the strongest RF pulses this is still three to four orders of magnitude less than the Larmor frequency.

When describing the interaction of RF pulses on a spin system it is convenient to use the rotating frame of reference. This being the result of constant rotation of the laboratory frame about $\boldsymbol{B}_0$ at the Larmor frequency.

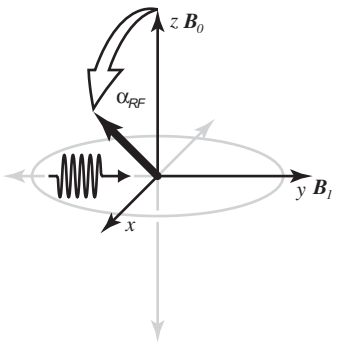

***Figure 3.2**: The effect of an α_y pulse on the equilibrium state $\hat{I}_z$.*

When the RF field is created by the coil, an oscillating magnetic field $\boldsymbol{B}_{\mathrm{RF}}$ is applied perpendicular to $\boldsymbol{B}_0$. In the rotating frame the oscillating field $\boldsymbol{B}_{\mathrm{RF}}$ appears static, thus simplifying the treatment of RF pulses. The static field $\boldsymbol{B}_1$ applies a torque to the magnetisation, which in the initial equilibrium state is aligned along the z-axis, causing it to turn about the axis of the applied field, towards the xy plane. The effect of a pulse of the length t_{RF} is a rotation of the magnetisation by an angle α_{RF}:

$$\alpha_{\mathrm{RF}} = -\gamma B_1(t)\cdot t_{\mathrm{RF}} = \omega_1(t)\cdot t_{\mathrm{RF}} \tag{3.23}$$

Consequently, pulses are described by their resulting effect, i.e. a pulse applied along the y-axis resulting in a tip of the magnetisation from the z-axis into the x-axis according to the right-hand rule[†] is denoted as a 90°_y, or $\frac{\pi}{2}{}_y$ pulse (Figure 3.2). The phase of the RF irradiation ϕ_p is directly related to the phase of the pulse, i.e. if the phase of the RF irradiation was shifted by $\frac{\pi}{2}$ it would result in a 90°_x or $\frac{\pi}{2}{}_x$ pulse, placing the magnetisation along the $-y$-axis.

[†]Whether the pulse applies a clockwise or anticlockwise torque is arbitrary, however once chosen the convention must be retained throughout a description of an NMR experiment.

Product operator formalism

To simplify determining the outcome of a pulse on a system the product-operator formalism was introduced by Ernst and co-workers [Sørensen 83]. In the product-operator formalism the effect on the equilibrium magnetisation $\hat{I}_z$ during an α_y pulse simplifies to:

$$\hat{I}_z \xrightarrow{\alpha\hat{I}_y} \hat{I}_z \cos\alpha + \hat{I}_x \sin\alpha \tag{3.24}$$

with the common rotations listed in Table 3.1. The product operator formalism is not only restricted to the description of RF-pulses, but can also describe the time evolutions of most NMR interactions provided the corresponding Hamiltonian is time independent, or time averaged.

***Table 3.1**: The effect of propagators by the product operator formalism.*

	$\alpha\hat{I}_x$	$\alpha\hat{I}_y$	$\alpha\hat{I}_z$
$\hat{I}_x$	$\hat{I}_x$	$\hat{I}_x\cos\alpha - \hat{I}_z\sin\alpha$	$\hat{I}_x\cos\alpha + \hat{I}_y\sin\alpha$
$\hat{I}_y$	$\hat{I}_y\cos\alpha + \hat{I}_z\sin\alpha$	$\hat{I}_y$	$\hat{I}_y\cos\alpha - \hat{I}_x\sin\alpha$
$\hat{I}_z$	$\hat{I}_z\cos\alpha - \hat{I}_y\sin\alpha$	$\hat{I}_z\cos\alpha + \hat{I}_x\sin\alpha$	$\hat{I}_z$

3.1.3 Quadrupolar coupling

Nuclei with a spin $I \geq 1$ exhibit a nuclear-electric quadrupole moment which interacts with the local electric field gradient of the molecule. It is quite extraordinary that all nuclei with $I < 1$, no matter how many nucleons are present, do not interact with the electric field and can be treated as a single point charge. The Hamiltonian for the quadrupolar coupling is given by:

$$\mathfrak{H}_Q = \hat{I}_i \cdot \underline{Q} \cdot \hat{I}_i \tag{3.25}$$

where $\underline{Q}$ is the electric quadrupolar interaction tensor, defined as:

$$\underline{Q} = \frac{e \cdot Q}{2I(2I-1)\hbar} \cdot \underline{V} \tag{3.26}$$

where $\underline{V}$ is the local electric field gradient tensor. For deuterons ($I = 1$) the quadrupolar splitting is around 125 kHz, which is sufficiently lower than the Larmor frequency and thus the secular approximation remains valid. The NMR spectra of deuterons are however dominated by the quadrupolar interaction. If θ and ϕ are the polar orientation of the $\boldsymbol{B}_0$-field with respect to a defined principle axis system (PAS) of the quadrupolar coupling tensor, the quadrupolar frequency is given by:

$$\omega_Q = \pm\frac{\delta_Q}{2}\left(3\cos^2\theta - 1 - \eta_Q \sin^2\theta\cos 2\phi\right) \tag{3.27}$$

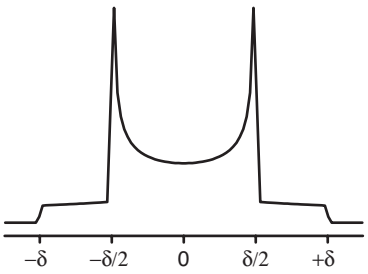

***Figure 3.3**: Pake-pattern.*

The orientation dependence of the quadrupolar coupling with the second Legendre polynomial P_2 leads to the well-known Pake-pattern in the solid-state [Pake 48]. Due to an isotropic distribution of nuclei amongst all possible orientations this is also known as a powder average of the quadrupolar coupling, leading to a powder pattern (Figure 3.3). Typically, molecular motion leads to a characteristic narrowing of the Pake-pattern, yielding information on the geometry and the timescale of a dynamic process.

3.1.4 Chemical shift

The chemical shift is the most important internal interaction in NMR since it is highly sensitive to the chemical enviroment. This has led to NMR becoming one of the most important, if not the most important, structure elucidation techniques available to mankind today. The chemical shift is caused by the electrons surrounding nuclei shielding them from the external magnetic field $\boldsymbol{B}_0$. Thus the nuclei experience an effective magnetic field;

$$\boldsymbol{B}_{\text{eff}} = \boldsymbol{B}_0 - \left(\underline{\sigma} \cdot \boldsymbol{B}_0 \right) \tag{3.28}$$

With the electron density around a particular nucleus not only depending on the nuclei involved in bonding, but also the type and geometry of bonding, the chemical shift is highly sensitive to the chemical environment. Due to the sensitivity towards geometry, the chemical shielding is generally anisotropic in nature and is best described by the chemical shielding tensor $\underline{\sigma}$ such that:

$$\hat{\mathcal{H}}_{\text{CS}} = \gamma \hat{I} \cdot \underline{\sigma} \cdot \boldsymbol{B}_0 \tag{3.29}$$

which under the secular approximation reduces to:

$$\hat{\mathcal{H}}^0_{\text{CS}} = \gamma \left(\hat{I}_x \sigma^{\text{LAB}}_{xz} + \hat{I}_y \sigma^{\text{LAB}}_{yz} + \hat{I}_z \sigma^{\text{LAB}}_{zz} \right) B_0 \tag{3.30}$$

The chemical shielding tensor $\underline{\sigma}$ can be decomposed into isotropic, symmetric and anti-symmetric parts according to Equation 3.8:

$$\underline{\sigma} = \sigma_{\text{iso}} + \boldsymbol{\sigma}_{\text{asym}} + \boldsymbol{\sigma}_{\text{sym}} \tag{3.31}$$

However, the antisymmetric part $\boldsymbol{\sigma}_{\text{asym}}$ can be neglected within the secular approximation and will not be further discussed.

Chemical shift anisotropy

When diagonalised, the symmetric part of the chemical shift Hamiltonian $\boldsymbol{\sigma}_{\mathrm{sym}}$ provides information regarding the anisotropy of the shielding. This is because the placing of all elements onto the diagonal is equivalent to a transformation into the principal axis system [Spiess 78]. In the principle axis system $\underline{\sigma}$ has the following form:

$$\underline{\sigma} = \sigma_{\mathrm{iso}} + \Delta \begin{pmatrix} -\frac{1}{2} + \frac{\eta}{2} & 0 & 0 \\ 0 & -\frac{1}{2} - \frac{\eta}{2} & 0 \\ 0 & 0 & 1 \end{pmatrix} \tag{3.32}$$

where Δ is the so-called anisotropy parameter and η is the asymmetry parameter:

$$\Delta = \omega_L(\sigma_{zz}^{\mathrm{PAS}} - \sigma_{\mathrm{iso}}) \qquad \eta = \frac{\sigma_{yy}^{\mathrm{PAS}} - \sigma_{xx}^{\mathrm{PAS}}}{\sigma_{zz}^{\mathrm{PAS}} - \sigma_{\mathrm{iso}}} \tag{3.33}$$

The symmetric part of the chemical shielding tensor $\boldsymbol{\sigma}_{\mathrm{sym}}$ is commonly referred to as chemical shift anisotropy (CSA). In gases, liquids and solutions where fast isotropic motion readily occurs, the CSA is averaged to zero leaving only the isotropic chemical shift (see Equation 3.50). However, in solids where isotropic motion is not normally present, the orientation dependence of the CSA leads to significantly broader line shapes. If θ and ϕ are the polar orientation of the $\boldsymbol{B}_0$-field in the principle axis system of the chemical shielding tensor, the anisotropic frequency (in analogy to Equation 3.27) is given by:

$$\omega_{\mathrm{CS}} = \frac{\Delta}{2}\left(3\cos^2\theta - 1 - \eta\sin^2\theta\cos 2\phi\right) \tag{3.34}$$

The theoretical powder line shape has been calculated in general [Bloembergen 53] and can be found in most solid-state NMR textbooks [Mehring 83, Schmidt-Rohr 94]. For an isotropic distribution of orientations, i.e. a powder average, characteristic spectra for different η are seen (Figure 3.4).

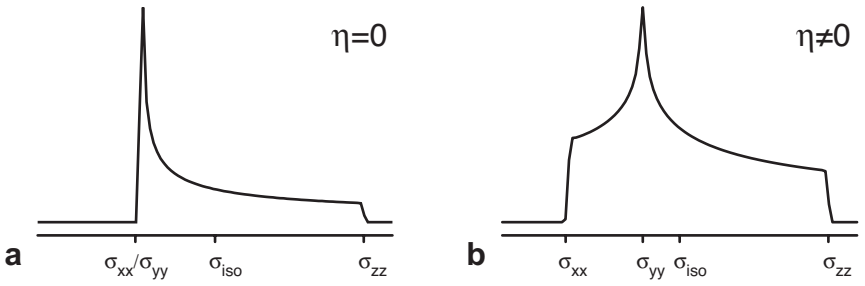

***Figure 3.4**: Typical line shapes for (a) symmetric and (b) asymmetric CSA tensors.*

Chemically shifted Larmor frequency

The chemical shift is not directly measured, with only the effect on the Larmor frequency detected. It is thus convenient to combine the Zeeman and chemical shift interactions:

$$\hat{\mathcal{H}}_Z + \hat{\mathcal{H}}_{CS} = \hat{\mathcal{H}}_{Z+CS} = \delta \hat{I}_z \tag{3.35}$$

where δ is the chemically shifted Larmor frequency, and is related to the chemical shift by:

$$\delta = -\gamma B_0(1+\sigma) \tag{3.36}$$

As these formulae neglect susceptibility effects the origin of the δ scale must be calibrated using a reference compound of known chemical shift. To allow comparison of spectra taken for the same nuclei at different external fields the unit for this scale is parts-per-million (ppm) of the corresponding Larmor frequency.

3.1.5 Dipole-dipole coupling

The dipole-dipole interaction involves the interaction of a spin $\hat{I}_j$ with the local magnetic field generated by another spin $\hat{I}_k$. The interaction is mutual, with spin $\hat{I}_k$ also interacting with the magnetic field generated by spin $\hat{I}_j$. Thus, spin-coupling occurs. This interaction propagates through the intervening space between nuclei without the involvement of electrons. The full title for the interaction is the direct through-space dipole-dipole interaction, or more concisely the dipolar coupling.

The full form of the spin Hamiltonian for dipole-dipole interaction between spins $\hat{I}_j$ and $\hat{I}_k$ is given by:

$$\hat{\mathcal{H}}^{jk}_{D,full} = D_{jk}\left(3(\hat{\boldsymbol{I}}_j \cdot \boldsymbol{e}_{jk})(\hat{\boldsymbol{I}}_k \cdot \boldsymbol{e}_{jk}) - \hat{\boldsymbol{I}}_j \cdot \hat{\boldsymbol{I}}_k\right) \tag{3.37}$$

where $\boldsymbol{e}_{jk}$ is a unit vector parallel to the internuclear vector, such that $\boldsymbol{e}_{kj} \cdot \boldsymbol{e}_{jk} = 1$. The magnitude of the interaction is given by the dipolar coupling constant D_{jk}:

$$D_{jk} = -\frac{\mu_0}{4\pi}\frac{\gamma_j \gamma_k \hbar}{r^3_{jk}} \tag{3.38}$$

where γ_j and γ_k are the gyromagnetic ratios of the two spins and r_{jk} the distance between the spins. The interaction also scales linearly with the gyromagnetic ratio of each spin, thus for the same internuclear distance and $\gamma_I > \gamma_S$: $D_{II} > D_{IS} > D_{SS}$. For example, for two spins with $r_{jk} = 1$ Å : $D_{HH} = 120.1$ kHz, $D_{CH} = 30.2$ kHz and $D_{CC} = 7.6$ kHz. With such large proton homonuclear dipolar coupling, one would expect the ^{1}H spectrum to be dominated by the dipolar coupling, and this is true

in the solid-state. In liquids and gases however, the rapid molecular motion present averages the dipolar coupling to its isotropic value of zero (Section 3.2.1).

Although the dipolar coupling constant D_{jk} is not orientation dependent the dipolar Hamiltonian $\hat{\mathcal{H}}_{\mathrm{D}}$ is, due to the internuclear vector term $\boldsymbol{e}_{jk}$ (Equation 3.37). The nature of this orientation dependence is clearly seen when the secular approximation is applied to the dipolar interaction.

Secular dipole-dipole coupling

In a sample containing many spins, each pair of spins has a dipolar coupling, leading to the overall dipolar Hamiltonian being given by:

$$\hat{\mathcal{H}}^{jk}_{\mathrm{D},full} = \sum_{k}\sum_{j}^{k-1} \hat{\mathcal{H}}^{jk}_{\mathrm{D},full} = \sum_{j<k} \hat{\mathcal{H}}^{jk}_{\mathrm{D},full} \tag{3.39}$$

For homonuclear dipolar coupling the secular part of the dipolar spin Hamiltonian is given by:

$$\hat{\mathcal{H}}^{jk}_{\mathrm{D}} = d_{jk}\left(3\hat{I}^{j}_{z}\hat{I}^{k}_{z} - \hat{\boldsymbol{I}}_{j}\cdot\hat{\boldsymbol{I}}_{k}\right) \tag{3.40}$$

For heteronuclear dipolar coupling the secular part of the dipolar Hamaltonian simplifies to:

$$\hat{\mathcal{H}}^{jk}_{\mathrm{D}} = d_{jk}\left(2\hat{I}^{j}_{z}\hat{I}^{k}_{z}\right) \tag{3.41}$$

Both the homonuclear (Equation 3.40) and heteronuclear (Equation 3.41) dipolar coupling Hamiltonians contain the secular dipolar coupling constant d_{jk}. The full dipolar coupling constant D_{jk} is only dependent on the distance between the spins, and not orientation. The secular dipolar coupling constant d_{jk} however depends on both the distance and orientation. The secular dipolar coupling constant d_{jk} is related to the full dipolar coupling constant D_{jk} in the following way:

$$d_{jk} = D_{jk}\frac{1}{2}\left(3\cos^{2}\theta_{jk} - 1\right) \tag{3.42}$$

where θ_{jk} is the angle between the internuclear vector and the external magnetic field such that $\cos\theta_{jk} = \boldsymbol{e}_{jk}\cdot\boldsymbol{e}_{z}$. There are two important points to note about Equation 3.42; firstly d_{jk} has opposite signs for spin-pairs aligned with the field ($\theta_{jk} = 0$) as compared to spin-pairs oriented perpendicular to the field ($\theta_{jk} = \pi/2$). Secondly, d_{jk} is equal to zero when $\theta_{jk} = 54.74^{\circ} = \arctan\sqrt{2}$, satisfying the equation: [†]

$$3\cos^{2}\theta_{jk} - 1 = 0 \tag{3.43}$$

[†] there is also a solution to Equation 3.43 at $\theta_{jk} = \pi - \theta_{M} \approx 125.26^{\circ}$

These two observations have important repercussions as they allow the dipolar interaction to be averaged by physical manipulation of the sample with respect to the field.

3.1.6 J-coupling

The J-coupling interaction involves the indirect, electron-mediated coupling of spin $\hat{I}_j$ to spin $\hat{I}_k$ and *vice versa*. Each spin weakly magnetises the molecular electrons, generating a weak magnetic field at the site of the second spin. For this reason the J-coupling is also known as the indirect spin-spin coupling, in contrast to the direct spin-spin coupling of dipolar-coupling. The J-coupling is exclusively intramolecular in nature and only occurs between two spins linked through a small number of chemical bonds.

The full form of the spin Hamiltonian for J-coupling interaction between spins $\hat{I}_j$ and $\hat{I}_k$ is given by:

$$\hat{\mathcal{H}}^{jk}_{\mathrm{J},full} = \hat{\boldsymbol{I}}_j \cdot \underline{J}_{jk} \cdot \hat{\boldsymbol{I}}_k \tag{3.44}$$

where $\underline{J}_{jk}$ is the J-coupling tensor. Since the J-coupling interaction is orientation dependent it is also averaged to an isotropic value by rapid molecular motion. In contrast to chemical shift, J-coupling does not depend on the applied magnetic field. Thus, one-bond heteronucler J-couplings between ^{1}H and ^{13}C nuclei are typically 135 Hz with lower values of 50 Hz observed for one-bond homonuclear J-couplings between two ^{13}C nuclei.[†]

Secular J-coupling

For homonuclear J-coupling the secular part of the J-coupling Hamiltonian is:

$$\hat{\mathcal{H}}^{jk}_{\mathrm{J}} = J_{jk}\left(\hat{\boldsymbol{I}}_j \cdot \hat{\boldsymbol{I}}_k\right) \tag{3.45}$$

Whereas for the heteronuclear J-coupling the secular part of the J-coupling Hamiltonian simplifies to:

$$\hat{\mathcal{H}}^{jk}_{\mathrm{J}} = J_{jk}\left(\hat{I}^j_z \hat{I}^k_z\right) \tag{3.46}$$

Both the homonuclear (Equation 3.45) and heteronuclear (Equation 3.46) J-coupling Hamiltonians contain the the secular J-coupling constant J_{jk}. For the case of isotropic motion this is equal to one third the trace of the J-coupling tensor $\underline{J}_{jk}$.

[†] A factor or 2π is needed in Equations 3.44–3.46 in order to give J-couplings in the common units of Hz.

3.2 Motional interaction averaging

Molecular motion leads to time-dependent interaction Hamiltonians $\hat{\mathcal{H}}_\lambda(t)$. However depending on the type of motion and the timescale over which this molecular motion takes place, an averaged Hamiltonian $\overline{\hat{\mathcal{H}}}_\lambda$ may be used as an approximation instead of the full time-dependant Hamiltonian.

The relevant modes of molecular motion are molecular translations and rotations which both depend on the phase of matter in which the studied sample resides. Such relevant molecular translations occur readily in liquids and gases while molecular rotations may be found in gases, liquids and some solids. Anisotropic motion may also be found in liquid-crystals, however such anisotropic-liquids will not be further discussed [Levitt 01].

Due to the anisotropic nature of most of the interaction Hamiltonians, molecular rotations are of particular importance to NMR. Such rotations change the spatial orientation of the molecule and, with sufficient time, result in the molecules sampling all possible spatial orientations [Levitt 01]. This allows the initial time-average to be replaced by an orientational average Hamiltonian containing the probability density $p(\Theta)$ of the molecule having a certain orientation Θ. The orientational average Hamiltonian is then given by integration over all Θ:

$$\overline{\hat{\mathcal{H}}}_\lambda = \tau^{-1} \int_0^\tau \hat{\mathcal{H}}_\lambda(\Theta, t)\, \mathrm{d}t = \int p(\Theta) \hat{\mathcal{H}}_\lambda \, \mathrm{d}\Theta \tag{3.47}$$

3.2.1 Isotropic molecular motion

In gases and isotropic liquids, where $p(\Theta)$ is the same for all orientations, molecular rotations average all intramolecular spin interactions to their isotropic average values $\hat{\mathcal{H}}_\lambda^{iso}$:

$$\hat{\mathcal{H}}_\lambda^{iso} = N^{-1} \int \hat{\mathcal{H}}_\lambda(\Theta)\, \mathrm{d}\Theta \tag{3.48}$$

where N is the normalisation constant so that the total probability is equal to unity.

Additionally, the rapid molecular translations present in gases also average all intermolecular spin interactions essentially to zero. In contrast, only the short-range intermolecular spin interactions are averaged to zero in isotropic liquids due to the diffusional motion of the molecules.

Isotropic chemical shift

Under true isotropic motion, the chemical shift anisotropy (CSA) is averaged to zero and the motionally averaged chemical shift Hamiltonian becomes purely dependent

on the isotropic part σ_{iso} of the chemical shielding tensor:

$$\hat{\mathcal{H}}_{\mathrm{CS}}^{iso} = -\gamma \hat{I}_z \cdot \sigma_{iso} \cdot B_0 \tag{3.49}$$

where σ_{iso} is the isotropic chemical shift and is equal to the trace of the chemical shielding tensor. The isotropic chemical shift is also equal to the average of σ_{zz} over all possible molecular orientations:

$$\sigma_{\mathrm{iso}} = \frac{1}{3}\mathsf{Tr}\,\underline{\sigma} = \frac{1}{3}\Big(\sigma_{xx} + \sigma_{yy} + \sigma_{zz}\Big) = N^{-1}\int \sigma_{zz}(\Theta)\,\mathrm{d}\Theta \tag{3.50}$$

Although the individual terms σ_{xx}, σ_{yy} and σ_{zz} are dependent on molecular orientation, their sum and orientational average is not. Hence, the isotropic chemical shift σ_{iso} is orientation independent and only provides information regarding the magnitude of the interaction.

Isotropic quadrupolar coupling

In an isotropic liquid, the orientation dependant quadrupolar frequency ω_{Q} (Equation 3.27) averages to zero, and hence so does the quadrupolar Hamiltonian $\hat{\mathcal{H}}_{\mathrm{Q}}^{iso} = 0$. While the quadrupolar interactions do not change the isotropic chemical shifts, they do have a strong influence on the relaxation of nuclear spins $> \frac{1}{2}$ in isotropic environments (Equation 3.5).

Isotropic dipolar coupling

With isotropic molecular rotations sampling all orientations, the secular part of the intramolecular dipolar coupling averages to zero due to its orientation dependence (Equation 3.37). This can be shown by integrating the orientation-dependent secular dipolar coupling constant (Equation 3.42), weighted by $\sin\theta_{jk}$, with respect to θ_{jk}:

$$\int_0^{\pi} \sin\theta_{jk} \cdot D_{jk}\,\mathrm{d}\theta_{jk} = \int_0^{\pi} \sin\theta_{jk}\left(3\cos^2\theta_{jk} - 1\right)\,\mathrm{d}\theta_{jk} = 0 \tag{3.51}$$

The $\sin\theta_{jk}$ weighting function gives all orientations equal probability, as more states are possible when the internuclear vector $\mathbf{e}_{jk}$ is perpendicular to the field ($\theta_{jk} = \frac{\pi}{2}$) than parallel ($\theta_{jk} = 0$ and π).

In contrast, when considering molecular translations, only the short-range intermolecular dipolar couplings are averaged to zero while the long-range dipolar couplings are so small that they can be ignored for the most part. Thus, in a fully isotropic liquid all secular dipolar couplings essentially vanish such that $\hat{\mathcal{H}}_{\mathrm{D}}^{iso} \approx 0$.

Isotropic J-coupling

As with the chemical shift, under isotropic motion the orientation-dependent J-coupling tensor $\underline{J}_{jk}$ is averaged to its isotropic value. This isotropic value is termed the isotropic secular J-coupling constant J_{jk} and is given by the trace of the J-coupling tensor $\underline{J}_{jk}$:

$$J_{jk} = \frac{1}{3}\mathsf{Tr}\,\underline{J}_{jk} = \frac{1}{3}\left(J_{xx}^{jk} + J_{yy}^{jk} + J_{zz}^{jk}\right) \tag{3.52}$$

The isotropic J-coupling Hamiltonian depends only on the isotropic secular J-coupling constant and the spin vector operators of the coupled spins and is thus independent of molecular orientation:

$$\hat{\mathcal{H}}_{\mathrm{J}}^{iso} = J_{jk}\hat{\boldsymbol{I}}_j \cdot \hat{\boldsymbol{I}}_k \tag{3.53}$$

3.2.2 Semi-isotropic molecular motion

Semi-isotropic motion occurs when the conditions for full isotropic averaging are not quite reached, i.e. not all molecular orientations are sampled equally. This results in an average Hamiltonian mostly based on the isotropic Hamiltonian, with residual anisotropic behaviour imparted by the anisotropic Hamiltonian:

$$\hat{\mathcal{H}}_{\lambda}^{semi\text{-}iso} \propto \hat{\mathcal{H}}_{\lambda}^{iso} + \hat{\mathcal{H}}_{\lambda}^{aniso}(\Theta) \tag{3.54}$$

Such motional behaviour is seen for partially immobilised systems, such as swollen gels and viscous molten systems. With the latter case being of relevance here.

In the melt-state, although molecular motion is much less restricted than in the solid, full isotropic motion is not achieved and the degree of motional averaging is related to the viscosity. The situation is further complicated for polymer melts due to their non isotropic flow behaviour. Thus, both intramolecular and intermolecular spin interactions are only partially averaged resulting in the effect of residual anisotropic spin interactions being observed.

Practically, the residual anisotropic interactions result in line broadening with respect to the fully isotropic case. The anisotropic interactions are still however much less than those observed for a solid. Such residual anisotropic interactions my be removed, leaving only the isotropic interactions through the use of magic-angle spinning (MAS) (Section 3.2.3). When applied to systems with semi-isotropic motion this is usually termed high-resolution MAS (HR-MAS).

3.2.3 Magic-angle spinning (MAS)

In the solid-state, molecular translation and rotation is highly restricted and neither intramolecular nor intermolecular spin interactions are motionally averaged. This results in the internal spin Hamiltonian terms being dependent on the sample orientation with respect to the external magnetic field. Similarly, for systems exhibiting semi-isotropic motion, such as polymer melts, the residual anisotropic interactions also result in a partial dependence on the sample orientation.

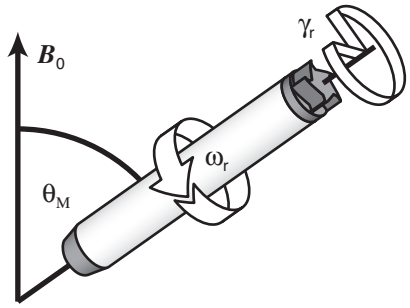

***Figure 3.5**: Magic-angle spinning (MAS)*

Due to the specific angular dependence of the various spin interaction Hamaltonians the motional averaging effects of isotropic motion can be mimicked via physical rotation of the whole sample during the NMR measurement (Figure 3.5). Such sample rotation introduces the second Legendre polynomial P_2 into the anisotropic parts of the time-averaged Hamiltonian.

$$P_2(\theta) = \frac{1}{2}(3\cos^2\Theta - 1) \tag{3.55}$$

Under sample rotation at $\theta = 54.74°$, such that $P_2(\theta) = 0$, the anisotropic parts of the spin interactions can be averaged to zero with only the isotropic interactions remaining. Because of this behaviour $\theta = 54.74°$ is also known as the magic-angle θ_M and the overall technique is called magic-angle spinning (MAS) [Andrew 58, Lowe 59]. More specifically, MAS imposes a $\sin(\omega_r)$ modulation[†] on the anisotropic part of the spin interaction Hamiltonian.

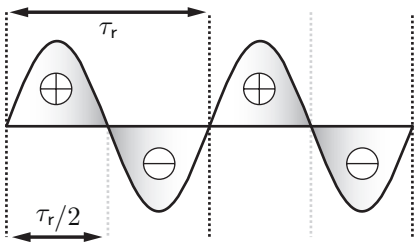

***Figure 3.6**: The sine modulation of an anisotropic interaction Hamiltonian by MAS showing the associated time period $\tau_r = \omega_r^{-1}$. (Shading indicates average interaction intensity)*

The $\sin(\omega_r)$ modulation can be depicted schematically, with the sign of the oscillation labelled $\oplus$ and $\ominus$ respectively (Figure 3.6). Under MAS the contribution from the first half ($\oplus$) and the second half ($\ominus$) of the rotor period cancel. Hence after an integer number of rotor periods, the anisotropic part of the interaction Hamiltonian modulated by MAS is averaged to zero:

$$\int_t^{t+n\cdot\tau_r} \hat{\mathfrak{H}}^{MAS}_{\lambda,aniso}(\theta,t)\,\mathrm{d}t = 0 \tag{3.56}$$

With the refocusing behaviour of MAS proportional to the MAS time period τ_r so-called *rotor-echos* are introduced into the FID every $n \cdot \tau_r$. These rotor-echos lead to MAS artifacts known as *spinning-sidebands* in the associated spectra. Due to the reciprocal nature of the Fourier-transform these occur at $\delta_{iso} \pm n \cdot \tau_r^{-1} = \delta_{iso} \pm n \cdot \omega_r$.

[†] as well as a weaker $2 \cdot \omega_r$ modulation.

With the anisotropic interactions causing line broadening, the application of MAS results in a line narrowing effect. However, complete averaging of an anisotropic interaction to zero is only achieved when the sample is spun with a rotational frequency much greater than the characteristic frequency of the interaction, i.e. $\omega_r \gg \omega_\lambda$. Hence, while the CSA can be completely removed under MAS, the line broadening effects of residual dipolar couplings are usually still seen for solid and molten samples. For this reason considerable effort has been taken to achieve the highest possible MAS frequency. Currently, commercially available MAS hardware is capable of spinning at 35 kHz utilising 2.5 mm outer diameter zirconia sample containers, or rotors. With specialised custom-built probeheads, and slightly smaller rotors, spinning speeds of up to 70 kHz are achievable [Samoson 03].

3.3 Nuclear relaxation

As shown in Section 3.1.2, the application of a pulse moves the bulk magnetisation vector $\boldsymbol{M}_0$ from its position at thermal equilibrium along the z-axis into the xy-plane. The relaxation of the bulk magnetisation back to thermal equilibrium is described by the Bloch equations [Bloch 46]. From the Bloch equations the trajectory of the bulk magnetisation with time may be derived:

$$M_x(t) = M_0 \cdot \cos(\omega_L \cdot t) \cdot \exp\{-t/T_2\} \quad (3.57)$$

$$M_y(t) = M_0 \cdot \sin(\omega_L \cdot t) \cdot \exp\{-t/T_2\} \quad (3.58)$$

$$M_z(t) = M_0 \cdot \left[1 - \exp\{-t/T_1\}\right] \quad (3.59)$$

This phenomenological approach distinguishes two relaxation processes the spin-lattice relaxation, governed by the time constant T_1, and spin-spin relaxation, governed by the time constant T_2. Both these relaxation processes, to all extents and purposes, show an exponential dependance with time.

3.3.1 Spin-lattice relaxation

The interaction of a nuclear-spin in a non equilibrium state with its environment results in an energy loss. For historical reasons the environment with which the spin interacts is termed a lattice, and thus this process as a whole is termed spin-lattice relaxation. The loss in energy results in the bulk magnetisation vector returning to its equilibrium state, where it is aligned with the $+z$-axis. For this reason this enthalpic process is sometimes called longitudinal-relaxation with the characteristic time constant T_1 ranging from hundreds of milliseconds to tens of seconds.

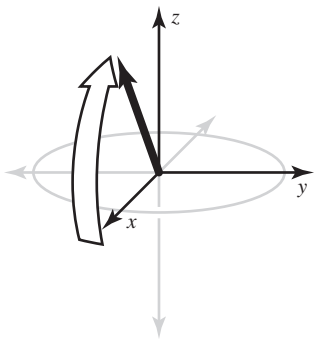

***Figure 3.7**: The effect of spin-lattice (longitudinal) relaxation causes the bulk magnetisation to return to its equilibrium state aligned with the z-axis.*

After a $\frac{\pi}{2}$ pulse the magnetisation resides in the xy-plane, from where it freely relaxes back to the equilibrium state (Figure 3.7). In order to allow full relaxation an infinite time must pass, due to the exponential nature of the decay process. However, if only 99.3% of all the spins in the ensemble are required to have relaxed back to equilibrium then only a time period of $5 \times T_1$ is needed (Figure 3.8).[†] If full relaxation is not allowed any subsequent pulses can not be considered to act upon the equilibrium state of magnetisation. This results in saturation effects, which are most typically manifested as a loss of signal intensity. Such effects are of particular im-

[†]From Equation 3.59, e.g. $M_z/M_0 = 100\% \times (1 - \exp\{-5\}) = 99.3262\%$.

portance for quantitative NMR, as the area of a peak in the spectrum becomes proportional to the signal intensity and relaxation behaviour.

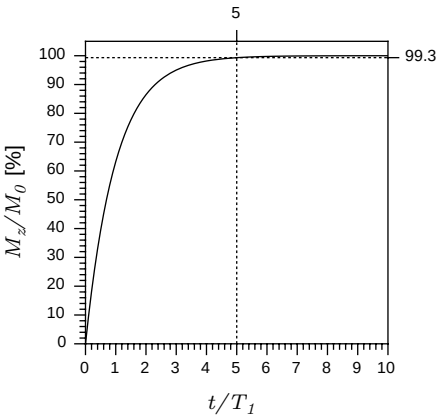

***Figure 3.8**: The recovery of longitudinal magnetisation (M_z) as a function of time showing that 99.3% of the magnetisation has returned to the equilibrium state after a time period of* $5 \times T_1$.

Spin-lattice relaxation is induced by the fluctuating magnetic fields caused by molecular motion. This motion is characterised by the rotational correlation time τ_c, defined as the average time for a molecule to rotate through one radian. Thus, short correlation times correspond to rapid molecular rotations and vice versa. The normalised spectral density function $\mathcal{J}(\omega)$ describes the distribution of correlation times with frequency for different motional processes (Figure 3.9), and is given by:

$$\mathcal{J}(\omega) = \frac{\tau_c}{1 + \omega^2 \tau_c^2} \tag{3.60}$$

Both slow and fast motional processes have a low probability of inducing spin-lattice relaxation, and thus long T_1 relaxation times occur. In contrast, intermediate motional processes result in short T_1 relaxation times (Figure 3.10).[†] Since the Larmor frequency is field dependent the minimum in T_1 is shifted to faster motions at higher external magnetic fields.

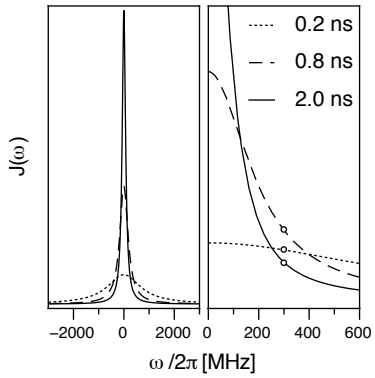

***Figure 3.9**: The spectral density as a function of frequency $\mathcal{J}(\omega)$, for slow (τ_c=2.0 ns), intermediate (τ_c=0.8 ns) and fast (τ_c=0.2 ns) motional processes.*

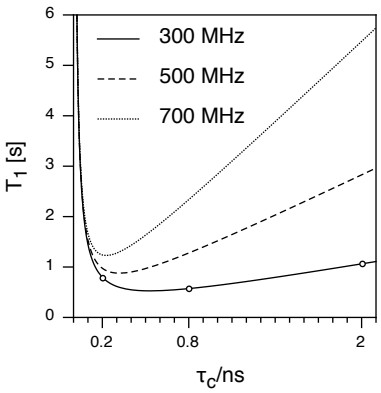

***Figure 3.10**: The Dependence of T_1 on correlation time (τ_c) and the Larmor frequency.*

[†]Figure 3.10 calculated for ^{1}H using: $T_1^{-1} = \gamma^2 \cdot \langle B_x^2 \rangle \cdot \mathcal{J}(\omega_L)$ with $\langle B_x^2 \rangle = 10^{-8}$ T^2.

3.3.2 Spin-spin relaxation

Spin-spin relaxation occurs due to each nuclei experiencing a slightly different magnetic field. This results in each spin precessing at a slightly different Larmor frequency, and thus with time the individual magnetisation vectors dephase in the transverse plane (Figure 3.11). Because of this behaviour the spin-spin relaxation process is also called transverse relaxation.

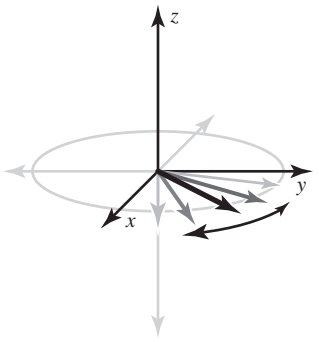

***Figure 3.11**: The effect of spin-spin (transverse) relaxation causes a dephasing of the bulk magnetisation.*

The differences in magnetic field are caused by either instrument-related external magnetic field inhomogeneity, or sample-related differences in local magnetic fields. The internal sample-related processes are characterised by the time constant T_2, while the external influences are characterised by T_2^{Δ}. Practically, both sources result in dephasing and the observed combined process is characterised by the time constant T_2^*, defined such that;

$$\frac{1}{T_2^*} = \frac{1}{T_2} + \frac{1}{T_2^{\Delta}} \tag{3.61}$$

Generally short T_2^* times results in faster dephasing of the transverse magnetisation and a greater frequency distribution in the frequency domain (Figure 3.12). Thus, the full-width at half-maximum (FWHM) of a peak in the NMR spectrum is inversely proportional to the total rate of transverse-relaxation, i.e. FWHM $= 1/(\pi \cdot T_2^*)$.

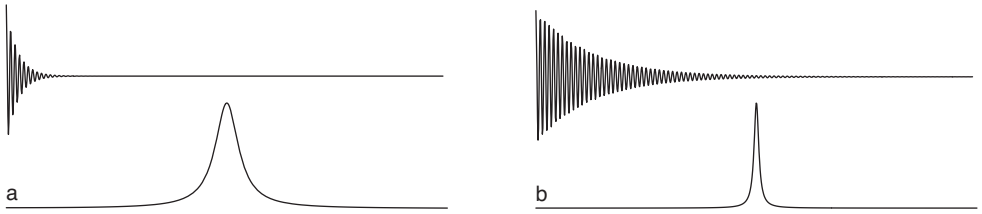

***Figure 3.12**: Illustration of a (a) rapidly dephasing signal (short T_2^*) resulting in a short time-domain and broad frequency-domain signal. In contrast for a (b) slowly dephasing signal (long T_2^*) a longer time-domain and narrower frequency-domain signal is observed.*

With both spin-spin and spin-lattice relaxation mostly caused by the same local fluctuations in magnetic field, T_2 can never be longer than T_1. However, with additional relaxation mechanisms possible for spin-spin relaxation, T_2 may be shorter than T_1. For rapidly tumbling molecules spin-spin and spin-lattice relaxation times are identical. In this extreme narrowing limit increased mobility results in slower relaxation and hence narrower linewidths. In contrast, decreased mobility reduces the relaxation times and broadens the signals (Figure 3.13).[†]

[†]Figure 3.13 calculated using: $T_1^{-1} = \frac{3}{10} D_{jk}^2 \{\mathcal{J}(\omega_L) + 4\mathcal{J}(2\omega_L)\}$ and
$T_2^{-1} = \frac{3}{20} D_{jk}^2 \{3\mathcal{J}(0) + 5\mathcal{J}(\omega_L) + 2\mathcal{J}(2\omega_L)\}$ with $D_{jk} = 50$ kHz and $\omega_L = 500$ MHz.

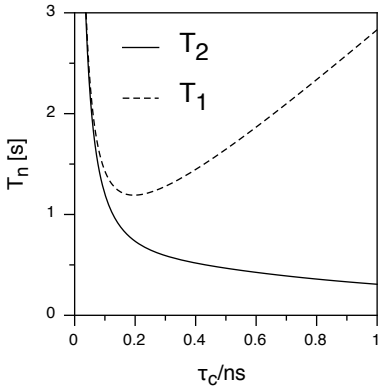

***Figure 3.13**: Dependence of T_1 and T_2 on correlation time (τ_c).*

In contrast to spin-lattice relaxation, which is an enthalpic process, spin-spin relaxation is an entropic process. This relaxation mechanism occurs via energy-conserving flip-flop processes, which mutually exchange energy between spins, and can be stimulated by very low frequency fluctuations. Thus, for slowly tumbling molecules, such as macromolecules, a combination of short T_2 and long T_1 relaxation times are observed (Figure 3.13).

3.3.3 Cross relaxation

Another important relaxation mechanism is nuclear cross-relaxation, also known as the nuclear Overhauser effect (NOE). This is defined as the change in intensity of one resonance (S) when spin transitions of another resonance (I) are perturbed from their equilibrium population.[†]

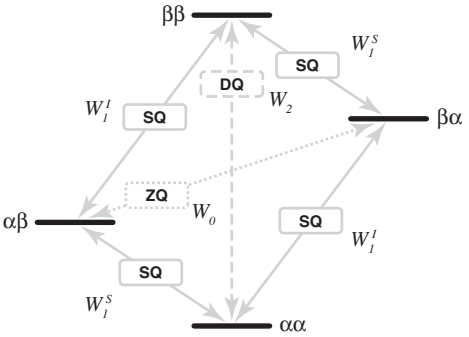

***Figure 3.14**: The six transitions and their respective transitions probabilities for a coupled two-spin system.*

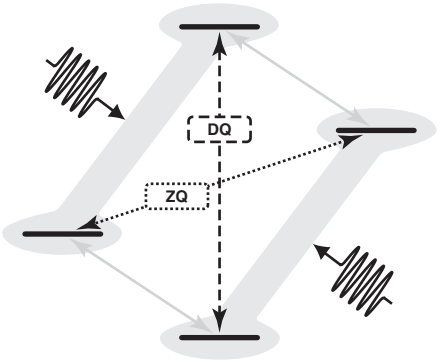

***Figure 3.15**: Saturation of the I SQ transitions encouraging relaxation via the ZQ and DQ transitions.*

The NOE is mediated by direct through-space magnetic interactions between spins, i.e. dipole-dipole couplings, and can hence only be observed for spins in close proximity to each other due to the r^{-3} dependence (Equation 3.38). Furthermore, the amplitude and sign of the NOE are determined by the various sample-dependent transition probabilities of the single-quantum (SQ), zero-quantum (ZQ) and double-quantum (DQ) transitions possible for coupled spin systems, denoted W_1, W_2 and W_2 respectively (Figure 3.14). Unlike the SQ transitions, both the ZQ and DQ transitions require a simultaneous flip of both I and S spins.

[†]Commonly in the NOE literature S represents the saturated and I the influenced spin [Solomon 55]. However, this is in contrast to the usual NMR notation where I and S represents high and low abundance spins of significantly different Larmor frequency.

Continuous irradiation of the I spins causes the equilibrium population differences across the SQ I transitions to zero and thus saturates these spins. In contrast to this, the equilibrium population differences across the SQ S transitions are retained. In this saturated state, only the ZQ and DQ transitions are available to re-establish the equilibrium population differences of the I spins. If DQ transitions occur the population differences across the S transitions are increased, because the flip of the I spin is accompanied by that of an S spin. This results in a positive NOE being observed. In contrast, if the ZQ transition occurs a decrease in the S transition population differences is observed, due to each I spin flip being accompanied by an S spin counter-flip. This situation results in a negative NOE being seen [Claridge 99]. Practically both processes occur and are in competition with each other, hence the importance of the ZQ and DQ transition probabilities W_0 and W_2.

After the ZQ or DQ transitions take place the SQ S transitions allow the spin system to relax to an equilibrium population difference across the S transitions, hence reducing both the positive and the negative NOE effects. It is because of this that the magnitude of either negative or positive NOE depends on the relative transition probabilities of not only W_0 and W_2 but also that of the W_1^S transitions.

The transition probabilities W_n also depend upon the correlation times τ_c of the motional processes present for a given sample, and the Larmor frequencies ω_L^S and ω_L^I of the coupled nuclei [Ernst 87]:

$$W_0 = \frac{1}{20} \cdot D_{jk}^2 \cdot \jmath(\omega_L^S - \omega_L^I) \tag{3.62}$$

$$W_1^S = \frac{3}{40} \cdot D_{jk}^2 \cdot \jmath(\omega_L^S) \tag{3.63}$$

$$W_1^I = \frac{3}{40} \cdot D_{jk}^2 \cdot \jmath(\omega_L^I) \tag{3.64}$$

$$W_2 = \frac{3}{10} \cdot D_{jk}^2 \cdot \jmath(\omega_L^S + \omega_L^I) \tag{3.65}$$

where D_{jk} is the dipolar coupling constant (Equation 3.38) and $\jmath(\omega_L)$ is the spectral density function (Equation 3.60).

For the homonuclear case $W_1^I = W_1^S = W_1$. At long correlation times in the slow motion regime the ZQ transition is dominant (Figure 3.16a). With $W_0 > W_2 > W_1$, this leads to a negative NOE. In contrast, for short correlation times in the fast motion regime the DQ transition is dominant, resulting in positive NOE with $W_2 > W_1 > W_0$.

For the hetronuclear case, similar behaviour to that seen for the homonuclear cased is observed in the fast motion regime, with $W_2 > W_1 > W_0$ leading to a positive NOE (Figure 3.16b). However, with $W_1^I \neq W_1^S$ different behaviour is seen in the slow motion regime. It should be noted that the transition probabilities for the heteronuclear case also significantly change with the sign of γ_S, due to their dependence on the dipolar coupling constant D_{jk}, however for simplicity only positive gamma nuclei

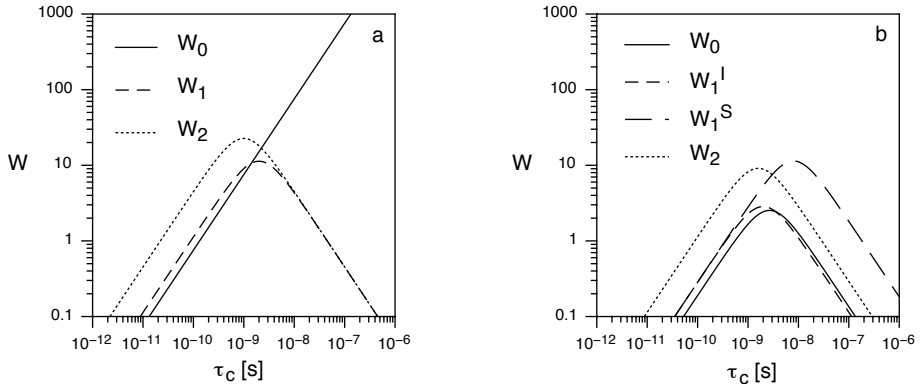

***Figure 3.16**: The dependence of the transition probabilities W_n with correlation time τ_c for a (a) homonuclear (^{1}H–^{1}H) and (b) heteronuclear (^{1}H–^{13}C) two-spin system. (Calculated using Equations 3.62–3.65 for $\mathbf{B}_0$=11.4 T.)*

such as ^{1}H and ^{13}C are considered here [Levitt 01].

The influence of the NOE on a dipolar-coupled two-spin systems can be described quantitatively using the Solomon equations [Solomon 55]. These coupled differential equations relate the rate of change of the magnetisation along the z-axis, for both S (Equation 3.66) and I spins (Equation 3.67), as a function of time to the equilibrium intensities using the transition probabilities W_0, W_1^S, W_1^I and W_2.

$$\frac{\mathrm{d}}{\mathrm{d}t} S_z(t) = -(W_0 + 2W_1^S + W_2)[S_z(t) - S_z^0] - (W_2 - W_0)[I_z(t) - I_z^0] \tag{3.66}$$

$$\frac{\mathrm{d}}{\mathrm{d}t} I_z(t) = -(W_0 + 2W_1^I + W_2)[I_z(t) - I_z^0] - (W_2 - W_0)[S_z(t) - S_z^0] \tag{3.67}$$

Depending on whether the I magnetisation is saturated or inverted prior to detection on S, two types of NOE my be distinguished: steady-state NOE and transient NOE.

Steady-state NOE

When the I spin transitions are saturated for a sufficiently long time directly prior to detection on S, e.g. by decoupling during the recycle-delay,[†] a so-called steady-state NOE is obtained (Figure 3.17).

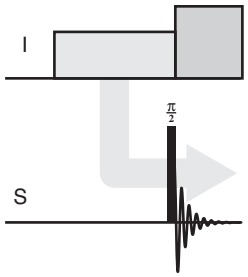

***Figure 3.17**: Pulse sequence for the observation of steady-state NOE.*

Under these conditions both $\frac{\mathrm{d}}{\mathrm{d}t}S_z(t)$ and $I_z(t)$ can be set to zero in Equation 3.66 and I_z^0 replaced by $\frac{\gamma_I}{\gamma_S}S_z^0$ [Neuhaus 89]. Subsequent rearrangement can then be used to give the maximum NOE enhancement η:

$$\eta = \frac{S_z - S_z^0}{S_z^0} = \frac{\gamma_I}{\gamma_S} \cdot \frac{W_2 - W_0}{W_0 + 2W_1^S + W_2} \tag{3.68}$$

In the fast motion regime, due to the dependence of the transition probabilities on the correlation time, Equation 3.68 may be simplified resulting in the maximum steady-state NOE enhancement of a dipolar-coupled spin-pair of:

$$\eta = \frac{\gamma_I}{2\gamma_S} \tag{3.69}$$

It should be noted that because $S_z = S_z^0(1 + \eta)$ an NOE enhancement factor [Schilling 78, Doddrell 72, Qiu 00] may also be defined as: $NOE = 1 + \eta$. Thus, for a dipolar-coupled ^{13}C–^{1}H spin-pair a maximum steady-state NOE enhancement of $\eta = 2$ ($NOE = 3$) is observed. Whereas for the homonuclear case a steady state NOE enhancement of only $\eta = \frac{1}{2}$ ($NOE = 1.5$) is seen [Claridge 99].

Transient NOE

An alternative method of observing cross-relaxation involves inverting the I spin populations using a π-pulse (Figure 3.18).

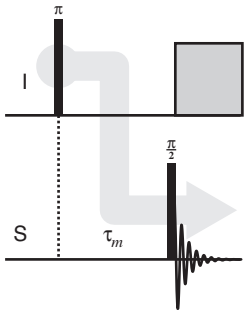

***Figure 3.18**: Pulse sequence for the observation of transient NOE.*

After I spin inversion the IS spin system is allowed to evolve purely under the influence of the NOE[‡] for a mixing time τ_m [Neuhaus 89, Claridge 99]. This so-called transient NOE affects the S and I signal intensities as a function of τ_m and can be described by solving the coupled Solomon equations for both S (Equation 3.66) and I spins (Equation 3.67) simultaneously. The resulting equations relate the rate of change of the magnetisation along the z-axis for both S and I spins as a function of mixing-time after initial I spin inversion. The competing processes are

[†] as found in gated (τ_{rd}) and power-gated (τ_{aq}+τ_{rd}), but not inverse-gated (τ_{aq}), solution-state decoupling.
[‡] i.e. no other pulses are applied on either I or S during τ_m

described by two rates, the dipolar relaxation rate ρ and the cross-relaxation rate σ. Both ρ and σ are related to the transition probabilities according to:

$$\rho = W_0 + 2W_1 + W_2 \tag{3.70}$$

$$\sigma = W_2 - W_0 \tag{3.71}$$

The cross-relaxation rate σ describes how quickly an NOE enhancement is transferred between I and S. From Equation 3.71 it can be seen that σ is positive when $W_2 > W_0$ and negative when $W_2 < W_0$. Using this sign convention σ also represents the sign of the transient NOE [Neuhaus 89].

The dipolar relaxation rate ρ_{SI} describes the purely dipolar relaxation of an S spin caused by an I spin in a two-spin system, and *vice versa* for ρ_{IS}. When ρ is expressed as a function of the spectral density function $\mathcal{J}(\omega)$ (Equation 3.60) it can be seen that for the heteronuclear case $\rho_{SI} \neq \rho_{IS}$, due to its asymmetric dependence on ω_L:

$$\rho_{jk} \propto 6\mathcal{J}(\omega_L^j + \omega_L^k) - \mathcal{J}(\omega_L^k - \omega_L^j) \tag{3.72}$$

However, the distinction between ρ_{SI} and ρ_{IS} is only important for the heteronuclar case if either I or S is not in the fast motion regime. For the homonuclear case, due to $\omega_S \approx \omega_I$ the distinction between ρ_{SI} and ρ_{IS} is always negligible. Thus in the fast motion regime, for both homonuclear and heteronuclar cases, the time dependance of the S_z and I_z with mixing time τ_m is given by:

$$\frac{S_z(\tau_m)}{S_z^0} = 1 - e^{-(\rho+\sigma)\tau_m} - e^{-(\rho+\sigma)\tau_m} \tag{3.73}$$

$$\frac{I_z(\tau_m)}{I_z^0} = 1 - e^{-(\rho+\sigma)\tau_m} + e^{-(\rho+\sigma)\tau_m} \tag{3.74}$$

3.4 General NMR techniques

In this section the various NMR techniques used will be introduced. The single-pulse excitation experiment and basic signal detection will be presented first (Section 3.4.1), followed by common heteronuclear techniques such as dipolar decoupling (Section 3.4.2) and cross-polarisation (Section 3.4.3). Pulse sequences utilising the J-coupling will then be discussed (Sections 3.4.4–3.4.6) as well as methods for determining the spin-lattice relaxation time constant T_1 (Sections 3.4.7 and 3.4.8).

3.4.1 Single-pulse excitation (SPE)

The application of a single RF pulse to nuclei with $I \geq \frac{1}{2}$ and monitoring their return to equilibrium is the epitome of FT-NMR spectroscopy (Figure 3.19).

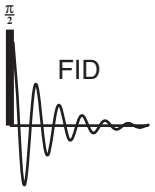

***Figure 3.19**: Single-pulse excitation.*

The pulse in question is described as a 90° or $\frac{\pi}{2}$ pulse since it results in the bulk magnetisation being flipped from along the z-axis, to being aligned in the xy-plane. The exact orientation of the magnetisation in the xy-plane depends on the phase of the RF during the pulse. Such a pulse can be achieved in two ways; by a long pulse of low power, resulting in a weak $\boldsymbol{B}_1$ field, or a short pulse of high power, resulting in a strong $\boldsymbol{B}_1$ field. These two classes of pulses are generally described as being 'soft' or 'hard' pulses respectively, and differ in the time taken to achieve the desired effect.

After the $\frac{\pi}{2}$ pulse, the Larmor precession of the transverse magnetisation induces a weak voltage in the RF-coil, which is subsequently detected as the NMR signal $S(t)$. Technically, the signal is mixed-down with a reference carrier frequency to aid digitisation, and is equivalent to observing the response in the rotating frame. With modern spectrometers capable of separately detecting both the x and y-components of the precessing magnetisation a complex signal is measured. Such phase-sensitive or quadrature detection allows the distinction of signals differing from the carrier by the same frequency, but of opposite sign i.e. $\omega_{\text{ref}} \pm \omega$. Thus doubling the effective spectral window.

The spin system in a perturbed state, with observable transverse magnetisation, is free to relax back to the equilibrium state, with no observable transverse magnetisation. This free induction decay (FID) signal from the observable magnetisation is characterised by the relaxation time constants T_1 (Section 3.3.1) and T_2 (Section 3.3.2). These time constants describe the time taken for the bulk magnetisation to return to equilibrium and how long the coherent signal lasts.

3.4.2 Heteronuclear spin decoupling

When dealing with low natural abundance nuclei S, such as 1.1% ^{13}C, generally homonuclear couplings can safely be neglected due to the low probability of two S nuclei occurring in close proximity. However, heteronuclear couplings between low abundance S and high abundance I nuclei, such as ^{1}H, cause significant line broadening in solid-state spectra, and spectral crowding in solution-state spectra. Although the heteronuclear J-couplings are still present in the solid-state spectra they are dwarfed by the dipolar couplings. To overcome these line broadening interactions a number of heteronuclear *decoupling* schemes have been developed, and continue to be an important field of research [De Paëpe 03, Ernst 03, Khitrin 03].

The simplest form of heteronuclear decoupling is a train of π pulses on the I spins whilst simultaneously acquiring the FID of the S nuclei (Figure 3.20a). The π pulses refocus the heteronuclar coupling interactions and thus remove its effects. Under limiting conditions, where the free evolution time $\tau \rightarrow 0$, this is equivalent to continuously irradiation of the I spins (Figure 3.20b). Due to the stronger nature of the dipolar coupling, higher power RF-fields are needed for dipolar decoupling than are required for J-decoupling. Because of this, dipolar-decopling inevitably results in the removal of all heteronuclear J-couplings as well.

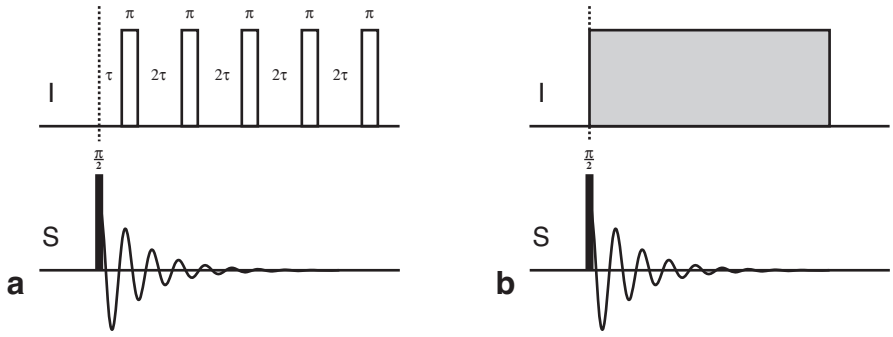

***Figure 3.20**: (a) A train of π pulses can be used to decouple the I spins from the S spins during acquisition. (b) In the limiting scenario, when $\tau \rightarrow 0$, such decoupling is equivalent to the application of continuous RF-irradiation during the whole data acquisition period.*

In solid-state NMR high-power continuous-wave (CW) decoupling was initially used to achieve heteronuclear decoupling (Figure 3.20b). In order to obtain sufficient decoupling efficiency, and avoid interference between the physical rotation of MAS and spin rotation of RF decoupling, high-power decoupling with strong RF-fields of 50–150 kHz is necessary. At present, high-power multiple-pulse decoupling schemes are considered the most efficient methods for solids under MAS, and in the worst case are equal in efficiency to CW decoupling. The most widely adopted scheme is the two-pulse phase-modulated (TPPM) decoupling sequence [Bennett 95], which provides significant improvement in both linewidth and intensity under a wide range of experimental conditions.

In contrast to the high-power dipolar-decoupling methods used in solid-state NMR, only low-power J-decoupling methods are needed in the solution-state, due the dipolar coupling being motionally averaged to its isotropic value of zero. In contrast to the solid-state method, J-decoupling generally relies on well defined manipulation of the I spins during acquisition using a decoupling pulse sequence. As composite π pulses [Levitt 79] are commonly used for such decoupling sequences these are generally know as composite pulse decoupling sequences. A commonly used composite pulse decoupling sequence is WALTZ-16 [Shaka 83b, Shaka 83a]. This involves the continuous application of composite π pulses on the ^{1}H channel and provides effective decoupling over a wide bandwidth. The basic inversion element (R) used for WALTZ is:

$$R = 90^\circ_x \, 180^\circ_{-x} \, 270^\circ_x \tag{3.75}$$

Such a composite π pulse is much less susceptible to pulse imperfections than a normal π pulse. When the sequence given in Equation 3.75 is expressed as multiples of 90° pulses, denoted 1, it may be written: $1\bar{2}3$, where the bar denotes phase inversion. The expansion of the basic inversion element R with successive cyclic permutations with 90°_x and 90°_{-x} pulses and combination with its phase-inverted counterpart ($\bar{R}$) results in the effective WALTZ-16 composite pulse decoupling sequence; $Q\bar{Q}\bar{Q}Q$, with $Q = \bar{3}4\bar{2}3\bar{1}2\bar{4}2\bar{3}$.

3.4.3 Cross-polarisation (CP)

With the maximum polarisation achievable by single pulse excitation governed by the gyromagnetic ratio of the nucleus under investigation, signal intensity for low abundant low-γ nuclei (S), such as ^{13}C and ^{15}N, can be problematic. One common method to circumvent this is to transfer polarisation from the more abundant high-γ nuclei (I) such as protons, which are typically also present. This technique was first applied by A. Pines, M. Gibby and J. S. Waugh [Pines 72, Pines 73] and has become known as *cross-polarisation*.

Practically, after an initial $\frac{\pi}{2}$ pulse on the I nuclei generates transverse magnetisation, polarisation is transferred to the S nuclei by simultaneous irradiation for 50 μs to 5 ms on both I and S channels. After this so-called contact-time (τ_{CP}) the enhanced signal from the S nuclei is detected, usually in the presence of heteronuclear dipolar decoupling (Figure 3.21a). The maximum polarisation transfer occurs when the Hartmann-Hahn match condition is satisfied:

$$-\gamma_S B_1(S) = -\gamma_I B_1(I) \qquad \text{or} \qquad \omega_1(S) = \omega_1(I) \tag{3.76}$$

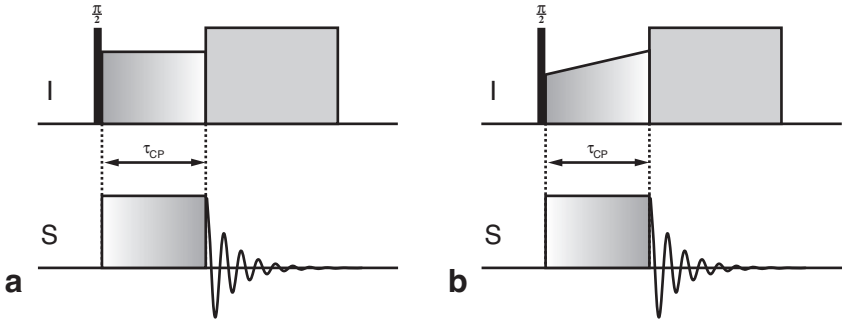

***Figure 3.21**: The cross-polarization experiment: (a) Hartmann-Hahn-CP and (b) Ramp-CP.*

The match condition represents the Zeeman levels of both S and I becoming degenerate when the two lock-fields are applied. Under these conditions, both spin species precess with the same frequency $\nu_1 = -\gamma B_1/2\pi$, about the axis of the lock-field, in their respective rotating frames. With both rotating frames sharing a common z-axis, and both z components of the I and S magnetisation oscillating at the same frequency, energy transfer and thus polarisation transfer is permitted. To allow such a transfer to occur a mediating interaction is also required, this typically being the heteronuclear dipolar coupling. Formally, satisfying the match condition reintroduces flip-flop terms (e.g. $2\hat{I}_z\hat{S}_z$) from the heteronuclear dipolar coupling into the effective dipolar Hamiltonian responsible for polarisation transfer. Hence, the efficiency of the cross-polarisation process is governed by the magnitude of the dipolar interaction between I and S spins. Thus, the maximum signal enhancement is given by the factor γ_I/γ_S.

With increasing contact time, S magnetisation M_S builds up with a time constant T_{IS} characteristic of the dipolar coupling strength. However, as the I and S nuclei are still subject to relaxation during their spin-locks the S magnetisation passes through a maximum before decaying. The characteristic time constants for such longitudinal relaxation in the rotating frame are termed $T_{1\rho}^I$ and $T_{1\rho}^S$ for the I and S spins respectively. For dilute S spins in a large system of I spins the contact time dependence of the S magnitisation $M_S(\tau_{\mathrm{CP}})$ is given by Equation 3.77 [Mehring 83, Slichter 96]:

$$M_S(\tau_{\mathrm{CP}}) = \frac{M_0}{\lambda} \cdot \left[1 - \exp\left\{-\frac{\lambda \cdot \tau_{\mathrm{CP}}}{T_{IS}}\right\}\right] \cdot \exp\left\{-\frac{\tau_{\mathrm{CP}}}{T_{1\rho}^I}\right\} \tag{3.77}$$

where:

$$\lambda = 1 + \frac{T_{IS}}{T_{1\rho}^S} - \frac{T_{IS}}{T_{1\rho}^I} \tag{3.78}$$

The relationship described in Equation 3.77 can be derived using thermodynamic principles when considering a large system of coupled I spins, e.g. protons in organic solids. However, for an isolated two-spin system an oscillatory dependence on contact time is observed for M_S. Strongly coupled nuclei exhibit a small T_{IS} and thus S magnetisation is built up quickly, with the opposite trend seen for weakly coupled nuclei. With molecular motion reducing dipolar couplings, the site specific build up behaviour can provide qualitative insight into site mobility. A more quantitative analysis requires the knowledge of the individual relaxation time constants [Völkel 88].

Another important advantage of the CP experiment is the dependence of the recycle delay on T_1^I, and not T_1^S, which is typically the larger. Thus, in contrast to the SPE experiment, where T_1^S governs the recycle-delay, shorter recycle delays are possible facilitating shorter measurement time.

Under MAS the Hartmann-Hahn match condition (Equation 3.76) changes to:

$$\omega_1(S) = \omega_1(I) \pm n \cdot \omega_{\mathrm{r}} \tag{3.79}$$

and shows a strong mismatch dependence if the MAS frequency and dipolar coupling are of the same order of magnitude. At higher MAS frequencies the maximum signal intensity is observed for $n = \pm 1$, this leads to difficulties in both establishing and maintaining an efficient match condition. A flat matching profile, over a wide range of match conditions, can be produced by linearly increasing the amplitude of either the I or S lock pulse during the contact time (Figure 3.21b). This is commonly known as ramp-CP [Metz 94].

3.4.4 INEPT

Insensitive nuclei my also be enhanced by polarisation transfer mediated by the J-coupling. The insensitive nuclei enhanced by polarisation transfer (INEPT) experiment can also be used for spectral editing, allowing IS, I_2S and I_3S groups to be distinguished based on their multiplicity constants [Morris 79].

After the initial $\frac{\pi}{2}$ pulse the I magnetisation is allowed to evolve for a period of time τ_1 under the effects of chemical shift and heteronuclear J-coupling (Figure 3.22). Two simultaneous π pulses on both I and S refocus the chemical shift evolution and ensure continued evolution of the heteronuclear J-coupling during the second τ_1 delay. The τ_1 delays are set such that $\tau_1 = \frac{1}{4}J_{IS}^{-1}$. This results in the two I spin vectors of a couplied IS pair being antiphase to each other along the $\pm x$-axis. The subsequent $\frac{\pi}{2}$ I pulse aligns the magnetisation along the $\pm z$-axis, while the simultaneous $\frac{\pi}{2}$ S pulse transfers the polarisation from I to S. The S spin magnetisation is then allowed to refocus for a period τ_2 under heteronuclear J-coupling, with the simultaneous I and S π pulses after τ_2 again removing the effects of chemical shift evolution.

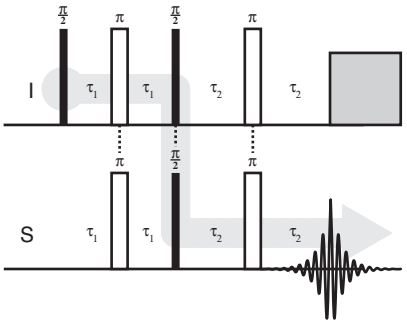

***Figure 3.22**: The refocused decoupled J-mediated INEPT pulse sequence.*

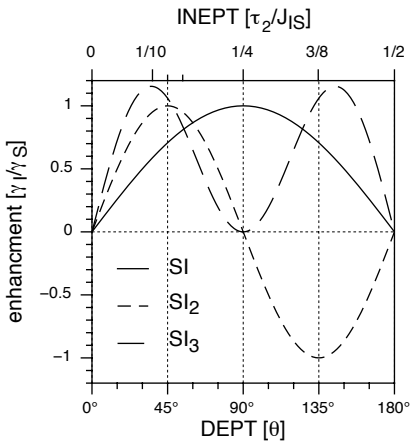

***Figure 3.23**: The intensity of SI, SI_2 and SI_3 groups as a function of τ_2 (INEPT) and α (DEPT).*

Optimum sensitivity for SI, SI_2 and SI_3 groups is dependent on the length of the refocusing period τ_2, this needing to be set to $\frac{1}{4}J_{IS}^{-1}$, $\frac{1}{8}J_{IS}^{-1}$ and $\frac{1}{10}J_{IS}^{-1}$ respectively (Figure 3.23).[†] When all three groups are to be observed simultaneously a compromise setting of $\tau_2 \approx \frac{1}{6.6}J_{IS}^{-1}$ can be used and results in an enhanced sensitivity over direct polarisation using SPE. It should also be noted that for S sites without SI J-coupling polarisation transfer is not possible and thus quaternary carbons do not appear in ^{13}C–^{1}H INEPT spectra. In general an enhancement of ≈ 4 can be achieved for carbons in I_nS spin systems using this method.

In addition to the sensitivity enhancement, the appropriate choice of τ_2 also allows the determination of the multiplicity for unknown peaks. While a delay of $\tau_2 = \frac{1}{8}J_{IS}^{-1}$

[†]Calculated using: $SI = \sin(\phi)$, $SI_2 = 2\sin(\phi)\cos(\phi)$ and $SI_3 = 3\sin(\phi)\cos^2(\phi)$ where $\phi = \frac{\tau_2}{2\pi \cdot J_{IS}} = \theta$.

produces a spectrum with all groups, $\tau_2 = \frac{1}{4}J_{IS}^{-1}$ displays only IS groups and $\tau_2 = \frac{3}{8}J_{IS}^{-1}$ gives positive SI and SI_3 groups and negative SI_2 groups (Figure 3.23). Thus for $^{13}C-^{1}H$ INEPT spectra methyl (CH_3), methylene (CH_2) and methine (CH) sites can be distinguished [Claridge 99].

As with cross-polarisation, shorter T_1^H limited recycle delays can also be used for INEPT due to the transfer of polarisation form protons to carbons.

3.4.5 DEPT

An alternative J-mediated polarisation transfer experiment is the distortionless enhancement by polarisation transfer (DEPT) experiment [Doddrell 82]. Like INPET this also results in a sensitivity enhancement over SPE and allows spectral editing, however it has a number of advantages over INEPT [Claridge 99].

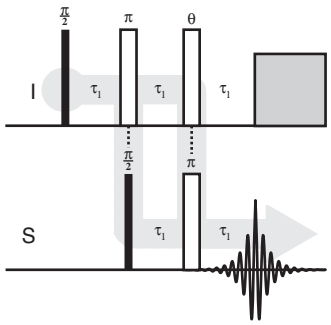

***Figure 3.24**: Pulse sequence for the DEPT experiment.*

As with INPET after the initial $\frac{\pi}{2}$ pulse on I and an evolution period of $\tau_1 = \frac{1}{2}J^{-1}$, the two I vectors of an SI pair lie antiphase along the $\pm x$-axis. While the subsequent π pulse on I refocuses the proton chemical shift evolution, the $\frac{\pi}{2}$ pulse on S generates a state of heteronuclear multiple-quantum coherence (HMQC). The HMQC is allowed to evolve for another τ_1 period under the influence of both proton and carbon chemical shift, but independent of IS J-coupling. The θ pulse on the I spins generates observable magnetisation by transferring the HMQC into antiphase transverse S magnetisation. The simultaneously applied π pulse on the S spins refocused the S chemical shift evolution. During the final τ_1 period the S magnetisation is refocuses under under the influence of J-coupling and thus can be detected without chemical shift dependent phase errors.

As with INEPT sensitivity enhancement and its implications towards spectral editing also apply to DEPT. With $\theta = 45^\circ$ positive SI, SI_2 and SI_3 groups are observed, while with an $\theta = 90^\circ$ pulse only SI groups are seen (Figure 3.23). Using a pulse angle of 135° leads to positive SI and SI_3 groups and negative SI_2 groups.

With DEPT the phase and intensity of a given signal depend solely on the tip-angle of the θ-pulse and are thus J-independent. Hence the DEPT sequence tends to be superior to INEPT regarding spectral editing when a range of J-coupling constants are encountered [Claridge 99].

3.4.6 INADEQUATE

As well as the heteronuclear J-couplings (J_{SI}) homonuclear J-couplings (J_{SS}) between low abundant nuclei, although rare, are also able to be used to gain structural information. One example of this is the incredible natural abundance double quantum transfer experiment (INADEQUATE) which allows full access to all SS connectivities in non-isotopically enriched samples [Bax 80, Bax 81].

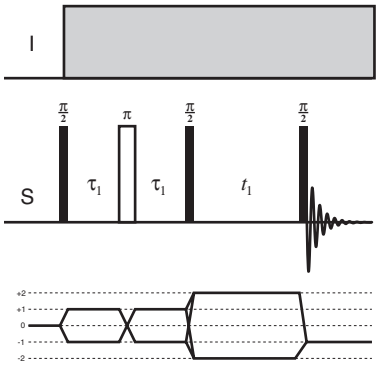

***Figure 3.25**: Pulse sequence and coherence transfer pathway for the 2D INADEQUATE experiment.*

With a low abundance of S spins two adjacent NMR active spins are extremely rare. Hence, the majority of the spectrum consists of isolated non-interacting S spin singlets. The rare SS spin-pairs resulting in low intensity doublets about their associated singlets. The INADEQUATE method suppresses the singlets, allowing clear observation of the SS doublets, using a double-quantum filter. Double-quantum coherence (DQC) is generated using the antiphase magnetisation of the coupled S spins created by a homonuclear spin-echo (Figure 3.25).

After initial excitation by the $\frac{\pi}{2}$ pulse the magnetisation is allowed to evolve under the influence of the homonuclear J-coupling for a time period $\tau_1 = \frac{1}{4}J_{SS}^{-1}$. A π pulse refocuses the chemical shift evolution and after the second τ_1 period only the magnetisation vectors of the J-coupled SS spin-pairs are antiphase. The antiphase magnetisation is then converted into double-quantum coherence (DQC) by the second $\frac{\pi}{2}$ pulse. These DQCs evolve during the variable evolution interval t_1 before being reconverted to observable single-quantum coherences by the final $\frac{\pi}{2}$ pulse.

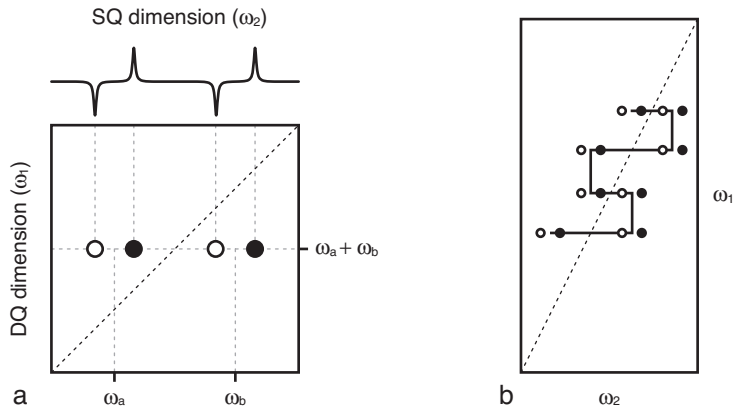

***Figure 3.26**: INADEQUATE spectra of a (a) single and (b) multiple SS spin-pair system*

The 2D spectra consist of antiphase doublets symmetrically located about the DQ diagonal at conventional chemical shift frequencies in ω_2 and the sum of the compo-

nents in ω_1 showing full through-bond spin connectivity (Figure 3.26).

3.4.7 Inversion-recovery

With motional information accessible via the spin-lattice relaxation (Section 2.4.3) a number of methods for determining the longitudinal time constant T_1 have been developed.

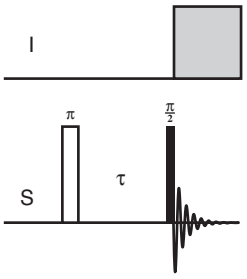

***Figure 3.27**: The inversion-recovery pulse sequence.*

The inversion-recovery method uses an initial π pulse to place the equilibrium magnetisation along the $-z$-axis. After a given period of time τ a $\frac{\pi}{2}$ pulse transfers the magnetisation into the xy-plane (Figure 3.27). Detection of this signal as a function of τ allows the relaxation of magnetisation from $-z$ to $+z$ to be monitored, and hence gives access to the T_1 time constant. The time constant T_1 is obtained by fitting the signal intensity as a function of τ with:

$$M(\tau) = M_0(1 - 2 \cdot \exp\left\{\frac{-\tau}{T_1}\right\}) \tag{3.80}$$

Due to an initial state of thermal equilibrium being needed, a long enough recycle delay τ_{rd} allowing relaxation back to this state is required. This leads to the cyclic problem of needing to know the value of T_1 in order to measure T_1. This results in two experiments, a rough estimate and a final measurement with $\tau_{rd} > 5 \times T_1$.

3.4.8 Saturation-recovery

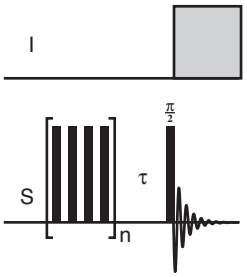

***Figure 3.28**: The saturation recovery pulse sequence.*

In contrast to the inversion-recovery method (Section 3.4.7), the saturation-recovery method uses a train of $\frac{\pi}{2}$ pulses to saturate the S spins prior to measuring the relaxation (Figure 3.28). This allows a non-equilibrium initial state to be used and thus circumvents the use of $\tau_{rd} > 5 \times T_1$ and the need to know T_1 before measurement. The time constant T_1 is obtained by fitting the signal intensity as a function of τ with:

$$M(\tau) = M_0(1 - \exp\left\{\frac{-\tau}{T_1}\right\}) \tag{3.81}$$

Due to longitudinal relaxation only occurring on the $+z$-axis, as opposed to both the $+z$ and $-z$ axes, this method is less accurate than inversion-recovery. However, with long recycle delays not needed saturation-recovery can be considerably faster than inversion-recovery.

3.5 General NMR processing techniques

An important aspect of NMR is the processing of the raw FID signal prior to Fourier-transformation. Such processing is needed to suppress spectral artefacts caused by FID truncation. Additionally resolution, sensitivity or both may also be increased by processing techniques [Hoch 96].

3.5.1 FID truncation and apodisation

An FID that does not decay to zero at the end of the acquisition time is said to be truncated. Fourier-transformation of such a truncated FID leads to a distorted spectrum with truncation artefacts caused by the discontinuity at the end of the FID. The Fourier-transform of such a discontinuous rectangular function $\Pi(t)$ produces a sinc function;

$$\Pi(t) \xrightarrow{\mathcal{FT}_t^{\omega}} \text{sinc}(\omega) = \frac{\sin(\omega)}{\omega} \tag{3.82}$$

Truncated signals thus result in peaks in the spectrum with so-called sinc artefacts (Figure 3.29b). Such sinc artefacts may be removed through the use of apodisation[†] where a truncated FID is convoluted with a decaying function. This procedure forces the end of the FID to zero and thus removes the rectangular function of the truncated FID. However, as such window-functions also effect the rest of the FID they inevitably result in a degree of artificial line broadening (Figure 3.29d). Several window functions have been developed to improve both sensitivity and resolution by emphasising different parts of the FID [Hoch 96].

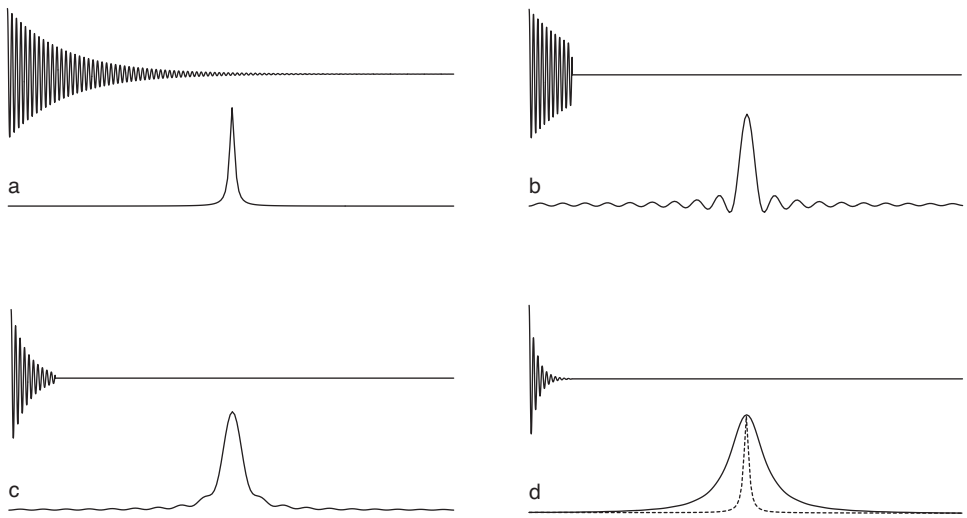

***Figure 3.29**: (a) Full and (b) truncated FID, with corresponding normalised spectra showing possible sinc function convolution. Artefacts removed using apodisation window-functions with relatively (c) slow and (d) fast decay.*

[†]literally meaning 'the removal of the feet'!

Exponential window function

The exponential window function has a single user defined variable a and is defined as:

$$f_E(t) = e^{-\pi \cdot a \cdot t} \tag{3.83}$$

The parameter a is always positive and defines the rate of decay of the function and hence how quickly the truncated FID is forced to zero (Figure 3.30). The stronger the FID truncation the larger a needs to be to suppress the truncation artefacts. An exponential window function also strongly broadens the line widths, especially their 'feet' (Figure 3.31). Hence the gain in sensitivity is always accompanied by a loss in resolution.

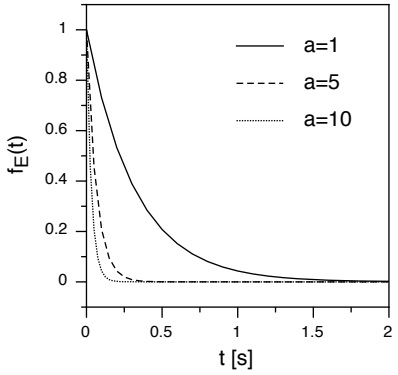

***Figure 3.30**: The form of the exponential window function using different values of a.*

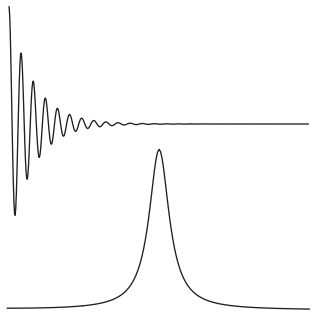

***Figure 3.31**: The Lorentzian line shape resulting from the application of the exponential window function.*

Gaussian window function

A more popular alternative to the exponential window function is the Lorentz-Gauss transformation. Generally this window function is referred to as simply the Gaussian window function, however technically this implies a different window function not commonly used.[†] From here after the Lorentz-Gauss transform will be referred to as the Gaussian window function for simplicity.

This Gaussian window function has two user defined variables a and b;

$$f_G(t) = e^{\pi \cdot a \cdot t} e^{-b \cdot t^2} \tag{3.84}$$

The parameter a is again always positive, however it is now responsible for countering the natural decay of the FID, hence the sign change between Equation 3.83 and Equation 3.84. The parameter b then governs the degree of true Gaussian line

[†] A true Gaussian window function would be described by; $f_{G'}(t) = e^{-b \cdot t^2}$ c.f. Equation 3.84.

broadening and is also always positive in value (Figure 3.32). The Gaussian window function thus transforms a Lorentzian line-shape into a Gaussian line-shape, reducing the width of the lower half of the peak (Figure 3.33). For this reason the Gaussian window function is a popular function for general resolution enhancement, especially concerning closely spaced peaks.

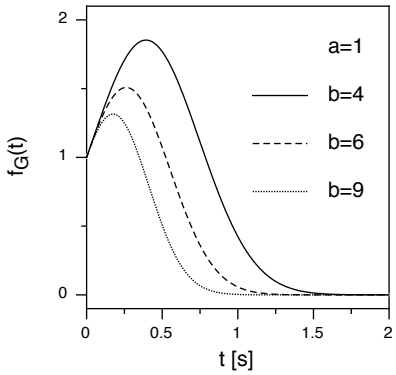

***Figure 3.32**: The form of the Gaussian window function for constant a and varying b parameters.*

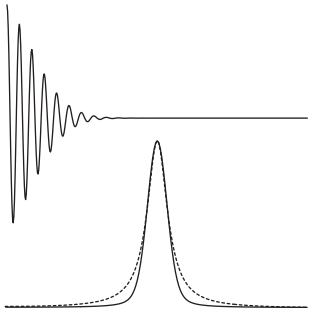

***Figure 3.33**: The Gaussian-like line shape (solid line) resulting from the application of the Gaussian window function as compared to a Lorentzian line shape (dashed line) showing broader 'feet'*

Sine-bell window function

The sine-bell window function always has a value of zero at the end of the FID, and thus efficiently eliminates strong truncation artefacts found in some 2D NMR experiments. However the resolution enhancement is also accompanied by line-shape distortions and a degradation in sensitivity.

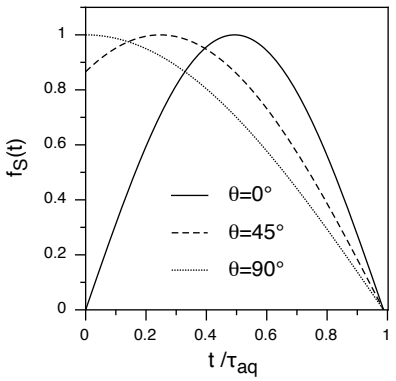

***Figure 3.34**: The form of the sine-bell window function for different phase shifts θ.*

In order to always place the 180° null at the end of the FID, the acquisition time τ_{aq} is also needed as a parameter for this window function;

$$f_S(t) = \sin\left(\left(\frac{\pi - \theta}{\tau_{aq}}\right) t + \theta\right) \tag{3.85}$$

The phase-shift θ is then used to adjust the behaviour of the window function, allowing the location of the maximum to be shifted closer to the start.[†] For $\theta = 0$ the window function takes the form of the first half-period of the sine function: being zero at both the beginning and end of the FID, and reaching a maximum half way through acquisition (Figure 3.34). By adjusting the phase-shift a balance between the gain in resolution and lineshape distortions/sensitivity degradation may be accomplished.

[†]Note: $\theta = \frac{\pi}{2}(SSB + 1)$ on Bruker spectrometers. Equivalently $SSB = \frac{2\theta}{\pi}$-1

3.5.2 Zero filling

The process of adding zeros to the end of an FID that has decayed to zero is called zero filling. This extrapolation in the time domain leads to interpolation in the frequency domain after Fourier-transformation.

Through the doubling of the number of data points in the time domain, it is possible to improve the resolution in the frequency domain. This is due to the Fourier-transform splitting the complex time domain data in the FID into both real and imaginary frequency domain spectra. Since only the real part is usually considered half of the information contained in the FID is effectively lost. Increasing the number of time-domain data points by a factor of 2 thus prevents this loss of information [Bartholdi 73].

Zero-filling beyond a factor of two only leads to an interpolation of data points, increasing the so-called digital resolution, without providing new information. However, this may help to enhance fine structure and improve line-shape definition.

Chapter 4

Solid-state MAS NMR

Solid-state NMR has been explored as an alternative to solution-state NMR of polyethylene, the latter being hindered by long preparation [Seger 04] and measurement times [Wood-Adams 00]. Measurement of the bulk state not only increases the amount of NMR active nuclei found within the detection coil volume, resulting in greater sensitivity per unit time, but also reduces preparation time.

The only truly quantitative pulse sequence, SPE is not commonly used for ^{13}C solid-state NMR [Hatfield 95]. Due to the lack of mobility within solid polyethylene, motional averaging of the anisotropic line broadening interactions does not occur. Thus broad ^{13}C spectral lines are seen, resulting in low sensitivity and resolution.

However, in a rigid spin system the sensitivity can be enhanced by transferring polarisation from the ubiquitous protons to the low abundance carbon nuclei by the process of cross-polarisation, CP. When cross-polarisation is applied in conjunction with MAS, both resolution and sensitivity are improved [Schaefer 77]. Unfortunately due to the mechanism of polarisation transfer, CP MAS spectra are not inherently quantitative. In the following chapter methods to obtain quantitative ^{13}C CP MAS spectra of polyethylene were investigated.

4.1 CP MAS of PE

The rate and efficiency of cross polarisation strongly depend on the ^{13}C–^{1}H heteronuclear dipolar coupling between nuclei (Section 3.4.3). For each carbon site the degree of cross-polarisation is thus proportional to the proximity and number of coupled protons [Laupretre 90]. Hence a CH_2 group will generally be polarised more rapidly than a quaternary carbon. The mobility of a particular site is also of importance, with only an effective dipolar coupling being experienced due to motional averaging of the anisotropic interaction. Thus, the rate of cross-polarisation to highly mobile car-

bon sites, such as CH_3 groups, is slower than that of more rigid sites. Generally, the cross-polarisation build-up rate $\frac{1}{T_{CH}}$ of different carbon types decreases in the order: nonprotonated carbon > rotating CH_3 > aromatic or aliphatic CH > CH_2 > static CH_3 [Yu 90, Axelson 86].

Polyethylene exhibits a heterogeneous morphology with a large gradient in molecular mobility. At room temperature the carbon nuclei of polyethylene can be found in either crystalline, interfacial or amorphous regions. The CH_3 groups predominantly occur in the amorphous regions [Kuwabara 97] with the backbone being mostly crystalline (Figure 4.1). For each region different cross polarisation build-up ($\frac{1}{T_{CH}}$) and decay rates ($\frac{1}{T^H_{1\rho}}$) are found. This leads to region-specific optimum contact times and Hartmann-Hahn match conditions. Thus for a given single contact time, the ratio of signal intensities may not reflect the true distribution of sites and results in the cross polarisation spectra not being quantitative. The large difference in molecular motion is also deemed responsible for greater than expected line broadening and poor reproducibility [Yu 90].

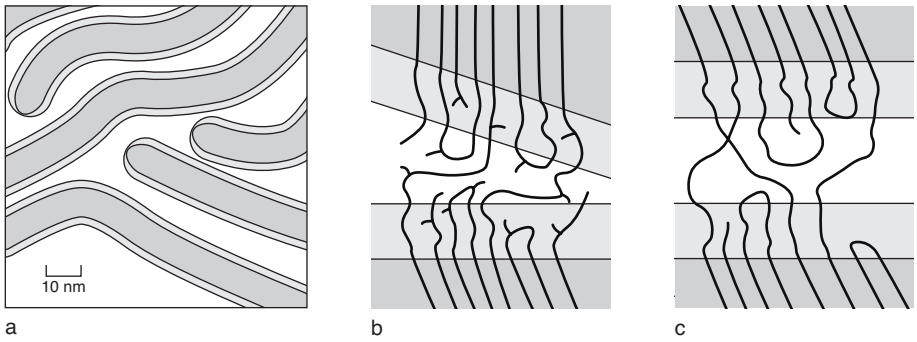

***Figure 4.1**: Schematic distribution of short-chain branching and end groups in the crystalline (dark gray), interfacial (light gray) and amorphous (white) regions for (b) LLDPEs and (c) HDPEs. Adapted from [Kuwabara 97].*

For these reasons CP MAS has predominantly been used to gain insight into the morphology and phase structure of polyethylene [Schmidtrohr 91, Guo 00, Litvinov 02]. Despite not being quantitative, CP MAS has been suggested as a rapid method of comonomer determination in polyolefin copolymers. However for accurate quantification of comonomer content it has generally been deemed ineffective due to the mobility gradient [Hatfield 95, Guo 00]. One possible method for the reduction of the influence of the mobility gradient may be the use of low-temperature cross-polarisation measurements, allowing access to semi-quantitative spectra [VanderHart 80].

4.1.1 Comparison with solution-state NMR

For a typical polyethylene-co-octene (PE8a-B) a CP MAS spectrum was measured at ν_{1_H} = 500 MHz using 3 kHz MAS and $\boldsymbol{B}_1$ = 50 kHz heteronuclear decoupling under ambient conditions. [†] To maximise sensitivity, rotors with an outer diameter of 7 mm were used, resulting in approximately 200 mg of polyethylene being placed within the detection coil. When compared to a solution-state spectrum[‡] the line widths of the CP MAS spectrum were approximately 100 times broader (Figure 4.2).

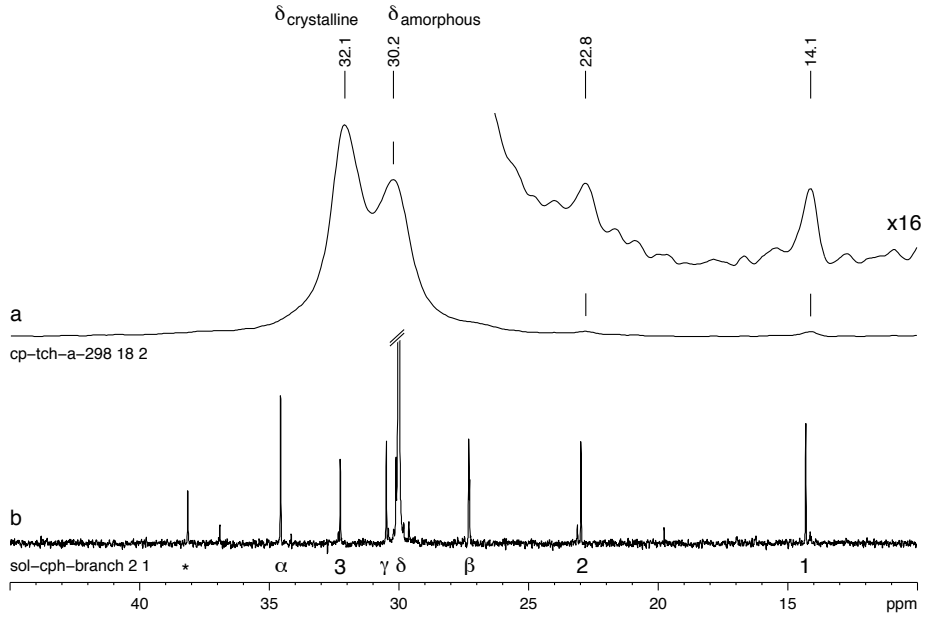

***Figure 4.2**: Comparison of (a) Hartmann-Hahn CP at 500 MHz (3 kHz MAS using 7 mm rotors) and (b) solution-state at 400 MHz ($T = 100°C$) of PE8a-B.*

In the CP MAS spectrum the δ sites in the crystalline and amorphous regions were observed at 32.1 and 30.2 ppm respectively. The terminal branch sites **1** and **2** (Figure 2.43) of the octene comonomer were seen at 14.1 and 22.8 ppm respectively. Although in theory both **1** and **2** could be used for branch quantification, in practice only the **1** site was found to be fully resolved to the baseline. However, the ratio $\int_1$:$\int_\delta$ does not accurately represent the true ratio of **1** and δ sites within the system. This being due to the difference in mobility, and thus degree of cross polarisation, between the CH_3 and CH_2 groups.

Due to the slow spinning, and residual line broadening interactions at 3 kHz MAS and 500 MHz, the first order spinning sidebands (SSB) encroached onto the broad 'foot' of the centre band (Figure 4.3). Although suppression of SSBs may be achieved by techniques such as TOSS [Dixon 82], the resulting spectra are not quantitative [Yu 90]. For this reason faster spinning speeds are used to increase the separation between the centre band and its sidebands. This also has the added advantage of reduc-

[†] All spectra in this chapter recorded using standard MAS probheads, c.f. Section 6.2.2.
[‡] Acquired using 10 mm NMR tubes with ≈ 200 mg of polyethylene dissolved in TCB at high temperature.

ing SSB intensity. However, at 500 MHz the rotor would have to be spun at greater than 10 kHz in order to achieve resolution to the baseline [Yu 90, Laupretre 90]. Although the problems associated with the spinning-sidebands could be reduced by using a lower $\boldsymbol{B}_0$ field the associated loss in sensitivity also has to be considered.

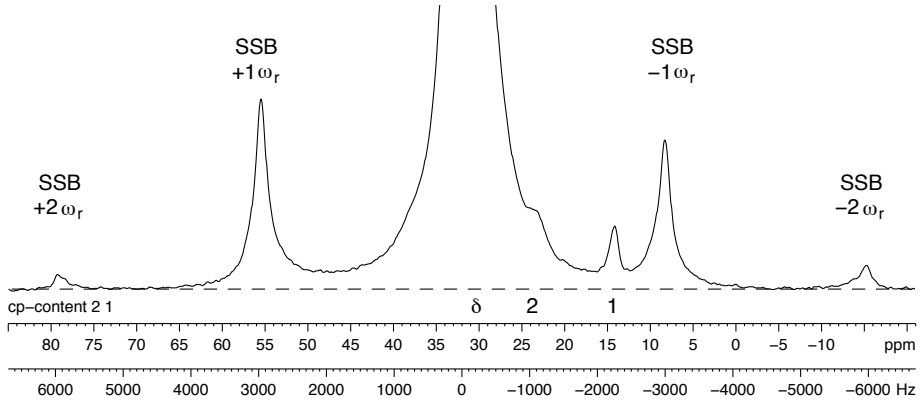

***Figure 4.3**: Relative position and size of the first and second order spinning-sidebands (SSB) of a typical polyethylene cooctene (PE8a-B) with MAS of 3 kHz and NS = 2048. (Baseline shown as dashed line.)*

4.1.2 Potential of fast MAS

As well as with RF irradiation during acquisition, spectral line narrowing by the partial removal of the heteronuclear dipolar coupling can also be achieved using MAS. However with the strong heteronuclear dipolar coupling found in solid polyethylene, fast-MAS of 30 kHz is needed. This also has the added advantage of reducing SSB intensity and increasing their separation from the centre band, allowing more accurate integration. In order to achieve such conditions MAS rotors with an outer diameter of 2.5 mm were used. The smaller rotors resulted in only 10 mg of polyethylene being placed within the detection coil and thus severely reduced sensitivity per unit time.

To investigate the possible improvement in quantification under such fast-MAS conditions a ramp-CP [Metz 94] spectrum of a polyethylene-co-octene (PE8b-C) was measured at 700 MHz and 30 kHz MAS (Figure 4.4a). Compared to the Hartmann-Hahn CP spectrum at 500 MHz using 3 kHz MAS (Figure 4.2a) approximately four times narrower spectral lines were obtained under fast-MAS. However both the higher external magnetic field and faster MAS contributed to the improvement in resolution. Even under these measurement conditions the resulting linewidths were still more than twenty times broader than those found in solution (Figure 4.4b).

Under fast-MAS further site resolution was achieved. In addition to the δ site $\star$, α, β, **2** and **3** were also detected at 37.9, 34.3, 27.3, 32.2 and 22.9 ppm respectively. However unlike previous CP spectra, separate resonances for the crystalline and amorphous forms of δ were not seen, with only a single peak at 30.2 ppm observed. This was most likely due to the greater frictional heating under such MAS conditions

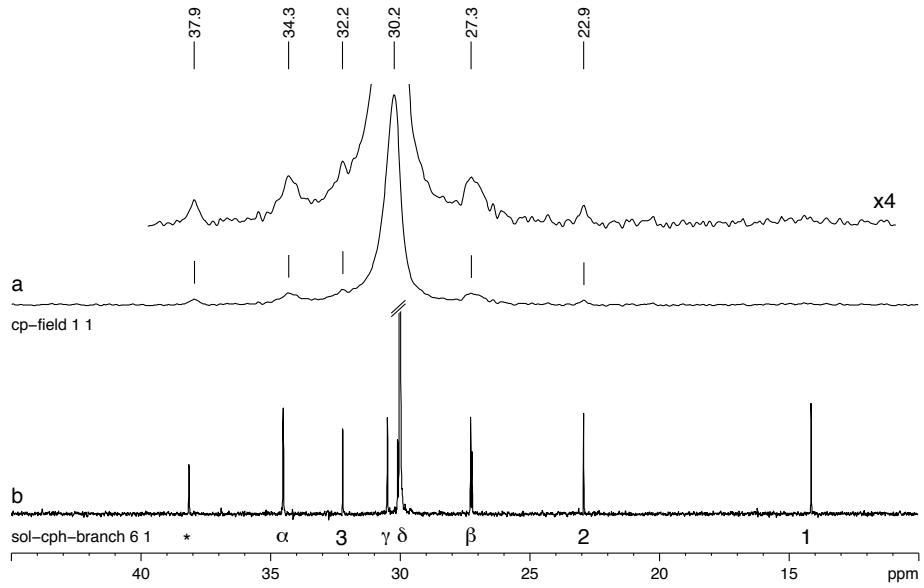

***Figure 4.4**: Comparison of (a) ramp-CP at 700 MHz (30 kHz MAS using 2.5 mm rotors) and (b) solution-state at 400 MHz ($T = 100°C$) of PE8b-C.*

[Langer 99]. The increased mobility in the sample was also thought to be responsible for the absence of the terminal branch site **1** at 14.1 ppm in the fast-MAS spectrum.

Despite the general increase in resolution, only the $\star$ and **2** sites were resolved to the baseline and thus suitable for quantification. This was purely due to the difference in chemical shift of these sites to that of δ. Although mobility of the $\star$ and δ sites may be similar, the different number of attached protons is expected to alter their degree of cross polarisation. In contrast, although the **2** and δ sites have the same number of attached protons, the difference in mobility is expected to impart different behaviour under cross polarisation. Thus, the ratios $A_\star$:A_δ and $A_\mathbf{2}$:A_δ were not expected to give an accurate representation of the true branch content of the sample. Both ratios should be more accurate than the ratio of $A_\mathbf{1}$:A_δ however, due to the unique combination of high mobility and three attached protons found for the **1** site. Although accurate quantification of the degree of branching is not achieved a semi-quantitative estimate can be made using the $\star$, **2** and δ sites.

The gain in resolution was accompanied by a loss of sensitivity due to the reduced available sample volume. This was most clearly illustrated by the overall measurement time needed to achieve similar signal-to-noise ratios for the sites used for quantification. Using 7 mm rotors at 500 MHz and 3 kHz MAS, a SNR of 7 for site **1** was achieved in 5 minutes. However, 22 hours of continuous measurement was needed to achieve a SNR of 6 for the $\star$ site using 2.5 mm rotors at 700 MHz and 30 kHz MAS. For this reason, fast-MAS was not considered a viable alternative for time-efficient branch quantification compared to large sample volume setups, even when combined with high external magnetic fields.

4.1.3 Variable temperature CP MAS

With only the peaks from the **1** and δ sites available for integration under 3 kHz MAS, the difference in degree of cross polarisation is a key limitation to branch quantification. The differences in mobility between the crystalline CH_2 and the amorphous CH_3 groups render the integral ratio of these sites unsuitable for branch quantification. An attempt was made to reduce the influence of the mobility gradient by measuring CP spectra of polyethylene at low-temperatures [VanderHart 80]. It was hoped that under such conditions the reduced motion of the methyl group would lead to a more comparable behaviour of the two other resolved sites, and thus a more quantitative integral ratio.

For the δ and **1** sites of a polyethylene-co-octene (PE8a-B) the temperature dependence of the intensity build-up and decay with contact time were measured (Figure 4.5).

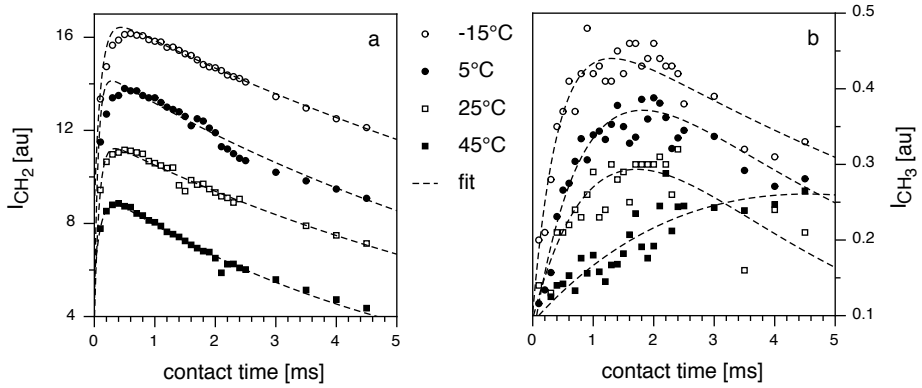

***Figure 4.5**: Contact-time dependent intensity of the (a) δ CH_2 groups and (b) **1** CH_3 groups of PE8a-B predominantly in the crystalline and amorphous regions respectively.*

The sites in the crystalline and amorphous regions clearly showed different behaviour at room temperature, with the more mobile CH_3 groups of the **1** site having the longer T_{CH} times. This directly resulted in the maximum signal intensity for each site being reached after a different contact time. At room temperature such maxima were reached for the sites in the amorphous and crystalline regions after 2 ms and 0.4–0.5 ms respectively. The disparity in cross polarisation behaviour was even greater at higher temperatures.

The contact-time dependence of the signal intensity for the δ sites in the crystalline phase was not significantly altered by lowering the temperature. However for the more mobile **1** sites in the amorphous region, T_{CH} was reduced. This resulted in the maximum signal intensity appearing at shorter contact times. For both sites sensitivity was generally increased, due to the different Boltzman distribution of the Zeeman levels and greater CP efficiency with less motional averaging of the mediating dipolar interaction.

Low temperature NMR allowed a common optimum contact time to be used for both δ and **1** sites due to the stronger influence of temperature on the T_{CH} of the **1** site. Thus, at $-15°$C a contact time of 1–1.2 ms was found to give signal intensities close to both respective maxima. This allowed access to semi-quantitative CP spectra of motionally heterogeneous polyethylene samples.

4.1.4 Effects of short recycle delays

In contrast to SPE where the carbon nuclei are directly polarised, under CP the polarisation originates on the protons and is then transferred to the carbon nuclei. Thus, the recycle delay required for quantitative spectra is only determined by the proton spin-lattice relaxation. With protons relaxing between 10–100 times faster than carbons in the solid-state [Axelson 82, Axelson 83, McFaddin 86], semi-quantitative CP spectra were expected to be more time efficient than fully quantitative SPE measurements, the latter limited by carbon relaxation. However the dense spin system of solid polyethylene showed non ideal relaxation behaviour. This behaviour is best illustrated when comparing the CP efficiency of the CH_2 and CH_3 groups in a polyethylene-oligomer (PE-O) [†] at different recycle delays (Figure 4.6). With a T_1^H of below 1 s, the plateau of maximum intensity for both CH_2 and CH_3 groups was expected to have been reached at a recycle delay of approximatly 4–5 s.

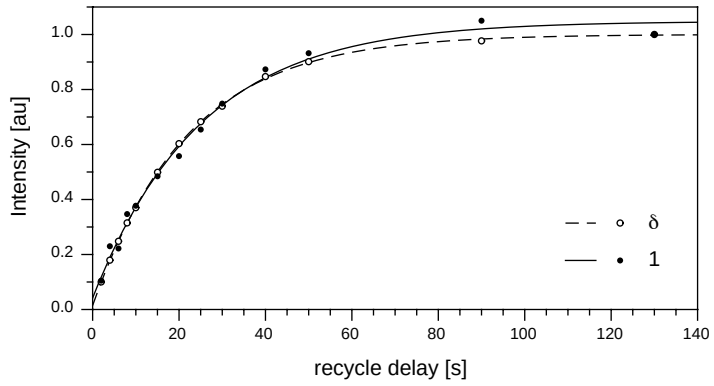

***Figure 4.6**: Intensities of **1** and δ sites in a polyethylene-oligomer as a function of recycle delay τ_{rd}.*

In contrast to expectations, the signal intensity of both groups was only found to reach such a plateau with recycle delays longer than 100 s. This indicated the possible presence of further relaxation processes, in addition to those expected for CP. Upon shortening the recycle delay, saturation of the spin system resulted in the expected reduction of signal intensity for both sites. Since both CH_2 and CH_3 polarisation decreased with roughly the same time constants (21.5 s and 23 s) their ratio at any given recycle delay remained approximately constant. Thus semi-quantitative

[†]Similar behaviour was also observed for the polymer but to a lesser degree.

CP MAS measurements at recycle delays as short as 2 s were shown to be feasible, allowing for a further improvement in time efficiency.

4.2 Applications of optimised CP MAS

In this section the potential of low-temperature CP MAS at $-15°C$, combined with reduced recycle delays of 2 s, was assessed. All polyethylene branch and end group quantification was undertaken using a 500 MHz spectrometer under 3 kHz MAS.

4.2.1 Branch quantification

A series of three polyethylene-co-octenes with increasing co-octene content were investigated to test the applicability of the optimised CP MAS method for branch quantification. The branch contents obtained by solid-state NMR were compared to those obtained by both solution-state and melt-state MAS NMR using SPE (discussed later in Chapter 6).

In the solution-state a recycle delay of 10 s was needed to allow full relaxation of the sites α and δ used for branch content quantification. Signal-to-noise ratios of 17–46 were obtained for α within 12 hours. In the melt-state, even with recycle delays of 60 s, similar signal-to-noise ratios for α were achieved in a maximum of 8 h 30 min due to the higher sensitivity per-unit-time. The low-temperature CP MAS spectra reached signal-to-noise ratios of 21–54 for site **1** using a recycle delay of 2 s after 1 h 10 min, making it the most time-efficient method. However, the long recycle delays of the melt-state MAS NMR ensured full relaxation of all sites and thus provided the most reliable branch contents overall.

With the **1** and δ sites not resolved to the baseline (Figure 4.7), the semi-automated integration method used for solution-state and melt-state spectra could not be applied (Section 7.2.8). Thus manual integral baseline correction was necessary, which unfortunately resulted in user-dependent branch contents. Furthermore, when the CP MAS spectra were integrated neglecting and including the contribution of the SSBs of δ, the branch contents differed by up to 20%. Compared to solution-state and melt-state results branch contents were generally lower when the SSBs were included. Despite this discrepancy, both solid-state integration methods gave branch contents comparable to that of solution- and melt-NMR, with the trend of increasing comonomer content still observed (Table 4.1).

***Table 4.1**: Comparison of branch contents obtained with solution, melt and solid-state NMR. For solid-state spectra the **1** sites were used for quantification as opposed to α for $\int_\delta$ including (+) and excluding (-) SSBs.*

B_{br} [1000 C $^{-1}$]	solution	melt	solid (+)	solid (-)
PE8a-A	4.5	5.1	4.5	5.3
PE8a-B	7.5	8.5	6.5	8.1
PE8a-C	10.8	10.5	9.4	11.7

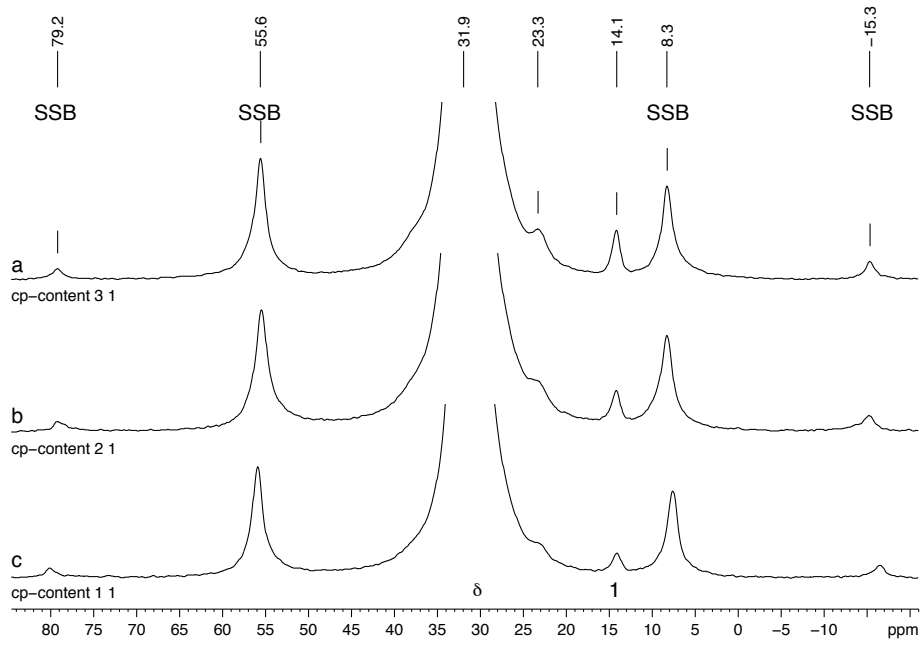

***Figure 4.7**: Low temperature CP MAS spectra of (a) PE8a-A (b) PE8a-B (c) PE8a-C. All spectra measured at $-15°C$ and 500 MHz with τ_{ct} = 1.2 ms, τ_{rd} = 2s and NS = 2048 using 7 mm rotors.*

Due to the low resolution, distinction of comonomer would only be possible when the **1** sites had different chemical shift values. Thus the presence of co-propene and co-butene may be detected as their end-groups would be distinguishable at 20.1 and 11.2 ppm respectively. Estimating their contents would however be imprecise as both end-groups lie in the 'feet' of adjacent peaks, and thus cannot be accurately integrated. Furthermore the branch contents determined via CP MAS only represent their true values if the comonomer contents are low, due to the inclusion of all the sites along the branch other than **1** into the bulk integral. Thus branch contents determined from CP MAS spectra will be systematically underestimated. It is thus concluded that optimised CP MAS at low temperatures is only applicable for the rapid estimation of polyethylene-co-α-olefin branch contents when the comonomer is both known and present in low concentration. Even when these criteria are met the results were still not deemed as reliable as solution-state and melt-state methods.

4.2.2 End group quantification

To explore the application of optimised CP MAS towards sparse end-group quantification, a high molecular weight polyethylene homopolymer (PE0a) was examined. Assuming no branching the number of CH_2 groups per CH_3 end group may then be used to determine the number average molecular weight M_n. The sparse nature of the end-groups was illustrated by the low signal-to-noise ratio of 6.7 achieved for the **1** sites after 24 hours of continuous measurement (Figure 4.8).

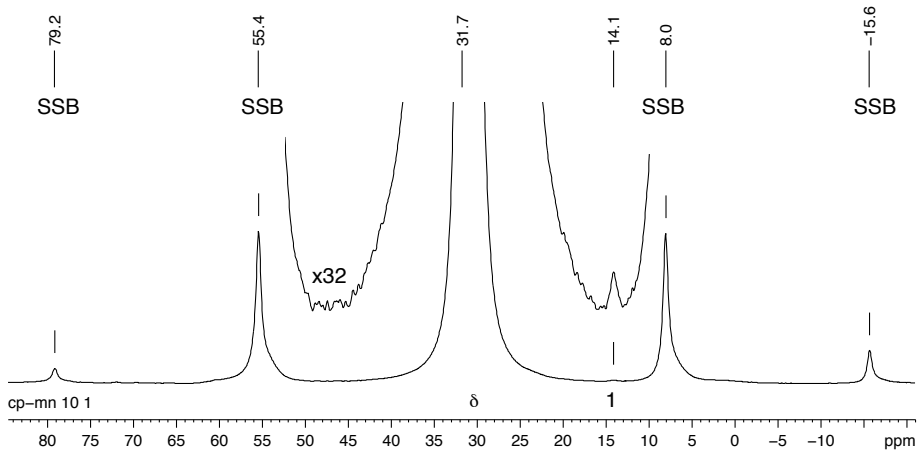

***Figure 4.8**: Low temperature CP MAS spectrum of PE0a measured at −15°C and 500 MHz with τ_{ct} = 1.0 ms, τ_{rd} = 2s and NS = 40,960.*

Manual correction of the integral $A_\mathbf{1}$ via slope and bias was required due to the **1** peak lying between the broad 'feet' of the δ peak and the first order SSB. In order to determine the degree of user-influence on the final results the same spectrum was manually integrated ten times, with both integrals being corrected for slope and bias each time. The same procedure was repeated including the area of the SSBs into the bulk integral.

End group concentrations of 3900–5100 and 3100–3900 CH_2 groups per CH_3 group were determined with and without consideration of the SSBs respectively. For each statistical distribution the average number of CH_2 groups and its standard deviation were determined (Table 4.2). Irrespective of whether the SSBs were included or not, manual integration and integral baseline correction led to standard deviations of 7–9%.

***Table 4.2**: End group ratio and M_n of PE0a determined via GPC and solid-state NMR, with $\int_\delta$ including (+) and excluding (-) SSBs.*

	GPC	solid (+)	solid (-)
$CH_2 : 1\ CH_3$	4100	4400 ± 375	3500 ± 260
M_n [kg mol^{-1}]	114	124 ± 11	99 ± 7

The two values of 99 and 124 kg mol $^{-1}$ obtained with CP MAS lie within 15% of the GPC determined value of 114 kg mol $^{-1}$. Thus solid-state NMR, even with its inherent deviation, was able to provide comparable results to GPC. However when considering both the long measurement time and the 25% difference between obtained results, low-temperature CP MAS was not deemed a viable option for sparse end-group quantification.

4.3 Summary

In this chapter the use of solid-state NMR for both branch and end group quantification in polyethylene was explored. The use of ^{1}H–^{13}C cross polarisation was found to offer significant advantages over single pulse excitation, due to the enhanced sensitivity and shorter, T_1^H dictated, recycle delays needed.

The effects of the mobility gradient between crystalline CH_2 δ sites and amorphous CH_3 **1** sites was found to lead to non-quantitative integral ratios. The effect was partially compensated for by the use of low temperature measurements which resulted in similar T_{CH} times, and increased CP efficiencies, for the amorphous and crystalline regions. It was shown that by undertaking CP MAS experiments at $-15°C$ semi-quantitative spectra could be achieved.

A further reduction in measurement time was found to be possible by shortening the recycle delay from $5 \times T_1^C$ to 2 s. Although the signals of both the δ and **1** sites decreased at the shorter recycle delays, due to saturation, it was shown that their ratio stayed approximately constant allowing quantification.

The maximum sensitivity per unit time was achieved using MAS rotors with an outer diameter of 7 mm. The use of these enabled the placement of $\approx$ 200 mg of polyethylene within the volume of the detection coil. At external magnetic field strength of 500 MHz and 3 kHz MAS, the strong heteronuclear dipolar coupling found within solid polyethylene still however resulted in CP spectra with broad spectral lines and thus low resolution. Although resolution was improved using a high external magnetic field of 700 MHz and fast-MAS of 30 kHz, the reduced sample volume resulted in much lower sensitivity. Thus this setup was deemed inappropriate for routine measurements.

Due to the low resolution, the use of a semi-automated integration method was not found to be possible for solid-state polyethylene spectra. Manual integration thus had to be used for all spectra, with individual baseline correction applied to the integrals of both the δ and **1** sites. The application of manual integration thus resulted in relatively high error of the determined quantities. For example, when the same spectrum was manually integrated ten times a user dependent distribution of integral ratios was obtained with standard deviations of 7–9%. Furthermore the determined quantities differed by up to 25% depending on whether the spinning side bands of δ were included into the main integral for δ or not.

Rapid estimation of polyethylene-co-α-olefin branch content and approximate M_n determination was demonstrated using the optimised solid-state CP MAS method. In general the method was not deemed suitable for accurate quantification, due to the relatively large variation of the determined quantities in question. The cause of which being identified as a combination of manual integration methods and the intense spinning-sidebands.

Chapter 5

Melt-state static NMR

In the previous chapter is was shown that only low-resolution spectra of polyethylene could be obtained, in a time efficient manner, by solid-state NMR. This was mostly due to the strong heteronuclear dipolar coupling. It was however also shown that the analysis of PE in bulk and the use of larger sample volumes resulted in greater sensitivity per-unit-time, and were thus more time-efficient. For this reason melt-state NMR was investigated as an alternative to solid-state and solution-state NMR. Melt-state NMR combines the greater sensitivity per-unit-time of the measurement of bulk PE with the enhanced resolution due to increased molecular mobility. The greater resolution resulting from motional averaging of the strong line broadening interactions which plague the solid-state. With both enhanced resolution and sensitivity, SPE may be used allowing access to truly quantitative melt-state NMR spectra. In contrast to solution-state NMR analysis of the melt-state also allows access to insoluble fractions.

Although melt-state NMR can also be carried out under MAS, providing further averaging of the line broadening interaction, the sample volumes accessible are limited by the size of the MAS rotors. Despite this, melt-state MAS NMR of polyolefins has shown great promise [Zeigler 94, Hatfield 95], and will be fully investigated in Chapter 6. In this chapter melt-state NMR will be limited to the static set-up.

In static NMR the sample is placed within a coil mounted perpendicular to the $\boldsymbol{B}_0$ field. Due to the sample container remaining stationary during measurement, considerably more flexibility is available regarding coil size and geometry. Previous investigation of PE under such conditions resulted in strongly broadened spectra at room temperature [Dechter 81]. At higher temperatures, although the static linewidth decreased by a factor of six, the resolution obtained was still far too low for quantification (Figure 5.1). After preliminarily investigations it was established that static melt-state NMR did in fact provide the resolution required for quantitative analysis. Several strategies for improving both sensitivity and resolution were thus explored for melt-state static NMR of PE.

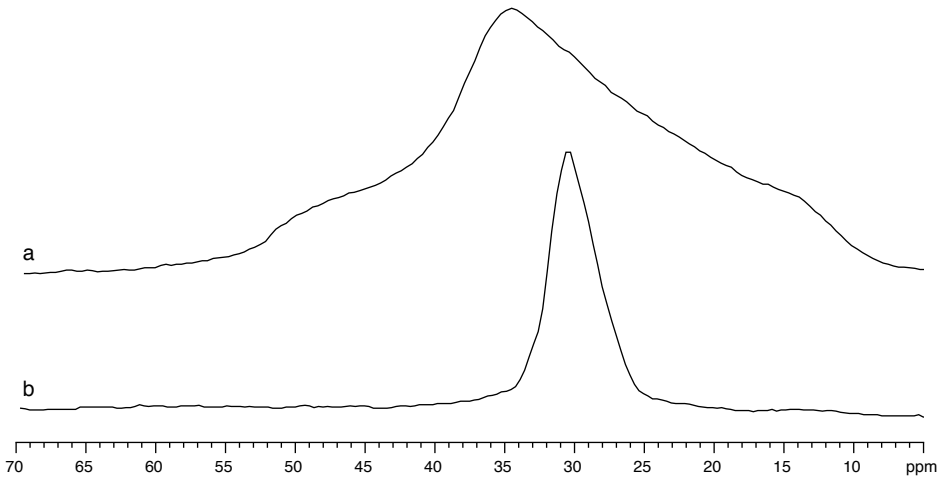

***Figure 5.1**: Reported ^{13}C static NMR spectra of PE at (a) room temperature and (b) 160°C showing the lack of spectral resolution. Reproduced from [Zeigler 94].*

5.1 Comparison of melt-state static and MAS NMR

In order to asses the spectral resolution achieved by melt-state static NMR a comparison of melt-state static and melt-state MAS was undertaken. Comparable spectra of a commercial PE-co-butene (PE4) were acquired with a 300 MHz magnet at 150°C[†] using static and MAS probeheads (Figure 5.2). The coil for the static probehead was 7.5 mm in diameter (ϕ_c), comparable to that used in the MAS probehead. A 7 mm MAS rotor was used as a sample container for both measurements. This resulted in $\approx$ 240 mg of PE being able to be packed into the rotor for static measurements. In order to allow stable spinning at 3 kHz MAS, a lesser amount of $\approx$ 200 mg was used for the MAS measurement.

Surprisingly high resolution was obtained under static conditions, with line narrowing solely achieved by motional averaging and heteronuclear dipolar decoupling (Figure 5.2a). The additional line narrowing provided by MAS resulted in a 20% reduction in line-widths (Figure 5.2b). All peaks necessary for branch quantification (δ, α, $\star$) were still clearly resolved in the static spectrum and allowed for spectral integration.

For quantitative comparison of sensitivity, spectral normalisation was needed. This was achieved by determining the standard deviation of the noise region (SD_{noise}) between 45–50 ppm for each spectrum individually. The absolute intensity values of the whole spectrum were then divided by their respective SD_{noise} value, i.e. after normalisation all spectra had an SD_{noise} value of unity. Sensitivity thus became proportional to the total spectral area (A_{all}) of the normalised spectrum. More specifically, the absolute sensitivity was quantified as the total normalised area divided by the

[†]Lowest temperature allowing melt-state NMR of polyethylene, c.f. Sections 5.5 & 6.2.3.

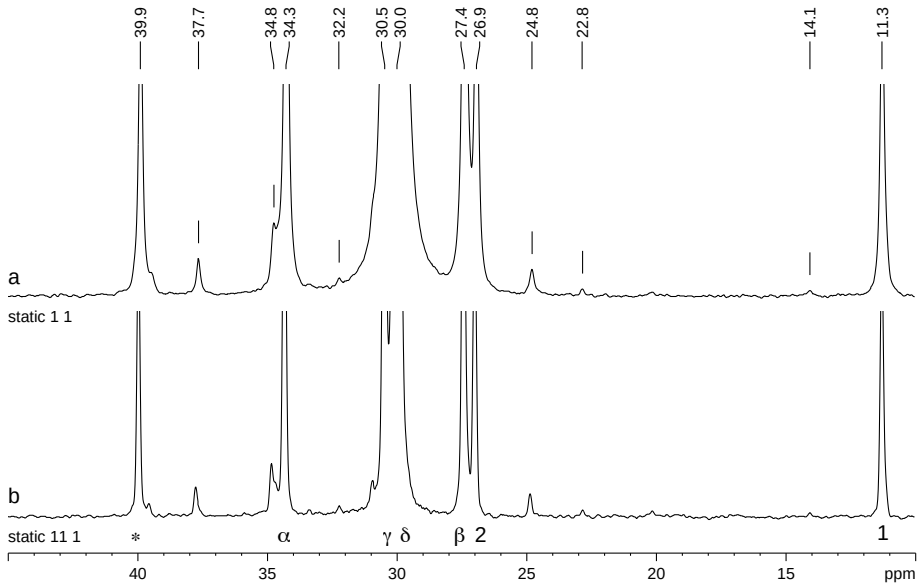

***Figure 5.2**: Normalised SPE spectra of PE4 at 300 MHz using (a) 7.5 mm static and (b) 7 mm MAS setups.*

square root of the time taken to acquire the spectrum in seconds, i.e. $A_{all} \cdot \sqrt{t}^{-1}$.[†] For simplicity only the relative sensitivity is given for each comparable series of spectra by normalising the sensitivity of the lowest value obtained to unity.

The absolute sensitivity of the static set-up was found to be a factor of two higher than that of the MAS setup (Table 5.1), this being equivalent to four times faster acquisition. This difference in sensitivity was attributed to a combination of the larger amount of sample used for the static experiments and the perpendicular orientation of the coil to the $\boldsymbol{B}_0$ field in the static setup, i.e. 100% efficiency of a coil at 90° to $\boldsymbol{B}_0$ as opposed to the 82% efficiency[‡] of an MAS coil inclined at 54.74°.

***Table 5.1**: Comparison of the coil diameter (ϕ_c), relative sensitivity, resolution and branch quantification using melt-state static and MAS measurements of PE4 at 300 MHz and 150°C.*

	ϕ_c	Sensitivity	FWHM$_\delta$	$B_\star$
	mm	$A_{All}\sqrt{t[s]}^{-1}$	ppm	10^{-3} C$_{bb}$
static	7.5	2.0	0.20	32.4
MAS	7.1	1.0	0.16	32.4

With comparable branch contents calculated from both static and MAS spectra, melt-state static NMR was shown to be a time efficient alternative to melt-state MAS, even with its decreased resolution. However when comparing the time-efficiency of two methods, the time taken for sample exchange also plays an important role.

The static setup required the removal of the whole probehead from the magnet to allow sample exchange. This resulted in probehead cooling and thus required a period of reheating prior to the commencement of the next measurement. For MAS mea-

[†] Accounting for the signal increasing with time but the noise increasing with the square root of time.
[‡] $82\% = 100\% \cdot \sin 54.74°$

surements the probehead could be kept at temperature during the sample exchange process due to the rotor being able to be separately ejected from the probehead. For high temperature MAS measurements disposable boron nitride (BN) rotor caps were required. These needed to be physically ground from the rotor for sample removal and rotor re-use. This process made sample exchange a time consuming process. Overall sample exchange took approximately the same amount time for both methods.

5.2 The potential of large detection coils

With melt-state static NMR shown to produce comparably high resolution spectra the use of larger detection coils, thus further improving the sensitivity per unit time, was investigated.

Due to the detection being an integral part of the resonance circuit, when the diameter of the detection coil ϕ_c is altered the resonance frequency of the circuit is also changed. Thus, for a larger ϕ_c the number of windings in the coil n_c has to be lowered to compensate. The number of windings limits the length l_c and overall volume V_c of the coil. The overall geometry of the coil is thus constrained by the ^{1}H and ^{13}C Larmor frequencies at which the resonance circuit needs to operate.

At a ^{1}H Larmor frequency of 300 MHz, three Helmholtz coils were investigated, these having diameters of 7.5, 10 and 15 mm (Figure 5.3).

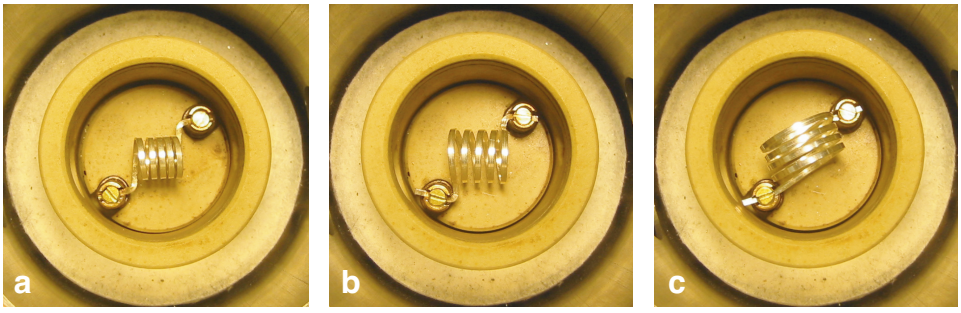

***Figure 5.3**: Coils for the 300 MHz static setup with an inner diameter (ϕ_c) of (a) 7.5, (b) 10 and (c) 15 mm.*

The 7.5 and 10 mm coils needed 5 windings to achieve the desired resonance frequencies, whereas for the larger 15 mm coil the number of windings had to be reduced to 4. This resulted in all coils being between 10–11 mm in length (l_c). Due to the relatively large difference in diameter the coil volume (V_c) ranged between 0.4–1.9 cm^3 (Figure 5.3). Although the 7.5 mm static coil was only 0.1 cm^3 larger than the MAS coil, the use of a 15 mm static coil resulted in 1.6 cm^3 more volume than the MAS coil. This enabled not only larger sample volumes (V_s) but also greater coil filling (V_s/V_c) to be achieved (Table 5.2). For the 7.5 mm static coil a zirconia 7 mm MAS rotor could be used as a sample container. For the larger coils glass tubes with

1 mm wall thickness were used instead, allowing more sample to be placed within the coil. To ensure maximum filling, pre-pressed melt plugs of 8 and 13 mm outer diameter were used for the 10 and 15 mm coils respectively. To prevent sample leakage from the glass tubes upon melting, PTFE end caps were used. Several forms of end cap were designed and tested (Figure 5.4). From all end caps tested, hollow undersized milled PTFE disks, with a small pressure equalisation hole, proved the most reliable (Figure 5.4d). The flow of PE between the glass tube and the end caps was prevented by the use of multiple layers of PTFE tape, allowing for thermal expansion without damage to the glass sample container and coil.

***Table 5.2**: Coil geometry and sample volume of the compared static and MAS coils operating at 300 MHz.*

	ϕ_c mm	l_c mm	n_c #	V_c cm^3	V_s cm^3	V_s/V_c %
static	15.0	11	4	1.9	1.5	75
	10.0	10	5	0.8	0.6	70
	7.5	10	5	0.4	0.2	53
MAS	7.0	8	5	0.3	0.2	-

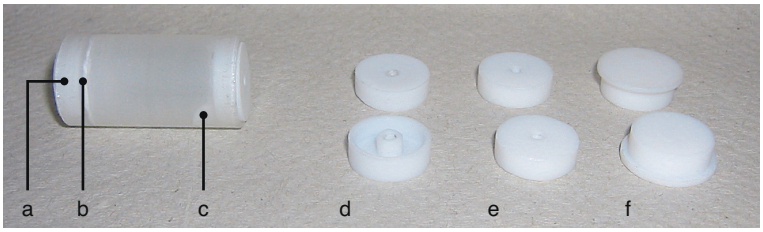

***Figure 5.4**: An example of a filled glass sample container showing the (a) end cap, (b) layer of PTFE tape and (c) a bubble formed in the sample upon cooling. (d–f) End cap designs investigated.*

To judge the relative sensitivity of these three static geometries comparable melt-state SPE spectra of PE4 were measured. As with the previous comparison of static and MAS NMR (Section 5.1), spectra were normalised to their noise to allow quantitative comparison. With respect to resolution little difference was seen between the different coil sizes (Figure 5.5). However, more importantly, as the coil diameter and thus sample volume increased the sensitivity was also seen to increase (Figure 5.6).

Comparison of spectra showed that similar linewidths were seen using the 10 mm and 7.5 mm static coils (Table 5.3). The gain in resolution seen using MAS was similar to that lost by increasing ϕ_c from 10 mm to 15 mm. Concerning the sensitivity, the 10 mm coil was found to be 1.5 times more sensitive than the 7.5 mm setup, with a three-fold increase in sensitivity over MAS. The best overall sensitivity was seen for the 15 mm coil, with five times greater sensitivity over MAS and 2.5 times over the 7.5 mm setup. Importantly, for all static coil geometries comparable branch contents were also able to be calculated from the obtained spectra.

Although large static coils could be used to reduce the actual measurement times by a factor of 25, due to their high sensitivity, initial setup and sample exchange proved problematic. The large PE melt plugs were often found to develop bubbles upon equilibration at measurement temperature (Figure 5.4c). These bubbles made

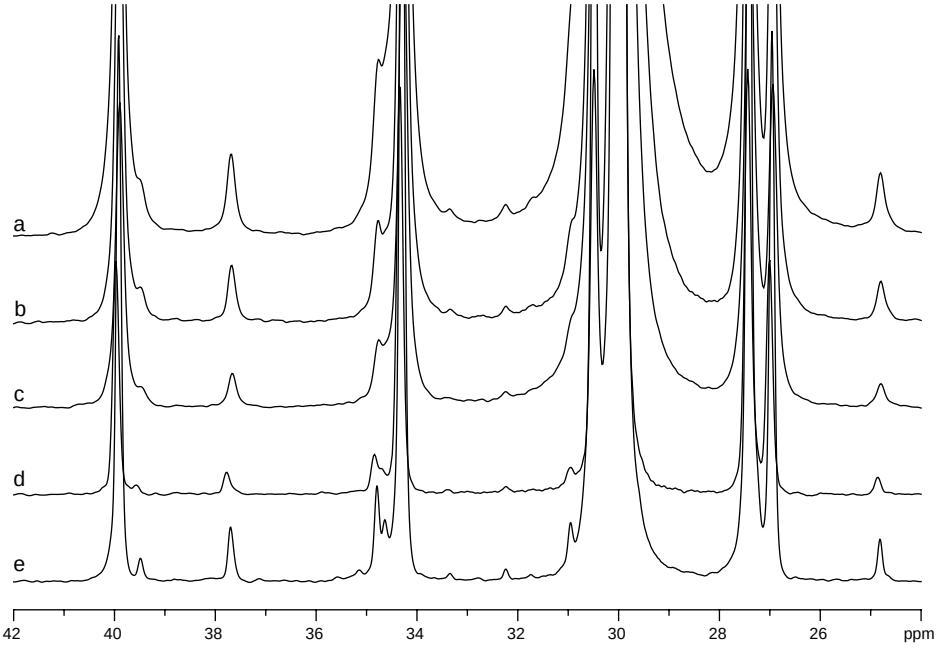

***Figure 5.5**: Normalised static spectra of PE4 obtained with coil diameters of (a) 15 (b) 10 and (c) 7.5 mm at 300 MHz. Comparable 7 mm MAS spectra measured at (d) 300 MHz and (e) 500 MHz are also shown.*

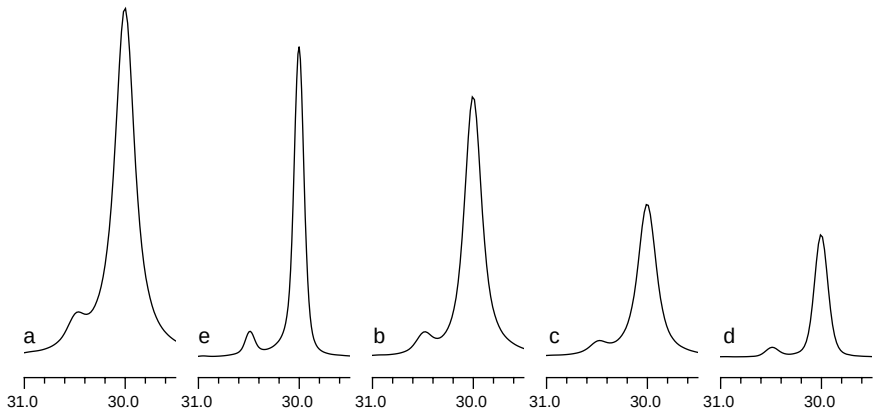

***Figure 5.6**: The δ peaks from the normalised static spectra of PE4 obtained with coil diameters of (a) 15 (b) 10 and (c) 7.5 mm at 300 MHz. The δ peaks of comparable 7 mm MAS spectra measured at (d) 300 MHz and (e) 500 MHz are also shown.*

***Table 5.3**: Effect of coil geometry on resolution and sensitivity of static melt spectra of PE4 at 300 MHz and 150°C.*

	ϕ_c	Sensitivity	FWHM_δ	$B_\star$
	mm	$A_{All} \cdot \sqrt{t[s]}^{-1}$	ppm	$10^{-3}\,\mathrm{C}_{bb}$
static	15	5.1	0.24	32.6
	10	3.1	0.20	31.9
	7.5	2.0	0.20	32.4
MAS	7	1.0	0.16	32.4

the achievement of a homogeneous magnetic field across the sample by shimming difficult and time consuming. Compounding this, after each sample exchange, even if the same sample was reused, shimming was necessary. This was a result of the large coils having to be removed from the probehead in order to allow sample exchange. The latter problem may be overcome by aligning the coil in such a way that allows sample removal without the coil needing to be dislodged.

5.3 Exploitation of stray B_1 field

In static NMR experiments the sample volume is usually chosen such that the length of the sample is equal to that of the detection coil, thus maximising the number of NMR active nuclei within the coil volume. Although extension of the sample beyond the coil volume is possible (Figure 5.7), it is not generally regarded as effective. Under such conditions the $\boldsymbol{B}_1$ field is not homogeneous across the whole sample, with the nuclei outside of the coil experiencing a lower field than those within the coil volume. Thus, pulse sequences relying upon accurate timing and spin manipulation of several consecutive pulses are rendered inefficient. However when using only single pulse excitation (SPE) the effects of such $\boldsymbol{B}_1$ inhomogeneity were found to be negligible. Indeed, it was shown that the absolute sensitivity could be enhanced by extending the sample into the stray field of the coil.

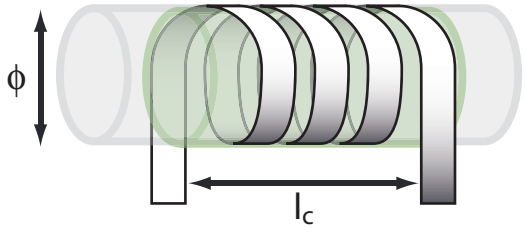

***Figure 5.7**: Extension of sample into the stray $\boldsymbol{B}_1$ field such that the volume of the sample is greater than the volume of the coil ($V_s > V_c$).*

By increasing the sample length l_s to two times the length of the coil l_c, a sample volume V_s greater than the coil volume V_c may be achieved. With the volume of the sample container also occupying some of the coil volume the theoretical maximum percentage coil filling of 100%$\cdot$ V_s/V_c = 200% was never reached. However for some geometries this procedure did result in a percentage coil filling of over 100% (Table 5.4). Although higher resolution was observed under MAS, the resolution achieved using the extended samples was still acceptable for quantitative branch determination (Figure 5.8). When the δ peaks of the normalised spectra are compared an increase in overall area can be seen for the spectra obtained with the greater coil filling (Figure 5.9).

***Table 5.4**: Static NMR coil and sample geometry for measurements at 300 MHz.*

	ϕ_c mm	l_c mm	n_c #	V_c cm^3	V_s cm^3	V_s/V_c %
static	15	11	4	1.9	2.7	137
	15	11	4	1.9	1.5	75
	10	10	5	0.8	1.1	134
	10	10	5	0.8	0.6	70
MAS	7	8	5	0.3	0.2	-

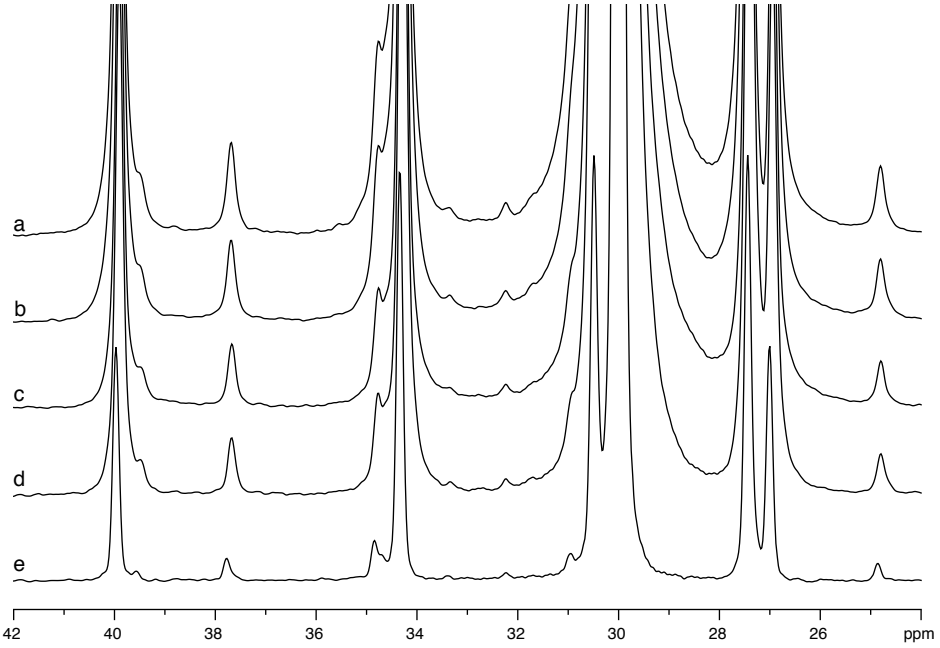

***Figure 5.8**: Normalised static spectra of PE4 obtained at 300 MHz with coil diameter/filling (mm/%) of (a) 15/137, (b) 15/75, (c) 10/134 and (d) 10/70. (e) Comparable 7 mm MAS spectrum at 300 MHz.*

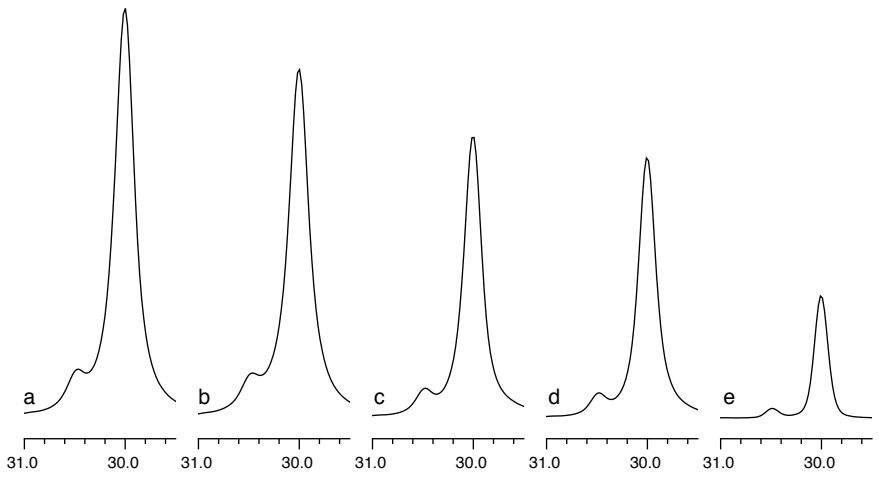

***Figure 5.9**: The δ peaks from the normalised static spectra of PE4 obtained at 300 MHz with coil diameter/filling (mm/%) of (a) 15/137, (b) 15/75, (c) 10/134 and (d) 10/70. (e) Comparable 7 mm MAS spectrum at 300 MHz.*

By exploiting the stray $\boldsymbol{B}_1$ field to excite the spins outside the coil an increase of 13–17 % in sensitivity was seen (Table 5.5). For both standard ($l_s = l_c$) and extended ($l_s = 2l_c$) sample geometries comparable branch contents were measured for both 10 and 15 mm coils. When compared to MAS measurement using the 7 mm probehead, the static 15 mm coil with 137 % coil filling was found to be 5.8 times greater in sensitivity. Such an increase in sensitivity may result in a reduction in measurement time by a factor of 36.

***Table 5.5**: Effect sample geometry on resolution and sensitivity of static melt spectra of PE4 at 300 MHz and 150°C.*

	ϕ_c	V_s/V_c	Sensitivity	FWHM$_\delta$	$B_\star$
	mm	%	$A_{All} \cdot \sqrt{t[s]}^{-1}$	ppm	10^{-3} C$_{bb}$
static	15	137	5.8	0.24	32.6
	15	75	5.1	0.24	32.6
	10	134	3.7	0.20	32.6
	10	70	3.1	0.20	31.9
MAS	7	-	1.0	0.16	32.4

5.4 High field static melt-state NMR

With higher polarisation possible at higher external magnetic fields, the potential of static melt-state NMR at high field was also investigated. To probe the effects of a higher external magnetic field on sensitivity and resolution, comparable spectra to the 300 MHz spectra previously discussed (Section 5.2 and Section 5.3) were measured using a 500 MHz spectrometer. Similarly an MAS spectrum was also recorded at 500 MHz using a 7 mm rotor at 3 kHz MAS. As with the previous study (Section 5.2) both static and MAS probeheads had a maximum operating temperature of 300°C. Furthermore the 7 mm MAS probehead was optimised for the ^{13}C resonance frequency making it more sensitive.[†]

At 500 MHz both the coil diameter and the number of windings were more constrained by the higher Larmor frequencies. For a coil diameter of $\phi_c = 7.5$ mm a coil with 3 windings was able to be produced (Figure 5.10a). However although a coil of $\phi_c = 10$ mm was possible, it only consisted of 2 windings. This resulted in a coil of only 4 mm in length (Figure 5.10b). More importantly, although the coil diameter had been increased from 7.5 to 10 mm, the overall coil volume had been decreased from 0.4 to 0.3 cm^3. Due to these constraints a modified 10 mm coil containing a third extra winding was investigated. In order to retain the desired resonance frequencies a compensating capacitor needed to be placed in series with the coil (Figure 5.10c). The final compensated 10 mm diameter coil was 14 mm long and had the largest volume of all 500 MHz static coils (Table 5.6).

For the 7.5 mm static coil an MAS rotor was used as the sample container to allow direct comparison of static and MAS melt-state NMR at 500 MHz. As with pre-

[†]The high-temperature ^{13}C–^{1}H optimised 7 mm MAS probehead for the 500 MHz spectrometer will be discussed in more detail in Chapter 6.

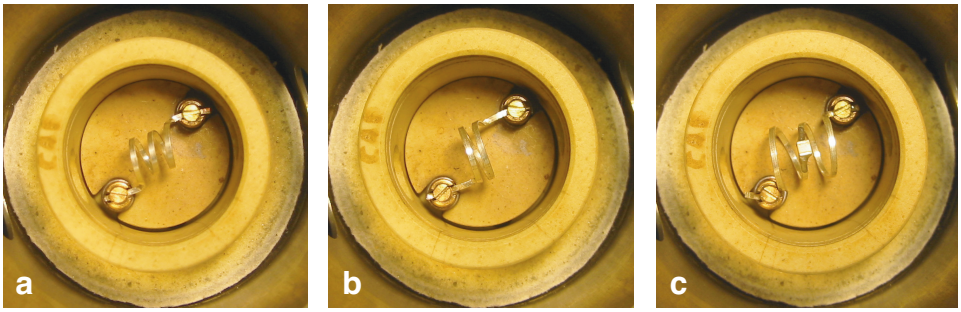

Figure 5.10: *500 MHz static coils with inner diameters and number of windings (mm/#) of (a) 7.5/3, (b) 10/2 and (c) 10/3. Note: additional capacitor needed to compensate for third coil winding of the 10 mm coil.*

vious static measurements glass sample tubes were used for the two 10 mm coils (Section 5.2). With the use of the stray $\boldsymbol{B}_1$ field having been shown to increase sensitivity (Section 5.3), for both 10 mm coils the sample lengths were chosen to be greater than that of their respective coils. However whereas this was easily achieved for the 4 mm long 2 winding coil, for the 14 mm long 3 winding coil this was problematic due to the spacial restrictions in the probehead. This resulted in sample lengths of 11 and 21 mm being used for the 2 and 3 winding coils respectively, and thus higher and lower than expected respective percentage coil filling values (Table 5.6).

Table 5.6: *Coil geometry and sample volume of static and MAS coils compared operating at 500 MHz. Note: additional capacitor needed to compensate for third coil winding of the 10 mm coil (denoted 3^+)*

	ϕ_c mm	l_c mm	n_c #	V_c cm^3	V_s cm^3	V_s/V_c %
static	10	14	3^+	1.1	1.1	96
	10	4	2	0.3	0.6	176
	7.5	9	3	0.4	0.2	59
MAS	7	8	4	0.3	0.2	-

Comparison of spectra showed that the resolution achieved using the 7.5 and 10 mm coils, without an extra capacitor, were surprisingly similar to that achieved by MAS spectra (Figure 5.11). In contrast the 3 winding 10 mm coil, with compensating capacitor, resulted in the lowest resolution spectrum overall (Figure 5.11a). The broad nature of the spectra produced using this coil was most clearly seen when only the peaks of the delta sites are shown (Figure 5.12).

No significant improvement in sensitivity was seen over MAS at higher magnetic field using larger static coil geometries (Table 5.7). This was in contrast to that seen at low field (Table 5.3). This was due to the relatively low coil volumes accessible at the higher field, caused by the geometry constraints imposed by the higher ^{1}H and ^{13}C Larmor frequencies. Only the compensated 10 mm 3 winding coil, with the largest volume, was significantly higher in sensitivity per-unit-time than MAS. However with shimming far more difficult, relatively low resolution was found for this configuration.

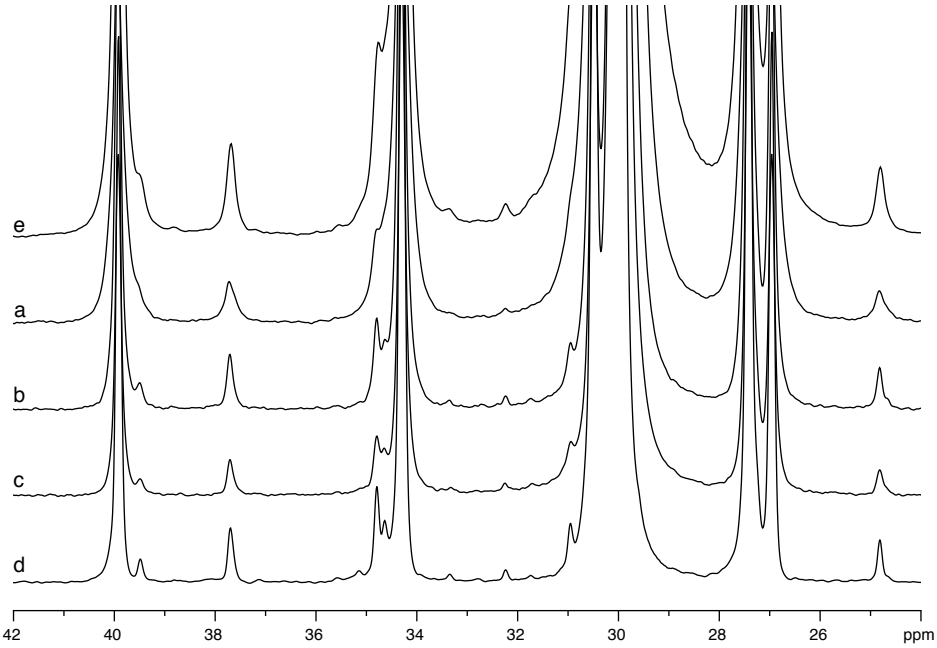

***Figure 5.11**: Normalised static spectra of PE4 obtained at 500 MHz with coil diameter/windings (mm/#) of (a) 10/3, (b) 10/2 and (c) 7.5/3. Comparable (d) 500 MHz 7 mm MAS and (e) 300 MHz static (15 mm/137%) spectra also shown.*

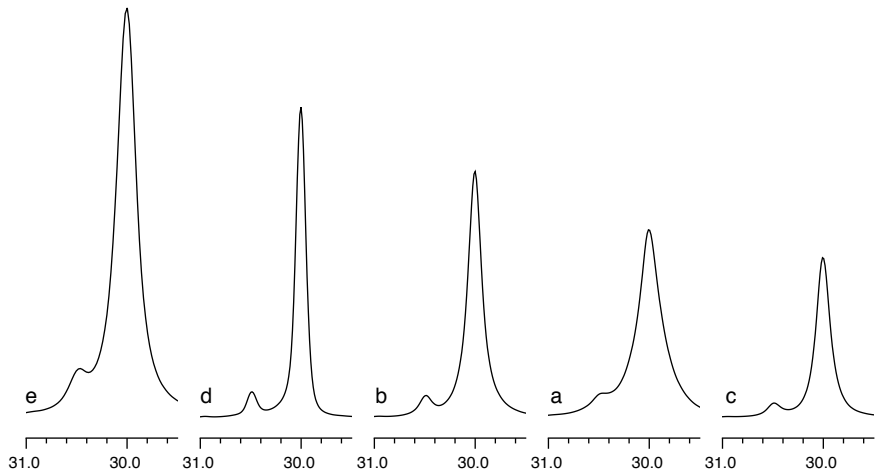

***Figure 5.12**: The δ peaks from the normalised static spectra of PE4 obtained at 500 MHz with coil diameter/windings (mm/#) of (a) 10/3, (b) 10/2 and (c) 7.5/3. Comparable (d) 500 MHz 7 mm MAS and (e) 300 MHz static (15 mm/137%) spectra also shown).*

***Table 5.7**: Effect of coil geometry, sample volume and external magnetic field on resolution and sensitivity of static melt-state spectra of PE4 at 500 MHz and 150°C.*

	ϕ_c	n_c	Sensitivity	FWHM$_\delta$	$B_\star$
	mm	#	$A_{All} \cdot \sqrt{t[s]}^{-1}$	ppm	10^{-3} C$_{bb}$
static	10	3^+	1.9	0.25	32.7
	10	2	1.5	0.16	32.6
	7.5	3	1.0	0.17	32.4
MAS	7	4	1.3	0.12	32.3

5.5 The effect of sample temperature on resolution

The broad line widths encountered in static melt-state NMR are due to the residual heteronuclear dipolar coupling. This being the remaining dipolar coupling that has not been averaged by the molecular motion within the molten sample. Thus, at the limit of RF based heteronuclear dipolar decoupling, further line-narrowing may only be achieved by raising the sample temperature, and hence increasing internal mobility. An alternative method of removing the residual heteronuclear dipolar coupling still present in the melt-state is MAS, which will be discussed in more detail in Chapter 6.

Although melt-state NMR of polyethylene has previously been undertaken at 200°C [Hatfield 95], the systems studied were commercial in nature. These systems would have contained additives, such as stabilisers and antioxidants, in order to limit degradation during processing. Preliminary investigation of unstabilised samples showed rapid sample degradation at temperatures between 190–200°C, even under nitrogen. With 150°C being the minimum temperature needed to insure all forms of polyethylenes are in a homogenous molten state, only a small temperature window between 150–190°C was available for optimisation.

To evaluate the effect of temperature on resolution and sensitivity, comparable spectra of the commercial polyethylene PE4 were measured at 150 and 170°C using the 15 mm static coil setup at 300 MHz previously described (Section 5.2). The resulting normalised spectra showed only minor differences in both resolution (Figure 5.13) and sensitivity (Table 5.8). As expected the lower viscosity of the molten polyethylene at 170°C resulted in higher internal motion and thus narrower line widths, due to motional averaging of the dipolar interaction. The absolute sensitivity was found to be slightly reduced for the higher temperature experiment. This could have either be caused by the shifted Boltzmann distribution between Zeeman levels or a loss in probehead sensitivity. With the same sample used for both experiments, and sensitivity remaining approximately constant, the observed reduction in line width resulted in higher signal-to-noise ratios for the 170°C experiment.

***Table 5.8**: Effect of temperature on resolution, sensitivity and signal-to-noise ratio (SNR) of static melt-state NMR.*

T	sensitivity	FWHM_δ	$B_\star$	SNR_δ
°C	$A_{All} \cdot \sqrt{t[s]}^{-1}$	ppm	$10^{-3}\ C_{bb}$	
150	1.1	0.24	32.6	4500
170	1.0	0.22	32.6	4800

With only a modest reduction in line width, combined with a slight loss in sensitivity, the risk of faster sample degradation at 170°C was deemed too great. Thus for all further static and MAS melt-state NMR of polyethylene the lower sample temperature of 150°C was used. This facilitated both the measurement of HDPEs (T_m = 140-145°C) and the slowing of thermal degradation processes. It should be noted that with the risk of thermal degradation during prolonged measurements accurate temperature

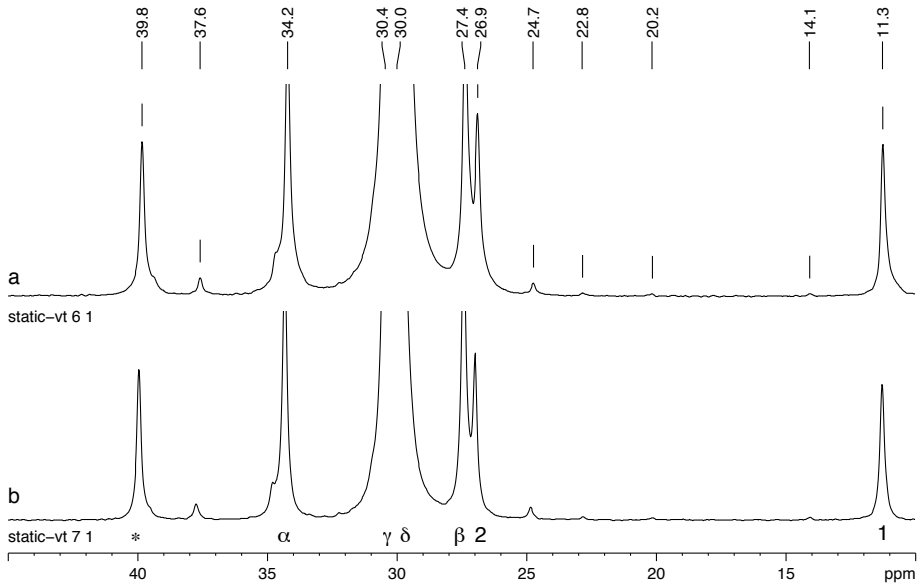

***Figure 5.13**: Static melt-state NMR spectra of PE4 using the 15 mm/300 MHz setup at (a) 150°C and (b) 170°C.*

calibration becomes important (Appendix B). By doing so the actual temperature at which the molten polyethylene resided is thus known.

5.6 The Potential of an orthogonal-coils setup

All NMR experiments discussed so far have been undertaken using probeheads containing a single double-resonance coil. The geometries of these double-resonance coils being defined by both the proton and carbon Larmor frequencies of the respective nuclei in a given magnetic field. Thus for a given coil diameter, the maximum number of coil windings is constrained in order to satisfy *both* desired resonance conditions. With both the maximum achievable sensitivity and maximum sample volume limited by the use of such single double-resonance coils an alternative approach was investigated.

A custom-built static probehead was constructed with two separate resonance circuits, with each resonance circuit having a separate coil. The ^{13}C coil was 15 mm in diameter, 30 mm long and consisted of 9 windings. This resulted in a coil volume of 5.3 cm^3, and was over two times larger than the 1.9 cm^3 found for a double-resonance 15 mm coil (Figure 5.14a). The proton coil was placed orthogonal to the ^{13}C coil and was stretched such that three of the six windings resided on each side of the carbon coil (Figure 5.14b). The proton coil was also 15 mm in diameter. With fully decoupled resonance circuits, and the increased number of windings in the carbon detection coil, the orthogonal-coil setup was expected to provide an increase in sensitivity.

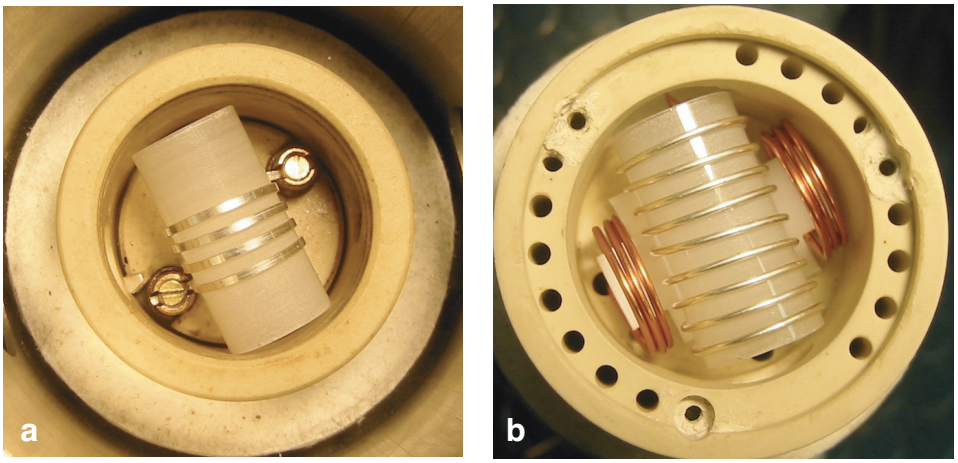

***Figure 5.14**: 300 MHz static probeheads with (a) one 15 mm double-resonance coil and (b) two 15 mm orthogonal single-resonance coils (custom-built).*

Unfortunately, even after extensive shimming, it was found that the ^{1}H line widths obtained with this setup could not be narrowed to below 0.54 ppm. This being almost 2.5 times wider than those achieved with the equivalent double resonance coils. This was attributed to both the size and geometry of the proton coils preventing a homogeneous proton $\boldsymbol{B}_1$ field from being established across the whole sample volume. However even when the sample was confined to the volume within the two sections of the proton coil, further line narrowing was not possible. As well as not being able to produce a homogeneous field, the ^{1}H coil was also only capable of sustaining a maximum decoupling field strength of 6.25 kHz. Thus the RF heteronuclear dipolar decoupling was much less than the 25 kHz possible, even for the largest double-resonance coils.

Overall, this resulted in ^{13}C line widths that were almost twice as wide as those obtained for the 15 mm double resonance coil, with FWHM$_\delta$ of 0.45 and 0.24 ppm respectively. Despite this, the melt-state static NMR spectrum of PE4 showed a higher than expected resolution (Figure 5.15a).

Due to the lack of sufficient decoupling only the **1** site was resolved to the baseline, with the 'feet' of all other peaks merging together. With the $\star$ site not fully resolved to the baseline, manual integration and integral baseline correction had to be undertaken. With all neighbouring peaks strongly encroaching on each other, the underestimation of A_δ became substantial. This resulted in a 15% higher branch content of 37.0 branches per 1000 backbone carbons. Due to the low resolution, and the consequent problems in accurate branch quantification, absolute assessment of the sensitivity of the orthogonal coil geometry was not possible. Although comparable spectra were not recorded, all evidence suggested that an increase in sensitivity was not achieved.

With both coils being soldered into the probehead, the carbon coil could not be removed for sample exchange. Thus the glass tube sample container needed to be slid

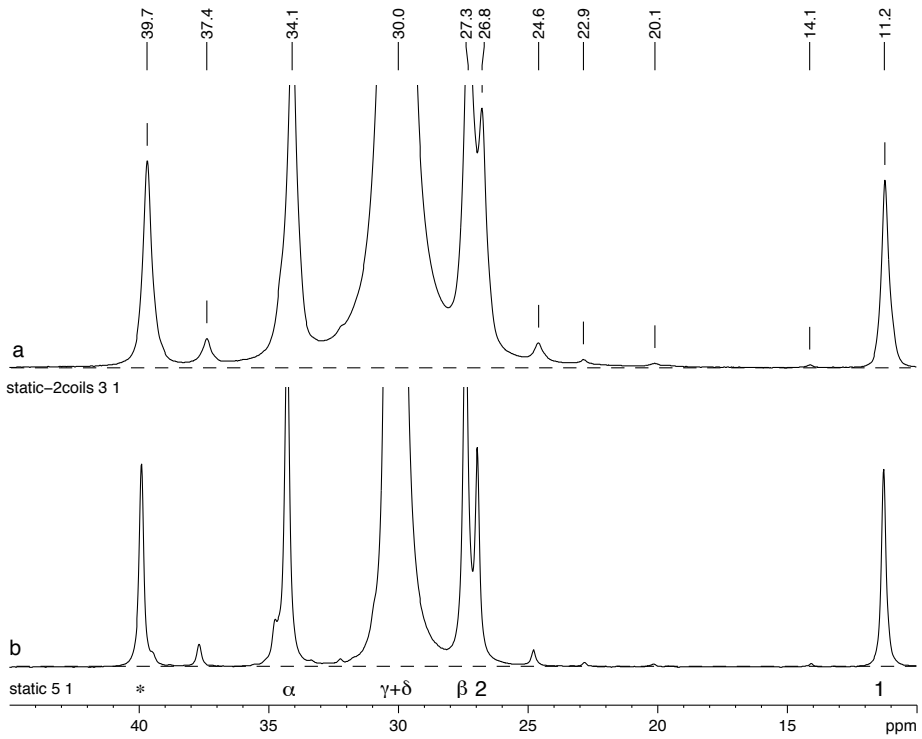

***Figure 5.15**: Static melt-state spectra of PE4 showing the best resolution achieved at 300 MHz using the (a) custom-built orthogonal coil probehead and (b) double-resonance probehead. Apodisation adjusted individually depending upon the degree of truncation and baselines shown to emphasise the broad nature of the peaks.*

from the ^{13}C coil. Due to the length of the ^{13}C coil, this manoeuvre was found to irreparably alter the coil geometry. This resulted in the sample being needed to be removed from the glass sample container *in situ*. Another problem was encountered when the glass tube broke due to the unregulated thermal expansion of the molten polyethylene sample. Unlike the other static setups, where the coil could be easily removed, upon the breaking of the glass tube the coil was damaged beyond repair. This necessitated the time consuming removal of the coil by unsoldering, fashioning of a new coil and re-soldering it into the circuit.

While the potential of an orthogonal coils design has been shown, the design of the probehead would need major improvement in order to make it a viable alternative to a commercial double resonance coil setup. Important improvements would be to make the ^{13}C coil removable to allow easier sample exchange, as well as the use of an inner sample container allowing sample removal without coil deformation.

5.7 Summary

In this chapter the feasibility of static NMR in the melt-state for polyethylene branch quantification was established. A comparison of 300 MHz MAS and static coils with similar diameters showed a two-fold enhancement in sensitivity, albeit with a reduction in resolution. More surprisingly the reduction in resolution seen when when going from MAS to a static setup was not as strong as expected. This was mostly attributed to the inherent mobility of the molten sample.

It was further shown that through the use of greater coil diameters and coil filling improved sensitivity could be achieved. This improvement in sensitivity was not found to be significantly offset by a further loss of resolution. Due to the constraints of the higher Larmor frequencies, high-field (500 MHz) measurements were not found to be more time efficient than low-field (300 MHz) measurements. Any possible advantage of measuring at the high-fields was removed due to the smaller coil volumes, resulting from lower number of turns and subsequent coil length.

No clear advantage was seen for undertaking high temperature measurements between 150–190°C. Any slight improvements in resolution were offset by the added risk of thermal sample degradation, especially for long measurement times.

The best absolute sensitivity, with acceptable resolution for accurate branch quantification, was found with a static 15 mm diameter double-resonance coil, operated via a 300 MHz spectrometer using high coil filling and a sample temperature of 150°C. This optimised setup resulted in sensitivity enhancement of roughly six times that of MAS at 300 MHz. More surprisingly this was also almost three times more sensitive than MAS at 500 MHz.

Compared to MAS, melt-state static NMR allowed faster branch quantification with reasonable resolution at lower $\boldsymbol{B}_0$ field strengths. The sample exchange procedures were however found to be equally as time-consuming as the removal of the disposable boron nitride caps used for high temperature MAS. The only disadvantage, other than the slight loss of resolution, was the sample quantity needed for this static method. For the high filling of a 15 mm coil between 2–2.5 g of polyethylene was needed, depending on the density. This was in contrast to the 200 mg needed to fill a 7 mm MAS rotor. Thus time efficient characterisation of polyethylene by melt-state static NMR was found to be limited to polyethylenes avalable on this scale.

Chapter 6

Melt-state MAS NMR

The potential of MAS to enhance carbon spectral resolution was shown for molten polyethylene (Chapter 5), in contrast to measurements under static conditions. It has previously been shown that such melt-state MAS NMR of polyolefins can achieve a greater signal-to-noise ratio (SNR) than that achieved by solution-state NMR, albeit at reduced resolution [Zeigler 94]. Although such an approach was estimated to reduce measurement times by a factor of 14 or more as compared to solution-state, in practice only a factor of 2–3 was typically achieved [Hatfield 95]. With the melt-state MAS NMR method showing great promise, several strategies for the improvement of both the time-efficiency and resolution were investigated.

6.1 Comparison with solution-state NMR

Since the previous melt-state MAS studies on polyethylene [Zeigler 94, Hatfield 95] high-field magnets have become more affordable and solid-state NMR hardware design has improved. It was thus deemed prudent to explore by how much modern equipment was able to reduce measurement times compared as to solution-state NMR.

Comparable solution-state and melt-state ^{13}C spectra of a typical PE-co-octene (PE8b-C) were obtained at fields corresponding to 400 and 300 MHz respectively, with 3 kHz MAS applied in the melt (Figure 6.1). For both setups a recycle delay of 10 s was employed, which only allowed branch quantification via those carbons with $T_1^C < 2$ s, ie. using the δ and α sites [De Pooter 91, Hatfield 95].

For comparison, both spectra were normalised to their respective standard deviation of the noise between 50–45 ppm (Section 5.1). As expected less resolution was seen in the melt-state, even under MAS, with the line width of the α site found to be over four times as broad as that in solution (Table 6.1). Despite this, a four time

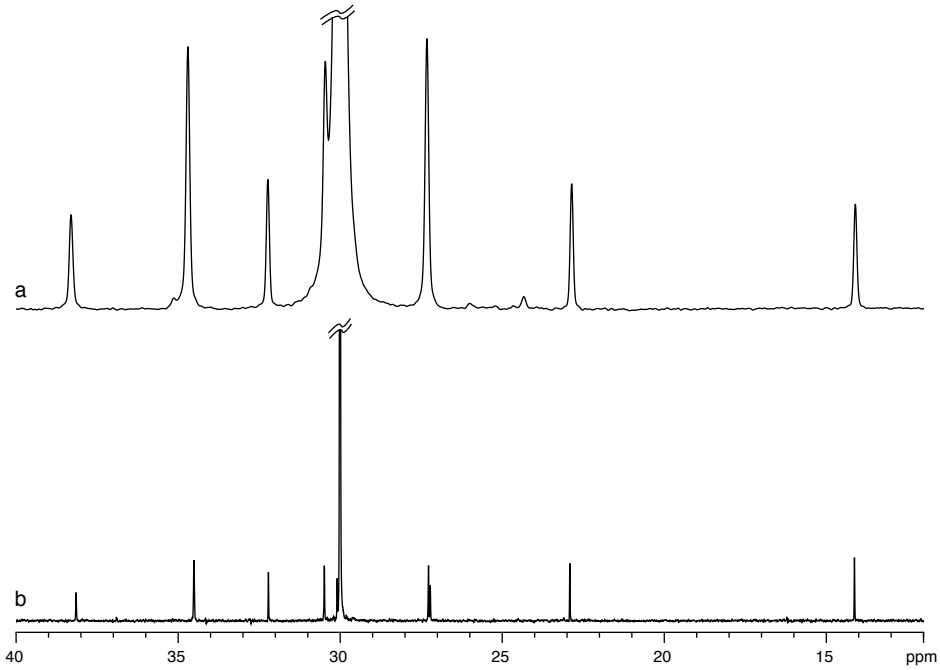

***Figure 6.1**: Normalised ^{13}C spectra of PE8b-C in the (a) melt-state at 300 MHz / 150°C under 3 kHz MAS and (b) solution-state at 400 MHz / 100°C.*

increase in intensity was observed for the same site in the melt-state spectrum, this being equivalent to a possible 16 fold reduction in measurement time. However in order to compare the absolute sensitivity of the two methods, the area of the peaks in question needed to be considered due to their inherently different line widths. For the melt-state MAS spectrum the area of the α peak was found to be almost 20 times greater than that observed in the solution-state. This is equivalent to a potential 400 fold reduction in measurement time.

***Table 6.1**: Comparison of melt-state MAS and solution-state NMR of PE8b-C showing the differences in resolution ($FWHM_\alpha$) and sensitivity (A_α). Similar branch contents (B_α) were obtained for both methods.*

NMR	$\nu_{^1H}$ MHz	τ_{rd} s	NS	T °C	$FWHM_\alpha$ ppm	SNR_α	A_α	B_α 10^{-3} C_{bb}
solution	400	10	4096	100	0.03	52	3.9	11.1
melt	300	10	4096	150	0.14	225	77.5	12.5

When compared to the more commonly implemented high-temperature solution-state NMR method, melt-state MAS NMR showed greatly increased sensitivity even without optimisation. If the reduction in resolution were to be deemed acceptable, melt-state MAS NMR showed great promise for time-efficient branch quantification. Due to this, the melt-state MAS NMR method was optimised by separately considering the contributions of hardware setup (Section 6.2), polarisation method (Section 6.3) and heteronuclear dipolar decoupling scheme (Section 6.4). This resulted in further increases not only in sensitivity but also in resolution.

6.2 Hardware setup

The optimisation of the hardware setup was divided into three sections; external magnetic field strength and MAS rotor size considerations (Section 6.2.1), the optimum probehead for branch quantification (Section 6.2.2) and sample preparation/setup/exchange procedures (Section 6.2.4).

More specifically, a comparison of sensitivity and resolution was undertaken on three spectrometers operating between 300–700 MHz, with both 4 and 7 mm MAS rotors investigated. Similarly, with standard MAS probeheads designed for multiple purposes the advantage of a custom-built high-temperature MAS probehead, solely optimised for ^{13}C and ^{1}H resonance frequencies, was explored. Although not related to the sensitivity of the measurement itself, the sample preparation, setup and exchange-time does directly affect the overall time efficiency of the measurement as a whole. The combination of optimised sample preparation and NMR setup resulted in substantial improvements in sensitivity and time-efficiency, as well as allowing high sample throughput.

6.2.1 Effects of external magnetic field and rotor size

Increasing the strength of the external magnetic field ($\boldsymbol{B}_0$) affects the Boltzmann distribution of the Zeeman levels. With higher polarisation possible, greater sensitivity is also possible. Since a number of hardware configurations were available, a direct comparison of static magnetic field $\boldsymbol{B}_0$ and MAS rotor size was carried out with respect to spectral resolution and sensitivity.

Comparable SPE spectra were measured on 300, 500 and 700 MHz spectrometers. To allow access to standard temperature range 4 mm probeheads ($T_{max} = 120$°C), a commercial PE-co-butene (PE4, T_m=90°C) was used. Thus enabling comparison of melt-state NMR at 110°C.

With the measurement time determined by the sensitivity of the hardware, the number of NMR active nuclei within the range of the detection coil is of key importance (Chapter 5). In contrast to the 70 mg of PE4 able to be packed into the 4 mm rotor, approximately 200 mg could be placed in a 7 mm rotor. It was thus deemed prudent to also obtain comparable spectra for 300 and 500 MHz spectrometers using 7 mm MAS probeheads (Figure 6.3). While 5 kHz MAS was possible with 4 mm rotors, only 3 kHz was achieved with the 7 mm rotors due to rotor instability.

Wide-bore 7 mm probeheads had the added advantage of higher maximum operating temperature ($T_{max} = 300$°C), thus allowing access to HDPEs with typical equilibrium melting points of 140°C. In addition to this, the 500 MHz 7 mm probehead was optimised for ^{13}C and ^{1}H resonance frequencies, further aiding sensitivity.

To allow evaluation of absolute sensitivity across different hardware and acquisition parameters, normalisation of comparable spectra was required (Section 5.1). It should be noted that after normalisation different noise autocorrelation functions were seen, due to there being more points per ppm at higher ν_{1_H}(Figure 6.2).

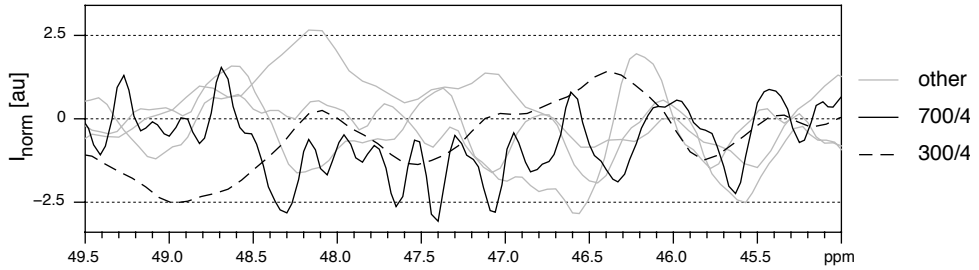

***Figure 6.2**: The noise region of the normalised SPE spectra of PE4 measured under comparable conditions showing that, although all spectra have the same standard deviation, the autocorrelation function of the noise was proportional to field.*

As expected, the strongest $\boldsymbol{B}_0$ field gave both the narrowest peaks and the highest sensitivity for measurements using 4 mm rotors (Table 6.2). The greater chemical shift dispersion at 700 MHz revealed several sites that were obscured by broad neighbouring peaks at lower fields (Figure 6.3). Although a gain in sensitivity was seen between the 500 and 700 MHz 4 mm spectra, the greatest improvement was found between 300 MHz and 500 MHz (Figure 6.4).

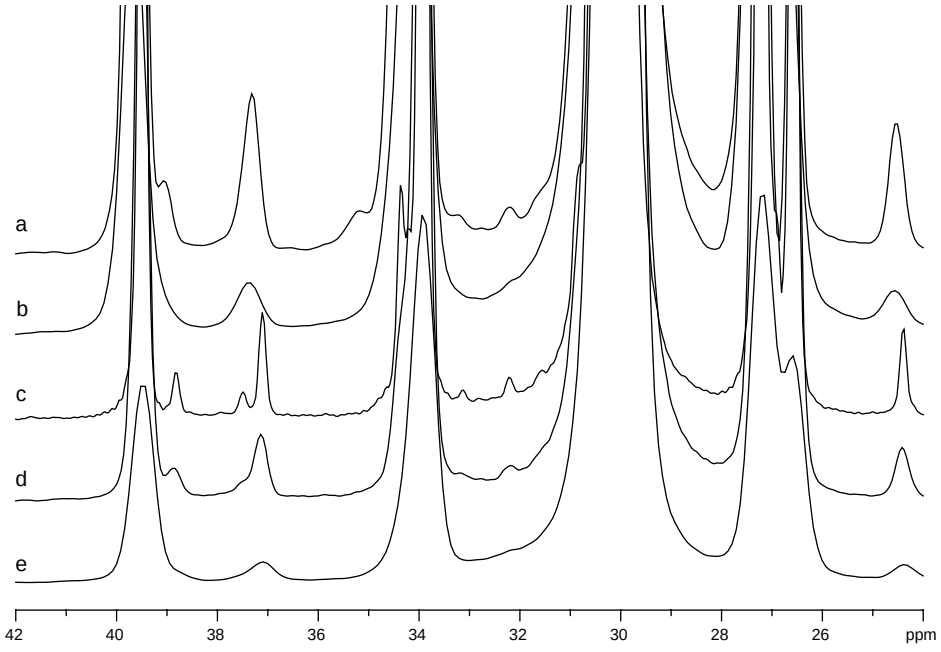

***Figure 6.3**: Normalised SPE spectra of PE4 measured under comparable conditions at field strength (ν_{1_H}) and MAS rotor size (MHz/mm): (a) 500/7, (b) 300/7, (c) 700/4, (d) 500/4 and (e) 300/4.*

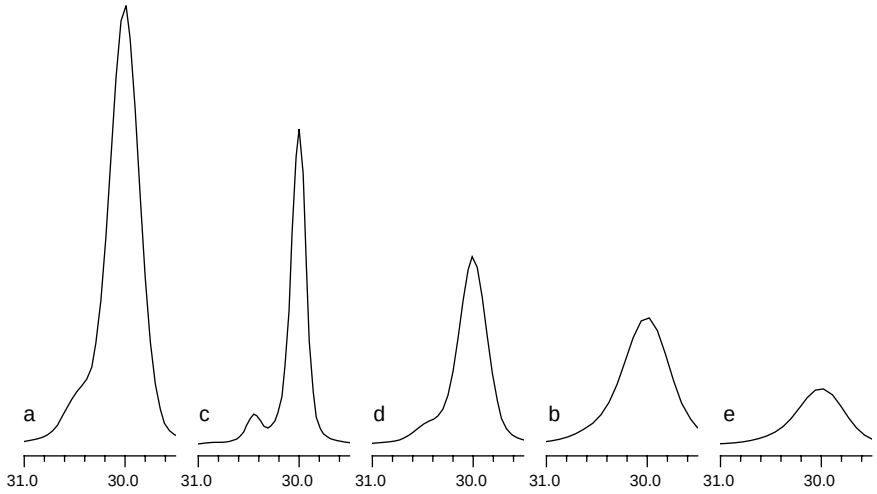

***Figure 6.4**: The δ peaks from the normalised SPE spectra of PE4 measured under comparable conditions at field strength (ν_{1_H}) and MAS rotor size (MHz/mm): (a) 500/7, (b) 300/7, (c) 700/4, (d) 500/4 and (e) 300/4.*

***Table 6.2**: Comparison of relative sensitivity and degree of branching ($B_\star$) of PE4 at three $\boldsymbol{B}_0$ field strengths using 4 and 7 mm MAS probeheads.*

ν_{1_H}	ϕ	sensitivity	$B_\star$
MHz	mm	$A_{All} \cdot \sqrt{t}^{-1}$	10^{-3} C_{bb}
300	4	1.0	33.3
500	4	1.8	33.3
700	4	2.0	34.2
300	7	2.3	33.8
500	7	5.0	34.4

The larger sample volume of the 7 mm rotors resulted in a greater sensitivity, even at 300 MHz, than that seen for the 4 mm probehead at 700 MHz, albeit at reduced resolution. At 500 MHz the 7 mm ^{13}C–^{1}H optimised probehead gave the best sensitivity overall and was 2.6 times more sensitive than the 700 MHz 4 mm setup. With this probehead showing resolution comparable to the 4 mm probehead at the same field, it was found to be the best compromise between optimum resolution and sensitivity. Using this setup, spectra with acceptable line widths could be obtained on a wide variety of PE samples in the shortest possible time.

6.2.2 The advantage of ^{13}C–^{1}H optimised probeheads

The sensitivity increase previously observed in Section 6.2.1 between the 7 mm MAS probeheads at 300 and 500 MHz was due to a combination of two factors; firstly the increased $\boldsymbol{B}_0$ field strength and secondly the optimised circuitry of the 500 MHz probehead. To provide insight into which of these two factors played the more significant role in increasing sensitivity two comparable spectra were recorded at 500 MHz using 7 mm MAS probeheads with optimised and unoptimised resonance circuits (Figure 6.5). Unfortunately a truly comparable unoptimised prodehead was unavailable for comparison and a probehead with a maximum operating temperature of

120 °C had to be used. With different materials used for the construction of probeheads with higher operating temperatures, variation in sensitivity is also seen. Commonly, slightly lower sensitivity is found for higher temperature range probeheads ($\approx$ 10%). However, such differences in sensitivity caused by the material are significantly less than that caused by resonance circuit optimisation [Hehn 05].

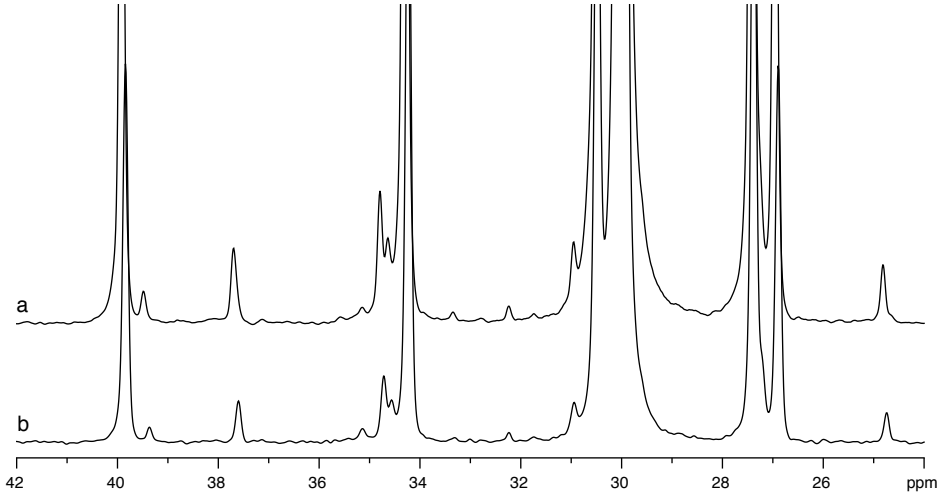

***Figure 6.5**: Normalised spectra of PE4 taken with the (a) ^{13}C–^{1}H optimised and (b) stardard 7 mm MAS probeheads at 500 MHz.*

***Table 6.3**: Comparison of relative sensitivity, resolution (FWHM$_\delta$) and degree of branching ($B_\star$) of PE4 for a standard and a ^{13}C–^{1}H optimised 7 mm MAS probehead at 500 MHz.*

	sensitivity $A_{All} \cdot \sqrt{t}^{-1}$	FWHM$_\delta$ ppm	$B_\star$ 10^{-3} C$_{bb}$
unoptimised	1.0	0.13	32.2
optimised	2.0	0.12	32.3

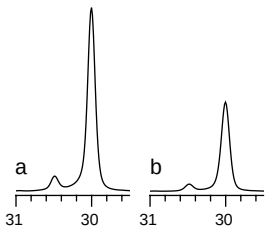

***Figure 6.6**: The δ peaks of the normalised spectra of PE4 taken with the (a) ^{13}C–^{1}H optimised and (b) standard 7 mm MAS probeheads at 500 MHz.*

Comparison of the normalised spectra showed a two-fold increase in sensitivity for the ^{13}C–^{1}H optimised probehead with respect to the unoptimised probehead (Figure 6.6), even when considering the differences in probehead construction (Table 6.3). Thus, it can be clearly seen that if an NMR setup is exclusively used for the measurement of ^{1}H and ^{13}C nuclei in polyolefins, resonance circuit optimisation of the probehead for these Larmor frequencies is advisable.

6.2.3 Optimum measurement temperature for unstabilised PEs

Apart from the initial comparison of solution- and melt-state NMR (Section 6.1) all previously described melt-state NMR measurements were conducted on commercial PE samples, these containing stabilisers to prevent thermal degradation (Section 2.4.5). However with such stabilisers commonly resulting in peaks within the region of interest for PE (Section 2.4), unstabilised samples are preferred for NMR experiments where branch quantification is desired. With long measurements at elevated temperatures required for melt-state NMR characterisation of sparse branching, the long-term thermal stability of an unstabilised model sample (PE8b-C) was investigated.

Melt-state NMR was undertaken on PE8b-C at the lower and upper end of the available temperature range of the hardware setup. A series of seven consecutive spectra of was acquired at both 150°C and 180°C. To insure a accurate comparison, separate melt plugs were prepared from unmeasured material for each temperature. It should be noted that due to signal averaging, each individual spectrum represented the average concentration of sites observed over 3k scans, equivalent to 5.3 h of measurement.

Comparing the first and the last spectra taken at 180°C, two peaks were seen to increase in intensity with time (Figure 6.7). This indicated a thermal degradation process had taken place.

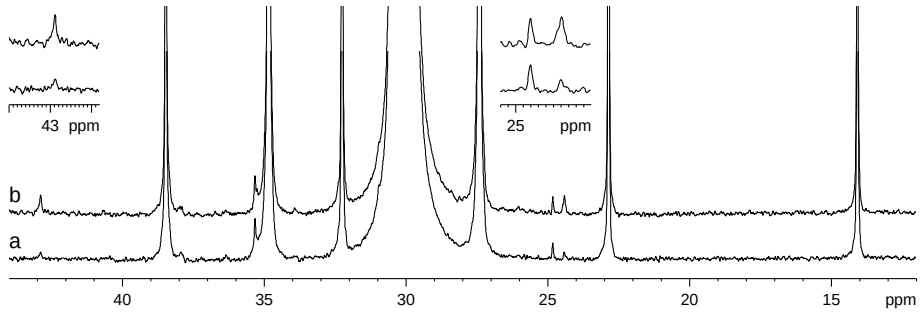

***Figure 6.7**: Observed thermal degradation in an unstabilised model system (PE8b-C). Comparison of the spectra of (a) the first and (b) the seventh 5.3 h measurement at 180°C.*

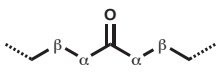

***Figure 6.8**: Assignment of the carbonyl sites resulting from thermal degradation.*

The two peaks at 42.9 and 24.4 ppm were assigned to the carbon sites α and β to a carbonyl group respectively (Figure 6.8). For each spectrum the average carbonyl group content was quantified by integrating both peaks and building a ratio with the δ peak in each spectrum. Considering their low SNR, good agreement was seen between the carbonyl contents determined using the α site and those determined using the β sites (Figure 6.9).

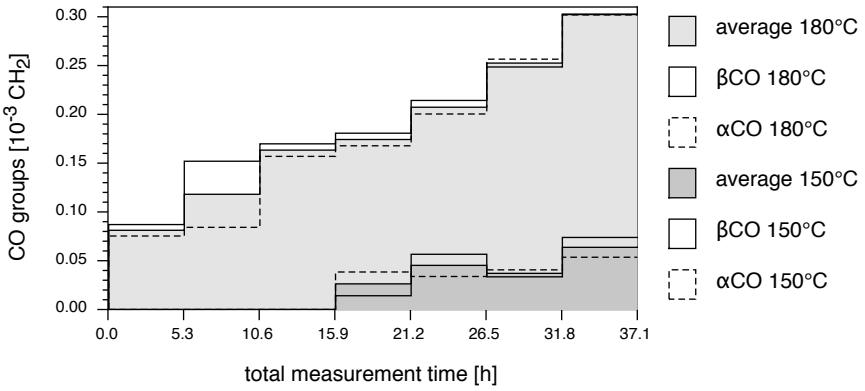

***Figure 6.9**: Comparison of the average carbonyl group content for each 5.3 h measurement at 150°C and 180°C.*

At the measurement temperature of 180°C the carbonyl groups were clearly seen in the first spectrum of the time series, i.e. after 5.3 h measurement (Figure 6.9). In contrast carbonyl groups were not observed during the first 15 h of continuous measurement at 150 °C, and could only be detected in the fourth spectrum of the series. When finally detected, not only were the carbonyl groups present at a lower content, the rate of degradation was also much slower than that seen at higher temperature.

With an increased rate of thermal degradation shown to occur at 180°C, lower measurement temperatures were shown to be needed to minimise thermal degradation of unstabilised systems. Thus for all subsequent NMR experiments, on both stabilised and unstabilised PEs, a measurement temperature of 150°C was used. This being the lowest temperature possible at which all types of PE, including HDPEs and UHMWPEs, are completely molten.

6.2.4 Sample preparation and MAS rotor packing

A rapid and reliable protocol for sample preparation and rotor packing was developed for melt-state MAS NMR. When combined with the increase in sensitivity previously seen in Section 6.2.1, rapid sample turnover was enabled. Emphasis was placed on packing as much sample into a 7 mm rotor as possible, whilst still retaining reliable spinning and low probability of sample leakage. In contrast to the long times needed to prepare solution-state NMR PE samples (e.g. 12 h [Seger 04]), sample preparation for melt-state MAS NMR took on average 10 minutes, even for commercial pelleted samples. The optimised sample preparation protocol was as follows.

Prior to measurement, approximately 200 mg of sample was melted into 7 mm zirconia rotors (Figure 6.10a) at $T = T_M + 20°C$, using a custom-built metal heating block under a constant stream of nitrogen. Upon cooling, $\approx$ 4 cm of PTFE tape was placed into the rotor, on top of the sample, and compressed using standard packing tools

(Figure 6.12b). Two such tight-fitting ≈ 1 mm thick PTFE plugs (Figure 6.10c) were routinely used to hinder the motion of the molten polymer whilst under MAS. This procedure was found to be especially useful for low molecular weight systems with associated low zero shear viscosities.

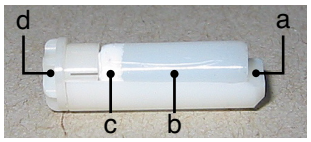

***Figure 6.10**: Cut through filled 7 mm MAS rotor. (a) Zirconia rotor (only lower half of cut rotor shown for illustrative purposes) containing (b) polymer melt-plug, (c) PTFE plugs and (d) zirconia rotor cap.*

Due to the high temperatures involved, measurements were initially carried out using disposable boron-nitride (BN) rotor caps (Figure 6.11c-d). Unfortunately the dimensions of these were found to vary by batch resulting in either the desired tight-fit or, more commonly, an undesirable loose-fit. The placement of PTFE tape between rotor and rotor cap aided adhesion but still resulted in occasional failure. When combined with the tedious and time consuming cap removal process an alternative to BN rotor caps was sought. For all subsequent measurements rotor caps made from the same material as the rotors, i.e. zirconia, were used (Figure 6.11a-b).

Since these caps were reusable they were found to greatly speed up the packing and unpacking of samples. However, more importantly they allowed the repacking of samples. Over long term usage, although initially approximately four times more expensive than equivalent BN caps, zirconia rotor caps were found to be much more economic and generally more convenient and predictable to use. After an initial lead time, regular reuse of the caps of up to 50 times was found to be possible.

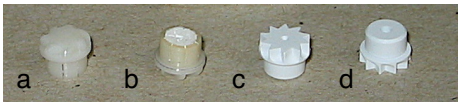

***Figure 6.11**: High-temperature 7 mm MAS rotor caps. (a-b) zirconia: ZrO_2 and (c-d) boron nitride: BN. Note: hollow inner recess of zircona caps (b) filled with PTFE to stop molten polymer entering the cap.*

Packed rotors were inserted into preheated probeheads and allowed to equilibrate under slow MAS of $\omega_r/2\pi < 1$ kHz for 5 minutes, or longer depending on sample viscosity. This was typically achieved by applying the final desired bearing pressure with a minimal drive pressure. If the melting point was unknown, the sample was confirmed to have melted by ^{1}H NMR spectroscopy.

Samples were spun to the desired spinning speed by slowly raising the drive gas whilst monitoring the spinning stability via an oscilloscope. If the sample did not spin above 1 kHz upon raising the drive pressure a number of things were tried; stopping-ejecting-reinserting, lowering bearing pressure while keeping drive pressure constant, removing and replacing the cap, removing and replacing the PTFE, trimming the melt-plug and finally repacking with a new melt-plug. All of which were thought to act by bringing the polymer melt inside the rotor into a more axially symmetric configuration.

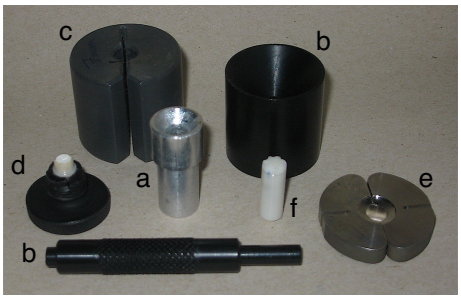

***Figure 6.12**: Rotor packing and unpacking tools used. (a) Adaptor for heating block allowing pressing of molten polymers directly into empty rotors by hand, (b) standard rotor packing tools, (c) tool for providing grip on rotors needed for unpacking, (d) device for griping rotor cap (shown in device) when torque applied with sponge cloth (not shown) and fingers failed to loosen cap, (e) standard tool for removing 7 mm caps (not used) and (f) a filled rotor with zirconia cap.*

After spinning $>$ 1 kHz was achieved, typically no further problems with spinning up to the desired 3 kHz were seen other than sample leakage. After reaching the desired spinning speed, the samples were allowed to reach thermal equilibrium and then individually shimmed.[†]

To monitor possible contamination of the MAS stator in the probehead, both the melt-plug and fully packed rotor were weighed before and after the measurement to check for sample loss. Other than unpacking the rotor and revealing polymer; above the PTFE, inside the cap or between the rotor and cap, the spinning speed proved extremely sensitive to sample loss. That is if under the same bearing and drive gas pressures the MAS spinning frequency was seen to slowly rise (1–2 Hz s^{-1}), the sample was considered to be leaking out of the rotor. In such a situation the polymer plug was trimmed and repacked, paying particular attention to the PTFE plugs.

In the case of sample leakage, the molten polymer usually spread over the porous stator. After disassembly of the probehead such contaminant was physically pealed from the stator, with this process aided by the addition of solvent ($CHCl_3$) to lower the cohesion of the polymer to the porous stator. Contaminant was also sometimes found in the Vespel drive gas jets. In such a case, whilst the probehead was at temperature (without a rotor present) the drive gas was raised to a high-pressure while maintaining the standard bearing pressure.

Upon completion of NMR measurements, rotors were spun down and ejected without lowering the probehead temperature. Immediately after sample ejection the bearing gas pressure was raised to that used for MAS, without a rotor being present. This procedure enabled the probehead to remain at measurement temperature without damage, facilitating rapid sample exchange due to reduced thermal equilibration times.

After ejection the zirconia rotor caps were immediately removed by applying even pressure around the rotor and twisting the cap between the fingers, using a sponge

[†]Shimming criteria for melt-state MAS NMR of polyethylene will be discussed in full in Section 7.2.1.

cloth to grip the fins. If the rotor cap did not freely rotate under moderate effort, a tool with a negative inset in the shape of the cap was used to apply greater torque (Figure 6.12:d). This tool was crudely fashioned by pressing an extremely hot rotor cap onto a block of thermoplastic hence melting an impression.

Once the cap had been taken off, the PTFE layers were removed and the filled rotors immersed in liquid nitrogen. The thermal contraction of the polyolefins, upon thorough cooling, was sufficient to allow samples to be easily pulled from their rotors. No further cleaning was required. The resulting cylindrical plugs could also then be reused multiple times.

6.3 Alternative methods of spin polarisation

With pulsed FT-NMR measuring the relaxation back to equilibrium from a perturbed state the method of initial spin polarisation plays an important role for heteronuclear experiments.

For polyolefins the heteronuclear spins in question, to all extents and purpose, consist solely of ^{13}C and ^{1}H nuclear spins. Thus initial polarisation may either be created directly on the observed ^{13}C nuclei, or initially created on the more abundant ^{1}H nuclei and then transferred to the observed ^{13}C nuclei (Figure 6.13).

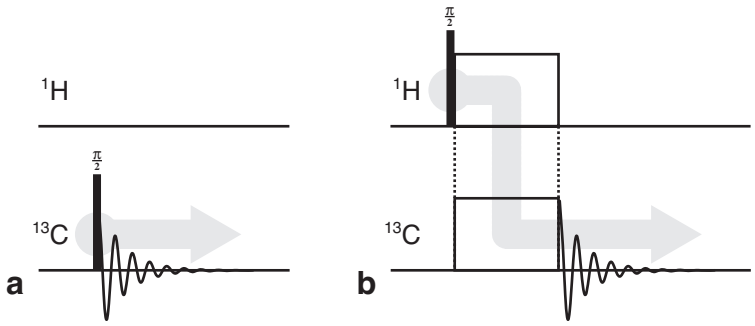

***Figure 6.13**: The two possible methods of spin polarisation of ^{13}C; (a) direct polarisation of ^{13}C by SPE and (b) initial polarisation of ^{1}H followed by polarisation transfer to ^{13}C via a mediating spin-coupling mechanism.*

Such polarisation transfer techniques have the added advantage of enabling higher polarisation of less abundant nuclei with low magnetogyric ratios, thus increasing overall sensitivity. However, due to various mechanisms of polarisation transfer, i.e. heteronuclear dipolar coupling or J-coupling, the intensity distribution of the ^{13}C NMR spectrum may vary as compared to that achieved using direct polarisation by SPE (Section 3.4). It is because of this that direct SPE is commonly thought to be the only polarisation method resulting in truly quantitative spectra.

In this section the applicability of both direct polarisation and J-coupling mediated polarisation transfer methods for branch quantification in molten polyolefins was investigated.

6.3.1 Direct polarisation via single pulse excitation

Single pulse excitation is commonly held as the only method of polarisation producing fully quantitative spectra. The method is thus routinely used in solution-state, melt-state and solid-state NMR for quantitative sample characterisation. However in order to be fully quantitative, the observed nuclei have to be allowed to fully relax back to their thermal equilibrium state between pulses. Commonly the criterion of $\tau_{rd} = 5\times\ T_1$ is used allowing for 99.3% of the nuclei to return to the equilibrium state. Due to the long T_1^C values observed for polyethylenes in both solution and melt-state [De Pooter 91, Hatfield 95, Pollard 04], recycle delays of over one minute can be necessary to achieve quantitative results. This criterion thus substantially increases the overall measurement time.

One strategy to reduce overall measurement time is the use of 10 s recycle delays and quantifying branching only via those sites with $T_1^C < 2$ s, such that the $\tau_{rd} = 5\times\ T_1^C$ for these sites still holds [De Pooter 91]. Alternatively, the addition of paramagnetic relaxation agents, to shorten the T_1^C of all sites sufficiently to allow shorter recycle delays, is routinely used for solution-state NMR of polyethylene [Wood-Adams 00].

With significant time improvements possible by the use of short recycle delays, the effect on signal intensity and area was investigated as a function of recycle delay for melt-state NMR of polyethylene. Emphasis was placed on the key question of whether quantification was still possible with $\tau_{rd} \approx T_1^C$. The use of relaxation agents in the melt was also investigated.

Effects of short recycle delays

A series of comparable SPE spectra were acquired for a typical polyethylene-co-α-olefin (PE8b-C) with increasingly shorter recycle delays, from 60 s down to 2 s. The areas of the main backbone (δ, α, $\star$) and branch sites (**1**, **2**) were determined as a function of recycle delay. To facilitate comparison between different sites, each series of peak areas was normalised to the area obtained with the longest recycle delay, for which full relaxation was assumed.

Approximately constant peak areas were seen for recycle delays between 10 and 60 s for all but the **1** site, with this site only remaining constant for recycle delays over 20 s (Figure 6.14a-c). For all the backbone sites an increase in normalised peak area was seen when going to shorter recycle delays . While the area of the δ peak grew by only 20% (Figure 6.14a), an increase of up to 40% was seen for both the $\star$ and α sites (Figure 6.14b). In contrast the more expected saturation behaviour was seen for the terminal branch sites **1** and **2**, with the normalised peak area decreasing by 50 and 25% respectively (Figure 6.14c). Such behaviour has previously been observed and its origin explained by a transient nuclear Overhauser effect (NOE) [Solomon 55, Okamoto 92, MacNamara 00, Alamo 02, Pollard 04]. In this situation

such an NOE arises due to the continuous inversion of the proton populations during the proton decoupling of the previous scan. After decoupling has stopped ^{1}H–^{13}C cross-relaxation may occur during the recycle delay, due to the protons taking several hundreds of milliseconds to relax. The recycle delay τ_{rd} now being equivalent to an NOE mixing time τ_m (Figure 3.18). If the next transient is acquired a short time period after the decoupling a signal enhancement may be observed [Okamoto 92].

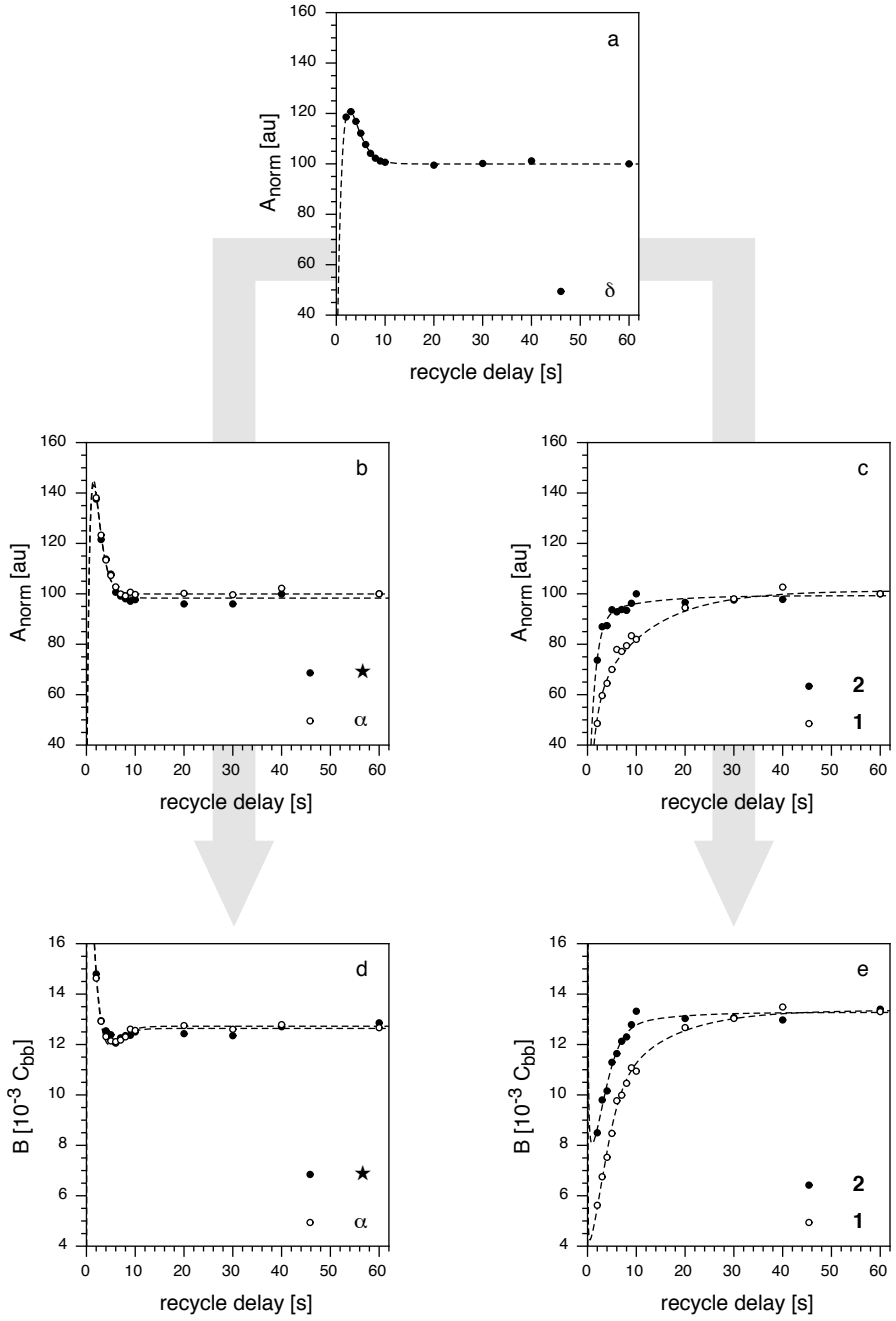

***Figure 6.14**: The effect of recycle delay on the normalised area of the (a) bulk δ site, (b) ⋆ and α backbone sites and (c) terminal branch sites, and its associated influence on determined branch content. (Fitted using Equation 6.3 with the parameters given in Table 6.4)*

To determine if the transient NOE was indeed responsible for the observed signal enhancement, comparable spectra were acquired without decoupling using similar recycle delays. Without decoupling the proton thermal equilibrium should remain undisturbed, with cross-relaxation not being able to take place during the recycle delay.

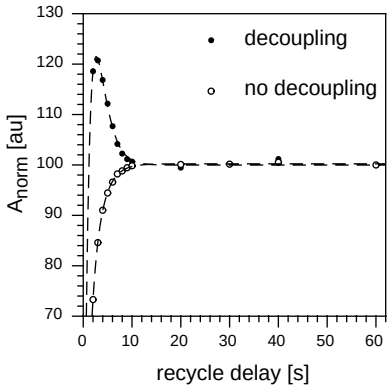

***Figure 6.15**: The influence of recycle delay on normalised δ peak area with and without heteronuclear decoupling. Fit: $\frac{T_1^C}{T_1^H}$ equals to $\frac{1.6}{1.4}$ and $\frac{2.1}{0.9}$ respectively.*

When the normalised areas of the δ peak obtained without decoupling were compared, no signal enhancement was seen, thus showing that a transient NOE only occurred with decoupling (Figure 6.15).

The influence of the transient NOE on the carbon magnetisation as a function of time can be described quantitatively by solving the Solomon equations for a heteronuclear two-spin system (Section 3.3.3). Under the assumption that relaxation occurs exclusively via intramolecular dipolar coupling interactions, the transition probabilities in the Solomon equations (Equations 3.66 and 3.67) can be replaced by the spin-lattice and cross-relaxation time constants [Solomon 55, Neuhaus 89]:

$$\frac{\mathrm{d}}{\mathrm{d}t}S_z(t) = -\frac{1}{T_1^C}[S_z(t) - S_z^0] - \frac{1}{T_{CH}}[\,I_z(t) - I_z^0] \tag{6.1}$$

$$\frac{\mathrm{d}}{\mathrm{d}t}I_z(t) = -\frac{1}{T_1^H}[\,I_z(t) - I_z^0] - \frac{1}{T_{HC}}[S_z(t) - S_z^0] \tag{6.2}$$

where T_1^{C} and T_1^{H} are the spin-lattice relaxation time constants, T_{CH} is the $^1\mathrm{H}\rightarrow{}^{13}\mathrm{C}$ cross-relaxation time constant and T_{HC} is the $^{13}\mathrm{C}\rightarrow{}^1\mathrm{H}$ cross-relaxation time constant.

Assuming that the abundant ^{1}H spins (I) are not influenced by the very dilute ^{13}C spins (S), i.e. $T_{HC} = 0$, and choosing boundary conditions at initial magnetisation and at equilibrium, an expression for the carbon magnetisation as a function of time is obtained [Alamo 02]:

$$\frac{S_z(t)}{S_z^0} = 1 + \left[\left(\frac{\eta}{1-\frac{T_1^C}{T_1^H}}\right)\cdot\exp\left\{\frac{-t}{T_1^H}\right\}\right] - \left[\left(1+\frac{\eta}{1-\frac{T_1^C}{T_1^H}}\right)\cdot\exp\left\{\frac{-t}{T_1^C}\right\}\right] \tag{6.3}$$

where η is the NOE enhancement defined as:

$$\eta = \frac{\gamma_H}{\gamma_C}\cdot\frac{T_1^C}{T_{CH}} \tag{6.4}$$

Considering Equation 6.3 it can be seen that the signal enhancment for a given site is dependent on its associated T_1^C and T_1^H time constants. It has previously been shown that if the protons relax at a faster rate than the nearest ^{13}C site ($T_1^H < T_1^C$) the ^{1}H→^{13}C cross relaxation is negligible [Alamo 02]. However when the protons relax at a similar or slower rate then the nearest ^{13}C ($T_1^C \leq T_1^H$), the transient NOE becomes significant and signal enhancement is seen.

The changes in signal intensity with recycle delay were fitted using Equation 6.3 with T_1^C, T_1^H, T_{CH} and S_z^0 as variables. The fitted curves showed good agreement with the measured normalised areas (Figure 6.14a-c). The T_1^C values obtained from the fit were however significantly higher than those directly measured by inversion recovery for all sites but δ (Table 6.4). This discrepancy was attributed to pure intramolecular dipolar coupling based relaxation not being the only active relaxation pathway [Neuhaus 89]. Assuming this, the total relaxation times obtained from the NOE fits can be decomposed into a pure intramolecular dipolar part and a miscellaneous part according to:

$$\frac{1}{T_1} = \frac{1}{T_1^D} + \frac{1}{T_1^{other}} \tag{6.5}$$

with the term T_1^{other} containg the contributions from the intermolecular dipolar relaxation as well as all other non-dipolar relaxation mechanisms, such as CSA, J-coupling and spin-rotation interactions [Neuhaus 89, Claridge 99].

***Table 6.4**: Comparison of relaxation parameters obtained from fitting the normalised areas in Figure 6.14 with Equation 6.3 and T_1^C times determined by inversion-recovery (ir-T_1^C).*

site	ir-T_1^C s	T_1^C s	T_1^H s	T_{CH} s	S_z^0 %
$\star$	0.64	1.4	0.7	1.6	98.3
α	0.53	1.0	0.9	1.9	99.9
δ	1.46	1.5	1.5	4.7	100.0
2	3.81	9.9	1.2	6.1	99.3
1	8.01	11.3	1.9	14.1	101.1

Although the areas deviated from equilibrium behaviour at short recycle delays several of the area ratios, and associated branch contents, showed different behaviour. Even at recycle delays of 3 s the areas of the backbone sites δ, $\star$ and α all showed approximately the same degree of enhancement. This resulted in the associated branch contents determined from these sites being only 1–2% higher than that determined at 60 s recycle delay (Figure 6.14d). Upon reduction of the recycle delay to 2 s the area of the δ decreased while the $\star$ and α site areas continued to increase. This resulted in an overestimation of the related branch contents by $\approx$ 15%. In contrast, the branch contents determined via the terminal branch sites **1** and **2** were found to be underestimated by over 50% at short recycle delays (Figure 6.14e). This strong deviation effectively rendered the **1** and **2** sites unsuitable for branch quantification at short recycle delays.

In addition to the over and underestimation at shorter recycle delays, differences were also observed between the equilibrium branch contents determined via the backbone (Figure 6.14d) and the terminal (Figure 6.14e) branch sites. The origin of this behaviour is still unclear, with discrepancies still seen with recycle delays of 100 s. This gave further reason to use only the backbone branch sites for quantification.

In conclusion it was shown that recycle delays as short as 2–3 s may be employed for branch quantification as long as only the backbone sites $\star$, α and δ are used for calculating the branch contents. At 3 s relatively accurate branch content could still be determined, while at 2 s systematic overestimation was seen. In practice the final choice between 3 or 2 s recycle-delays was made on a case-by-case basis depending on the level of accuracy required and measuring time available.

Relaxation agents

The long spin-lattice relaxation times encountered in the solution-state NMR of polyolefins can be reduced by the use of paramagnetic nuclear spin relaxation agents. These enable the use of recycle delays as short as 500 ms, dramatically reducing overall measurement times [Lamar 71, Levy 75, Prasad 91, Wood-Adams 00, Rego 04]. With the relaxation agent chromiumacetylacetonate, $Cr(C_5H_7O_2)_3$ or $Cr(acac)_3$, well established for solution-state NMR, its possible use in melt-state NMR of polyolefins was investigated.

For the relaxation agent to act upon all sites, and thus reduce all T_1^C values, homogeneous mixing on the molecular level was needed. Unfortunately simply dissolving PE in trichlorobenzene (TCB), adding $Cr(acac)_3$ and removing the solvent by vacuum distillation was not found to lead to the desired degree of mixing. An alternative method involving the use of a kugelrohr-oven proved more successful, allowing the sample to be continually rotated in a horizontal orientation while solvent is removed under heating. To further aid dissolution, PE pellets were first reduced in size by cryo-milling using liquid nitrogen. Specifically 500 mg of the milled PE was mixed with 25 mg (5-wt-%) of $Cr(acac)_3$ and dissolved in 20 ml of TCB over a 4 hour period in a kugelrohr-oven at 100°C, under weak vacuum (860 mbar). After a clear solution had been obtained the majority of the TCB was distilled off at 180°C lowering the vacuum to 50 mbar. The resulting thin film of PE was then flushed with argon and residual solvent removed by applying a strong vacuum (first 50 mbar, then 10 mbar) for 4.5 hours at 180°C. Homogeneous distribution of the relaxation agent was suggested by a uniform yellow colour within the polymer film. It should be noted that due to the high temperatures needed to completely remove the TCB, this method would probably need to be modified for unstabilised materials.

To assess the effect of the incorporated relaxation agent spin-lattice relaxation times were measured by inversion recovery of a commercial stabilised PE-co-butene (PE4b) with and without $Cr(acac)_3$. While PE4b showed typical T_1^C values, after the addition of relaxation agent T_1^C values were found to be reduced ≤ 1 s (Table 6.5).

***Table 6.5**: Spin-lattice relaxation time (T_1^C) and full-width at half-maximum (FWHM) for each resolved ^{13}C site of PE4b with (+) and without (−) $Cr(acac)_3$.*

site	T_1^C[s]		FWHM [Hz]	
	−	+	−	+
$\star$	1.41	0.68	10.4	11.3
α	1.03	0.56	10.4	11.3
δ	1.69	0.71	10.4	12.2
β	1.22	0.61	10.4	12.2
2	1.32	0.62	10.4	13.0
1	5.56	1.03	7.8	9.6

A consequence of reducing all spin-lattice relaxation times within the spin system was a loss of the transient NOE effect previously observed for the backbone carbon sites (Section 6.3.1). This resulted in the signal enhancement at short τ_{rd} for these sites no longer being observed (Figure 6.16a), with the areas of the δ and $\star$ sites staying approximately constant, even at τ_{rd} = 1 s (Figure 6.16b). Only the **1** site showed the expected decreased signal due to saturation effects at $\tau_{rd} \approx T_1^C$ (Figure 6.16c).

When the determined degree of branching is considered it can be seen that the ratio of $\star$ and δ remained closer to the real value at short recycle delays, with only small variation seen at very short recycle delays (Figure 6.16d). Similarly, the ratio of the **1** and δ sites also remained constant until very short recycle delays, as compared to the sample without relaxation agent (Figure 6.16e). At very short recycle delays however, the degree of branching determined by the **1** site was still seen to decrease by $\approx 10\%$.

However, the incorporation of relaxation agent also resulted in line broadening, due to the associated effect on T_2 relaxation. Practically this resulted in ^{13}C FWHM increasing by up to 25% depending on site,[†] thus leading to only a slight reduction in spectral resolution (Table 6.5).

In conclusion it was thus shown that relaxation agents are also applicable for melt-state NMR of polymers and allowed access to measurements with much shorter recycle delays. Homogeneous incorporation into the polymeric samples however proved impractical to implement on a regular basis.[‡] The incorporation of relaxation agents was found to limit the maximum spectral resolution and, more importantly, reduce overall sensitivity due to a lack of a transient NOE enhancement.

[†] ^1H FWHM increased from 21.4 to 43.8 Hz and thus strongly affected shimming.
[‡] Co-extrusion of polymer and relaxation agent could be an alternative, however homogeneity of the final blend would need to be investigated.

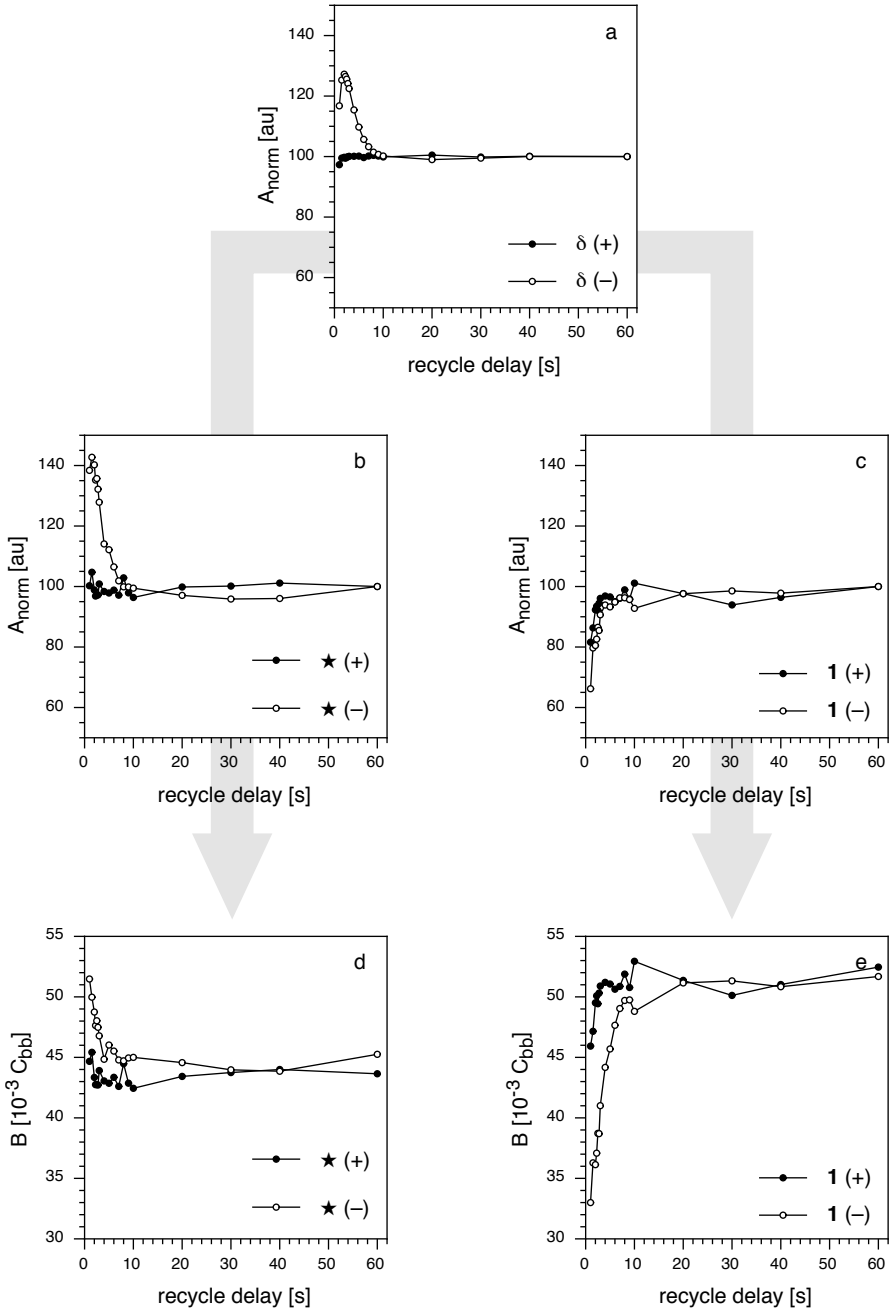

Figure 6.16: *The effect of reducing the recycle delay on the normalised areas of the (a) bulk δ site, (b) backbone (⋆) and (c) terminal (**1**) branch site and their associated influence on branch contents (d,e) with (+) and without (−) the use of the relaxation agent $Cr(acac)_3$. (PE8b-C at 423 K)*

6.3.2 J-mediated polarisation transfer methods

Polarisation transfer methods mediated by the J-coupling interaction were investigated with the hope of enabling branch quantification at even shorter recycle delays. Both INEPT (Section 3.4.4) and DEPT (Section 3.4.5) methods were investigated (Figure 6.17). For the comparison of sensitivity and assessment of applicability to branch quantification both methods were implemented such that all sites, irrespective of the number of attached protons, resulted in peaks of the same phase.

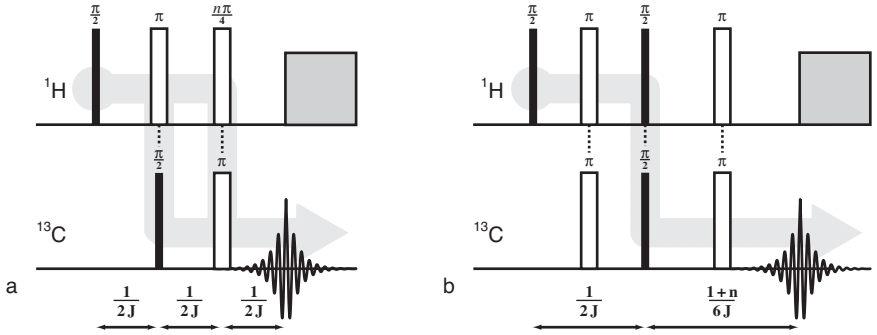

***Figure 6.17**: The pulse sequences for (a) DEPT and (b) INEPT, where $n = 1, 2, 3$.*

By the use of ^{1}H–^{13}C polarisation transfer the recycle delay used for these methods would be limited by the shorter T_1^{H} relaxation times as opposed to T_1^{C}. It was also hoped that the enhancement in sensitivity, known for these techniques in the solution-state, would also be present in the melt-state. As polarisation would initially be created on the protons the strong influence of heteronuclear NOE and saturation [Pollard 04] should also not be present, thus allowing quantification via the more resolved terminal branch sites **1** and **2**. Initial investigations showed that the high degree of molecular motion present in the melt-state gave sufficiently slow T_2^* relaxation times without decoupling, indicating that such methods were feasible.

When comparing DEPT, INEPT and SPE spectra of PE8b-C a decrease in SNR of the δ peak and area of the total spectrum (A_{All}) was seen when reducing the recycle delay from 60 to 2 s using the same number of scans (Table 6.6). This illustrated that the strong NOE observed for SPE was no longer present for DEPT and INEPT method.

***Table 6.6**: Comparison of absolute normalised spectral area (A_{all}) and signal-to-noise of the δ peak (SNR_δ) for comparable SPE, INEPT and DEPT spectra of PE8b-C.*

		Recycle delay (τ_{rd}) [s]				
		2	3	5	10	60
A_{all}	SPE	1032	964	875	757	731
	INEPT	799	954	938	961	1037
	DEPT	563	558	692	694	740
SNR_δ	SPE	2881	2766	2571	2209	2164
	INEPT	2078	2493	2476	2525	2725
	DEPT	1531	1509	1883	1883	2024

The difference between SPE and J-mediated polarisation transfer methods was more clearly seen when monitoring the relative areas of each site with decreasing recycle delay (Figure 6.18a).

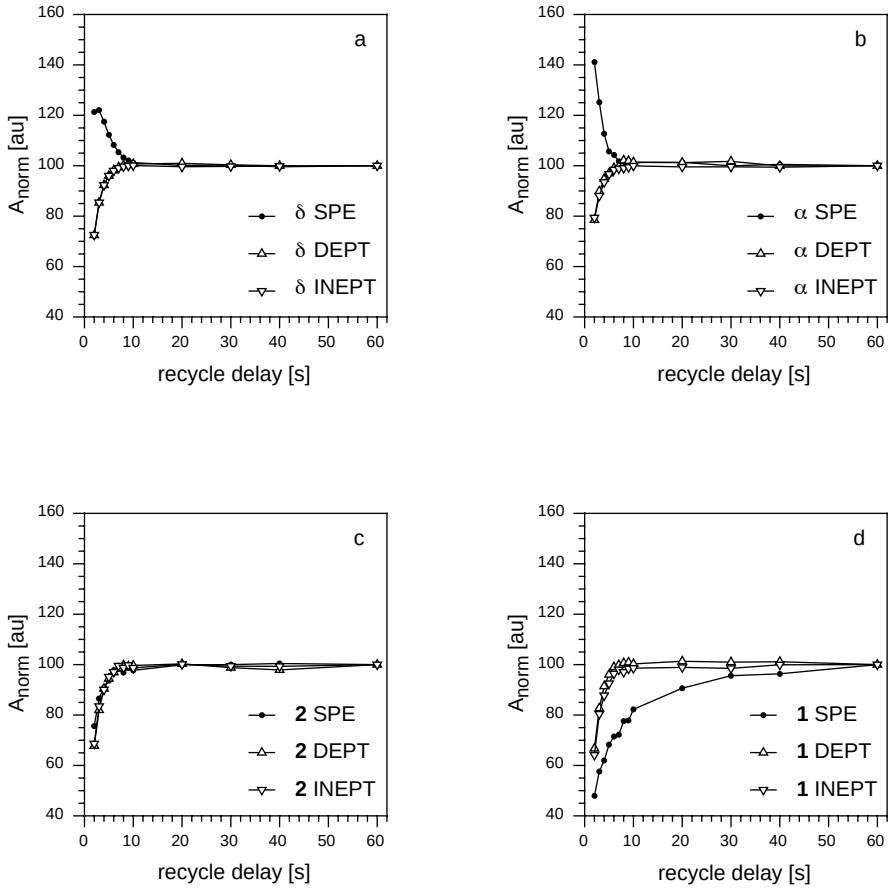

***Figure 6.18**: The difference between the effect of reducing the recycle delay on the normalised areas of the (a) δ, (b) α, (c) **1** and (d) **2** sites for SPE, DEPT and INEPT. (PE8b-C at 423 K)*

For SPE the relative areas of the backbone α and δ sites all showed the previously discussed NOE enhancement (Section 6.3.1), this effect started at recycle delays of $\approx$ 10 s. In contrast, for both INEPT and DEPT spectra a decrease in area for these sites was seen with shorter recycle delays (Figure 6.18a-b). This decrease in area only occurring at recycle delays of $\approx$ 8 s. For the **1** and **2** terminal branch sites no enhancement in intensity was seen regardless of polarisation method (Figure 6.18c). Although saturation was observed with decreasing recycle delay for both sites and all three polarisation methods the point at which this occurred varied. Saturation of the **2** site for all methods, and the **1** site for INEPT and DEPT, all started at a recycle delay of $\approx$ 8 s. This was in contrast to the relatively quick onset of saturation seen for the **1** site with SPE which took place at $\approx$ 40 s (Figure 6.18d).

The different behaviour at short recycle delays was directly due to the polarisation method. Direct polarisation via SPE inadvertently led to an NOE enhancement of

carbon sites with short T_1^C, while for those sites with long T_1^C saturation occurred. In contrast with ^{1}H–^{13}C polarisation transfer, the T_1^H was now the key parameter. Only when the protons were saturated did the intensity of the carbon signals decrease, with less polarisation transfer occurring. Due to T_1^H generally being shorter than T_1^C, ^{1}H saturation occurred at shorter recycle delays than for ^{13}C. This behaviour was confirmed by the different recycle delays at which saturation of the terminal branch site **1** occurred for SPE and INEPT/DEPT. With this site having a T_1^C of $\approx$ 8 s (Section 8.3), due to the rotational motion of the methyl group, saturation of the SPE signal occurred at a longer recycle delay than that of the signal produced from polarisation transfer.

Due to the lack of direct NOE enhancement of the carbon signal, neither the DEPT nor INEPT method could match the sensitivity of direct polarisation via SPE at the shortest recycle delays. This was most clearly seen when the total spectral area of spectra obtained using the three methods were compared to a reference SPE spectrum, measured with a recycle delay of 60 s (Table 6.7). It should also be noted that at 60 s recycle delay, signal enhancement can be seen in the INEPT spectra, when compared to the equivalent SPE and DEPT spectra. The lower sensitivity of INEPT and DEPT at shorter recycle delays was also seen when the absolute areas of the δ peaks of the three methods were compared (Figure 6.19).

***Table 6.7**: Comparison of sensitivity ($A_{all}\sqrt{t}^{-1}$) for comparable SPE, INEPT and DEPT spectra of PE8b-C.*

		τ_{rd}				
		2 s	3 s	5 s	10 s	60 s
$A_{All} \cdot \sqrt{t}^{-1}$	SPE	7.4	5.7	4.1	2.5	1.0
	INEPT	5.8	5.7	4.4	3.2	1.4
	DEPT	4.1	3.3	3.2	2.3	1.0

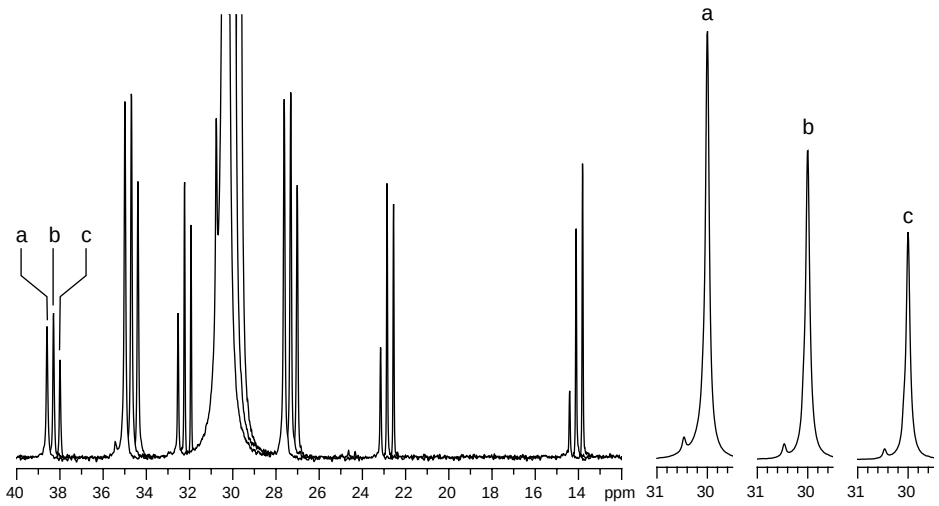

***Figure 6.19**: Comparison of normalised (a) SPE, (b) INEPT and (c) DEPT spectra of PE8b-C (a and c shifted by ±0.5 ppm with respect to b for comparison). Comparison of the absolute δ peak areas shows greatest signal for SPE.*

Effect of recycle delay on determined degree of branching

In contrast to SPE spectra recorded using short recycle delays, both DEPT and INEPT spectra were not found to underestimate the terminal branch sites **1**, **2** and **3**. This can be seen by inspection of these sites in comparable spectra (Figure 6.19). However, when branch contents were calculated from the terminal branch sites it became apparent that these were now considerably overestimated (Figure 6.20).

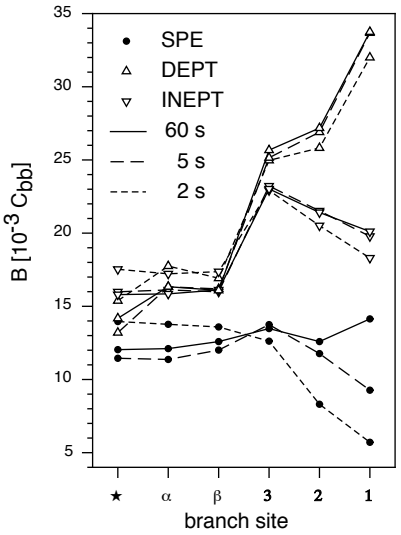

***Figure 6.20**: Branch contents (B) as determined by different sites using DEPT, INEPT and SPE at different recycle delays (τ_{rd}).*

It was thus concluded that, as with SPE spectra, DEPT and INEPT spectra could only be used for branch quantification via the α and $\star$ backbone sites. Although the β sites showed promise these sites were generally not fully resolved from the δ peak and thus introduced more error into the final determined branch content. It was found that branch contents determined by INEPT from α and $\star$ sites were 30-46% higher than those obtained by a reference SPE spectrum taken with 60 s recycle delay. While DEPT spectra gave 35-47% higher branch contents using the α site, only 10-28% higher branch contents were obtained using the $\star$ site. It was thus concluded that branch quantification using the $\star$ site in DEPT spectra was the most promising alternative to SPE for melt-state MAS NMR.

Effect of J-coupling constant on determined degree of branching

With the value of the J-coupling constant a prerequisite for the pulse timing of both DEPT and INEPT experiments, 2D heteronuclear J-resolution measurements [Aue 76] were undertaken for PE8b-C. This revealed a distribution of J-coupling constants from 115–135 Hz with J_{CH} varying by $\approx$ 9 Hz (Table 6.8). It was seen that no single coupling constant could be picked that would satisfy all sites.

***Table 6.8**: Determined heteronuclear J-coupling constants for each site in PE8b-C and the approximate distribution.*

site		J_{CH}		ΔJ_{CH}
$\star$	1:1	124.2	$\pm$	6.9
α	1:2:1	123.6	$\pm$	7.2
β	1:2:1	125.6	$\pm$	9.8
γ	1:2:1	124.6	$\pm$	10.3
δ	1:2:1	124.6	$\pm$	12.7
3	1:2:1	123.6	$\pm$	10.3
2	1:2:1	124.6	$\pm$	6.9
1	1:3:3:1	124.1	$\pm$	5.9

Under ideal circumstances the J-coupling constant used should not affect the intensity distribution of the sites in the resulting spectra, despite such a distribution in J-coupling constants. Comparison of DEPT and INEPT spectra recorded with J_{CH} varying from 115–135 Hz however showed that the intensity distribution varied with the coupling constant. More importantly, resulting from this intensity variation, the branch contents determined from DEPT and INEPT spectra were also found to vary with J_{CH} and the carbon site used (Figure 6.21).

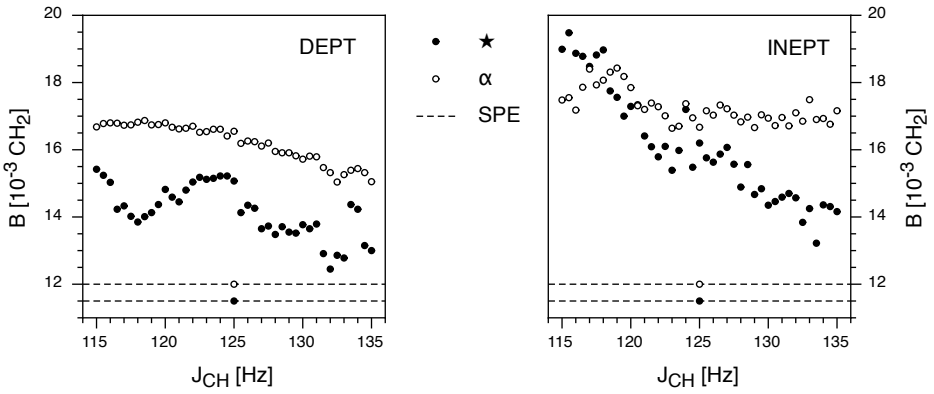

***Figure 6.21**: Branch contents (B) as determined by DEPT (left) and INEPT (right) via the ⋆ and α sites using different J-coupling constants (J_{CH}). Reference branch contents determined by SPE shown as dashed lines.*

The least variation in branch content was found using the α site for J-couplings between 126–132 Hz, thus for all comparative experiments $J_{CH} = 128$ Hz was used. The J-coupling constant needed for stable branch quantification may however also vary between samples and with recycle delay. Thus different coupling constants may be needed for reproducible branch quantification of different systems at short recycle-delays of 2 s.

The origin of this dependance on J_{CH} was thought to be due to the residual dipolar coupling during the periods of free evolution in the DEPT and INEPT experiments (Figure 6.17). Thus, unlike in the solution state were only J-couplings can be assumed to be acting in such periods, the evolution under dipolar coupling and MAS results in a change in intensity distribution in the final spectrum.

Despite the problems with quantification, both DEPT and INEPT when combined with melt-state MAS NMR were found to be extremely useful for the chemical characterisation of polyolefins (Chapter 8). With both methods capable of distinguishing between CH, CH_2 and CH_3 groups, assignment of unknown peaks was facilitated (Section 8.2).

6.4 Decoupling schemes

Due to the high molecular mobility present in the melt-state the line broadening interactions are partially removed and the FID persists for a relatively long time. However, unlike the solution-state full isotropic motion does not occur, thus leading to residual broadening caused by anisotropic interactions, albeit much reduced. Further averaging of the residual anisotropic interactions is achieved by the application MAS to samples in the melt-state, leading to increased resolution. In order to remove the remaining heteronuclear dipolar and J-couplings, high-power decoupling is needed during FID acquisition.

6.4.1 Decoupling limitations on acquisition time

Due to hardware constraints high-power decoupling can only be applied for relatively short periods of time. The maximum acquisition time (τ_{aq}^{max}) is limited by two factors; firstly the maximum length of a single continuous pulse, and secondly the duty-cycle of the proton high-power amplifiers. The length of a single continuous pulse depends on the probehead hardware, and was typically 200 ms for all probeheads considered in this work. The percentage duty-cycle $D_{\%}$ is related to both the recycle delay τ_{rd} and the percentage amplifier 'on-time' $O_{\%}$ of the decoupling scheme. The maximum acquisition time, constrained by duty cycle considerations, can be calculated according to:

$$\tau_{aq}^{max} = \frac{D_{\%} \cdot \tau_{rd}}{O_{\%} - D_{\%}} \tag{6.6}$$

Although 200 ms might be the absolute limit of acquisition time, at short recycle delays, duty cycle considerations significantly constrain the acquisition time. For example, high-power continuous wave (CW) decoupling ($O_{\%} = 100\%$) at a recycle delay of 2 s results in an extremely short acquisition time of 41 ms with the maximum duty cycle of 2%.

Such short acquisition times cause severe truncation of the FID resulting in sinc artefacts in the spectrum after Fourier transformation. In order to remove these artefacts, and thus enable branch quantification by integration, a window function is applied to the FID. resulting in artificial line broadening of spectrum from that of the natural T_2^*-based line widths. For polyethylene this situation is exacerbated by the large dynamic range of signal intensities seen for the δ site and the various sites related to branching.

Due to the constraints on acquisition time imposed by the decoupling method alternative decoupling methods were sought. It was hoped that these methods would allow for longer acquisition times and thus the use of less artificial line broadening improving resolution and aiding quantification.

6.4.2 Low power decoupling: WALTZ-16

In solution-state NMR low power decoupling schemes such as WALTZ-16 are often employed. During WALTZ-16 decoupling the proton amplifier is continuously 'on' during acquisition ($O_{\%} = 100\%$), however, due to the applied phase cycling lower decoupling fields are required [Shaka 83b, Shaka 83a, Seger 04]. Due to the lower power of this decoupling method it was hoped that the duty cycle may be extended beyond 2%, thus allowing better resolution.

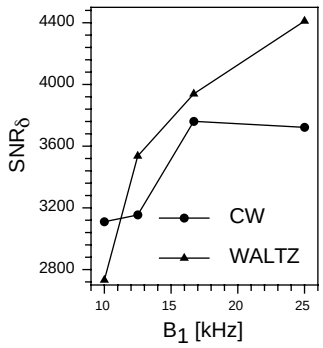

***Figure 6.22**: Influence of decoupling method and field strength ($\boldsymbol{B}_1$) on signal-to-noise ratio of the δ peak (SNR_δ) measured from normalised SPE spectra of PE8b-C.*

Unfortuantly in the melt-state WALTZ-16 did not show any advantage over CW decoupling at lower decoupling field strengths ($\boldsymbol{B}_1$). In fact at all decoupling fields tested, WALTZ-16 consistently showed broader peaks than CW decoupling. At high decoupling field strengths this effect could be compensated for by a higher signal-to-noise ratio (SNR) (Figure 6.22). However, at the lowest decoupling field of 10 kHz, which would have allowed an increase in acquisition time, both the broadest line shapes and lowest SNR were observed (Table 6.9). Thus, WALTZ-16 was not considered an alternative to CW decoupling.

***Table 6.9**: Full-width at half-maximum (FWHM) of the δ peak for normalised SPE spectra of PE8b-C acquired with WALTZ-16 (W) and continuous wave (CW) decoupling at various decoupling field strengths ($\boldsymbol{B}_1$) using τ_{rd} = 2 and 10 s.*

	τ_{rd}	$D_{\%}$	τ_{aq}	FWHM [Hz] @ $\boldsymbol{B}_1$[kHz]			
	s	%	ms	25.0	16.7	12.5	10.0
W	2	2	41	41.5	42.7	44.0	45.2
CW	2	2	41	39.1	39.1	44.0	44.0
W	10	2	204	9.8	11.0	11.0	11.0
CW	10	2	204	9.8	9.8	9.8	11.0

6.4.3 Stroboscopic decoupling: π-pulse-train

Another strategy to increase the acquisition time was to reduce the percentage 'on-time' ($O_{\%}$) of the amplifier during decoupling (Equation 6.6). This was achieved by applying a train of proton π-pulses during acquisition (Figure 6.23b).[†] A compromise between decoupling efficiency and 'on-time' was found with both the inter-pulse delay and π-pulses themselves being of equal length, typically 20 μs. This resulted in 50% on-time during acquisition as opposed to the 100% for CW and WALTZ-16. This allowed decoupling to be applied for longer periods extending the possible acquisition time.

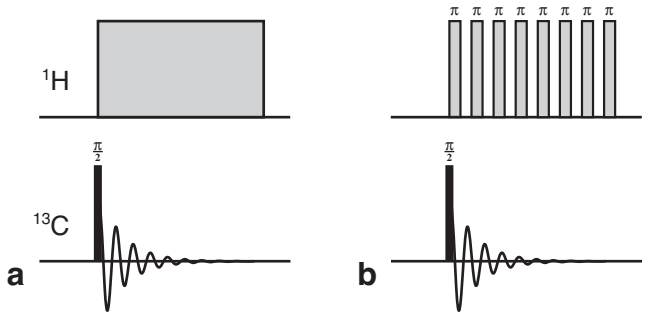

***Figure 6.23**: Comparison of (a) continuous wave (CW) and π-pulse-train heteronuclear decoupling schemes.*

Using the typical 2% duty cycle, π-decoupling resulted in a doubling of the acquisition time. This implementation is denoted π_2 to reflect the duty cycle used to calculate τ_{aq}. Due to the stroboscopic nature of π-decoupling less stress was placed on the coil and it thus became possible to increase the duty cycle beyond 2%. Measurement of the power being delivered to the coil suggested that under these conditions the duty-cycle could be extended up to 6% without hardware damage or significant heating.

Comparable spectra were measured using π-decoupling with duty cycles of up to 6%, i.e. π_6 decoupling. The decoupling field strength $\boldsymbol{B}_1$ did not seem to strongly effect the FWHM of the δ peak for recycle delays of 2 s (Table 6.10) and 10 s (Table 6.11).

***Table 6.10**: FWHM of the δ peak for different decoupling schemes and field strengths ($\boldsymbol{B}_1$) at τ_{rd} = 2 s.*

	$D_{\%}$	τ_{aq}	FWHM [Hz] @ $\boldsymbol{B}_1$[kHz]			
		ms	25.0	16.7	12.5	10.0
π_1	1	41	44.0	44.0	44.0	44.0
π_2	2	83	22.0	22.0	24.4	24.4
π_3	3	127	14.7	15.9	17.1	15.9
π_4	4	174	11.0	12.2	12.2	13.4
π_5	5	222	11.0	11.0	11.0	11.0
π_6	6	273	8.5	9.8	9.8	8.5

***Table 6.11**: FWHM of the δ peak for different decoupling schemes and field strengths ($\boldsymbol{B}_1$) at τ_{rd} = 10 s.*

	$D_{\%}$	τ_{aq}	FWHM [Hz] @ $\boldsymbol{B}_1$ [kHz]			
		ms	25.0	16.7	12.5	10.0
π_1	1	204	11.0	11.0	11.0	11.0
π_2	2	417	9.8	10.4	11.0	11.0
π_3	3	638	6.1	6.1	6.1	7.3
π_4	4	870	7.3	6.1	6.1	7.3
π_5	5	1111	7.3	6.1	6.1	6.1
π_6	6	1364	6.1	7.3	6.1	6.1

[†]See Appendix C.3 for experimental implementation.

When the SNR was considered it became clear that the strongest decoupling field gave the best results for all decoupling methods (Figure 6.24a). At the shorter 2 s recycle delay, under the strongest decoupling fields, the CW line width was reduced by more than 70% using π_6-decoupling (Figure 6.24b). The effect was less pronounced at 10 s recycle delay, although the peak could still be narrowed by over 30%.

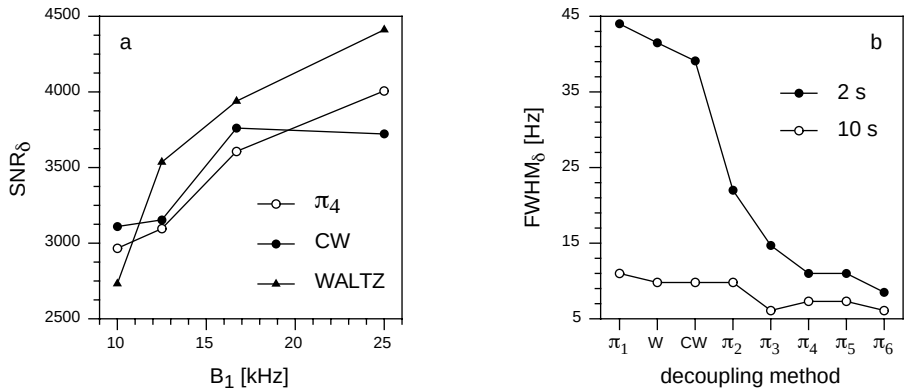

***Figure 6.24**: (a) Influence of decoupling field strength on signal-to-noise ratio of the δ peak for normalised SPE spectra taken with WALTZ-16 (W), continuous wave (CW) and π_4 decoupling at τ_{rd} = 2 s. (b) Comparison of full width at half-maximum of the δ peak for different decoupling methods at τ_{rd} = 2 and 10 s and $\boldsymbol{B}_1 = 25$ kHz.*

It should be noted that the increase in resolution was solely an effect of the longer acquisition time and not decoupling efficiency. Indeed, when using the same acquisition time as CW and WALTZ-16, π-decoupling (i.e π_1) was found to give the broadest peaks at all employed decoupling fields at recycle delays of both 10 and 2 s (Figure 6.24b). The longer acquisition times made accessible by π-decoupling however gave spectra with resolution much closer to that found in the solution-state (Figure 6.25).

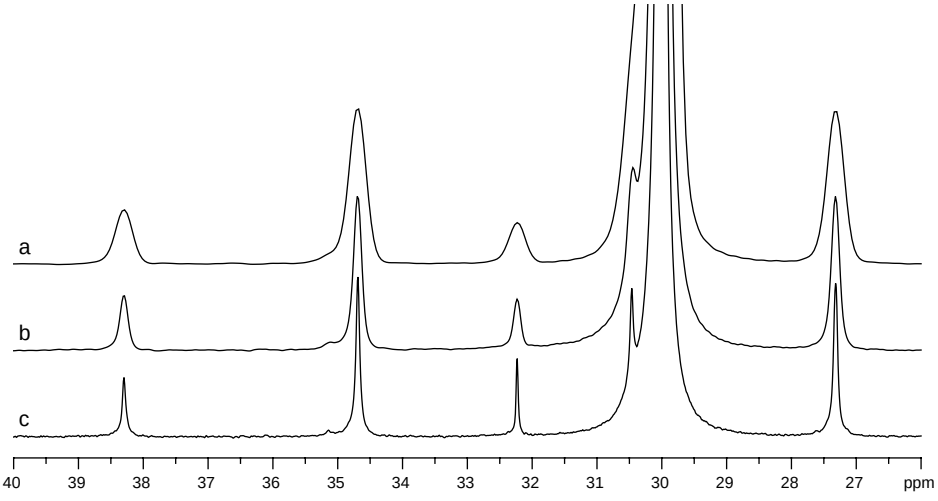

***Figure 6.25**: Comparison of normalised SPE spectra taken with different decoupling schemes and acquisition times (τ_{aq}): (a) CW (41 ms), (b) π_2 (82 ms) and (c) π_6 (272 ms). Apodisation adjusted for each spectrum individually depending upon the degree of truncation. (τ_{rd} = 2 s, $\boldsymbol{B}_1 = 25$ kHz)*

6.5 Summary

In this chapter the conditions for melt-state NMR under MAS have been optimised, and the method shown to be a viable alternative to solution-state NMR. As expected higher $\boldsymbol{B}_0$ fields and larger MAS rotor volumes gave higher sensitivity. Surprisingly little difference was seen between 4 mm MAS rotors using 500 and 700 MHz spectrometers. Further justification for use of wide-bore/low-field magnets was seen with 7 mm rotors at 300 MHz giving greater signal than 4 mm rotors at 700 MHz.

The compromise between sensitivity and resolution was found using 7 mm MAS rotors at 500 MHz. Further sensitivity was gained by using a $^{13}C-^{1}H$ optimised 7 mm MAS probehead. The relatively high-temperature range of this probehead also allowed access to all PE sample. The use of such a hardware setup allowed rapid sample throughput to be achieved by combining the convenience of MAS rotor sample containment and the ability to pre-press samples. The use of zirconia rotor caps was also found to significantly speed up the sample preparation stage.

Systematic studies of the influence of the recycle delay on peak areas showed that only the backbone sites could be used to quantify branch contents at short recycle delays. The transfer of polarisation from protons to carbons by a transient NOE, stemming from decoupling, resulted in up to 40% signal enhancement at short recycle delays. However for the terminal branch sites, up to 50% signal decrease was observed due to saturation effects.

The spin relaxation agent $Cr(acac)_3$ was also found to be applicable to samples in the melt state. The T_1^C values of all polyethylene sites were found to be reduced to at least 1 s. This reduction also however eliminated the favourable NOE signal enhancement seen at short recycle delays. Despite the advantage, homogeneous mixing was found to be time-consuming and generally problematic. It also itself carried an extra risk of sample degradation.

Polarisation enhancement techniques mediated by J-coupling were also found to be applicable in the melt state. Both techniques were found to be less susceptible to NOE and steady-state effects at short recycle delays. Unfortunately a dependence of branch content on the chosen coupling constant was observed, rendering these methods unsuitable for branch quantification in the melt-state. However, the distinction between CH, CH_2 and CH_3, also possible for these method proved useful when assigning unknown peaks.

Due to duty-cycle limitations, continuous decoupling methods were found to lead to substantial line broadening at short recycle delays. The resulting short maximum acquisition times resulted in severe FID truncation and thus strong artificial line broadening. Far longer acquisition times were possible using π pulse-train decoupling, due to its stroboscopic nature. The reduction in FID truncation resulted in less artificial line broadening having to be applied. This decoupling scheme was found

to be most applicable at short recycle delays where the FWHM of the δ peak was reduced by over 70% as compared to that obtained by CW.

In general, optimised melt-state MAS NMR was found to allow rapid branch quantification with greatly reduced preparation and measurement times whilst still retaining relatively high resolution.

Chapter 7

Quantitative analysis

With optimised melt-state MAS NMR found to be the most time efficient method of branch quantification (Chapter 6), the extraction of quantitative data from such spectra was investigated. Particular attention was paid to determining a setup and processing methodology which was not only accurate but also highly reproducible.

A standardised semi-automatic processing and analysis protocol was devised, minimising operator-related systematic errors on the final quantitative branch content determined. The resulting method provided measured properties and acceptance criteria for the stages of shimming, pulse power level tuning, zero-filling, apodisation, phase correction, baseline correction, integration region selection and choice of site used for quantification (Section 7.2).

Having considered such sources of error, the combination of optimised experimental method and standardised data processing method was evaluated with respect to its absolute accuracy and reproducibility (Section 7.3).

7.1 Measured properties and acceptance criteria

The error in the final determined property B can be considered to be proportional to a particular set of measured properties (X) and acceptance criteria (C) for an n stage processing process, with X_i and C_i corresponding to the i^{th} stage. For example, for the shimming stage X_{shim} could be the FWHM of the ^{1}H SPE spectrum with C_{shim} being < 20 Hz. The stage i is thus repeated until the test (X_i, C_i) returns true (Figure 7.1). Of particular importance, however, is how well the property X represents its particular stage, e.g. how well ^{1}H FWHM represents the quality of the shim.

The reproducibility for a single user is proportional to the inherent statistical variation of the measured property (σ), and the choice of measured properties and acceptance criteria (Figure 7.2a). However, the reproducibility between users is also

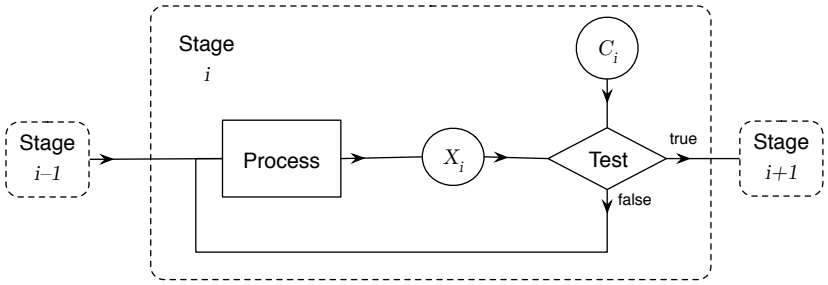

***Figure 7.1**: Illustration of the multi-stage nature of NMR data processing. Each processing stage is repeated until the measured property X_i meets the acceptance criterion C_i.*

proportional to the variation of the measured properties and acceptance criteria between users. Hence by providing all users with a common set of measured properties X_i and acceptance criteria C_i less variation will be seen.

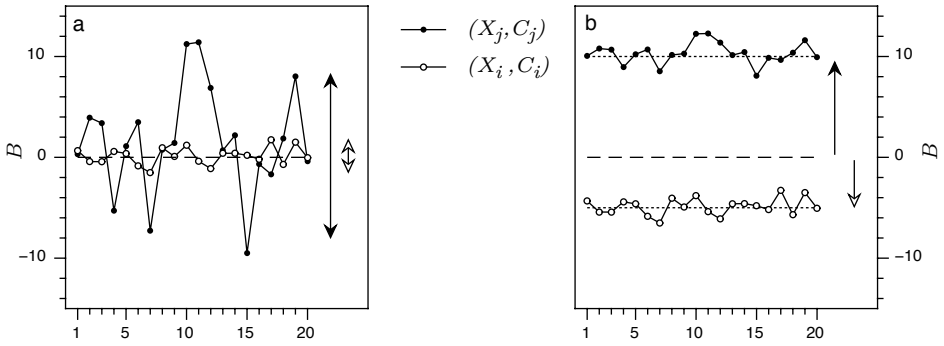

***Figure 7.2**: Illustration of the choice of measured property (X) and acceptance criteria (C) on (a) reproducibility and (b) accuracy of the final determined property B for two sets of parameters, where B has a true value of 0.*

With the absolute accuracy proportional to the choice of X_i and C_i standardisation can also be used to increase the overall accuracy of the final determined value, B (Figure 7.2b). For example, the baseline correction algorithm needs to be chosen such that the integral ratios of the sites in question are truly proportional to the number of spins present, and hence result in a more accurate branch content.

7.2 Standardised set-up and processing of NMR data

Error in the final determined degree of branch content is relatively easily introduced due to the different setup and processing practices commonly employed. The introduction of such systematic errors is compounded by the multi-stage nature of NMR data processing [De Pooter 91, Seger 04]. Hence standardisation of each each stage does not only lead to an increase in reproducibility, but also increased accuracy.

7.2.1 Shimming

With the achieved resolution based not only on the inherent spin-spin relaxation of the sites (T_2) but also on the inhomogeneity of the $\boldsymbol{B}_0$ field (T_2^{Δ}), shimming is of great importance. Shimming was thus conducted on the molten polymer samples themselves. The full-width at half-maximum (FWHM) of the bulk CH_2 site in the ^{1}H SPE spectra was chosen as the measured property reflecting the quality of the shimming.[†] A maximum ^{1}H FWHM of 25 Hz was defined as an acceptable line width for melt-state MAS NMR.[‡]

For unknown samples all shim values[§] were reset to zero. The shim values were then adjusted in a given order to achieve maximum signal intensity, as measured by the total integral of the FID, until the acceptance criterion of $\text{FWHM}_H \leq 25$ Hz was met. To standardise the shimming procedure between users, and generally improve reproducibility, the order in which the various shim values were adjusted was defined. With the complex synergistic relationship between the various shim coils, intermittent adjustment of the z and z^2 shims was found to result in the best overall shim. Thus the order for shim adjustment was as follows: [¶]

$$\{z, z^2, x, z, z^2, y, z, z^2, xz, z, z^2, yz, z, z^2, x^2 - y^2\}_n \tag{7.1}$$

In general, the same global minima were found for all molten samples, due to the standard geometry and amount of sample placed into the MAS rotor. Thus upon heating each sample a hollow cylinder of material of approximately the same dimensions was achieved, resulting in a common set of optimum shims. In practice after shimming from zero a number of times a previous set of shim values would commonly allow the shimming criterion to be reached without the need for further adjustment. However if the criterion was not reached, and adjustment of z and z^2 still did not achieve the desired result, full shimming from zero using the procedure shown in Equation 7.1 was needed.

7.2.2 Power-level determination

The exact tip angle of the applied ^{1}H and ^{13}C pulses may be adjusted either by varying pulse the duration while keeping the power constant or by varying the power and keeping the pulse duration constant. For quantitative measurements in order to apply the same $\boldsymbol{B}_1$ field on each sample, the latter method was used. This also allowed for the use of fixed length pulse for all experiments. The $\frac{\pi}{2}$ pulses for both ^{1}H and ^{13}C were typically 10 μs in length, equivalent to a 25 kHz $\boldsymbol{B}_1$ field. Power levels

[†]The ^{1}H FWHM also reflects the viscosity of the sample, with lower viscosity samples possessing more isotropic motion at a given temperature and thus resulting in narrower line-widths.
[‡]Equivalent to 0.083, 0.050 and 0.036 ppm at Larmor frequencies of 300, 500 and 700 MHz respectively.
[§]More correctly the currents applied to each individual shim coil.
[¶]Adjustment of higher order shims was not found to yield significant improvement.

were first set such that maximum intensity was obtained with a 10 μs pulse, and then fine-tuned so that a null in intensity occurred using a 40 μs 2π pulse. With constant $\boldsymbol{B}_1$ fields, power levels were found to slightly fluctuate both between systems and with general environmental condidions. For this reason both ^{1}H and ^{13}C power levels were adjusted on each individual sample immediately prior to measurement.

7.2.3 Digitised signal cropping

For measurements where a large number of transients were acquired, and/or the acquisition time was shorter than the persistence of the FID, a window-function was necessary to suppress truncation artefacts (see Section 7.2.5). In contrast, for measurements where only a few transients were required, and/or with the use of π-decoupling (Section 6.4.3), the acquisition time commonly exceeded the persistence of the FID and no window-function was necessary. With only noise present after the full decay of the FID, Fourier-transformation of the raw time domain signal would result in a higher level of noise in the spectrum than necessary. In order to reduce this digitised noise, the number of data points in the time domain (*TD*) were reduced to an effective number of data points (TD_{eff}) which only contained the FID and its inseparable noise.

7.2.4 Zero-filling

Increasing the number of data points in the time-domain by at least a factor of 2 has been shown to improve the resolution in the frequency-domain and prevent loss of information (Section 3.5.2). Zero-filling by a factor > 2, however, only results in an increase in digital resolution of the spectrum by interpolation [Claridge 99]. In order to obtain optimum frequency resolution all time-domain data was zero-filled such that the total number of real frequency-domain data points points *SI* met this criterion, i.e. $SI \geq 2 \times TD$.[†] If digitised signal cropping had been used (Section 7.2.3) $SI \geq 2 \times TD_{eff}$ was used.

The need for the use of $SI > 2 \times TD$ arose for some experiments due to the condition $SI = 2^n$ needing to be adhered to, allowing the use of the Fast-Fourier Transformation (FFT) algorithm [Cooley 65]. For example, if $TD = 1.5\text{k} = 1536$ it would lead to $SI = 2 \times TD = 3k = 3074$. However with $2^{10} = 1\text{k}$ and $2^{11} = 4\text{k}$, $SI = 4\text{k}$ needed to be used. Such zero filling with a factor > 2 was common for experiments employing π-decoupling. This was due to *TD* being determined by the maximum acquisition time, as the acquisition time varied with duty-cycle and the dwell time being held constant.

[†]It should be noted that the Bruker parameter *TD* represents the total number of *complex* data points in the FID, i.e. $(TD \times \Re) + (TD \times \Im)$ data points resulting in $2 \times TD$ individual data points in total. Similarly, the parameter *SI* represents the total number of data points making up the real *or* imaginary spectrum.

7.2.5 Apodisation

With the need for high-power heteronuclear dipolar decoupling a prerequisite for resolution in melt-state MAS NMR, FID truncation was common. With the resulting sinc truncation artefacts detrimental to spectral resolution and integration, window functions needed to be applied to the FID prior to Fourier transformation (Section 3.5.1). Due to their decaying nature, such window functions also result in artificial spectral line broadening of the natural T_2^* based line-widths. The rate at which a given window function decays is thus proportional to its line broadening behaviour, and can be controlled by the user. However with further line broadening undesirable, these variables were adjusted on a case-by-case basis. Thus allowing full removal of truncation artefacts with minimum artificial line broadening.

Considering the broad line shapes seen for melt-state MAS NMR of polyolefins, and the desire for the resulting spectra to remain quantitative, two basic window functions were assessed. These were the Bruker implementations of the exponential (Equation 3.83) and Gaussian (Equation 3.84) window-functions, resulting in more Lorentzian (Equation 7.2) and Gaussian-like (Equation 7.3) line shapes respectively.

$$f_E(t) = \exp\left\{\left(-\pi \cdot LB \cdot t\right)\right\} \tag{7.2}$$

$$f_G(t) = \exp\left\{\left(-\pi \cdot LB \cdot t\right) + \left(\frac{\pi \cdot LB \cdot t^2}{2 \cdot GB \cdot \tau_{aq}}\right)\right\} \tag{7.3}$$

The exponential function has a single user defined variable LB, whereas the Gaussian function has two, LB and GB. The variable LB has to be positive for the exponential function $f_E(t)$ and negative for the Gaussian function $f_G(t)$, whereas GB can take any value between 0 and 1. The Gaussian function is also proportional to the length of the FID, i.e. the effective aquisition time τ_{aq}. To assess which window function was generally better for melt-state MAS NMR of polyolefins, a heavily truncated FID was processed using no apodisation and minimal exponential and Gaussian window functions (Figure 7.3).

The removal of all truncation artefacts by use of the exponential window function required relatively large line broadening of $LB = 60$. This resulted in a further increase in width of the already broad 'feet' of the peaks (Table 7.1). The 'foot' of the δ peak became so broad that even distant signals, such as the $\star$ and **2** sites, were no longer resolved to the baseline (Figure 7.3b). The implication of this being inaccurate integration of smaller peaks in the vicinity of the δ peak.

***Table 7.1**: Comparison of signal intensity and resolution achieved for the bulk and branch sites (δ/α) using optimum exponential (E) and Gaussian (G) window functions.*

	SNR	FW-50%-M ppm	FW-5%-M ppm	B_α $10^{-3}C_{bb}$
$f_E(t)$	4000 / 207	0.6 / 0.6	2.4 / 3.3	17.68
$f_G(t)$	3900 / 192	0.4 / 0.4	1.0 / 0.9	14.72

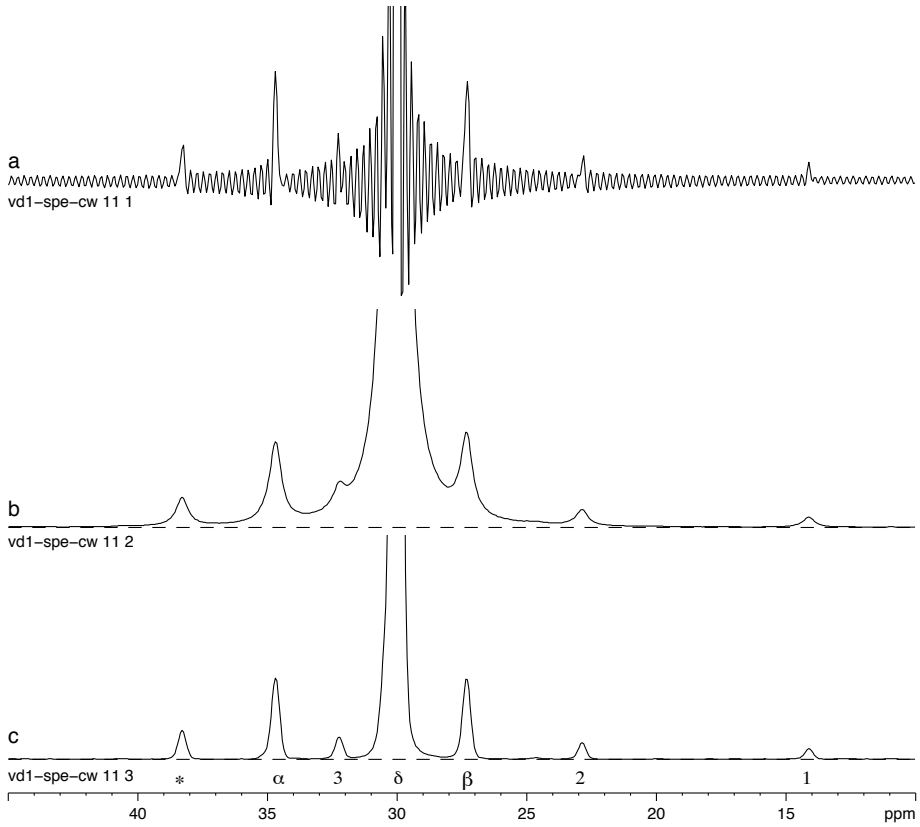

***Figure 7.3**: Comparison of (a) raw non-apodised spectrum of PE8b-C and apodised spectra using the minimum needed (b) exponential (LB = 60) and (c) Gaussian window function (LB = -0.01, GB = 8×10^{-5}). Note: all spectra enlarged to the same degree*

In contrast, the application of the Gaussian window function resulted in less broadening of the 'feet' of the peaks, this being primarily due to the difference between Lorentzian and Gaussian peaks (Figure 3.33). This phenomenon was characterised by a factor 2–3 narrower 'feet' as measured by the full width at 5% of the peak maxima (FW-5%-M) (Table 7.1).

In general Gaussian window functions were chosen to provide the best resolution for melt-state MAS NMR of polyolefins. The parameter *LB* was held constant at -0.01, with *GB* adjusted between 10^{-1} and 10^{-5} depending on the degree of truncation. Of particular importance for polyethylene, the Gaussian window function resulted in greatly enhanced resolution at the base of the δ peak, resulting in the α peak commonly being resolved to the baseline (Figure 7.3c). With truncation related to the acquisition time, and thus to the recycle delay by means of the limits on high-power decoupling, Gaussian window functions were of particular importance at short recycle delays.

7.2.6 Phase correction

Unlike solution-state NMR the use of automated phase correction routines generally failed to achieve satisfactory results for both solid and melt-state spectra. This behaviour is mostly due to the presence of broad spectral line shapes, relatively intense spinning sidebands and general baseline errors. Thus such spectra tend to have less baseline on which to assess the degree by which the baseline needs to be corrected.

For melt-state MAS NMR, even when such automated phase corrections methods showed promise, further manual correction was needed to achieve a phased spectra of acceptable quality. Hence, automated methods provided no advantage over pure manual phase correction. However, manual phase correction was found to be strongly influenced by the user. Different users were found to not only having different criteria for assessing if a spectrum was correctly phased, but more importantly, also had different methodologies for achieving such a state. For example, the number of zeroth order (ϕ_0)/first order (ϕ_1) correction cycles varied between users. Thus, to limit such systematic errors a defined phase correction procedure was implemented:

1. ϕ_0 and ϕ_1 set to zero, FT applied to window-functioned FID.
2. ϕ_0 pivot point set to coincide with approximate maximum of δ peak.[†]
3. ϕ_0 adjusted to achieve symmetric broad 'foot' of the δ peak.[‡]
4. ϕ_1 adjusted to phase a neighbouring well resolved peak (e.g $\star$).
5. ϕ_1 fine-tuned to bring all other peaks into phase.[§]
6. Steps 3–5 repeated until *both* acceptance criteria for 3 *and* 5 met. [¶]

Alternation between zeroth-order and first order phase correction was generally repeated three times to fine tune the phases of all peaks. The use of this protocol was was found to standardise the results of manual phase correction across multiple users with only negligible error remaining.

7.2.7 Baseline correction

With the absolute values of the spectral integrals of key importance for quantitative NMR accurate baseline correction was crucial. As with phase correction, fully-automated baseline correction routines, applied on the whole spectral window, did

[†]Maximum chosen based on visual assessment of ratio of absorptive-to-dispersive line shape.
[‡]Either by assessing line shape or distance between the spectrum and the baseline depending on number of other peaks in the vicinity.
[§]Spinning side-bands not considered as these were generally not in phase with the spectrum.
[¶]That is, symmetric δ peak *and* all other peaks except SSBs in phase.

not provide satisfactory results. However unlike phasing, unacceptably wide variation was seen when manual baseline correction was implemented. In order to provide more reproducible results with automated procedures, the spectral window was trimmed to 50–8 ppm prior to automatic baseline correction. This removed both the first order spinning sidebands of the δ peak and PTFE background signal ($\approx$ 110 ppm), thus allowing more accurate automatic baseline correction.

7.2.8 Spectral integration

The integration procedure was found to be another a major source of error resulting in strong variation between users and samples. The manual choice of integral limits, i.e. the starting and ending chemical shift values, as well as the individual baseline corrections for each integral were found to result in large variation of the final integral values determined by different users. In some cases up to 50% difference was seen. Thus standardisation of the integration procedure was key for the determination of accurate reproducible branch contents.

Semi-automatic integration

A significant improvement in reproducibility was found by the implementation of a semi-automated integration procedure. This procedure was based on the integration limits for each peak being calculated based on the chemical shift of the peak maxima and width. With the full-width at half-maximum (FWHM) of a Gaussian peak equal to 2.35 times the standard-deviation (SD) of the intensity distribution, integral limits were based on the SD of each peak.[†] This resulted in an integral region being defined as 15 standard deviations either side of the peak maximum (Figure 7.4). In the rare cases when spectra contained relevant peaks within 15 SD of a peak, the number of SDs was reduced.

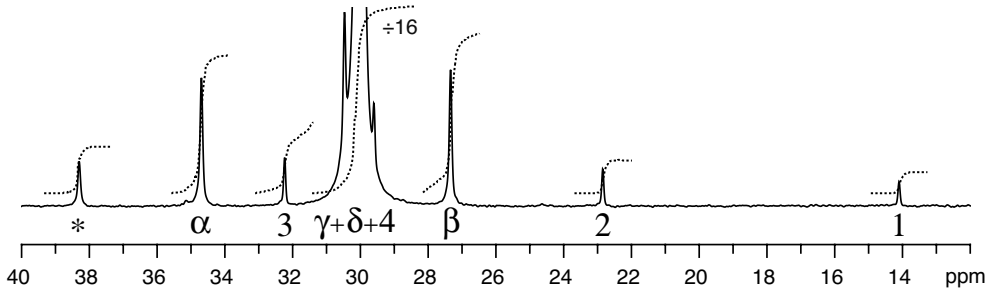

***Figure 7.4**: Illustration of the $\pm$15 SD integration regions, showing the inaccuracy of branch quantification via integrals A_3 and A_β.*

[†]Practically this was implemented using a combination of automation routines outlined in Appendix D.

The broad base of the δ peak however made the choice of an integral region both starting and ending in the spectral baseline impossible. This resulted in the δ integral being governed by the two neighbouring peaks in the spectra (Figure 7.4). The integral region was thus truncated on either side resulting in underestimation of the area of δ (A_{bulk}). This was an inherent limitation of melt-state NMR due to the broader line widths encountered. However, it can be shown that the area of the discarded sections relative to the true area was extremely small, due to the highly intense nature of this peak,[†] and could thus be safely disregarded (Figure 7.5).

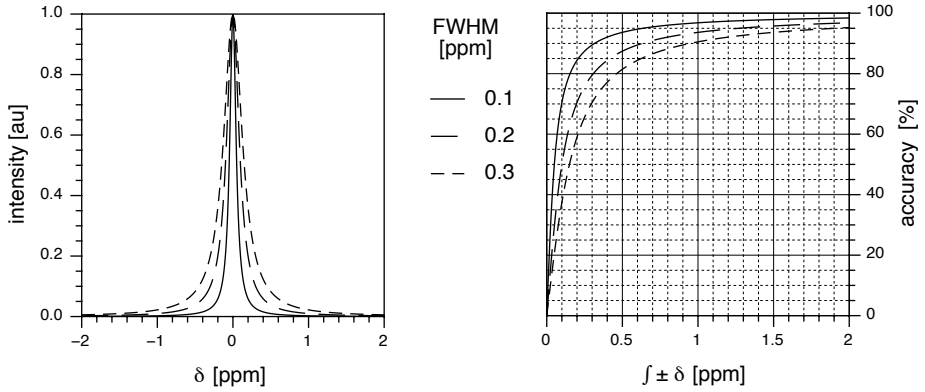

***Figure 7.5**: The percentage accuracy of the integration of a Lorentzian curve with different FWHM when integrated between $\pm\delta$ ppm of the peak maxima.*

For relatively high degrees of branching, e.g. PE-co-α-olefins, semi-automated methods proved sufficient to provide high quality integrals both starting and ending in the baseline of most of the resolved peaks. This allowed for accurate reproducible branch quantification via these sites. In contrast, due to their proximity to the 'foot' of the highly intense δ peak, the integrals of the **3** and β sites were of sufficient quality (Figure 7.4). Hence these integrals were deemed too inaccurate to be used for branch quantification.

Manual integral correction

Where possible, no individual manual baseline correction was applied to the integral in order to provide user-independent integral branch contents. However, for the quantification of very low degrees of branching, e.g. branching in PE homopolymers, such correction sometimes proved necessary. This was because of the lower degrees of branching encountered and thus apparently broader 'foot' of the δ peak. Practically this resulted in both the α and $\star$ sites no longer being fully resolved, and thus integral limits could not be placed in the baseline either side of the peak in question. The resulting integral thus contained both the area of the small peak as well as that of the 'foot' of the δ peak. This led to an overestimation in area of the

[†]By calculation of the percentage accuracy using: $100\% \cdot \frac{\int_{-x}^{+x} f_{(x)}\,\mathrm{d}x}{\int_{-\infty}^{+\infty} f_{(x)}\,\mathrm{d}x}$ where $f_{(x)} = \frac{1}{1+(\frac{2x}{\Delta x})^2}$, x is the chemical-shift and Δx the full-width at half-maximum.

smaller peak and a characteristically deformed integral. Consequently the baseline taken for that particular integral region needed to be manually corrected, ensuring only the area of the small peak contributes to the integral. This was achieved by the application of integral-slope and integral-bias correction resulting in an integral of the correct form (Figure 7.6).

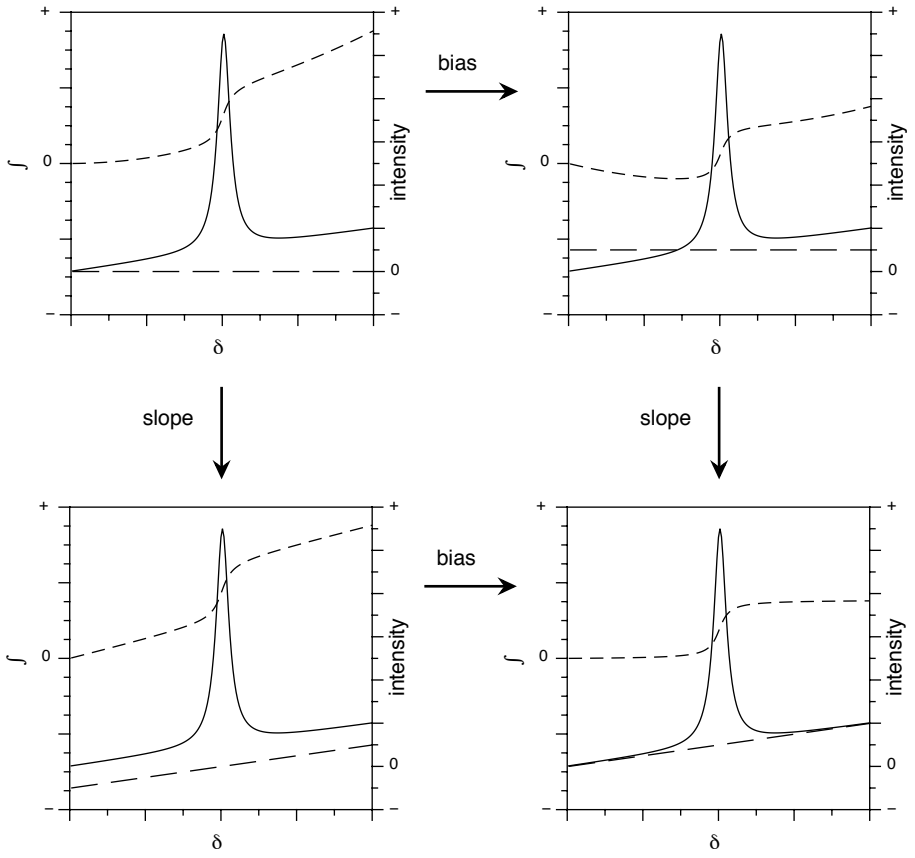

***Figure 7.6**: Illustration of the effects of integral-slope (vertical) and integral-bias (horizontal) on the form and accuracy of the integral.*

Integral-bias correction resulted in a constant being added to the spectrum, and was equivalent to a vertical shift of the baseline. Integral-slope correction resulted in a linear function of constant slope being added to the spectrum, and was equivalent to a pivot of the baseline. Through the choice of appropriate slope and bias correction factors an integral reflecting only the area of the small peak was able to be achieved. However with the choice of such correction factors being highly subjective, reproducibility became problematic (5-6%), especially between users (50–100%). Hence such manual integral correction was avoided whenever possible.

7.2.9 Branch sites used for quantification

With multiple branching sites found in the carbon spectra of polyethylenes, the question of which site to use for quantification was raised. Although β, γ and **2** sites were observed they were not fully resolved, as they lay too close to the δ peak for accurate integration (Figure 7.4). In contrast, although the **1** and **2** sites were resolved, their relatively long spin-lattice relaxation times resulted in these sites being non quantitative (Section 6.3.1). This left only the α and $\star$ sites available for accurate branch quantification. With only a single carbon associated with the $\star$ sites, and three for the α sites, quantification via the area of the α peak was both faster and more accurate for systems with a fully resolved α peak. Thus, wherever possible, branch quantification was undertaken using the α sites.

7.2.10 Calculation of branch content

Initially it might be thought that the simple ratio between the area of a branch site (A_{br}) and that of the bulk backbone sites (A_{bulk}) might result in accurate branch quantification (Equation 7.4).

$$B'_{br} = 1000 \cdot \frac{A_{br}}{A_{bulk}} \quad [10^{-3}\mathrm{CH_2}] \tag{7.4}$$

where $A_{br} = A_\star$ or $\frac{1}{3}A_\alpha$ etc.

However, the accuracy of this value is dependent of the degree of branching itself, with higher degrees of branching resulting in greater inaccuracy (Figure 7.7). This is due to the other branching sites in the backbone, i.e. α, β and γ sites, as well as the δ sites along the branches being neglected.

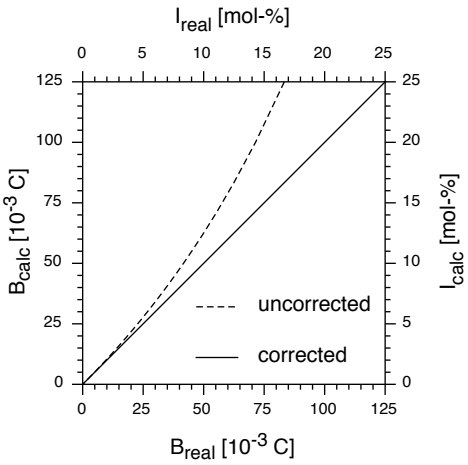

***Figure 7.7**: The deviation of degree of branching determined by Equation 7.4 (uncorrected) and Equation 7.5 (corrected) from the true value B_{real}.*

Such accuracy limitations may, however, be overcome by correcting the denominator in Equation 7.4 for these unaccounted for sites (Equation 7.5). This results in a significant improvement in accuracy (Figure 7.7). The magnitude of the correction is proportional to the chemical structure of the branch. Thus, this correction may only be applied when the type of branch is known, either by its chemical shift of the branching site or by knowledge of the synthetic route.

$$B_{br} = 1000 \cdot \frac{A_{br}}{A_{bulk} + (5 - n_\gamma - n_\delta - n_{\mathbf{4}})A_{br}} \quad [10^{-3}C_{bb}] \tag{7.5}$$

The integral A_{bulk} represents predominantly the δ and γ sites along the backbone, and hence underestimates the true backbone by 5 carbon sites per branch. These carbon sites corresponding to the single $\star$ and two α and β sites missing per branch (Figure 7.8a–b). Thus $5A_{br}$ was added to A_{bulk} (Equation 7.5).

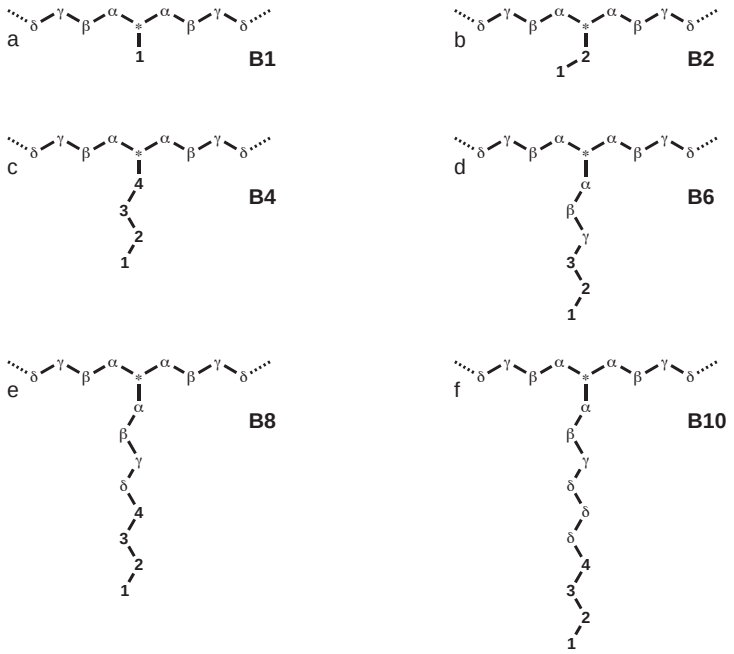

***Figure 7.8**: The general chemical structure of a single branch site in polyethylenes for branches of (a) 1, (b) 2, (c) 4, (d) 6, (e) 8 and (f) 12 carbons in length illustrating the different resolvable sites present.*

As well as the underestimation of the number of carbons in the backbone, some of the sites along the branch also cause an overestimation. For example, for branches containing six carbons or more, e.g. co-octene copolymers, the denominator also needs to be corrected for the **4** and γ sites along the branch (Figure 7.8c–d), as these are included in A_{bulk}. Similarly, for branches containing 7 carbons or more the δ sites located on the branches themselves also need to be considered (Figure 7.8e–f), as these are also included in A_{bulk}. Thus where applicable, the number n of additional γ, δ and **4** sites along the branch also had to be compensated for. This led to $(n_\gamma + n_\delta + n_{\mathbf{4}})A_{br}$ being substracted from A_{bulk} (Equation 7.5), with the respective values of n_γ, n_δ and $n_{\mathbf{4}}$ given in Table 7.2.

***Table 7.2**: The number of γ, δ and **4** sites along the branch present for branches of different lengths.*

branch	comonomer	n_γ	n_δ	$n_{\mathbf{4}}$
B1	propene	0	0	0
B2	1-butene	0	0	0
B4	1-hexene	0	0	0
B6	1-octene	1	0	0
B8	1-decene	1	1	1
B10	1-dodecene	1	3	1
B16	1-octadecene	1	9	1
B24	1-hexacosene	1	17	1

Another advantage of knowing the exact type of branching was that, either the actual or equivalent, percentage of cononomer incorporation (I_{br}) was able to be calculated in mol-% from B_{br} (Equation 7.6).

$$I_{br} = 100\% \cdot 2 \cdot \frac{B_{br}}{1000} \quad \text{[mol-\%]} \tag{7.6}$$

When the exact type of branching is not known Equation 7.5 cannot be used. For such cases only the approximate degree of branching B' (Equation 7.4) may then be given. However, as long as the degree of branching remains low, i.e. sparse branching such as LCB, B' is a good approximation of the true degree of branching B (Figure 7.7). The degree of branching B'_{br} may thus only given as branches per 1000 bulk sites ($10^{-3}CH_2$) and not branches per 1000 backbone sites ($10^{-3}C_{bb}$).

7.3 Statistical appraisal of optimised method

Having established a standard set-up, processing and analysis methodology the reproducibility of the overall optimised melt-state NMR method was investigated. Twenty identical 10 h measurements were undertaken on a high incorporation polyethylene-co-cotene (PE8-C) resulting in series of spectra with $SNR_{\alpha} \approx 520$ and $SNR_{\star} \approx 190$. In order to investigate the reproducibility of the set-up procedures, as well as the experimental and processing procedures, shimming and power-level determination was also undertaken independently for each measurement.

Statistical analysis of the series of spectra showed that the standard deviation (SD) of the SNR varied between 12–14%, depending on the site (Table 7.3). Similarly, the SD of the FWHM of each site varied between 7–11%. In general, the integral values (A_{br}) and more importantly the branch contents calculated from their ratios (B_{br}), showed substantially less variation. The only exception being the values determined from the **3** site, these having a SD of $\approx$ 15% for both A_{br} and B_{br}. This large variation was attributed to the **3** peak being situated in the broad 'foot' of the δ peak. For all other sites the SD of the integral values varied between 0.2–2.2%, and the branch contents between 0.6–2.2%. From Table 7.3 it can also be seen that the least variation in integral intensity was seen for the δ and α sites, with this being reflected in the low variation of the branch contents determined form the α site. It was thus shown that greater reproducibility was achieved through the use of the α site as opposed to the other branching sites available.

***Table 7.3**: Percentage standard deviation of the signal-to-noise ratio (SD_{SNR}), full-width at half-maximum (SD_{FWHM}), area ($SD_{A_{br}}$) and branch content ($SD_{B_{br}}$) of a given site measured after twenty repeat measurements.*

	SD_{SNR} %	SD_{FWHM} %	$SD_{A_{br}}$ %	$SD_{B_{br}}$ %
1	13.4	9.1	1.3	1.1
2	13.0	8.9	1.3	1.2
β	12.1	8.8	2.2	2.2
δ	11.9	6.3	0.2	-
3	12.6	10.8	15.4	15.1
α	12.0	7.2	0.7	0.6
$\star$	12.1	7.7	1.3	1.1

With measurement time directly related to the accuracy of branch quantification, further statistical measurements were undertaken to determine the minimum SNR needed to achieve an acceptable SD of the degree of branching. For a high and low incorporation polethylene-co-α-olefin (PE18-C and PE26-A), twenty spectra were recorded to a predetermined SNR_{α}. After full processing the average signal-to-noise ratio ($\overline{SNR}$) and standard deviation of the branch content, determined using either α or $\star$, were compared (Table 7.4). This showed a strong decrease in reproducibility for branch contents when the $SNR < 10$.

If the criterion for the critical SNR needed for a peak to be used for branch quantification is relaxed to 5, significantly reducing overall measurement time, it should be noted that the calculated integral ratios from such spectra carry an uncertainty of over 30%. This is greater than the expected value of 20% obtained from the inverse of the SNR (Figure 7.9).

***Table 7.4**: Average signal-to-noise ratio ($\overline{SNR}$), average branch content ($\overline{B}$) and standard deviation of branch content (SD_B), for both α and $\star$ sites, after twenty repeat measurements to a predefined signal-to-noise ratio.*

	$\overline{\text{SNR}}_\alpha$	$\overline{B}_\alpha$ $10^{-3}C_{bb}$	SD_{B_α} %	$\overline{\text{SNR}}_\star$	$\overline{B}_\star$ $10^{-3}C_{bb}$	$\text{SD}_{B_\star}$ %
PE26-A	45.4	2.4	2.9	15.3	1.9	7.1
PE26-A	10.4	1.9	8.1	3.3	1.3	49.6
PE26-A	4.4	1.5	33.6	1.8	0.8	201.4
PE18-C	44.7	11.5	2.0	15.4	10.7	7.0
PE18-C	23.7	11.2	5.6	8.3	10.4	16.3

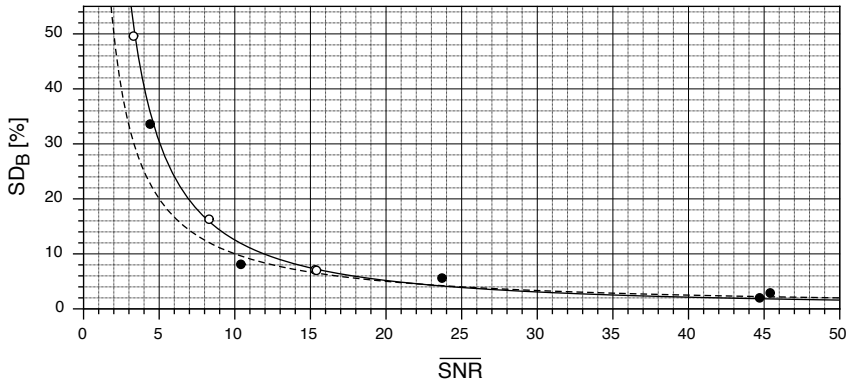

***Figure 7.9**: The standard deviation of branch content (SD_B) determined by both α (filled) and $\star$ (hollow) sites as a function of the average signal-to-noise ratio ($\overline{SNR}$) after twenty repeat measurements. Fit: (solid-line) $SD_B\% = 100\% \cdot 2.38 \cdot \overline{SNR}^{-1.28}$ Expected: (dashed-line) $SD_B\% = 100\% \cdot \overline{SNR}^{-1}$*

7.4 Summary

In this chapter the systematic errors contributing to the measured branch contents were identified. Through the use of standard setup, processing and analysis techniques the influence of these errors were minimised.

Not only were the setup stages of shimming and power-level determination investigated but also the processing and analysis steps of the quantitative method. Concerning the processing, digitised signal cropping, zero-filling, apodisation, phase correction, baseline correction and spectral integration were all investigated. Of these phase correction and integration were found to result in the largest influence on final determined branch contents.

The influence of user-specific phase correction and integral region choice was reduced by the implementation of standard methods. For phase correction, a series of phasing goals were set, with these being achieved in a specific order. This was found to reduce differences in phasing 'style' across users allowing comparison of data.

The manual choice of integral regions and use of individual baseline correction for these regions, i.e. integral-slope and integral-bias, were found to give rise to large variations in branch contents between users. To limit user-dependent branch contents a semi-automated integration procedure proved particularly successful. The semi-automated procedure defined the integral limits based on the full-width at half maximum of the peak in question. Depending on the sample, the relative width of all integrals could then be adjusted simultaneously to ensure each integral region started and ended in the baseline on either side of the peak. The problems associated with full integration of the broad 'foot' of the bulk δ site were investigated and the error introduced found to be negligible.

Accurate analysis of the resulting integral ratios was also investigated and found to be proportional to the overall degree of branch incorporation. These effects were compensated for in polyethylenes of known branch length, allowing calculation of branch contents in branches per backbone carbons as opposed to branches per bulk CH_2.

Repeat measurement and statistical evaluation of the method as a whole showed that the SNR criterion should not be relaxed to below 10, since at this point the standard deviation of the calculated branch content increased to over 30%. The measurement criterion of SNR = 50 was found to ensure a standard deviation of only 2% and was thus deemed preferential.

Chapter 8

Applications of optimised melt-state MAS NMR

Having optimised the experimental conditions (Chapters 4–6), as well as the process of quantitative analysis (Chapter 7), the applicability of melt-state MAS NMR was investigated. This was achieved by applying this method to a wide range of practical problems.

The time efficiency of the optimised melt-state NMR method was tested using a series of model PE-co-α-olefins with moderate to low comonomer contents. The sensitivity toward comonomer distribution was investigated by the analysis of industrial polyethylenes with high comonomer contents.

The general sensitivity increases achieved with the melt-state MAS method also allowed access to a number of experiments previously prohibited by their long experimental times. For example, the carbon spin-lattice relaxation times, T_1^C, were measured and their sensitivity toward the short-chain branch length explored. Similarly, model and commercial polyethylene homopolymers, containing very low levels of branching and sample degradation, were used to explore the lower limit of quantification possible.

Additionally the optimised melt-state MAS method was extended to branch content determination in polypropylenes. The comonomer contents of a number of polypropylene-co-α-olefins were studied. The sensitivity of the melt-state MAS method was again illustrated by implementation of the INADEQUATE ^{13}C–^{13}C double-quantum correlation technique, showing full assignment of a polypropylene-co-α-hexene. A series of γ-irradiated polypropylene homopolymers were also investigated and the degree of LCB estimated.

8.1 Comonomer content

The efficiency of the optimised melt-state MAS NMR method was shown by quantifying the comonomer incorporation in nine polyethylene-co-α-olefins. All samples were measured until the α peak at 34.7 ppm reached the desired signal-to-noise ratio of SNR_α = 50 using an automation routine (Appendix D.1.1). The number of scans and associated measuring time needed to achieve this criterion thus varied depending on the comonomer incorporation (Table 8.1). For the nine samples comonomer contents between 2.2–13.7 branches per 1000 backbone carbons (C_{bb}) were determined. These being equivalent to 0.4–2.9 mol-%. The high sensitivity of the melt-state MAS method was clearly reflected in the total measurement time of 45 min for all nine samples.

***Table 8.1**: Branch quantification of nine model polyethylene-co-α-olefins: number of scans, measuring time, degree of branching (B_α) and comonomer incorporation (I_α).*

	scans [#]			time [min:s]		
	A	B	C	A	B	C
PE8b	68	24	16	3:03	1:27	1:10
PE18	424	48	16	15:57	2:19	1:10
PE26	412	40	28	15:30	2:02	1:36

	B_α [10^{-3} C_{bb}]			I_α [mol-%]		
	A	B	C	A	B	C
PE8b	5.5	9.0	13.7	1.1	1.8	2.7
PE18	2.2	7.7	11.0	0.4	1.5	2.2
PE26	2.3	7.8	11.3	0.5	1.6	2.3

The short measuring times were primarily due to the use of short recycle delays combined with measurement in the bulk state. For PE8b-C, the sample with highest comonomer incorporation, only 16 scans were needed resulting in a measurement time of just over one minute.[†] Standard solution-state NMR measurements required 12 h to achieve an equivalent SNR_α for this sample (Figure 8.1).

Although both solution-state and melt-state SNR_α were equal, SNR_δ for the solution-state was twice that found in the melt-state. However, the areas of the α and δ peaks in the melt-state spectra were typically 3–4 times larger than those found in the solution-state spectra, leading to higher sensitivity. It should also be noted that unlike the solution state, where typically 24 hours were needed in order to achieve a homogeneous solution, sample preparation and set up times for the melt state were considerable less. Typically, only 15-20 min were needed for each sample, with this preparation time including, weighing, melt pressing, rotor packing, shimming and pulse power level determination. Thus due to the sensitive NMR method, the total sample preparation and set up time for each sample was longer than the total measurement time.

[†]It should be noted that for such experiments half of the actual measurement time was take up by dummy scans, allowing measurement of a steady-state. For example, DS=NS=16.

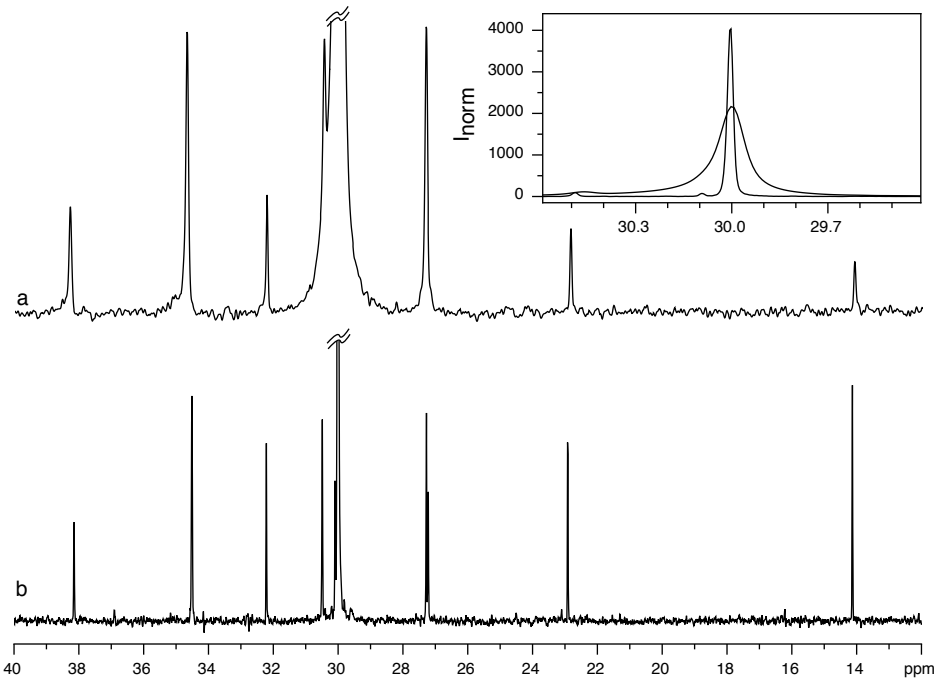

***Figure 8.1**: (a) Melt-state and (b) solution-state SPE spectrum of PE8b-C with $SNR_\alpha \approx 50$, measured in 70 s and 12 h respectively. Enlargement shows comparison of solution-state (narrow) and melt-state (broad) δ peaks illustrating that although SNR_δ is greater in the solution-state (2017:1082) the area of the δ peak (A_δ) is greater in the melt-state (360:111) .*

8.2 Comonomer distribution

With melt-state MAS NMR found to be a highly sensitive the applicability of the method toward comonomer sequences determination in polyethylene copolymers was investigated. For this purpose, two industrial LLDPEs, with high contents of co-butene (PE4b) and co-octene (PE8), were used. As well as standard SPE spectra, comparable INEPT spectra were also acquired for each sample to aid the assignment of the unknown peaks (Figures 8.2 & 8.4). The INEPT method was implemented to distinguish between CH, CH_2 and CH_3 sites by setting τ_2 to be $\frac{3}{8}J_{CH}^{-1}$ seconds in length (Sections 3.4.4 and 6.3.2). This resulted in positive peaks from CH/CH_3 groups and negative peaks from CH_2 groups.[†]

The extra information provided by the INEPT spectra allowed sequences of up to four consecutive monomer units, i.e. tetrads, to be identified in both samples (Figure 8.3). The combination of chemical shift and number of attached protons resulted in the assignment of the majority of the peaks in the SPE spectra (Table 8.2 and Table 8.3).

[†]INEPT spectra are usually phased such that CH_2 groups give positive intensity and CH/CH_3 groups negative intensity. However, due to the very high intensity of the δ CH_2 peak INEPT spectra of polyethylene are presented such that the CH_2 groups result in negative intensity, i.e. ϕ_0 is 180°out of phase.

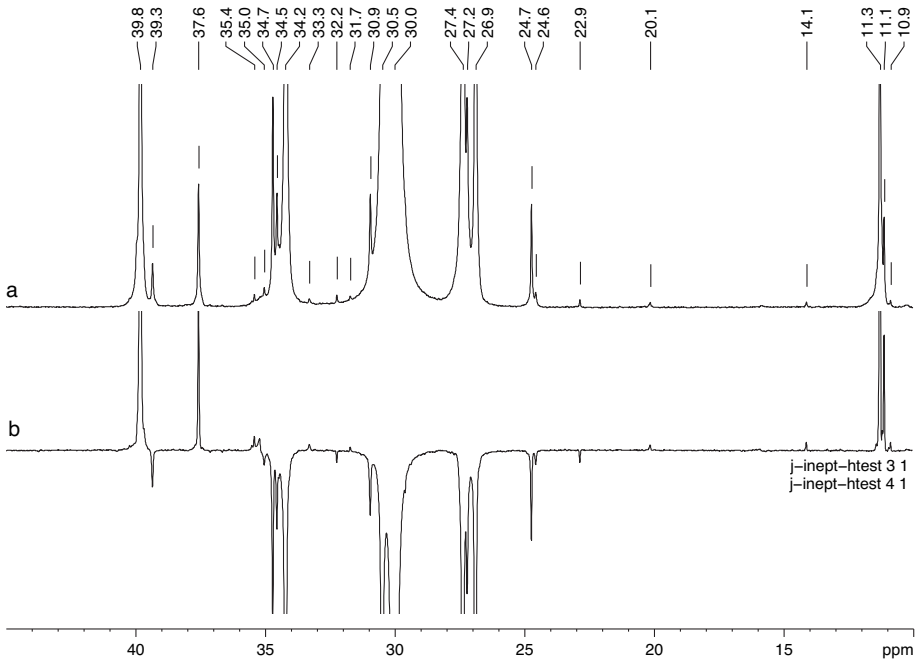

***Figure 8.2**: Comparison of the ^{13}C melt-state MAS (a) SPE and (b) INEPT spectra of PE4b.*

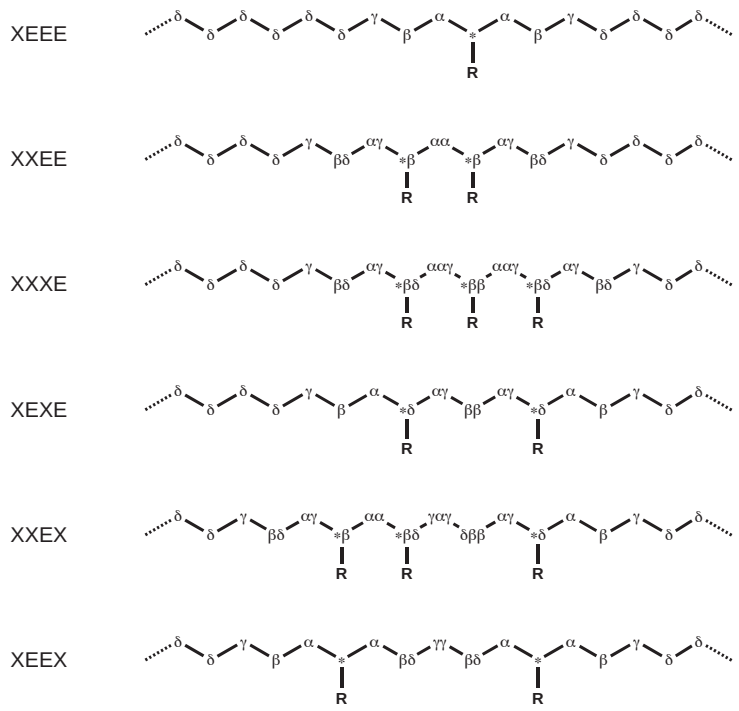

***Figure 8.3**: Chemical structure and site nomenclature (adapted from [Randall 89]) of the comonomer sequences identified in PE4b and PE8. Where X indicates the position of either the butene or octene comonomer.*

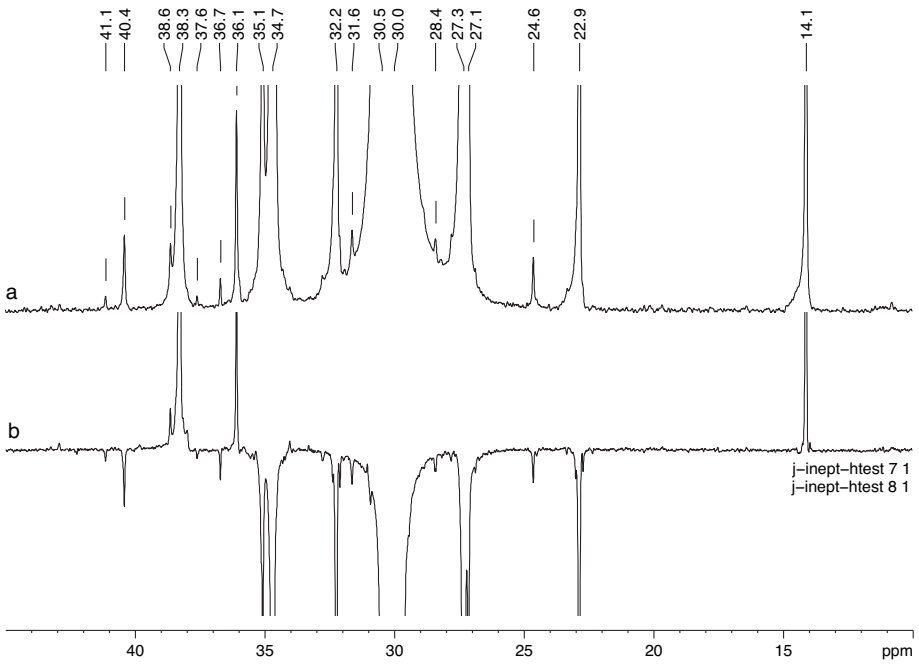

***Figure 8.4**: Comparison of the ^{13}C melt-state MAS (a) SPE and (b) INEPT spectra of PE8.*

***Table 8.2**: Assignment of the SPE spectrum of PE4b.*

ppm	site	sequence
39.8	$\star$B2	**B**EEE
	$\star\delta$B2	BE**B**E
39.3	$\alpha\alpha$B2	**BB**EE
37.6	$\star\beta$B2	B**B**EE
	$\star\beta\delta$B2	BB**B**E
	αB1	**P**EEE
35.4	$\star\beta\beta$B2	B**B**BE
35.0	$\gamma\alpha\gamma$B2	BB**E**B
34.7	$\alpha\gamma$B2	B**E**BE
34.5	$\alpha\gamma$B2	B**BE**E
34.2	αB2	**B**EEE
33.3	$\star$B1	**P**EEE
32.2	**3**	endgroup
31.7	?	
30.9	$\gamma\gamma$B2	B**EE**B
30.5	γB2	B**EE**E
30.0	δ	**EEEE**
27.4	βB2	**BE**EE
27.2	$\beta\delta$B2	B**BE**E
	$\beta\delta$B2	B**E**EB
	βB1	**P**EEE
26.9	2B2	**B**EEE
24.7	$\beta\beta$B2	B**E**BE
24.6	$\delta\beta\beta$B2	BB**E**B
22.9	**2**	endgroup
20.1	1B1	**P**EEE
14.1	**1**	endgroup
11.3	1B2	**B**EEE
11.1	1B2	B**B**EE
10.9	1B2	B**B**BE

***Table 8.3**: Assignment of the SPE spectrum of PE8.*

ppm	site	sequence
41.2	$\alpha\alpha\gamma$B6	O**OO**E
40.4	$\alpha\alpha$B6	**OO**EE
38.7	$\star\delta$B6	**O**EOE
38.3	$\star$B6	**O**EEE
37.6	αB1	**PE**EE
36.7	?	
36.1	$\star\beta$B6	O**O**EE
	$\star\beta\delta$B6	OO**O**E
35.1	$\alpha\gamma$B6	O**OE**E
34.7	αB6	**OE**EE
32.2	3B6	**O**EEE
	3	endgroup
31.6	$\gamma\gamma$B6	O**EE**O
30.5	γB6	O**EE**E
30.0	δ	**EEEE**
28.4	?	
27.3	βB6	**OE**EE
27.1	$\beta\delta$B6	O**OE**E
	$\beta\delta$B6	O**E**EO
24.6	$\beta\beta$B6	O**E**OE
22.9	2B6	**O**EEE
	2	endgroup
14.1	1B6	**O**EEE
	1	endgroup

Although a high degree of assignment was possible quantification remained problematic due to the lack of resolution. For a number of comonomer sequences, however, quantification was achieved using the resolved sites. The equations used to calculate the content for each sequence and comonomer differed from the standard equations used for single incorporation (Section 7.2.10) and are given explicitly in Appendix E.

For the PE4b co-butene system a low content of co-propene, as well as a high content of co-butene, was observed. The exact amount of single incorporation of both co-butene and co-propene was quantified via their $\star$ sites at 39.8 and 33.3 ppm respectively (Table 8.4). The INEPT spectrum showed that the small signal at 39.5 ppm, next to the $\star$B2 peak at 39.8 ppm, was not a CH but a CH_2 group. This was then assigned to the $\alpha\alpha$B2 site of a double incorporation sequence (BBEE) [Randall 89, De Pooter 91, Sahoo 03]. Although the two peaks at 39.8 and 39.5 ppm were only separated by 0.3 ppm individual integration was possible, and thus gave access to the ratio of single to double incorporation (Table 8.4).

***Table 8.4**: Quantification of comonomer sequences found in PE4b.*

sequence	site	chemical shift	content	
		ppm	10^{-3} C_{bb}	mol-%
PEEE	$\star$B1	33.3	0.2	0.04
BEEE	$\star$B2	39.8	47.4	9.48
BBEE	$\alpha\alpha$B2	39.3	7.8	1.56
BBBE	$\star\beta\beta$B2	35.4	0.6	0.12
BEBE	$\beta\beta$B2	24.7	22.1	4.41

The INEPT spectrum also allowed assignment of the signal at 35.4 ppm to the $\star\beta\beta$B2 sites of triple comonomer incorporation sequences (BBBE). However due to the location of this peak, the baseline of the integral needed to be manually adjusted to achieve quantification. The corresponding triple incorporation $\alpha\alpha\gamma$B2 sites, expected at $\approx$ 40.0 ppm, were thought to be hidden in the 'foot' of the $\star$B2 resonance at 39.8 ppm. The peak at 37.6 ppm was found to represent the $\star\beta$B2 sites of double and triple incorporation sequences as well as the single incorporation αB1 sites. Since this peak contained groups of several different comonomer sequences, it could not be used for sequence quantification despite being well resolved. Several non-consecutive comonomer incorporation sequences were also observed. The BEEB sequence was detected via its $\gamma\gamma$B2 site at 30.9 ppm, however due to its position in the 'foot' of the δ peak could not be quantified. The comonomer sequences of BEBE and BBEB were identified by the $\beta\beta$B2 site at 24.7 ppm and the $\beta\beta\delta$B2 site at 24.6 ppm respectively. Due to their lack of resolution, separate integration of these peaks was not possible. With the intensity of the BBEB sequence peak relatively small however, only a minor error was introduced when calculating the total BEBE sequence content using the integral of both $\beta\beta$B2 and $\beta\beta\delta$B2 peaks (Table 8.4).

For the co-octene system, PE8, a high content of co-octene was seen with no other comonomers detected. With the help of the INEPT spectrum, the peaks at 41.2 and 40.4 ppm were assigned to the $\alpha\alpha\gamma$B6 and $\alpha\alpha$B6 sites of triple and double

comonomer incorporation sequences respectively [Randall 89, De Pooter 91, Liu 01]. Both sequences contained $\star\beta$B6 sites at 36.1 ppm, and after manual integral baseline adjustment the resulting total content of double and triple incorporation was in good agreement with the sum of the separately determined values (Table 8.5). The non-consecutive comonomer incorporation sequence OEEO was also detected via its $\gamma\gamma$B6 site at 31.6 ppm, but could not be integrated due to lack of resolution. The OEOE sequence was quantified using the $\beta\beta$B6 site at 24.6 ppm.

***Table 8.5**: Quantification of comonomer sequences found in PE8.*

sequence	site	chemical shift	content	
		ppm	10^{-3} C_{bb}	mol-%
OEEE	$\star$B6	38.3	18.5	3.69
OOEE	$\alpha\alpha$B6	40.4	2.0	0.41
OOOE	$\alpha\alpha\gamma$B6	41.2	0.1	0.02
OOEE + OOOE	$\star\beta$B6 + $\star\beta\delta$B6	36.1	2.3	0.46
OEOE	$\beta\beta$B6	24.6	2.1	0.42

8.3 Comonomer length and NMR relaxation

Due to the high sensitivity, access to time efficient quantification of ^{13}C nuclear relaxation parameters was possible. This allowed the investigation of the influence of branch length on these parameters, and thus possibly providing insight beyond the inherent limits of chemical shift resolution.

8.3.1 The distinction of branch length

For polyethylene melt-state NMR, as well as polyethylene solution-state NMR, resolvable differences in chemical shift only allow the distinction between methyl (B1), ethyl (B2), butyl (B4) and hexyl (B6) branches.[†] Thus branches containing more than six carbons can not be discerned from hexyl branches, since they show the same chemical shifts. For this reason these branches are collectively termed B6$^+$. Because of this, branches with six or more carbons are considered as long-chain branches with respect to NMR spectroscopy. This is in strong contrast to the rheological classification of long-chain branches, where only branches exceeding the entanglement molecular weight are considered as long-chain branches, i.e. B60$^+$.[‡] The question is thus raised if distinction between the various branch lengths present in B6$^+$ branching is possible by NMR.

[†]Distinction between butyl and hexyl branches is achieved using the presence, or lack there of, of the **2**B4 site, as the $\star$ and α sites for both B4 and B6 branches are indistinguishable.

[‡]Considerable confusion is present in the literature regarding the different detection limit based on NMR and rheology classification criteria. Statements of LCB quantification by ^{13}C NMR are frequently encountered with no qualification indicating that only B4$^+$ or B6$^+$ branching was measured, as opposed to B60$^+$ branching as implied.

The use of nuclear relaxation

With chemical shift information having been found to not distinguish between branches of 6 carbons or longer an alternative approach was needed. Studies of polyethylene-copolymers containing comonomers of different lengths have shown that the various branch lengths impart different local segmental mobility [Qiu 00]. Nuclear relaxation phenomena, due to their sensitivity towards local segmental mobility, may thus be used to probe such changes in branch length. The effect of comonomer length on ^{13}C spin-lattice relaxation time has been investigated in both the solution-state [De Pooter 91] and the melt-state [Hatfield 95].† For polyethylene-co-α-olefins ranging from co-propenes to co-octenes, T_1^C was found to stay approximately constant for the backbone branching sites. In contrast, for the terminal branch sites T_1^C increased in an approximately linear fashion with comonomer length (Figure 8.5).

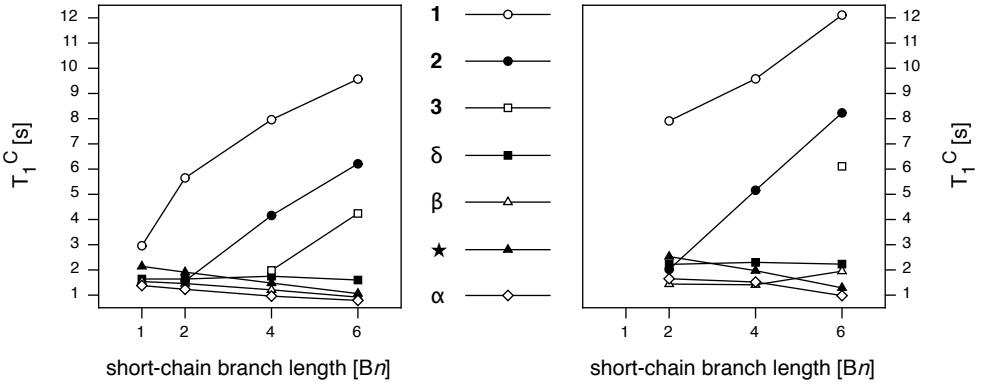

***Figure 8.5**: The trend of T_1^C with increasing comonomer length as determined in the (left) solution-state and (right) melt-state for a series of polyethylene-co-α-olefins, ranging from co-propenes to co-octenes. Adapted from [De Pooter 91, Hatfield 95].*

From these two studies the T_1^C values determined in the melt-state were generally found to be 20–40% higher than those measured in the solution state. However, when considering these T_1^C relaxation times the experimental conditions used need to be considered. While the solution-state measurements were conducted at 130°C, melt-state measurements were undertaken at 200°C [De Pooter 91, Hatfield 95]. Such temperature differences have previously been shown to strongly influence the relaxation behaviour of polyethylene, with longer T_1^C times found at higher temperatures in the solid-state [Qiu 00].

†Two other studies using solution-state NMR were discounted in this section due the low quality of spectra [Axelson 77] and highly speculative deconvolution methods employed [Hansen 97].

8.3.2 Effect of longer branches on nuclear relaxation

Although the effect of branching up to 6 carbons in length (B6) has been studied, the influence of longer branching has not yet been investigated. To address this the T_1^C times of the polyethylene copolymers studied in Section 8.1, as well as two other systems synthesised using the same method and catalyst, were determined. With these systems having commoners ranging from octene to hexacosene, an extension of the previous studies toward longer branch lengths of 8, 10, 16 and 24 was achieved. To increase the accuracy systems with relatively high copolymer contents (1.7–2.7 mol-%) were investigated (Table 8.6).

***Table 8.6**: The polethylene-co-α olefins studied concerning the influence of branch length on T_1^C.*

	comonomer		I	B_α	T_m	T_m+20
		Bn	mol-%	$10^{-3}C_{bb}$	°C	°C
PE8b-C	octene	6	2.7	13.7	112	132
PE10	decene	8	1.7	8.4	116	136
PE12	dodecene	10	1.7	8.4	116	136
PE18-C	octadecene	16	2.2	11.0	116	136
PE26-C	hexacosene	24	2.3	11.3	113	133

With T_1^C proportional to the degree of segmental motion, individual measurement temperatures for each system were used. The sample temperature were set to 20°C above their respective melting points (T_m+20), thus enabling true comparison of determined T_1^C times between systems. Given the small variation in T_m+20 (132–136°C) any error in T_1^C incurred using this method, instead of an average T_m+20 (134.6°C) was considered negligible.

Inversion-recovery measurements at high and low-field

Initially T_1^C times for all resolvable site were measured using the inversion-recovery method at two external magnetic field strengths, corresponding to 300 and 500 MHz proton larmor frequencies. To allow full relaxation of all carbon sites between scans a long recycle delay of 100 s was used. To ensure measurement of steady-state T_1^C,16 dummy scans were applied prior to each set of 64 scans.[†] The combination of these accuracy retaining steps led to long measurement times of up to 30 h per sample. The reproducibility of the determined T_1^C times was assessed by repeating the PE26-C measurement three times. For each site the standard deviation of these three T_1^C times was then used as the uncertainty for all of the samples investigated.

At both high and low-field a similar trend was seen for T_1^C as a function of comonomer length (Figure 8.6a-b), with the main difference being the lower sensitivity at lower field resulting in greater uncertainty (Table 8.7 and Table 8.8). For both external magnetic field strengths the T_1^C of the backbone carbons ($\star$, α, β and δ) were observed to stay approximately constant for all branch lengths, as previously

[†]Dummy scans were applied for each delay increment and not just prior to the start of the experiment as a whole, i.e. before each slice of the pseudo-2D experiment.

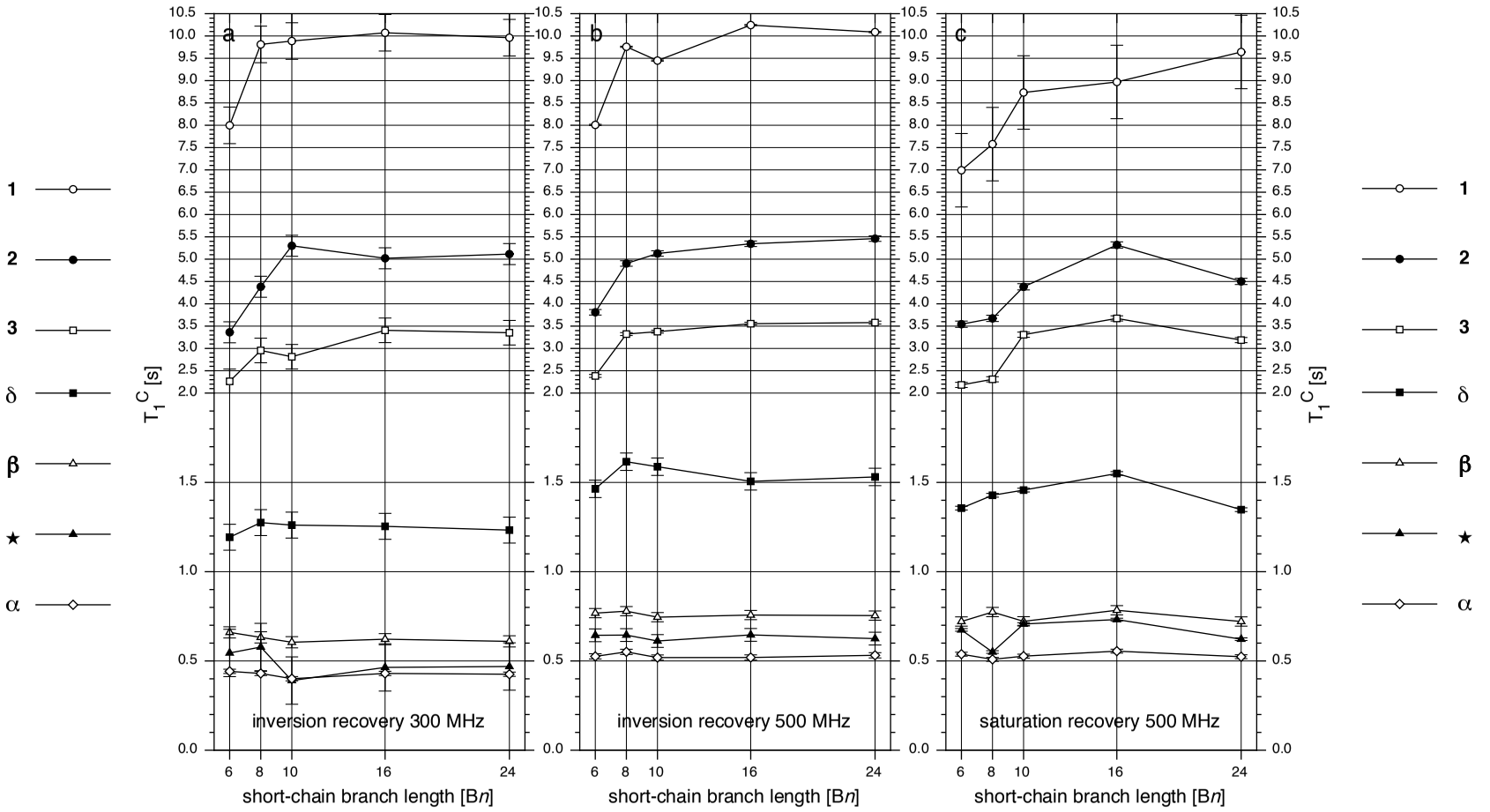

***Figure 8.6**: The trend of ^{13}C spin-lattice relaxation time T_1^C with short-chain branch length, as determined by inversion-recovery method (high and low field) and saturation-recovery (high-field).*

reported [De Pooter 91, Hatfield 95]. However, the T_1^C times of the terminal branch sites (**1**, **2** and **3**) were found to approach a finite limit, with increasing branch length, after an initial increase. For the **2** and **3** terminal branch sites T_1^C increased gradually between B6 and B16, at which point their respective finite T_1^C relaxation times were reached. In contrast, the T_1^C time of the **1** site increased sharply between B6 and B8 with the 'plateau' observed between B8 and B24. The range of T_1^C times for a given terminal branch site was also seen to increase when moving toward the end of the branch. The difference between minimum and maximum T_1^C values being 1, 1.5 and 2 s for the **3**, **2** and **1** sites respectively.

***Table 8.7**: The low-field ^{13}C spin-lattice relaxation times, T_1^C, as a function of branch length determined with inversion-recovery at T_m+20. Reproducibility given as the standard deviation (SD) of three repeat measurements of PE26-C.*

T_1^C [s] 300/IR	B*n*	6 PE8b-C	8 PE10	10 PE12	16 PE18-C	24 PE26-C	SD PE26-C
	$\star$	0.54	0.58	0.39	0.46	0.47	± 0.13
	α	0.44	0.43	0.40	0.43	0.43	± 0.01
	β	0.66	0.63	0.60	0.62	0.61	± 0.03
	δ	1.19	1.28	1.26	1.25	1.23	± 0.07
	3	2.26	2.96	2.81	3.41	3.35	± 0.28
	2	3.36	4.38	5.30	5.02	5.11	± 0.24
	1	8.00	9.81	9.89	10.07	9.96	± 0.41

***Table 8.8**: The high-field ^{13}C spin-lattice relaxation times, T_1^C, as a function of branch length determined with inversion-recovery at T_m+20. Reproducibility given as the standard deviation (SD) of three repeat measurements of PE26-C.*

T_1^C [s] 500/IR	B*n*	6 PE8b-C	8 PE10	10 PE12	16 PE18-C	24 PE26-C	SD PE26-C
	$\star$	0.64	0.65	0.61	0.65	0.63	± 0.04
	α	0.53	0.55	0.52	0.52	0.53	± 0.01
	β	0.77	0.78	0.75	0.76	0.75	± 0.03
	δ	1.46	1.62	1.59	1.51	1.53	± 0.05
	3	2.38	3.32	3.38	3.55	3.58	± 0.03
	2	3.81	4.90	5.13	5.35	5.46	± 0.06
	1	8.01	9.76	9.45	10.24	10.09	± 0.01

With respect to branch length differentiation based on T_1^C relaxation times more promise was seen using the **1** and **2** sites. The origin of the erratic trend seen for the **1** site at high-field however remains unclear despite its relatively high reproducibility (Figure 8.7a). Unfortunately, the low-field data for the **1** site does not provide further insight into this behaviour, due to its relatively high uncertainty.

One possible explanation for the erratic behaviour of the **1** site could be remaining transient NOE, despite the extreme precautions taken to avoid this. This is partially corroborated by the behaviour of the **2** site at high-field (Figure 8.7b), with the **2** site known to be less influenced by NOE interactions than the **1** site. It was thus thought that, although greater differences were seen for the T_1^C times of the **1** site, the use of the **2** site may allow for more accurate characterisation. With respect to the previously published studies [De Pooter 91, Hatfield 95], it has been shown that branch length still influences T_1^C up to branches containing 16 carbons.

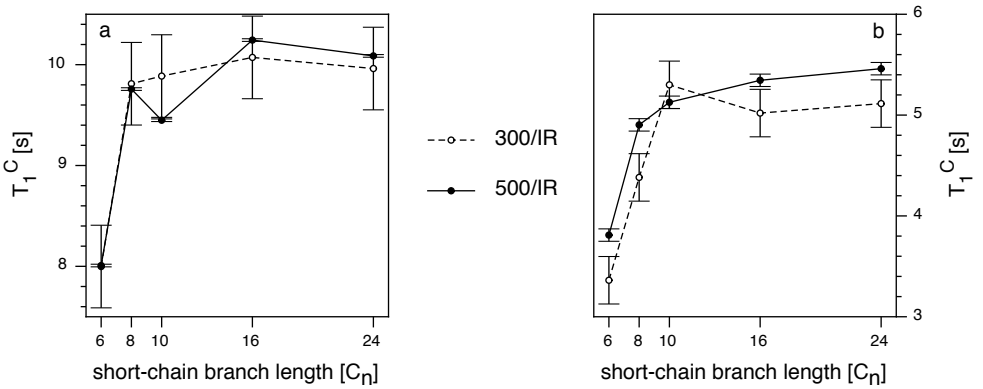

***Figure 8.7**: The trend of ^{13}C spin-lattice relaxation time T_1^C with short-chain branch length for the (a) **1** and (b) **2** terminal branch sites as determined by the inversion-recovery method at 300 and 500 MHz.*

The potential of the saturation-recovery method

With the determination of T_1^C relaxation times via inversion-recovery being highly time consuming, the applicability of saturation-recovery was explored. Due to the pre-saturation, this method does not require all spins to be fully relaxed prior to the commencement of the next scan. Thus for these measurements the recycle delay was able to be reduced from 100 s to 10 s. This allowed T_1^C values to be determined in just 3 h per sample. Although saturation-recovery should provide the same absolute results as inversion-recovary, the relaxation times determined are less accurate. The T_1^C relaxation times measured for the set of polyethylene copolymers using the saturation-recovery method are given in Table 8.9.

***Table 8.9**: High-field ^{13}C spin-lattice relaxation times, T_1^C, as a function of branch length determined with saturation-recovery at T_m+20. Reproducibility given as the standard deviation (SD) of three repeat measurements of PE26-C. Asterisk denotes initial data points deleted to achieve an acceptable fit.*

T_1^C [s] 500/SR	B*n*	6 PE8b-C	8 PE10	10 PE12	16 PE18-C	24 PE26-C	SD PE26-C
	$\star$	0.67	0.55	0.71	0.73	0.62	$\pm$ 0.01
	α	0.54	0.51	0.53	0.56	0.52	$\pm$ 0.01
	β	0.72	0.77	0.72	0.78	0.72	$\pm$ 0.03
	δ	1.36	1.43	1.46	1.55	1.35	$\pm$ 0.01
	3	2.18	2.31	3.31	3.67	3.19	$\pm$ 0.06
	2	3.54	3.67	4.38	5.32	4.50	$\pm$ 0.07
	1	6.99	7.58*	8.73	8.97	9.64	$\pm$ 0.82

For the backbone sites approximately the same T_1^C relaxation times were observed for inversion-recovery and saturation-recovary (Figure 8.6b-c). However for the terminal branch sites, saturation-recovery gave lower T_1^C relaxation times with higher uncertainty. Of even more significance were the maxima in T_1^C seen for the **2**, **3** and δ sites at B16. This different trend in T_1^C with branch length unfortunately puts all T_1^C relaxation times determined by saturation-recovery into question.

8.4 Quantification of sample degradation

The high sensitivity achieved with the optimised melt-state MAS NMR method enabled quantification of low levels of thermal sample degradation in polyethylene (Section 6.2.3). It has previously been shown that the primary oxidation products of polyethylene are mainly hydroperoxides. It is however the further decomposition of these hydroperoxide groups into secondary oxidation products that results in detection. These secondary oxidation products are alcohols, ketones, carboxylic acids and esters, as well as a general increased in the number of methyl and unsaturated groups [Cheng 76, Jelinski 84, Assink 00, Gugumus 02, Al-Malaika 04]. For an extremely temperature sensitive unstabilised model polyethylene homopolymer[†] (PE0c) such secondary oxidation products were able to be detected.

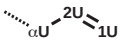

***Figure 8.8**: Unsaturated sites.*

Secondary alcohol groups were identified both directly, using their ⋆C-OH site at 71.9 ppm, and indirectly using their αC-OH and βC-OH sites at 38.3 and 26.0 ppm (Figure 8.9). In contrast, due to their high chemical-shift, ketone groups were only indirectly identified by their αC=O and βC=O sites at 42.8 and 24.3 ppm respectively.[‡] For unsaturated groups (U) both the **1**U and **2**U sites, as well as the αU sites, were detectable at 114.4, 138.9 and 33.9 ppm respectively (Figure 8.8). The broad resonance seen at 108.7 ppm originates from the C-F sites, these occurring mainly in the PTFE tape used for rotor packing as well as the fluoropolymers within the probehead.[§]

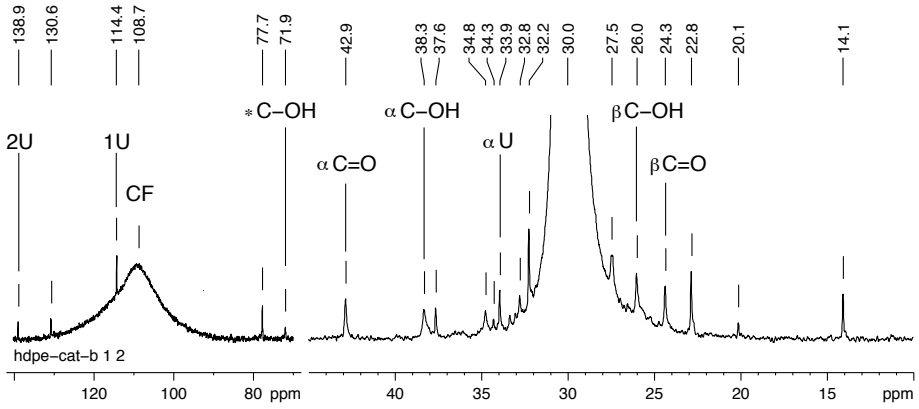

***Figure 8.9**: Melt-state NMR spectrum of an unstabilised model polyethylene homopolymer (PE0c) showing signs of thermal degradation.*

The presence of thermal oxidation, as well as proof that it had occurred during melt-state MAS under an inert atmosphere, was confirmed by attenuated total reflection (ATR) IR spectroscopy (Figure 8.10). The IR spectrum taken after the NMR measurement revealed that the degradation process produced not only carbonyl (1743 cm^{-1}), hydroxyl (3340 cm^{-1}) and unsaturated groups (822 cm^{-1}), but also methyl groups (1371 cm^{-1}) [Luongo 60]. From the NMR spectra the content of secondary alcohol and ketone groups was able to be quantified, however manual integral baseline correction was needed. Good agreement was found between

[†]Rheologial measurement, even with the addition of stabilisers, also showed that degradation was highly likely even in an N_2 inert atmosphere.

[‡]The spectral window could be extended using a smaller dwell-time, however this would result in a loss in resolution of the main spectral region between 10–40 ppm.

[§]Signal mainly results from C-F groups *within* the rotor as these experience the line narrowing effects of MAS. In contrast, the static groups generally result in an extremely broad signal of similar chemical-shift.

the various sites used for quantification of each secondary oxidation product (Table 8.10). Melt-state MAS NMR quantified all thermal degradation products to be present in concentrations of ≈ 20 groups per 100,000 CH_2.

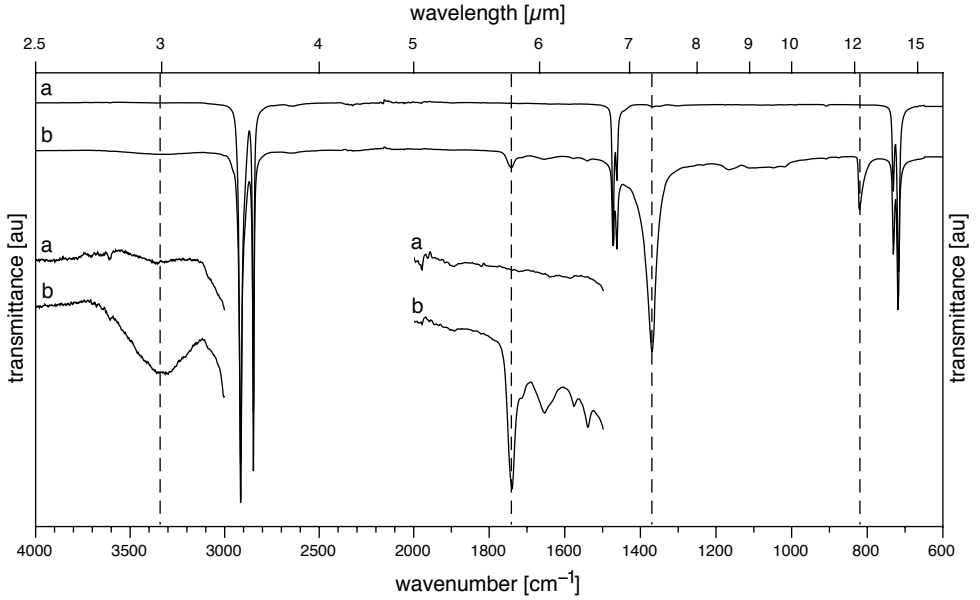

***Figure 8.10**: Comparison of the FTIR spectra of an unstabilised HDPE sample (PE0c) (a) before and (b) after NMR measurements at 150°C for 18.5 hours. Additional signals apear post NMR at: 3340 (O-H), 1743 (C=O), 1371 (CH_3) and 822 (C=C) cm^{-1}.*

***Table 8.10**: NMR Assignment and quantification of the secondary degradation products present in the unstabilised model polyethylene homopolymer PE0c.*

	assignment		content
group	site	ppm	10^{-5} CH_2
C=O	αC=O	42.8	19
	βC=O	24.3	17
C-OH	$\star$C-OH	71.9	18
	αC-OH	38.3	19
	βC-OH	26.0	18

8.5 Quantification of very low branch contents

To illustrate the sensitivity of the optimised melt-state MAS method very low branch concentrations were quantified in an industrial polyethylene homopolymer (PE0b). Due to the inclusion of stabilisers during the industrial pelletisation stage extended measurement was possible on this system. Three forms of branching were observed in very low concentrations after 21k scans with τ_{rd}= 2 s (13 h) (Figure 8.11). These consisted of branches with two (B2), four (B4) and five or more ($B5^+$) carbons per branch. As well as these branch sites, unsaturated groups were also detected by their adjacent CH_2 sites (αU) at 33.9 ppm.

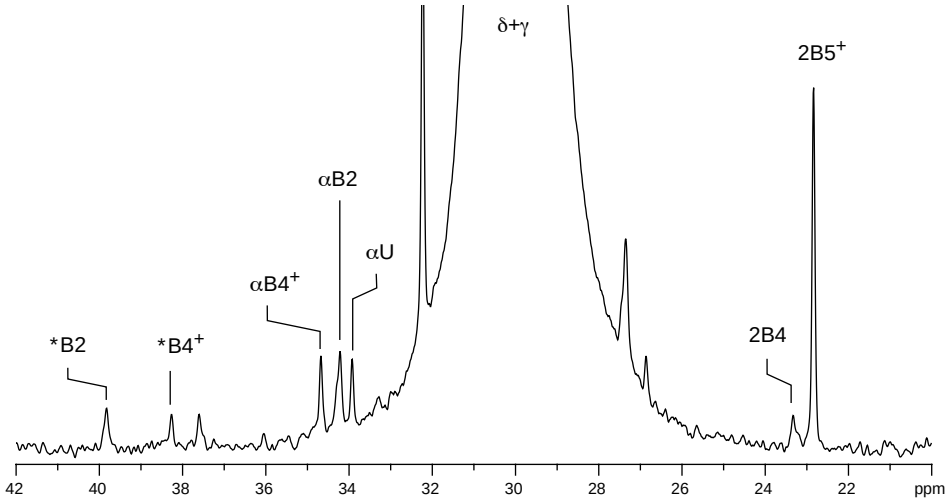

***Figure 8.11**: Melt-state SPE spectrum of PE0b showing 7 ethyl and 5–8 butyl or longer branches per 100,000 CH_2. Measurement undertaken at ν_{1_H} = 500 MHz, τ_{rd}= 2 s using 21k scans corresponding to 12 h 55 min of continuous measurement.*

The B2 branches were quantified via the ⋆B2 site seen at 39.8 ppm (SNR = 4.5), and were found at a concentration of 7 ethyl branches per 100,000 CH_2. With the chemical shifts of the ⋆ and α sites of B4 and B5$^+$ branches indistinguishable, only combined quantification of both B4 and B5$^+$ branching was possible. These branches being collectively termed B4$^+$. When B4$^+$ branches were quantified by the ⋆B4 peak at 38.3 ppm (SNR$_\star$ = 3.7) branch concentrations of 5 butyl or longer branches per 100,000 CH_2 were determined. By comparison, using the αB4 peak at 34.7 ppm, and accounting for the broad 'foot' of the δ peak, branch concentrations of 8 butyl or longer branches per 100,000 CH_2 were determined at a SNR$_\alpha$ of 9.4. With SNR$_\alpha$ > SNR$_\star$ quantification via α was considered more accurate, however error will no-doubt have been introduced by the manual integral baseline correction needed to account for the δ peak. As well as the absolution concentrations, the distribution of B4 and B5$^+$ branching within B4$^+$ was estimated as ≈ 11% B4 via the ratio of 2B4 and 2B5$^+$ sites at 23.3 and 22.8 ppm respectively. It should be reiterated that absolute quantification via these terminal branch sites was not possible due to the short recycle delay used.

8.6 Extension to polypropylene-co-α-olefins

The potential of the optimised melt-state MAS NMR method towards analysis of other polyolefins was demonstrated for two isotactic polypropylene-co-hexenes (PP6-A and PP6-B). To facilitate melt-state MAS analysis of these systems the MAS rotational frequency was increased from 3 kHz to 4 kHz, thus avoiding overlap of spinning-sidebands with the spectral region of interest (Figure 8.12). Due to the the changes in MAS bearing and drive gas pressure needed for the higher MAS

rotational frequency, separate temperature calibration was carried out for this MAS setup (Appendix B).

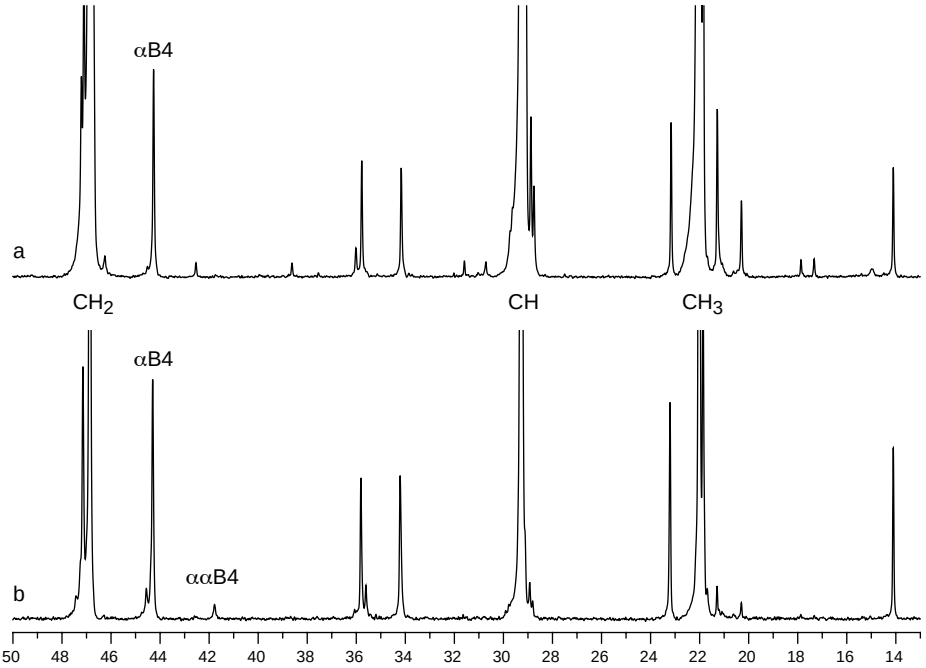

***Figure 8.12**: Melt-state SPE spectra of (a) PP6-A and (b) PP6-B undertaken at ν_{1_H} = 500 MHz, $\omega_r/2\pi = 4$ kHz, τ_{rd}= 4 s, τ_{aq}= 272 ms using 3200 and 280 scans respectively.*

Comonomer incorporation was quantified via the relative intensity of the αB4 and bulk CH_2 sites at 44.3 and 46.8 ppm respectively (Figure 8.12). As both these sites were found to have T_1^C relaxation times of 400 and 700 ms respectively, fully quantitative spectra were recorded with recycle delays of 4 s.

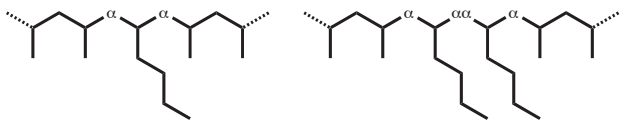

***Figure 8.13**: Assignment of carbons for single and double cohexene incorporation.*

Comonomer incorporations of 1.7 and 10.3 mol-% were determined for PP6-A and PP6-B respectively, with a $SNR_{\alpha B4} \approx 180$ using 3200 and 280 scans (3 h 48 min and 20 min) respectively. For PP6-B consecutive comonomer incorporation was also quantified at ≈ 1 mol-% using the $\alpha\alpha$B4 site at 41.8 ppm ($SNR_{\alpha\alpha B4} \approx 10$) (Figure 8.13). When related to the degree of comonomer incorporation, the degree of consecutive incorporation suggested a statistical distribution of comonomer within the copolymer.

8.7 Melt-state DQ correlation spectroscopy

The sensitivity of the melt-state MAS method was further illustrated by 2D incredible natural abundance double-quantum transfer experiments (INADEQUATE) [Bax 80, Bax 81]. Full ^{13}C connectivity was shown for both polyethylene and polypropylene by the generation of double quantum coherence (DQC) mediated by the homonuclear J-coupling interaction. If ^{13}C is present in natural abundance (1.07%), and the DQCs only form between two directly bonded ^{13}C nuclei, the likelihood of such ^{13}C–^{13}C pairs is only 0.01%, or 10 per 100,000 carbons.

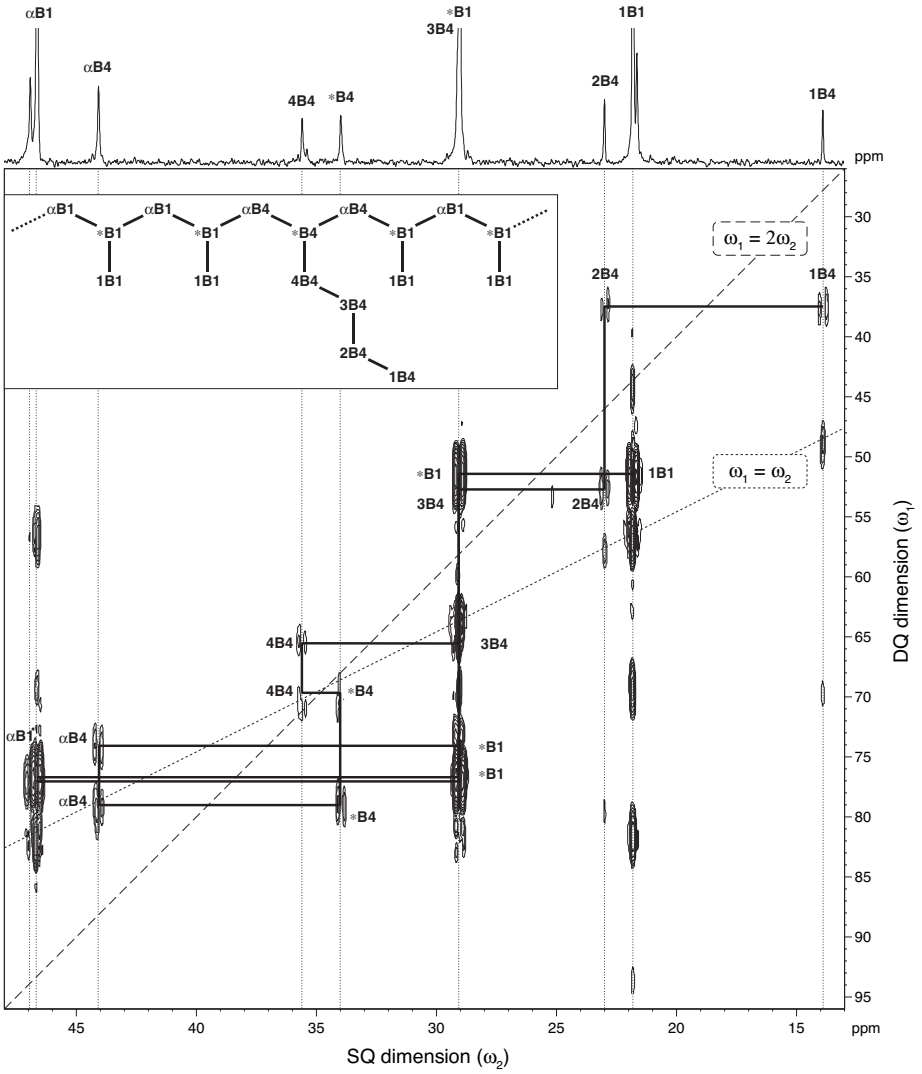

Figure 8.14: 2D-INADEQUATE spectrum of PP6-B, with (top) ^{13}C SPE spectrum and (insert) nomenclature. Due to incomplete singlet suppression single-quantum (SQ) auto-correlation of bulk peaks also seen at $\omega_1 = \omega_2$. Total measurement time 24 hours, using τ_{rd} = 2 s, τ_{aq} = 273 ms, 256 scans and 148 increments in the indirect dimension. Note: sine-bell window functions (SSB=1) used for both dimensions to increase resolution.

For the polypropylene-co-hexene PP6-B full correlation along the backbone and branch was clearly seen (Figure 8.14). Due to the highly intense nature of the bulk

αB1, $\star$B1 and **1**B1 sites in polypropylene full suppression of the singlets, leaving only the coupled ^{13}C doublets, was not achieved. This resulted in a 'break-through' of these signals and their corresponding single-quantum (SQ) auto-correlation peaks along $\omega_1 = \omega_2$. Full singlet suppression was found to be far more difficult for polyethylene, due to the single highly intense bulk δ site. In general, satisfactory results for polyethylene with ^{13}C present in natural abundance were not achieved. However full correlation relating to end-groups and ethyl branches, with the exception of the $\star$B2-**2**B2 DQC, was seen for a 4% ^{13}C double-labelled polyethylene[†] (Figure 8.15). Although spectra of samples with ^{13}C present in natural abundance were prone to artefacts, the potential of this technique for structure elucidation of molten polyolefin systems was demonstrated.

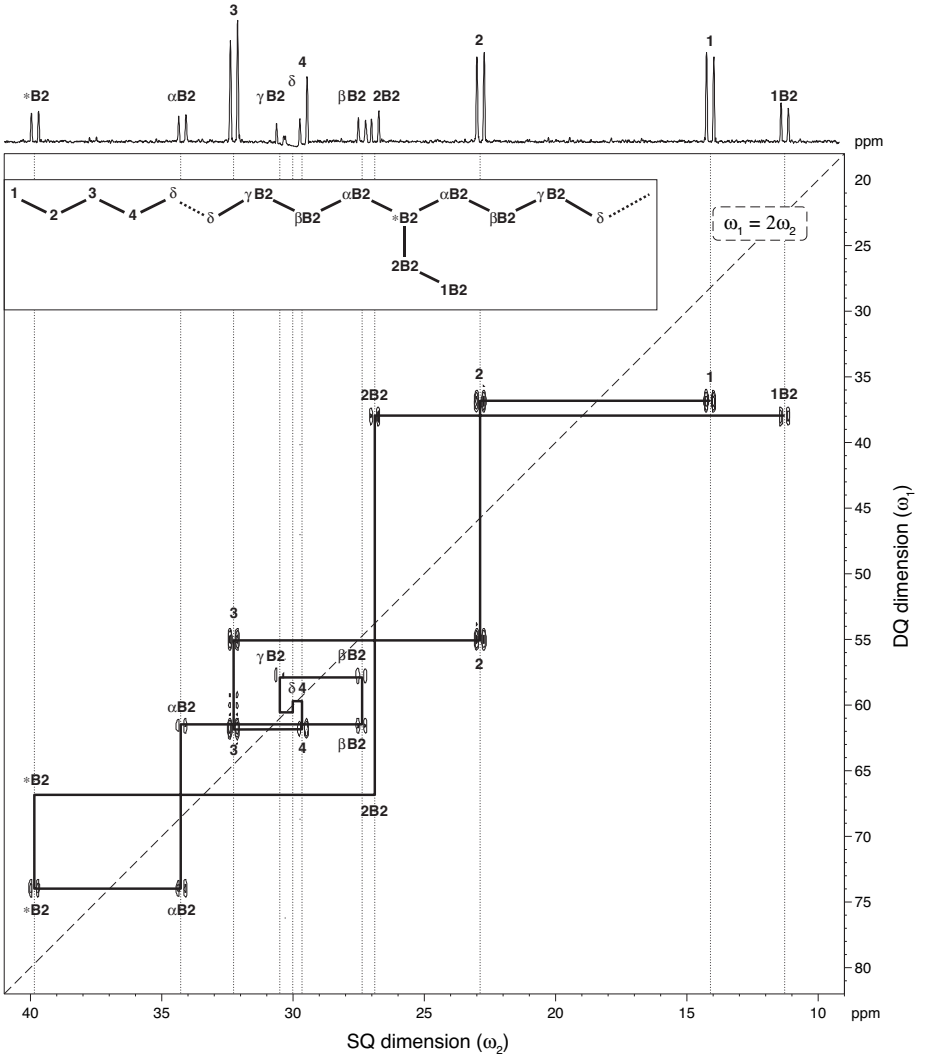

***Figure 8.15**: 2D-INADEQUATE spectrum of ^{13}C labelled polyethylene with (top) SQ projection and (insert) nomenclature. Total measurement time 6 hours, using τ_{rd} = 2 s, τ_{aq} = 273 ms, 64 scans and 148 increments in the indirect dimension. Singlet 'break-through' at ω_1=30 was suppressed during processing [Marion 89].(See Appendix* A *Figure* A.1 *for raw spectrum.) Note: sine-bell window functions (SSB=1) used for both dimensions.*

[†] M_n = 19 kg mol^{-1}, M_w = 58 kg mol^{-1} $PDI = 3.1$

8.8 Quantification of LCB in polypropylene

Although quantification by NMR of rhelologically active LCB is highly problematic for polyethylenes (Section 8.3.1), more success was found with LCB in polypropylene [Busfield 87, Busfield 91, Mowery 05].

Unlike polyethylene the formation of LCB in polypropylene is not commonly achieved through catalyst activity, during the initial polymerisation reaction.[†] Post-processing is the most common method of inducing LCB in PP. Long-chaing branching may be induced by either irradiation (e^- or γ) [Busfield 87, Busfield 91, Auhl 04, Mowery 05] or reactive extrusion with peroxides [Lagendijk 01], both inducing chain scission and recombination through a variety of radical reactions.

The applicability of melt-state MAS NMR toward quantification of LCB was tested using a series of γ-irradiated polypropylenes. This series consisted of a single batch of a commercial polypropylene that was subjected to 60, 100 and 150 kGy of γ-irradiation (PP-γ-60, PP-γ-100, PP-γ-150). The irradiated samples were then compared to the control unirradiated sample PP-γ-0. Rheological measurements had shown that PP-γ-0 did not contain LCB while the the degree of LCB for the irradiated samples increased with the irradiation dose [Auhl 05]. Similar behaviour with irradiation was seen by SEC-MALLS [Auhl 05].

The melt-state ^{13}C NMR spectra of all 4 samples showed the typical sites of an isotactic polypropylene containing isolated ethylene units.[‡] The main bulk CH_2, CH and CH_3 sites ($\star$B1, αB1, **1**B1) were seen at 46.6, 29.0 and 21.8 ppm respectively while the majority of the neighbouring lower intensity peaks resulted from the isolated ethylene units, as well as stereo and regio-irregularities. The $\beta\beta$B1, $\alpha\gamma$B1, $\delta\star$B1 and $\epsilon\alpha$B1 sites, arising from isolated ethylene units (Figure 8.16), are clearly visible in the spectrum of PP-γ-0 at 24.2, 37.8, 30.9 and 46.1 ppm respectively (Figure 8.17).

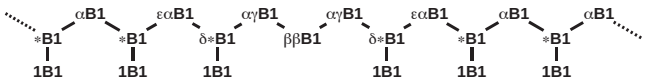

***Figure 8.16**: Nomenclature of the isolated ethylene units and their surrounding propylene units.*

Upon enlargement several additional low intensity peaks were observed in the spectra of the irradiated samples (Figure 8.18). These additional peaks were thought to originate from end groups and LCB, formed by the various radical processes (Figure 8.19).

[†]Recently new metallocene catalysts have been found to incorporate LCB into PP during polymerisation [Shiono 99, Weng 02].

[‡]Quantification via the integral ratio of $\beta\beta$B1 and αB1 sites resulted in an incorporation of ≈ 0.5 mol-%. However, it is unclear whether this system is actually a copolymer or if the ethylene units resulted from processing additives.

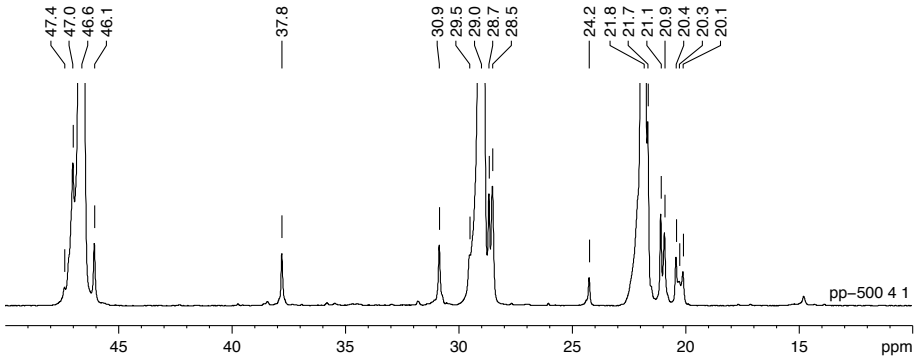

Figure 8.17: *Melt-state MAS NMR spectrum of PP-γ-0 showing the bulk polypropylene sites, isolated ethylene incorperation sites and stereo- and regio-irregularities.*

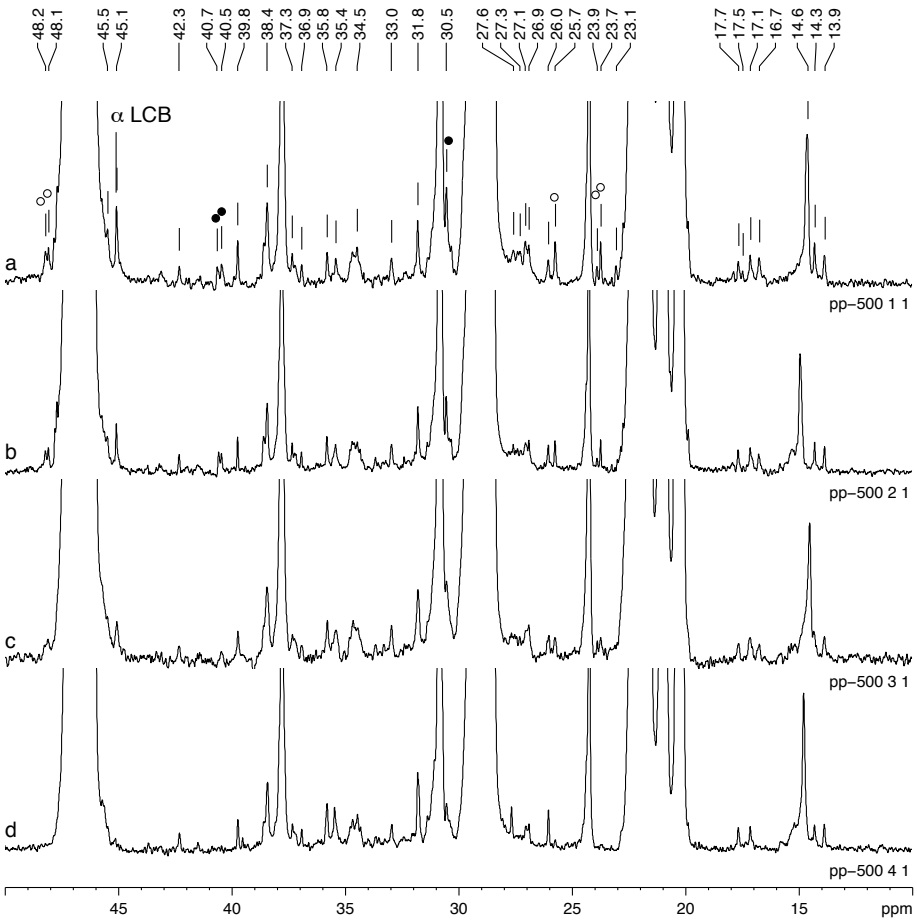

Figure 8.18: *Comparison of the enlarged optimised melt-state MAS NMR spectra of (a) PP-γ-150, (b) PP-γ-100, (c) PP-γ-60 and (d) PP-γ-0. Symbols mark the isopropyl (open circles) and propyl (full circles) end groups caused by irradiation.*

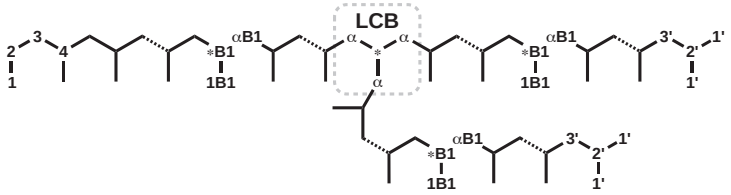

***Figure 8.19**: Structure and nomenclature for the carbons of the propyl (**1**, **2**, **3**, **4**) and isopropyl (**1′**, **2′**, **3′**) end groups as well as the LCB branch point (αLCB, ⋆LCB) formed upon irradiation.*

The two end-group types (Figure 8.19) were found at increased concentrations in the γ-irradiated samples (Table 8.11). For the isopropyl end groups (open circles in Figure 8.18) all three carbon sites, **1**, **2** and **3** were detected [Busfield 91]. In contrast, only the **3′** and **4′** sites of the propyl end groups (full circles in Figure 8.18) were visible, with the **1′** and **2′** sites obscured by neighbouring peaks. It should be noted that two peaks were observed for the **1**, **3** and **3′** sites because of their sensitivity towards configurational sequence differences of the monomer units adjacent to the end groups [Busfield 91].

The small peak at 45.1 ppm corresponded to the three sites adjacent (αLCB) to the LCB branch point (⋆LCB), with peaks between 44–45 ppm having previously been assigned by solution-state NMR [Shiono 99, Weng 02, Ye 03].[†] Unfortunately the ⋆LCB site itself, expected at $\approx$ 31.7 ppm, was obscured by a neighbouring peak and could not be used to confirm the assignment of the αLCB site.

***Table 8.11**: Assignment of the additional peaks seen only in the irradiated samples corresponding to the end-group and branching sites formed upon irradiation.*

chemical shift	assignment	
ppm	group	site
48.2	isopropyl end-group	**3′**
48.1	isopropyl end-group	**3′**
45.1	long-chain branching	αLCB
40.6	propyl end-group	**3**
40.5	propyl end-group	**3**
30.5	propyl end-group	**4**
25.8	isopropyl end-group	**2′**
23.9	isopropyl end-group	**1′**
23.7	isopropyl end-group	**1′**

The degree of LCB (B_{LCB}) was quantified using the integral ratio of the αLCB and αB1 sites, with αLCB representing three carbons per branch and αB1 used to calculate the total number of carbons per chain (Equation 8.1). The contribution of the branching and end-group sites (A_{other}) to the total number of carbons was not considered, however, when taking the low degree of branching into account, the error introduced by this approximation was thought to be negligible.

$$B_{LCB} = \frac{A_{LCB}}{A_{all}} = \frac{\frac{1}{3} \cdot A_{\alpha LCB}}{(3 \cdot A_{\alpha B1}) + A_{other}} \approx 100,000 \cdot \frac{A_{\alpha LCB}}{9 \cdot A_{\alpha B1}} \quad [10^{-5}\mathrm{C}] \tag{8.1}$$

[†]Absolute comparison of chemical shift values of polypropylene is problematic due to solvent susceptibility and the γ-gauche effects [Busico 01]. Differences of up to 5 ppm have been observed between melt-state and solution state spectra of the same material [Parkinson 04]

Due to the position of the αLCB peak in the 'foot' of the bulk CH_2 (αB1) peak (Figure 8.20), both the integration region and integral baseline needed to be manually chosen. To reduce the error introduced by this integration procedure the degree of LCB was determined ten times, adjusting the manual parameters each time, and the average taken. The standard deviation of the determined degree of LCB was calculated to be between 5.3–5.7%. As a control for this method of quantification similar analysis of the unirradiated sample (PP-γ-0) was also undertaken. Although no LCB could be detected by rheology, a degree of LCB was still obtained from NMR using Equation 8.1 due to the noise and associated finite nature of the integrals. This was then used as the maximum error for this method for all samples (Table 8.12). It should be noted that although a finite degree of branching was determined for the unirradiated sample, over the ten measurements a higher standard deviation of 15.5% was obtained reflecting the random nature of the determined value.

From the melt-state NMR results the determined degree of LCB was seen to increase with γ-irradiation dose (Figure 8.21), confirming the rheology and SEC-MALLS data.

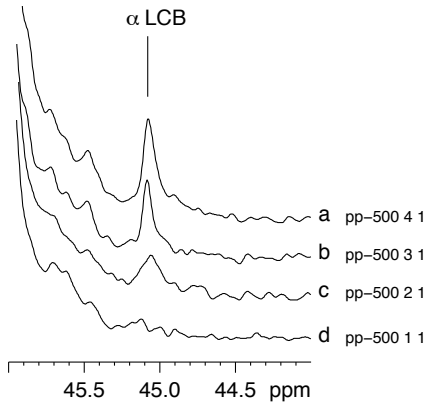

***Figure 8.20**: Enlargement of the α-LCB peak at 45.1 ppm illustrating its growing intensity with γ-irradiation dose of (a) 150, (b) 100, (c) 60 and (d) 0 kGy.*

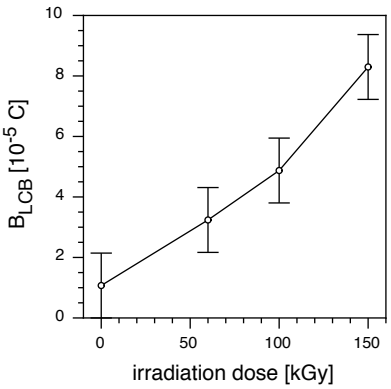

***Figure 8.21**: The trend of determined degree of LCB (B_{LCB}) in polypropylene with γ-irradiation dose. Error bars based on B_{LCB} of the unirradiated control sample.*

***Table 8.12**: Determined degree of polypropylene LCB assuming the peak at 45.1 ppm represents 3 α carbons.*

	γ	B_{LCB}	error	SD
	kGy	10^{-5}C	$\pm$	%
PP-γ-0	-	1	1	15.5
PP-γ-60	60	3	1	5.3
PP-γ-100	100	5	1	5.3
PP-γ-150	150	8	1	5.7

8.9 Summary

In this chapter optimised melt-state MAS NMR was shown to be applicable to a wide range of practical problems.

Time efficient quantification of comonomer content was demonstrated for a series of nine model polyethylene copolymers. In contrast to the available solution-state NMR data, where each sample was measured for 12 hours, the comonomer incorporation of all nine samples was determined in only 45 minutes. For industrial polyethylenes, with high comonomer contents, comonomer sequences up to the tetrad level were detected and quantified. Despite the lower resolution in the melt-state, both consecutive and non-consecutive comonomer sequences were able to be quantified.

A clear trend of carbon spin-lattice relaxation times, T_1^C, with short-chain branch length was shown for branches between 6–24 carbons in length. For the **1** and **2** terminal branch sites T_1^C times clearly increased with branch length. Although greater absolute differences were seen for the **1** site, the **2** site was deemed more suited for branch length characterisation.

The formation of thermal oxidation products during melt-state NMR was further investigated using an unstabilised, highly temperature-sensitive, polyethylene homopolymer. Comparison of IR spectra before and after NMR confirmed that thermal oxidation had occurred during the NMR measurement, even when conducted in an inert atmosphere. However, when the oxidation products were assigned and quantified by NMR they were found to be present in concentrations of only ≈ 20 groups per 100,000 CH_2. The sensitivity of the technique was further demonstrated by the quantification of sparse branching in a stabilised polyethylene homopolymer. Branch contents as low as 8 branches per 100,000 CH_2 were quantified in under 13 hours, with a reproducibility of $\approx 10\%$.

The melt-state MAS NMR method was also shown to be applicable to branch content determination in polypropylenes. The degree of SCB was determined for a number of polypropylene-co-α-olefins, with both single and double comonomer incorporation able to be quantified. The high sensitivity also allowed access to INADEQUATE ^{13}C–^{13}C double-quantum correlation spectroscopy, enabling full assignment of the polyolefins. More so, for a series of γ-irradiated polypropylenes the degree of LCB was able to be estimated. The determined degree of LCB ranged from 3–8 long-chain branches per 100,000 carbons depending on the irradiation dose.

In general, the optimised melt-state MAS NMR method was found to be a highly versatile tool for the characterisation of a wide variety of polyolefins. Common spectroscopic problems were found to be easily addressed with the technique, requiring only minor adjustments to standard solution-state and solid-state methods.

Chapter 9

Summary & Outlook

Solid-state NMR was initially investigated regarding time efficient branch determination in polyolefins [Pollard 04]. It was, however, not found to be a viable alternative to solution-state NMR due to low spectral resolution (Figure 9.1).

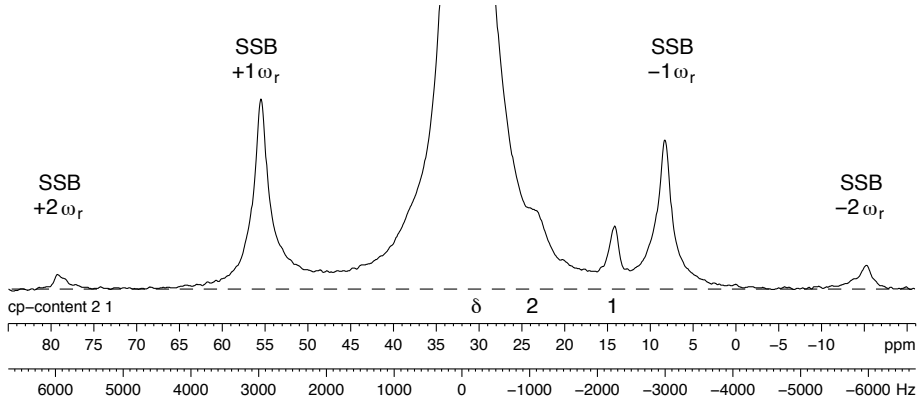

***Figure 9.1**: Solid-state NMR spectra at 3 kHz MAS showing low resolution and intense spinning-sidebands.*

In contrast to the solid-state NMR results, melt-state NMR was found to show great potential for polyolefin branch quantification. A substantial enhancement in sensitivity and resolution was achieved by conducting NMR on systems in the molten-state [Klimke 06], especially through the use of an over-filled 15 mm diameter static double-resonance coil (Figure 9.2).

A combination of high sensitivity and resolution was achieved through the use of melt-state MAS NMR. Initial attempts to find the optimum hardware setup for melt-state MAS NMR showed that, although higher $\boldsymbol{B}_0$ fields gave better resolution, larger MAS rotor volumes gave higher sensitivity (Section 6.2.1). An acceptable compromise between resolution and sensitivity was found using 7 mm MAS rotors at magnetic field strengths equivalent to a proton Larmor frequency of 500 MHz. Further sensitivity with this setup was gained through the use of a custom-built

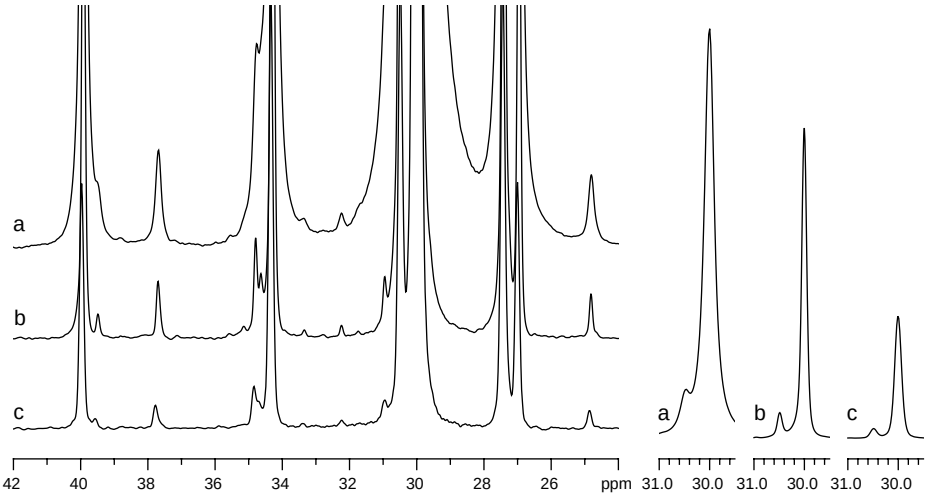

***Figure 9.2**: Comparison of melt-state NMR resolution and sensitivity achieved with (a) static at 300 MHz and MAS at (b) 500 MHz and (c) 300 MHz.*

high-temperature probehead optimised for $^{13}C-^{1}H$ resonance frequencies only (Section 6.2.2). As well as the NMR hardware considerations, sample preparation and sample exchange procedures for the MAS setup were found to further improve the time efficiency of the method by enabling rapid sample throughput (Section 6.2.4).

With long ^{13}C spin-lattice relaxation times encountered for molten polyolefins, strategies were sought to allow fully quantitative SPE with reduced recycle delays and hence measurement times. While the addition of the spin relaxation agent $Cr(acac)_3$ also lowered T_1^C in the melt-state, the procedure for incorporating the relaxation agent into the polymer was found to be highly time-consuming (Section 6.3.1). Polarisation transfer techniques mediated by the $^{1}H-^{13}C$ heteronuclear J-coupling, although possible, were found to be non-quantitative (Section 6.3.2) and were thus limited to structure elucidation (Section 8.2).

In contrast to common expectation, accurate branch quantification was found to be possible via SPE using recycle delays less than the common $\tau_{rd} = 5 \times T_1^C$ [Pollard 04], and even with recycle delays as short as 2 s when only backbone sites were used (Section 6.3.1). An added advantage of reducing the recycle delay was a transient-NOE based signal enhancements of up to 40% for all backbone sites. This phenomenon was found to be directly related to the decoupling of the previous applied pulse for experiments where multiple transients were acquired.

Although considerable sensitivity was achieved using melt-state NMR, reduced resolution as compared to solution-state NMR was also seen. Resolution enhancement was achieved through the implementation of a π pulse-train based heteronuclear dipolar-decoupling method (Section 6.4). While the so-called π-decoupling was not a more efficient decoupling scheme *per se*, its stroboscopic nature allowed for much

longer acquisition times than other 'always-on' decoupling methods, such as CW and WALTZ. With limited FID truncation less artificial line broadening was needed, thus reducing $FWHM_\delta$ by over 70% at short recycle delays (Figure 9.3).

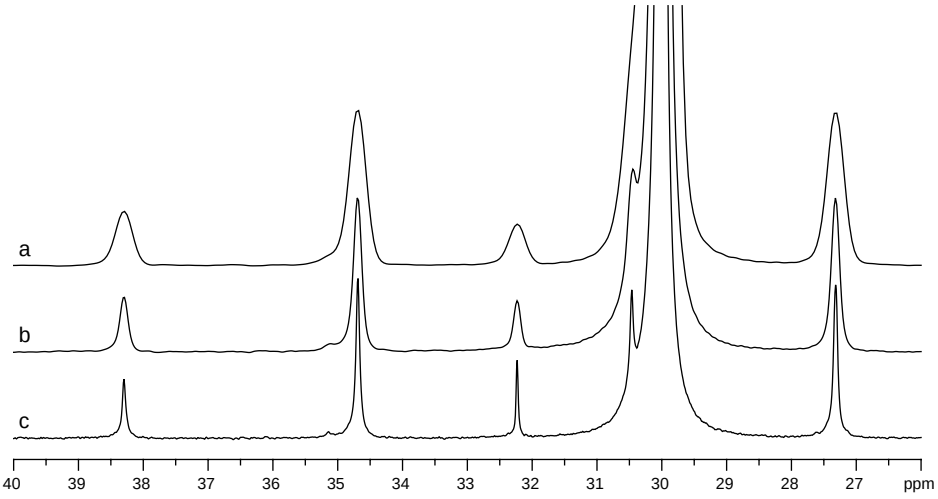

***Figure 9.3**: Resolution obtained with (a) CW, (b) π_4 and (c) π_6 heteronuclear dipolar-decoupling.*

With reproducibility and accuracy of key importance for any quantitative method, both the practical implementation and the post acquisition data processing were analysed with these areas in mind. The development of standard setup, processing and analysis techniques was undertaken to minimise systematic errors (Section 7.2). The implementation of a semi-automated integration procedure, defining the integral limits based on their FWHM, proved particularly successful for improving reproducibility and reducing user related systematic errors (Section 7.2.8). Statistical evaluation of the method as a whole also showed that a measurement criterion of SNR = 50 ensured a standard deviation of only 2% in the final calculated branch contents (Section 7.3), with this increasing to over 30% for SNR < 10.

In general, the optimised melt-state MAS NMR method developed was found to be highly efficient and applicable to a wide variety of problems encountered in the field of polyolefin characterisation. The time efficient nature of the method was clearly demonstrated by the quantification of comonomer contents in polyethylene copolymers (Figure 9.4), and despite the lower resolution, comonomer sequences up to the tetrad level were still able to be detected and quantified (Sections 8.1–8.2).

The high sensitivity also allowed access to a number of experiments previously prohibited by their long experimental times. Melt-state T_1^C times of the terminal branch sites (T_1^C approx 10 s) were able to be efficiently determined for a series of polyethylene copolymers (Section 8.3), and branching in the range of 5-8 per 100,000 CH_2 were able to be quantified in under 13 hours retaining an $\approx$ 10% reproducibility (Section 8.5).

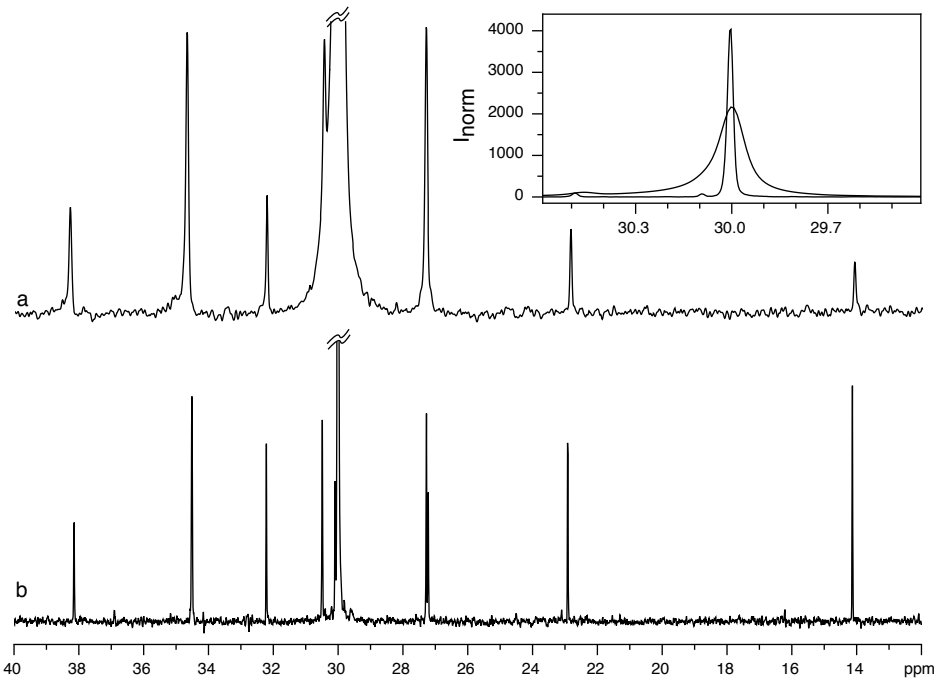

***Figure 9.4**: (a) Melt-state MAS and (b) solution-state SPE spectra with $SNR_\alpha \approx 50$, measured in 70 s and 12 h respectively.*

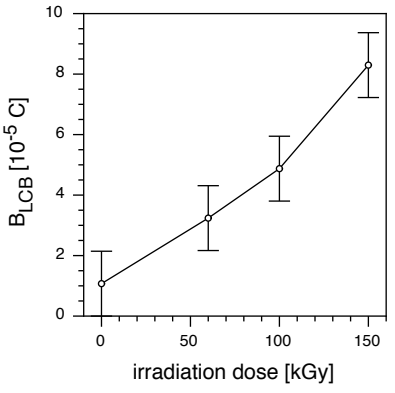

***Figure 9.5**: Long-chain branching as a function of γ-irradiation.*

The optimised melt-state MAS method was found to be equally applicable to polypropylene characterisation, with quantification of single and double comonomer incorporation demonstrated (Section 8.6). Full assignment was achieved via ^{13}C–^{13}C INADEQUATE spectroscopy (Section 8.7), again illustrating the enhanced sensitivity. The quantification of LCB was also demonstrated for a series of γ-irradiated polypropylene homopolymers (Section 8.8), with concentrations as low as 3 long-chain branches per 100,000 carbons being determined in only 24 hours (Figure 9.5).

In conclusion, the developed optimised melt-state MAS NMR method was found to be a highly time efficient alternative to solution-state NMR, and applicable to a wide range of common spectroscopic problems regarding polyolefins [Stadler 06, Klimke 06].

Outlook

The general applicability of the melt-state MAS method towards other polymeric sample is of interest, and considerable industrial importance [McCormick 06], with this method having been shown to provide rapid, accurate quantification of branching and insight into the molecular structure of polyolefins.

Regarding further optimisation of the melt-state MAS method, strategies for increasing the duty cycle at short recycle delays have been identified as an area of key importance. These, combined with alternate decoupling methods, would possibly allow a further decrease of FID truncation and ideally result in no artificial line broadening being required.

A gain in spectral resolution could also be achieved by the application of MAS at rotational frequencies greater than 3 kHz, as homogeneous sample distribution was found for viscous molten systems under MAS. However, risk of sample leakage would need to be further investigated towards long-term applicability and limitation of hardware damage.

The use of relaxation agents in the melt-state was also identified as a potential area of interest. However, with homogeneous incorporation found to be difficult, alternative method of mixing such as co-extrusion could possibly prove more fruitful.

With respect to polyolefin characterisation, the development of further hybrid solution-state/solid-state NMR techniques was found to be promising. In particular, the adaption of HR-MAS methods to systems with a higher degree of dipolar coupling merits attention.

Appendix A

Experimental

Melt-state and solid-state NMR was performed on three dedicated solid-state Bruker (Karlsruhe, Germany) Avance type NMR spectrometers at the Max Planck Institute for Polymer Research (MPIP), Mainz: a narrow-bore DRX700, a wide-bore DSX500 and a wide-bore DSX300. These operated at ^{1}H and ^{13}C Larmor frequencies ν_{1_H} (ν_{13_C}) of 700.13 (176.05), 500.13 (125.75) and 300.23 (75.49) MHz respectively. All measurements were undertaken using a range of commercial Bruker MAS and static geometry probeheads. The 7 mm probehead at used at the 500 MHz spectrometer was also optimised for ^{13}C–^{1}H frequencies only.

Nitrogen gas was used for all pneumatics to limit thermal sample oxidation and ensure stable MAS at low temperatures. Where possible, compensation for MAS frictional heating and general decompression-cooling was undertaken using lead nitrate and known melting point based temperature calibration (Appendix B).

Unless otherwise stated, all solid-state spectra were acquired at $\omega_r/2\pi$ = 3 kHz MAS, using Hartmann-Hahn cross polarisation (CP) with contact times (τ_{ct}) of 1–1.5 ms and strong continuous wave (CW) heteronuclear dipolar-decoupling ($\boldsymbol{B}_1$= 50 kHz). Cross-polarisation under fast MAS ($\omega_r/2\pi = 30$ kHz) was acquired using ramped-CP with τ_{ct} = 2.3 ms and TPPM heteronuclear dipolar-decoupling.

Unless otherwise stated all melt-state measurements were conducted at $\omega_r/2\pi$ = 3 kHz MAS with sample temperatures of 150°C. Shimming was undertaken on the ^{1}H resonance of the molten sample with a full-width at half-maximum (FWHM) $\leq$ 25 Hz being deemed acceptable. Unless otherwise stated single pulse excitation (SPE) with either CW, WALTZ-16 or π-pulse train heteronuclear dipolar-decoupling was used for all experiments. Typically, $\frac{\pi}{2}$ pulse lengths of 10 μs ($\boldsymbol{B}_1 = 25$ kHz) were used on both channels. To ensure measurement of steady-state magnetisation, 16 dummy scans were used before all measurements.

Melt-state spin-lattice relaxation times were measured using both inversion-recovary and saturation-recovery experiments. These were both conducted at T= T_m + 20°C.

A combination of 16 dummy scans and 64 real scans were used per delay to compensate for saturation effects. A recycle delay of 100 s was used for inversion-recovary, with the delay between π and $\frac{\pi}{2}$ pulses varying from 100 ms–40 s in 12 non linear steps. For saturation recovery a train of 24 $\frac{\pi}{2}$ pulses, separated by intervals of varying length, were applied to the carbon channel to create the saturated state. A recycle delay of 10 s was used with the delay varing from 500 ms–40 s in non linear steps.

All solution-state NMR spectra were acquired in the group of Prof. Kaminsky (University of Hamburg). A Bruker Avance spectrometer was used, operating at $\nu_{1_H}(\nu_{13_C})$ Larmor frequencies of 400.15(100.63) MHz respectively. All measurements were conducted at 100°C using perchlorobutadiene (PCB) and 1,1,2,2-tetrachloro-1,2-dideuterioethane (TCE) as solvents. Sample concentrations of $\sim$ 10 wt-% was achieved using 10 mm NMR tubes. Typically, SPE spectra were measured using a 30° Ernst angle and inverse-gated heteronuclear dipolar-decoupling.

Infrared spectroscopy was undertaken on a Nicolet 730 instrument fitted with an attenuated total reflection (ATR) accessory.

All melting points (T_m) were determined via differential scanning calorimetry (DSC). Depending on the sample, DSC measurements were either conducted at the MPIP, in the group of Prof. Kaminsky or in the group of Prof. Münstedt (University of Nürnberg-Erlangen).

For samples PE-oligomer and PE0a, characterisation of the molecular weight and molecular weight distribution was obtained from the supplier (Polymer Standards Service, Mainz). For all other samples, size exclusion chromatography (SEC) was either conducted at the MPIP, in the group of Prof. Kaminsky or by J. Kaschta in the group of Prof. Münstedt.

A.1 Raw 2D-INADEQUATE spectra

The raw 2D-INADEQUATE spectrum of 4% ^{13}C double-labelled polyethylene showing the singlet breakthrough 't_1-noise' at ω_2 = 30 ppm. The spectrum with the 't_1-noise' suppressed during processing [Marion 89] is shown in Chapter 8 as Figure 8.15.

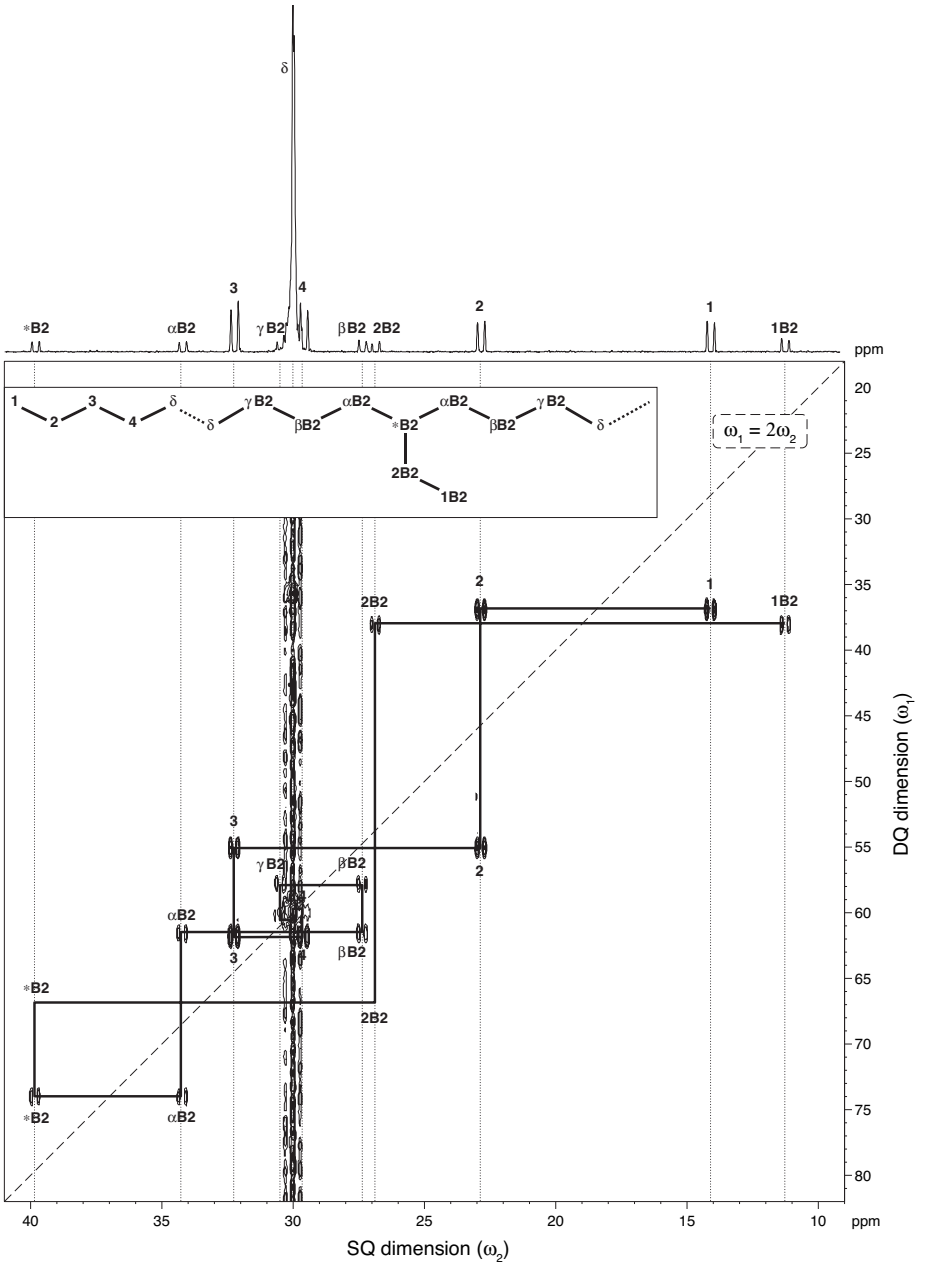

***Figure A.1**: 2D-INADEQUATE spectrum of ^{13}C labelled polyethylene with (top) SQ projection and (insert) nomenclature. Total measurement time 6 hours, using τ_{rd} = 2 s, τ_{aq} = 273 ms, 64 scans and 148 increments in the indirect dimension. Illustrating singlet breakthrough at ω_1 = 30, ω_2 = 60 ppm. Note: sine-bell windowfunctions (SSB = 1) used for both dimensions.*

A.2 Selected experimental parameters

Figure	Page	*PP*	*DD*	$\nu_{^{13}C}$	*T*	*NS*	τ_{rd}	τ_{aq}
				MHz	°C	#	s	ms
4.2a	87	CP	CW	500	25	64	4	62
4.2b	87	SPE	W16	400	100	4k	10	652
4.3	88	CP	CW	500	−15	2k	2	62
4.4a	89	CP	CW	700	27	7800	10	144
4.4b	89	SPE	W16	400	100	4k	10	652
4.7	93	CP	CW	500	−15	2k	2	62
4.8	94	CP	CW	500	−15	40k	2	41
5.2	98	SPE	CW	300	150	2k	6	123
5.5a	101	SPE	CW	300	150	2k	6	123
5.5b	101	SPE	CW	300	150	2k	6	123
5.5c	101	SPE	CW	300	150	2k	6	123
5.5d	101	SPE	CW	300	150	2k	6	123
5.5e	101	SPE	CW	500	150	2k	6	123
5.8	103	SPE	CW	300	150	2k	6	123
5.11a	106	SPE	CW	500	150	2k	6	123
5.11b	106	SPE	CW	500	150	2k	6	123
5.11c	106	SPE	CW	500	150	2k	6	123
5.11d	106	SPE	CW	500	150	2k	6	123
5.11e	106	SPE	CW	300	150	2k	6	123
5.13a	108	SPE	CW	300	150	256	6	123
5.13b	108	SPE	CW	300	170	256	6	123
5.15a	110	SPE	π	300	120	22k	2	164
5.15b	110	SPE	CW	300	150	2k	6	123
6.1a	113	SPE	CW	300	150	4k	10	204
6.1b	113	SPE	W16	400	100	4k	10	652
6.3a	115	SPE	CW	500	110	20k	2	41
6.3b	115	SPE	CW	300	110	20k	2	41
6.3c	115	SPE	CW	700	110	20k	2	41
6.3d	115	SPE	CW	500	110	20k	2	41
6.3e	115	SPE	CW	300	110	20k	2	41
6.5	117	SPE	CW	500	150	2k	6	123
6.7	118	SPE	π	500	180	3k	6	123

Figure	Page	*PP*	*DD*	$\nu_{^{13}C}$	*T*	*NS*	τ_{rd}	τ_{aq}
				MHz	°C	#	s	ms
6.19a	132	SPE	π	500	150	128	2	174
6.19b	132	INEPT	π	500	150	128	2	174
6.19c	132	DEPT	π	500	150	128	2	174
6.25a	138	SPE	CW	500	150	256	2	41
6.25b	138	SPE	π	500	150	256	2	82
6.25c	138	SPE	π	500	150	256	2	273
7.3	146	SPE	CW	500	150	512	2	41
8.1a	159	SPE	π	500	150	16	2	174
8.1b	159	SPE	W16	400	100	4k	10	652
8.2a	160	SPE	π	500	150	6k	2	273
8.2b	160	INEPT	π	500	150	6k	2	273
8.4a	161	SPE	π	500	150	6k	2	273
8.4b	161	INEPT	π	500	150	6k	2	273
8.9	169	SPE	π	500	150	30k	2	164
8.11	171	SPE	π	500	150	21k	2	174
8.12a	172	SPE	π	500	180	3200	4	273
8.12b	172	SPE	π	500	180	280	4	273
8.18	176	SPE	π	500	180	36k	2	273
9.1	180	CP	CW	500	−15	2k	2	62
9.2a	181	SPE	CW	300	150	2k	6	123
9.2b	181	SPE	CW	500	150	2k	6	123
9.2c	181	SPE	CW	300	150	2k	6	123
9.3a	182	SPE	CW	500	150	256	2	41
9.3b	182	SPE	π	500	150	256	2	82
9.3c	182	SPE	π	500	150	256	2	273
9.4a	183	SPE	π	500	150	16	2	174
9.4b	183	SPE	W16	400	100	4k	10	652

Appendix B

Temperature calibration

For all variable-temperature (VT) NMR measurements, knowledge of the true sample temperature is essential. However due to physical limitations the thermocouple used for temperature regulation cannot be placed in the sample container. This results in the temperature reading given by the thermocouple not truly representing the actual sample temperature. The thermocouple reading is thus only an apparent sample temperature and is dependant on a number of paramaters including; gas temperature, gas flow rate and sample container material etc.

For both static and MAS VT-NMR sample heating is achieved be heating a gas, usually N_2, and passing this heated gas over the sample container. For MAS experiments only the bearing gas is usually heated. Due to decompression of the gas as it enters the atmosphere cooling occurs, lowering the sample temperatures. In contrast, for MAS measurements friction between the outer wall of the rotor and the atmosphere leads to heating, increasing the sample temperatures [Grimmer 97]. It has been shown that under 35 kHz MAS that the combination of decompression-cooling and frictional-heating resulted in actual sample temperatures up to 40°C higher than the apparent sample temperature [Langer 99]. With significant differences seen between actual and apparent sample temperature, even under moderate conditions, temperature calibration is necessary. Such temperature calibration correlates the apparent sample temperature ($T_{apparent}$) with the actual sample temperature (T_{sample}) for a given set of measurement conditions. In the temperature range in question only first-order effects need be considered, resulting in only a proportionality (k_1) and offset (k_0) constant needing to be determined (Equation B.1).[†]

$$T_{apparent} = (k_1 \times T_{sample}) + k_0 \tag{B.1}$$

[†]It should be noted that the given values of k_0 and k_1 in this section only refer to both $T_{apparent}$ and T_{sample} being given in units of Kelvin.

B.1 Static VT-NMR

Temperature calibration of the static probeheads had previously been established by Gaborieau *et.al.* using a series of substances with known melting points, such as dimethylformaide and citric acid [Gaborieau 05]. For the static setups the only free parameter needing to be controlled was the nitrogen flow rate, as this strongly effects heat transfer. For measurements undertaken on the 300 and 500 MHz spectrometers the predetermined flow rates of 1200 and 1000 lh^{-1} were used. The determined temperature calibration constants and setup conditions are given in Table B.1. Additionally, at 500 MHz a long glass dewar was used to remove the hot exit gas from the probhead, thus limiting unnecessary heating of the magnet.

***Table B.1**: Temperature calibration parameters for static probeheads used.*

ν_{1_H}	flow rate	k_0	k_1
MHz	lh^{-1}	K	
300	1200	46.156	0.8626
500	1000	42.770	0.8604

B.2 MAS VT-NMR

Unlike the temperature calibration of the static probeheads, under MAS the melting-point method could not be used due to rotor instability upon melting.[†] Alternatively, for the temperature calibration of the various MAS probeheads, a solid samples with a temperature dependent isotropic chemical shift was used.

The paramagnetic lanthanide stannate, $Sm_2Sn_2O_7$, had previously been used for temperature calibration of the 4 mm probeheads at 300, 500 and 700 MHz[Grey 93, Vanmoorsel 95, Grimmer 97, Langer 99]. For all 4 mm probeheads used, within the temperature range of interest, the apparent sample temperature had previously been found to correspond to the sample temperature [Yefeng 03]. Unfortunatly the quantity of $Sm_2Sn_2O_7$ needed for temperature calibration of 7 mm probeheads was not available, and lead nitrate $Pb(NO_3)_2$ was used instead.

The temperature dependence of the ^{207}Pb chemical shift having previously been established under measurement conditions similar to those used in this study [Bielecki 95, Neue 96, Neue 97, Takahashi 99, Beckmann 00]. With the isotropic chemical shift previously being reported to change linearly with the sample temperature at a rate of 0.758 ($\pm$ 0.002) ppm$\cdot K^{-1}$ [Beckmann 00].

As a fixed point-of-reference the isotropic ^{207}Pb chemical shift was measured at room-temperature. Each magnet/probehead/rotor combination was left at equilibrate at room temperature for at least four hours with no gas flow whatsoever.

[†]The risk of stator contamination with this method was also deemed too high, with molten small molecules having very low zero-shear viscosities increasing the risk of the sample flowing between rotor and cap.

Under these condition the assumption could be made that the apparent sample temperature was equal to the actual sample temperature, i.e. $T_{apparent} = T_{sample}$. Under these static NMR conditions the ^{207}Pb chemical-shift anisotropy (CSA) tensor was measured and the isotropic chemical shift determined (Figure B.1). This isotropic chemical shift was then taken to be ^{207}Pb chemical-shift at this apparent and actual sample temperature.[†]

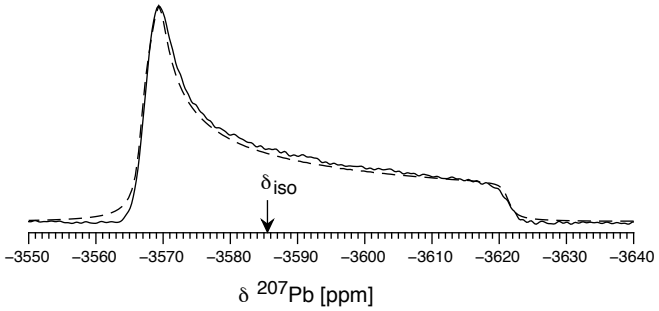

***Figure B.1**: Static ^{207}Pb chemical-shift tensor measured at $T_{apparent} = T_{sample} = 21.6°C$ using the ^{13}C–^{1}H optimised 7 mm probehead at 500 MHz. (Fit: δ_{iso} = -3585.8 ppm, η = 0.08 and Δ = 54.4 ppm)*

For all 7 mm MAS probeheads, the apparent temperature was measured using a thermocouple located in the bearing gas stream between heating element and stator.[‡] Due to its high density only a small quantity of lead nitrate was placed in the rotors to ensure stable spinning when required. Two thin layers of lead nitrate were placed at the lower end and in the middle of the rotor between compressed plugs of PTFE tape. This allowed the monitoring of a temperature gradient inside the rotor between these two positions based on the different chemical shifts of these two layers.

The known temperature dependance of lead nitrate with actual sample temperature (Figure B.2a) was then compared to the determined temperature dependance with apparent sample temperature (Figure B.2b) for each hardware setup and MAS speed. From the difference between the apparent and actual to the sample temperature for a given chemical shift value a calibration curve can be determined relating apparent and sample temperature (Figure B.3).From the temperature calibration curves the constants k_0 and k_1 may then be determined for each set of conditions (Table B.2).

***Table B.2**: Temperature calibration parameters for curves for the 7 mm probeheads used.*

ν_{1_H} MHz	T_{max} °C	MAS kHz	$P_{bearing}$ mBar	k_0 K	k_1
300	300	3	960	47.605	0.8437
500	120	3	960	-6.251	1.0185
500	300	3	960	21.550	0.9224
500	300	4	1500	28.360	0.8996

[†]External ^{207}Pb chemical shift calibration was not undertaken, due to the highly toxic nature of the $Pb(Me)_4$ standard, and the given values are only relative to each other.
[‡]That is, temperature regulation was undertaken on *in-coming*, as opposed to *out-going*, gas temperature.

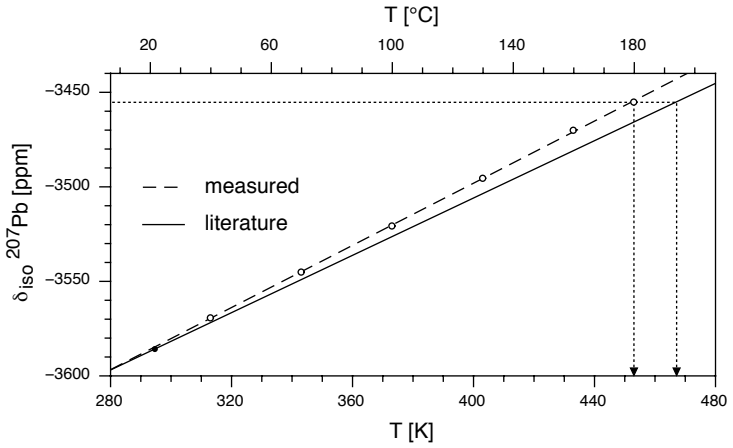

***Figure B.2**: The known temperature dependence of ^{207}Pb isotropic chemical shift with actual sample temperature (solid line) and the determined temperature dependence with apparent sample temperature (dashed line) for the ^{13}C–^{1}H optimised 7 mm probehead at 500 MHz under 3 kHz MAS.*

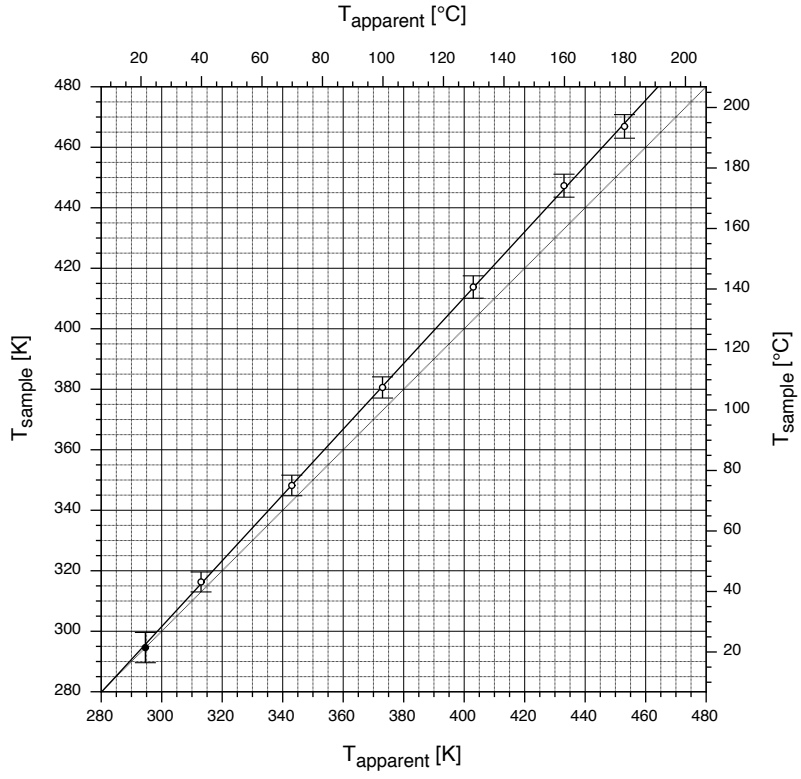

***Figure B.3**: Calibration curve realting the apparent ($T_{apparent}$) and actual (T_{sample}) sample temperature for the ^{1}H–^{13}C optimised 7 mm MAS probehead at 500 MHz under 3 kHz MAS.*

B.3 Temperature gradient

Temperature calibration curves showed homogeneous heating of the sample, with no temperature gradient, for all static and MAS probeheads. However, when 7 mm MAS probehead with an alternative heating system was investigated, strong temperature gradients were seen across the rotor. For standard MAS probeheads for VT-NMR the bearing gas is heated and then directed onto both ends of the rotor while the drive gas remains as room temperature. In the alternative design both bearing and drive gas were kept at room temperature while a third gas stream was heated and then directed onto the middle of the rotor.

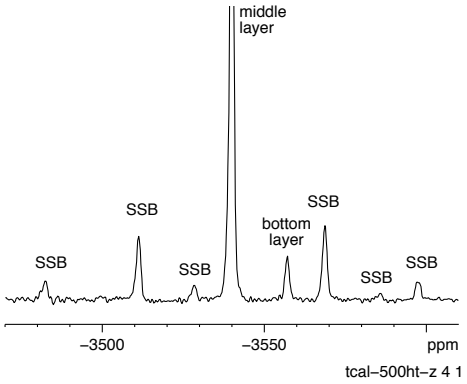

***Figure B.4**: The two isotropic ^{207}Pb chemical shifts seen under MAS resulting from a temperature gradient between the bottom end and middle of the rotor.*

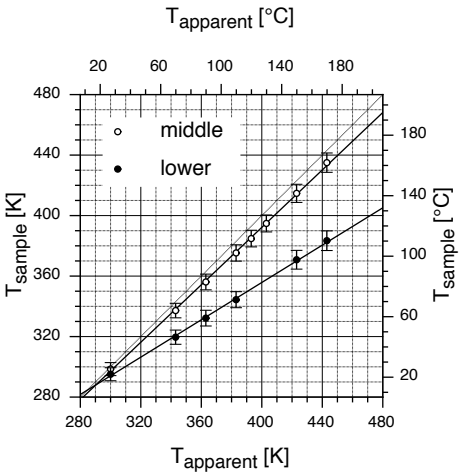

***Figure B.5**: Calibration curves relating $T_{apparent}$ and T_{sample} showing a 45°C difference at 150°C.*

A large temperature gradient was observed within the rotor when the alternative heating system was used. This was indicated by a second ^{207}Pb signal of lower intensity from the layer lead nitrate layer at the lower end of the rotor (Figure B.4). This resulted in separate temperature calibration curves being obtained for the lower end and middle of the rotor (Figure B.5). With homogeneous heating and stable melt-state NMR not possible with such a gradient the use of such a heating system was deemed unsuitable.

Appendix C

Pulse sequences

C.1 SPE

```
1 ze
2 d1
  p1 ph1
  go=2 ph31
  20m wr #0
exit

ph1  = 0 1 2 3
ph31 = 3 0 1 2
```

C.2 SPE/DD

```
1 ze
  10u pl1:f1
  10u pl2:f2
2 d1
  (p1 ph1):f1
  3u cpd2:f2
  go=2 ph31
  20u do:f2
  20m wr #0
exit

ph1  = 0 1 2 3
ph31 = 0 1 2 3
```

C.3 π-decoupling

```
1 pcpd:0  pl=pl2
  d31     pl=120
  pcpd:90 pl=pl31
  d31     pl=120
  pcpd:0  pl=pl31
  d31     pl=120
  pcpd:90 pl=pl31
  d31     pl=120
  pcpd:90 pl=pl31
  d31     pl=120
  pcpd:0  pl=pl31
  d31     pl=120
  pcpd:90 pl=pl31
  d31     pl=120
  pcpd:0  pl=pl31
  d31     pl=120
jump to 1
```

C.4 SPE/DD-2D

```
1 ze
  10u pl1:f1
  10u pl2:f2
2 d1
  (p1 ph1):f1
  3u cpd2:f2
  go=2 ph31
  3m do:f2
  100m wr #0 if #0 zd
  lo to 2 times td1
exit

ph1  = 0 1 2 3
ph31 = 0 1 2 3
```

C.5 CP/DD

```
1 ze
2 d1 do:f2
  10u pl1:f1 pl2:f2
  (p3 ph1):f2
  3u
3 (p15 ph2):f1 (p15 ph3):f2
  2u pl12:f2
  2u cw:f2
  go=2 ph31
  1m do:f2
  100m wr #0
exit

ph1  = 1 3
ph2  = 0 0 1 1 2 2 3 3
ph3  = 0
ph31 = 0 2 1 3 2 0 3 1
```

C.6 Inversion-recovery

```
"p2=2*p1"

1 ze
  10u pl1:f1 pl2:f2
2 d1 do:f2
  (p2 ph1):f1
  vd
  (p1 ph2):f1
  3u cpd2:f2
  go=2 ph31
  3m do:f2
  100m wr #0 if #0 ivd ze
  lo to 2 times td1
exit

ph1  = 0 2 0 2
ph2  = 0 1 2 3
ph31 = 0 1 2 3
```

C.7 Saturation-recovery

```
1 ze
  10u pl2:f2
  10u pl1:f1
2 d1 do:f2
3 (p1 ph20^):f1
  13m
  (p1 ph21^):f1
  7m
  (p1 ph22^):f1
  1m
  (p1 ph23^):f1
  3m
  lo to 3 times 8
  vd
  (p1 ph1):f1
  3u cpd2:f2
  go=2 ph31
  3m do:f2
  100m wr #0 if #0 ivd ze
  lo to 2 times td1
exit

ph1  = 0 1 2 3
ph20 = 0 1 2 3
ph21 = 1 2 3 0
ph22 = 2 3 0 1
ph23 = 3 0 1 2
ph31 = 0 1 2 3
```

C.8 DEPT

```
"p2=p1*2"
"p4=p3*2"
"d2=1s/(cnst2*2)"
"d12=20u"
"d31=p1*4/3.1416"

1 ze
2 d1 do:f2
  d12 pl2:f2
3 (p3 ph1):f2
  d2
  (p4 ph2):f2 (p1 ph4 d2):f1
  (p0 ph3):f2 (p2 ph5 d2):f1
  d31 pl12:f2
  go=2 ph31 cpd2:f2
  d12 do:f2
  wr #0
exit

ph1  = 0
ph2  = 0 2 1 3
ph3  = 1 1 1 1 3 3 3 3
ph4  = 0 0 0 0 0 0 0 0 1 1 1 1 1 1 1 1
       2 2 2 2 2 2 2 2 3 3 3 3 3 3 3 3
ph5  = 0 2 0 2 0 2 0 2 1 3 1 3 1 3 1 3
ph31 = 1 1 3 3 3 3 1 1 2 2 0 0 0 0 2 2
       3 3 1 1 1 1 3 3 0 0 2 2 2 2 0 0
```

C.9 INEPT

```
"p2=p1*2"
"p4=p3*2"
"d3=1s/(cnst2*cnst11)"
"d4=1s/(cnst2*4)"

1 ze
2 d1 do:f2
3 3m pl2:f2
  (p3 ph1):f2
  d4
  (p4 ph2):f2  (p2 ph4)
  d4
  (p3 ph3):f2  (p1 ph5)
  d3
  (p4 ph2):f2  (p2 ph6)
  d3 pl12:f2
  go=2 ph31 cpd2:f2
  wr #0
  d4 do:f2
exit

ph1  = 0 0 0 0 0 0 0 0 2 2 2 2 2 2 2 2
ph2  = 0 2
ph3  = 1 1 3 3
ph4  = 0 2
ph5  = 0 0 0 0 1 1 1 1 2 2 2 2 3 3 3 3
ph6  = 0 2 0 2 1 3 1 3
ph31 = 0 0 2 2 1 1 3 3
```

C.10 INADEQUATE

```
"d0=2u"
"p2=p1*2"
"d2=1s/(4*cnst3)"
"d3=((1s*cnst4)/cnst31)-((p1+p2)/2)"

1 d2 ze
2 d1 do:f2
3 10u pl1:f1 pl12:f2
  10u cw:f2
  (p1 ph1):f1
  d3
  (p2 ph2):f1
  d3
  (p1 ph3):f1
  d0
  (p1 ph4):f1
  ;2u do:f2
  go=2 ph31 cpd2:f2
  2u do:f2
  10m wr #0 if #0
  zd
  id0
  lo to 2 times td1
exit

ph1  = (8) 0 7 2 1  4 7 6 5  2 5 4 3  6 1 0 7
           3 6 5 4  7 2 1 0  1 4 3 2  5 0 7 6
ph2  = (8) 0 3 2 1  4 7 6 5  2 5 4 3  6 1 0 7
           3 6 5 4  7 2 1 0  1 4 3 2  5 0 7 6
           4 7 6 5  0 3 2 1  6 1 0 7  2 5 4 3
           7 2 1 0  3 6 5 4  5 0 7 6  1 4 3 2
ph3  = ph1
ph4  = 0 3 2 1
ph31 = {{0}*8}^2^3^1
```

Appendix D

Automation routines

D.1 Bruker AU programs

D.1.1 pmsinozg

```
/* PMSINOZG   Matt Parkinson    1/12/2004*/
/* runs in go mode until desired sino real reached   */
/* outputs file sino.log in dataset showing progtess */
/* NOTE NS = maximum number of scans     */

char logfilepath[200],endmessage[100];
int ns, nscheck,loops, runningns,rns,desiredsinoi;
float sino, desiredsino, tta, et,tns,rd,aq,rt,rta;
FILE *logfile;
float time,days,hours,mins,secs;
int minsi,hoursi,daysi;
GETCURDATA
sprintf(logfilepath,"%s/data/%s/%s/%s/%i/sino.log",disk,user,type,name,expno);
FETCHPAR("NS",&ns) /* Maximum number of scans*/
FETCHPAR("D 1",&rd)
FETCHPAR("AQ",&aq)
desiredsinoi=50;
GETINT("Enter desired SINO: ",desiredsinoi);
desiredsino=(float)desiredsinoi;
GETINT("Enter maximum number of scans (DON'T USE k): ",ns);
STOREPAR("NS",ns); /* scanf to allow for 1k = 1024*/
nscheck=4;
GETINT("Number of scans per SINO check: ",nscheck);
loops=ns/nscheck;
logfile = fopen(logfilepath, "w");
fprintf(logfile,"Desired SINO of %.2f\n
Maximum of %i scans in %i x %i increments\n
  NS    SINO     NS     rNS    d  h  m  s\n
",desiredsino,ns,loops,nscheck);
fclose(logfile);
STOREPAR("NS",nscheck);
TIMES(loops)
if ( loopcount1 == 0 )
{
STOREPAR("DS",16);
ZG
```

```
STOREPAR("DS",0);
}
else
GO
GFP
ABS
XCMD("sino real noprint");
FETCHPARS("SINO",&sino)
runningns=(loopcount1+1)*nscheck                    /* number of scan done so far     */
tns=pow(((sqrtf(runningns)*desiredsino)/sino),2);  /* Theoretical # scans until SINO */
rns=(int)(tns/nscheck);                             /* convet to integer i.e Floor    */
rns=(rns+1)*nscheck;                                /* Real # scans until SINO        */
rta=(rns-runningns)*(rd+aq);                        /* time to go until finished      */
if ( sino >= desiredsino )
break;
else
{
mins=rta/60;
minsi=(int)mins;
secs=(mins-minsi)*60;
mins=(float)minsi;
hours=(mins/60);
hoursi=(int)hours;
mins=(hours-hoursi)*60;
hours=(float)hoursi;
days=hours/24;
daysi=(int)days;
hours=(days-daysi)*24;
logfile = fopen(logfilepath, "a");
fprintf(logfile,"%4i %7.2f %6.1f => %4i = %2i %2.0f %2.0f %2.0f\n
,runningns,sino,tns,rns,daysi,hours,mins,secs);
fclose(logfile);
}
END
et=runningns*(rd+aq);
mins=et/60;
minsi=(int)mins;
secs=(mins-minsi)*60;
mins=(float)minsi;
hours=(mins/60);
hoursi=(int)hours;
mins=(hours-hoursi)*60;
hours=(float)hoursi;
days=hours/24;
daysi=(int)days;
hours=(days-daysi)*24;
if ( sino >= desiredsino )
sprintf(endmessage,"Reached desired SINO of %.2f\n
NS=%4i SINO= %5.2f in %id %2.0fh %2.0fm %2.0fs\n
",desiredsino,runningns,sino,daysi,hours,mins,secs);
else
sprintf(endmessage,"Did NOT reach desired SINO of %.2f\n
NS=%4i SINO= %5.2f in %id %2.0fh %2.0fm %2.0fs\n
",desiredsino,runningns,sino,daysi,hours,mins,secs);
logfile = fopen(logfilepath, "a");
fprintf(logfile,"%s",endmessage);
fclose(logfile);
STOREPAR("NS",ns);
QUITMSG(endmessage)
```

D.1.2 make2d

```
/* MAKE2D     Matt parkinson    23/7/2004               */
/* Combines identical 1D experiments into a 2D data set */

char dataset[200], command[200],endmessage[200], fids[200], fid[10];
int number, output, status, n, nmax;
GETCURDATA
GETINT("Enter expno of 2D dataset to be created : ",output);
GETINT("Enter number of 1D experiements : ",number);
WRPA(name, output, 1, disk, user);
sprintf(dataset,"/%s/data/%s/nmr/%s/",disk,user,name);
sprintf(command,"cd %s/%i/ ;
rm -r fid; cd pdata/1; rm -r 1i 1r intrng title peaks", dataset,output);
status=system(command);
sprintf(fids," ");
n=expno;
nmax=expno+number;
for(n=expno;n<nmax;n++){
    sprintf(fid,"%i/fid ",n);
    sprintf(fids,"%s%s",fids, fid);
}
sprintf(command,"cd %s; cat %s > %i/ser",dataset,fids,output);
status=system(command);
n=expno;
nmax=expno+number-1;
DATASET(name, output, 1, disk, user);
sprintf(command,"cd %s/%i/pdata/1;
rm -r meta* *.txt; echo pseudo-2D > title", dataset,output);
status=system(command);
XCMD("parmode 2D");
VIEWDATA;
STOREPAR1S("TD",number);
STOREPAR1("TD",number);
STOREPAR1("SI",number);
STOREPAR1("WDW",0);
STOREPAR1("PH_MOD",0);
XCMD("1s nd0 2");
XCMD("1s in0 1");
XCMD("xf2");
sprintf(command,"Pseudo-2D ser file made from\n EXPNO: %i to %i", n,nmax);
QUITMSG(command)
```

D.1.3 calibrate

```
/* CALIBRATE     Matt Parkinson     13/1/2005      */
/* automatic calibration of highest intensity peak */

char command[100],path[100],statusmessage[200], tempfilepath[100];
float delta, sr, hz,ppm;
double sfoone,bfone,oone;
FILE *temp;
GETCURDATA
delta=30;              /* default values */
STOREPAR("MAXI",100);
if ( strlen( cmd ) == 0 )
    {GETFLOAT("Chemical shift of maximum intensity peak =: ",delta);
    }
  else
    {
    if (1 != sscanf(cmd, "%f", &delta))
        {STOPMSG("Only numbers are allowed for this value.")};
    }

FETCHPARS("SR",&sr);  /* get paramaters from acqus files */
FETCHPARS("SFO1",&sfoone);

STOREPAR("PSCAL",0);  /* set values and peak pick        */
XCMD("f1p 100000");
XCMD("f2p -100000");
XCMD("cy 100");
STOREPAR("MI",0.1);
XCMD("maxi 101");
XCMD("xwp_pp");      /* get hz from peak.txt file via temp file */
sprintf(path,"/%s/data/%s/nmr/%s/%i/pdata/%i/",disk,user,name,expno,procno);
sprintf(tempfilepath,"%s/calibrate.temp", path);
sprintf(command,"tail +5 %s/peak.txt |
awk ' /100.00/ {print $3}'>%s", path, tempfilepath);
system(command);
temp=fopen(tempfilepath,"r");
fscanf(temp, "%f", &hz);
fclose(temp);
sprintf(command,"rm %s", tempfilepath);
system(command);
sr=sr+hz-(delta*(sfoone)) + (0.000001*sfoone*delta*delta); /* do the maths */
STOREPARS("SR",sr);
VIEWDATA;
XCMD("fp");
sprintf( statusmessage, "Peak of maximum intensity calibrated to %6.3f ppm",delta );
Show_status(statusmessage);
QUIT;
```

D.1.4 trim

```
/* TRIM     Matt Parkinson     14/1/2005             */
/* trim spectra via STSR/STSI to given region in ppm */

double sfo1;
float offset, hzppt, min, max;
int stsr, stsi;
char statusmessage[100];
GETCURDATA
max=45;
min=5;
```

```
if ( strlen( cmd ) == 0 )
{
GETFLOAT("Chemical shift of upper bound =: ",max);
GETFLOAT("Chemical shift of lower bound =: ",min);
}
else
{
    if (2 != sscanf(cmd,"%f %f", &max, &min))
    {
    STOPMSG("two numbers were not given.");
    }
}
FETCHPAR("STSI",&stsi);
if (stsi != 0)
{
    stsi=0;
    STOREPAR("STSI",stsi);
    XCMD("ft");
}
FETCHPARS("OFFSET",&offset);
FETCHPARS("HZPPT",&hzppt);
FETCHPARS("SFO1",&sfo1);
stsr=(offset-max)/(hzppt/sfo1);
stsi=3+(max-min)/(hzppt/sfo1);
STOREPAR("STSR",stsr);
STOREPAR("STSI",stsi);
XCMD("fp");
sprintf( statusmessage, "Spectral window trimmed to %.1f-%.1f ppm.",max,min);
Show_status(statusmessage);
QUIT;
```

D.1.5 asciiregion

```
/* asciiregion andrew.gibbs@bruker.co.uk                */
/* output a specified region as ascii data              */
/* specify region as parameters, otherwise program asks */
/* asciiregion                  (asks!)                 */
/* xau asciiregion 5.2 4.2                              */

/* Modified by Matt Parkinson 30/1/2005                 */
/* output file contains only Hz, ppm and intensity      */
/* and output file = $dataset_$expno_$procno.csv        */

/* Mofified by Matt Parkinson 7/2/2005                  */
/* FTSIZE used for ppmppt for trimmed data (STSI != 0)  */
/* output file contains Hz, ppm, I and I*(2^-n_proc)    */

char message[255];
char inname[255];
char outname[255];
char cdisk[100], cuser[100], cname[100];
int cexpno, cprocno;
int csize, ftsize;
int i, start, finish;
long ncproc;
float coffset;
float cwidth;
float hzppt, ppmppt, temp;
float upper, lower;
float ppmval, hzval;
double csfo1;
```

```
FILE *file;
long *ldata, pld;
double sscale, intensity;
int readin;

GETCURDATA

FETCHPARS("SI", &csize)          /* used for actual number of data points read in */
FETCHPARS("FTSIZE", &ftsize)     /* Use FTSIZE as SI=STSI if trimmed corect hzppt */
FETCHPARS("SFO1", &csfo1)
FETCHPARS("OFFSET", &coffset)
FETCHPARS("SWH", &cwidth)
FETCHPARS("nc_proc", &ncproc)

hzppt = cwidth/ftsize;           /*calculate as hzppt from acqu2 can be incorrect */
ppmppt = hzppt/csfo1;

/* calculate scale factor, each point is stored as a 32 bit */
/* integer on disk, true number is * 2^N, where N=nc_proc   */
/* This allows full precision to be retained                */

sscale = pow(2.0, ncproc);
readin = sscanf(cmd, "%f%f", &upper, &lower);      /* get region from CLI or ask! */

if (readin != 2)
{
  upper=coffset; lower=upper-(csize*ppmppt);
  GETFLOAT("output from ppm = ", upper);
  GETFLOAT("to ppm = ", lower);
}

if (lower > upper)                          /* reverse order if entered wrongly! */
{
  temp = lower;
  lower = upper;
  upper = temp;
}

start = ((coffset - upper) * csfo1) / hzppt;
finish = ((coffset - lower) * csfo1) / hzppt;

if (start > csize || start < 0 || finish > csize || finish < 0)
{
  printf(" region (%f to %f) not in this dataset!\n", upper, lower);
}
else
{                                           /*get the data */
 sprintf(inname, "%s/data/%s/nmr/%s/%d/pdata/%d/1r", disk, user, name, expno, procno);
 sprintf(outname, "%s/data/%s/nmr/%s/%d/pdata/%d/%s_%d_%d.csv",\\
 disk, user, name, expno, procno,name,expno,procno);

/* allocate memory for arrays */
if ( ( ldata = (long *)malloc( sizeof(long) * csize ) )==NULL )
  {
  STOPMSG("Could not allocate memory for data?")
  }
  if ( ( file = fopen(inname, "r") ) == NULL)
  {
  Proc_err(INFO_OPT, "Could not open file %s!", inname);
  }
  else if ( (readin = fread(ldata, sizeof(long), csize, file)) != csize)
  {
    Proc_err(INFO_OPT, "read only %d of %d points from %s!", readin, csize, inname);
    fclose(file);
```

```
  }
  else
  {
    fclose(file);
    if ( ( file = fopen(outname, "w") ) == NULL)
    {
      Proc_err(ERROR_OPT, "Could not open output file %s for write?", outname);
    }
    else
    {
      fprintf(file, "Hz, ppm, I*(2^nc_proc),I\n");
      pld = ldata + start;                    /* do the output */
        for (i = start; i < finish; i++)
        {
        pld = ldata[i];                 /* pld = stored long integer (Y) %ld  */
        intensity = pld * sscale;       /* intensity = true value    (Y) %lf  */
        ppmval = coffset - ppmppt*i;    /* ppmval = ppm of position  (X) %f   */
        hzval = ppmval * csfo1;         /* hzval = Hz of position    (X) %f   */
        fprintf(file, "%f,%f,%lf,%1d\n", hzval,ppmval, intensity, pld);
        }
      fclose(file);
    }
  }
  free(ldata);
}
strcat(outname, " - File written.");
Show_status(outname);

QUIT
```

D.1.6 xwpd

```
/* XWPD            Matt Parkinson     23/7/2004                */
/* writes parm.txt in pdata containing dataset expno & procno   */

char path[200],parameters[200],statusmessage[200];
FILE *f;
GETCURDATA
sprintf(path,"%s/data/%s/%s/%s/%i/pdata/%i/parm.txt",disk,user,type,name,expno,procno);
sprintf(parameters,"%s %i %i\n",name,expno,procno);
f=fopen(path,"w");
fprintf(f,parameters);
fclose(f);
sprintf(statusmessage," %s",parameters);
Show_status(statusmessage);
QUIT;
```

D.2 AWK scripts

Implementation of AWK [Aho 88] scripts from the UNIX comand-line interface via:

```
$ awk -f filename.awk file
```

D.2.1 peaklist2intrng.awk

Conversion from Bruker *peaklist* to *intrng* integration region file based on peak width.

```
BEGIN {nsigma=(15/2.35);                                  # +/- 15 SDs of Gaussian
print "H 0";getline;getline}                              # print headers
{printf ("%2.2f %2.2f\n", ($1+nsigma*$2), ($1-nsigma*$2))} # print limits
```

D.2.2 intrng2intrngpe.awk

Selection of polyethylene integration limits from *intrng* file created by *peaklist2intrng*.

```
/H/ {
print $0;getline;          # \star
print $0;getline;          # \alpha
print $0;getline;          # \three
high=$2;print $0;getline;  # upper \delta = lower \three
getline;                   # skip \gamma
getline;                   # skip \delta
#getline;                   # skip \four
low=$1;print high" "low;   # lower \delta = upper \beta
print $0;getline;          # \beta
print $0;getline;          # \two
print $0}                  # \one
```

Combination of *peaklist2intrng* and *intrng2intrngpe* as follows:

```
$ awk -f peaklist2intrng.awk peaklist | awk -f intrng2intrngpe.awk > intrng
```

D.2.3 int1d2csv.awk

Conversion of relative integral values from Bruker *int1d* file to comma separated values (CSV).

```
BEGIN   {ORS=""}    # no output record separator
/ 1 / && !/NAME/ {  # needed to not find exp/proc no
print$4",";getline; # \star
print$4",";getline; # \alpha
print$4",";getline; # \three
print$4",";getline; # \delta
print$4",";getline; # \beta
print$4",";getline; # \two
print$4"\n"}        # \one
```

Conversion of multiple *int1d* files to CSV in reverse time time order as follows:

```
$ awk -f int1d2csv.awk ‘ls -trc1 */pdata/1/int1d‘
```

Appendix E

Comonomer sequence equations

Polyethylene-co-butenes

Equations used to calculate the content of individual comonomer sequences in polyethylene-co-butenes:

$$B_{EBE} = \frac{A_{\star B2}}{A_{bulk} + (5 \cdot A_{\star B2})} \tag{E.1}$$

$$B_{EBBE} = \frac{2 \cdot A_{\alpha\alpha B2}}{A_{bulk} + (7 \cdot A_{\alpha\alpha B2})} \tag{E.2}$$

$$= \frac{A_{\star\beta B2}}{A_{bulk} + (\frac{7}{2} \cdot A_{\star\beta B2})} \tag{E.3}$$

$$B_{EBBBE} = \frac{3 \cdot A_{\star\beta\beta B2}}{A_{bulk} + (9 \cdot A_{\star\beta\beta B2})} \tag{E.4}$$

$$B_{EBEBE} = \frac{2 \cdot A_{\beta\beta B2}}{A_{bulk} + (9 \cdot A_{\beta\beta B2})} \tag{E.5}$$

$$B_{EBBEBE} = \frac{3 \cdot A_{\beta\beta\delta B2}}{A_{bulk} + (11 \cdot A_{\beta\beta\delta B2})} \tag{E.6}$$

Polyethylene-co-octenes

Equations used to calculate the content of individual comonomer sequences in polyethylene-co-octenes:

$$B_{EOE} = \frac{A_{\star B_6}}{A_{bulk} + (4 \cdot A_{\star B_6})} \tag{E.7}$$

$$B_{EOOE} = \frac{2 \cdot A_{\alpha\alpha B_6}}{A_{bulk} + (5 \cdot A_{\alpha\alpha B_6})} \tag{E.8}$$

$$= \frac{A_{\star\beta B_6}}{A_{bulk} + (\frac{5}{2} \cdot A_{\star\beta B_6})} \tag{E.9}$$

$$B_{EOOOE} = \frac{3 \cdot A_{\star\beta\beta B_6}}{A_{bulk} + (6 \cdot A_{\star\beta\beta B_6})} \tag{E.10}$$

$$B_{EOEOE} = \frac{2 \cdot A_{\beta\beta B_6}}{A_{bulk} + (7 \cdot A_{\beta\beta B_6})} \tag{E.11}$$

Appendix F

Starting parameters

Suggested starting conditions for melt-state MAS NMR of an unknown polyolefin.

probehead	$T_{max} > 150°C$, ^{13}C–^{1}H optimised	Sections 6.2.1 & 6.2.2
sample temperature	150°C (calibrated)	Sections 6.2.3 & B.2
rotor material	ZrO_2	Section 6.2.4
rotor size	7 mm	Section 6.2.1
cap material	ZrO_2	Section 6.2.4
sample quantity	200 mg	Section 6.2.4
MAS speed	3 kHz	Section 6.2.4
shimming	$FWHM_H \leq 25$ Hz	Section 7.2.1
pulse sequence	single pulse excitation	Section 6.3.1
	$\boldsymbol{B}_1$= 25 kHz ($\frac{\pi}{2}$=10 μs)	Section 7.2.2
carrier	PE: on resonance with bulk site	Appendix A
	PP: center of spectral window	Appendix A
recycle delay	unknown samples: 2 s, $B_{br} \pm 15\%$	Section 6.3.1
	defined samples: 3 s, $B_{br} \pm$ 2%	Section 6.3.1
decoupling	on resonance π_6-decoupling	Section 6.4.3
	$\boldsymbol{B}_1$= 25 kHz ($\frac{\pi}{2}$ = 10 μs)	Section 6.4.3
acquisition time	273 ms (π_6, τ_{rd} = 2 s)	Section 6.4.1
	409 ms (π_6, τ_{rd} = 3 s)	Section 6.4.1
dwell time	50 μs	Appendix A
dummy scans	16	Section 6.3.1
effective time domain	excess noise trimmed ($TD_{eff} < TD$)	Section 7.2.3
zerofilling	$SI \geq 2 \times TD$ or $2 \times TD_{eff}$	Section 7.2.4
window function	gaussian ($LB = -0.01$, $GB = 0.1$ to 0.00001)	Section 7.2.5

Appendix G

Abbreviations

A_{all}	total spectral area
A_{br}	area of branch site
ABS	polyacrylonitrile-co-butadiene-co-styrene
A_{bulk}	area of bulk backbone sites
aPP	atactic polypropylene
ASA	polyacrylonitrile-co-styrene-co-acrylate
$\boldsymbol{B}_0$	external magnetic field
$\boldsymbol{B}_1$	transverse magnetic field
B_{br}	branch content
BN	boron nitride
C_{bb}	backbone carbons
CGC	constrained geometry catalysts
C_i	acceptance criterion for stage i
CP	cross polarisation
CS	chemical shift
CSA	chemical shift anisotropy
CV	capillary viscometer
CW	continuous-wave decoupling
δ	rheology: phase angle / NMR: bulk backbone site
δ_c	characteristic phase angle
DEPT	distortionless enhancement by polarization transfer
D_i	LCB density
$D_{\%}$	percentage duty-cycle
DQ	double-quantum transition
DQC	double-quantum coherence
DRI	differential refractive index

DSC	differential scanning calorimetry
η	NOE enhancement
$[\eta]$	intrinsic viscosity
η_0	zero shear viscosity
EPS	expandable polystyrene
F	LCB frequency
FID	free induction decay
FT	Fourier-transform
FTIR	fourier-transform infrared spectroscopy
FWHM	full-width at half maximum
g	branching factor
g'	viscosity branching factor
G_c	characteristic modulus
GPC	gel permeation chromatography
$\|G^*\|$	complex modulus
HDPE	high density polyethylene
HMQC	heteronuclear multiple-quantum coherence
HMS-PP	high melt strength polypropylene
I_{br}	mol-% comonomer incorporation
INADEQUATE	incredible natural abundance double quantum transfer experiment
INEPT	insensitive nuclei enhanced by polarization transfer
iPP	isotactic polypropylene
IR	infrared
J_e^0	steady-state creep recovery compliance
$J(t')$	creep compliance
$J_R(t)$	creep recovery compliance
LAOS	large angle oscillatory shear
l_c	detection coil length
LCB	long chain branches
LDPE	low density polyethylene
LLDPE	linear low density polyethylene
LS	light scattering
m	metallocene
MALLS	multi angle laser light scattering
MAO	methylaluminoxane
MAS	magic angle spinning
M_e	entanglement molecular weight
M_n	number average molecular weight
MSL	methylene sequence length

M_w	weight average molecular weight
MW	molecular weight
MWD	molecular weight distribution
n_c	number of detection coil windings
NMR	nuclear magnetic resonance
NOE	nuclear Overhauser effect
NOE	NOE enhancement factor
$O_{\%}$	percentage amplifier 'on-time'
PAS	principle axis system
PDI	polydispersity index
PE	polyethylene
PET	polyethylene terephthalate
PFG	pulsed field gradient
ϕ_c	detection coil diameter
ϕ_1	first order phase correction
ϕ_0	zeroth order phase correction
PP	polypropylene
ppm	parts-per-million
PTFE	polytetrafluoroethylene
PS	polystyrene
PUR	polyurethane
PVC	polyvinyl chloride
RF	radio frequency
$\langle {R_g}^2 \rangle$	mean square radius of gyration
SAN	polystyrene-co-acrylonitrile
SCB	short chain branches
SD	standard deviation
SEC	size exclusion chromatography
SNA	successive nucleation and annealing
SNR	signal to noise ratio
SPE	single pulse excitation
sPP	syndiotactic polypropylene
SQ	single-quantum transition
SSB	spinning side band
τ_{aq}	acquisition time
TCB	1,2,4-trichlorobenxene
T_{CH}	cross polarisation build-up rate
τ_{ct}	contact time
TD	number of data points in the time domain

TF	thermally fractionated
T_g	glass transition temperature
T_m	melting point
T_{max}	maximum probehead operating temperature
TPPM	two-pulse phase-modulated decoupling
τ_{rd}	recycle delay
TREF	temperature rising elution fractionation
T_1	spin-lattice relaxation time
$T_{1\rho}$	spin-lattice relaxation time in the rotating frame
TOSS	total suppression of sidebands
T_2	spin-spin relaxation time
UHMWPE	ultra high molecular weight polyethylene
V_c	detection coil volume
V_s	sample volume
VT	variable-temperature
X_i	measured property for stage i
Z-N	Ziegler-Natta
ZQ	zero-quantum transition

Bibliography

[Aho 88] A. V. Aho, B. W. Kernighan, P. J. Weinberger. The AWK Programming Language. Addison-Wesley (1988).

[Al-Malaika 04] S. Al-Malaika. Perspectives in Stabilisation of Polyolefins. In Long-Term Properties of Polyolefins, Band 169 (*Advances in Polymer Science*), pp 121–150. Springer (2004).

[Alamo 02] R. G. Alamo, J. A. Blanco, I. Carrilero, R. Fu. Measurement of the ^{13}C spin-lattice relaxation time of the non-crystalline regions of semicrystalline polymers by a CP MAS-based method. *Polymer* **43**(6), 1857–1865 (2002).

[Andresen 76] A. Andresen, H.G. Cordes, J. Herwig, W. Kaminsky, A. Merck, R. Mottweiler, J. Pein, H. Sinn, H.J. Vollmer. Halogen-free soluble Ziegler catalysts for polymerization of ethylene - control of molecular-weight by choice of temperature. *Angew. Chem. Int. Ed.* **15**(10), 630–632 (1976).

[Andrew 58] E. R. Andrew, A. Bradbury, R. G. Eades. Nuclear Magnetic Resonance Spectra from a Crystal Rotated at High Speed. *Nature* **182**, 1659 (1958).

[Assink 00] R. A. Assink, M. Celina, T. D. Dunbar, T. M. Alam, R. L. Clough, K. T. Gillen. Analysis of hydroperoxides in solid polyethylene by MAS ^{13}C NMR and EPR. *Macromolecules* **33**(11), 4023–4029 (2000).

[Aue 76] W. P. Aue, E. Bartholdi, R. R. Ernst. Two-Dimensional Spectroscopy: Application to Nuclear Magnetic Resonance. *J. Chem. Phys.* **64**, 2229 (1976).

[Auhl 04] D. Auhl, J. Stange, H. Münstedt, B. Krause, D. Voigt, A. Lederer, U. Lappan, K. Lunkwitz. Long-Chain Branched Polypropylenes by Electron Beam Irradiation and Their Rheological Properties. *Macromolecules* **37**, 9465–9472 (2004).

[Auhl 05] D. Auhl. Personal communication. Increase in the degree of LCB with irradiation dose observed by D. Auhl (2005).

[Axelson 77] D. E. Axelson, L. Mandelkern, G. C. Levy. ^{13}C Spin Relaxation Parameters of Branched Polyethylenes - Ramifications For Quantitative-Analysis. *Macromolecules* **10**(3), 557–558 (1977).

[Axelson 82] D. E. Axelson. Crystalline Order In Polyethylene - A ^{13}C NMR CP Mas Solid- State T_1 Study. *J. Polym. Sci., Part B: Polym. Phys.* **20**(8), 1427–1435 (1982).

[Axelson 83] D. E. Axelson, L. Mandelkern, R. Popli, P. Mathieu. ^{13}C NMR of Polyethylenes - Correlation of the Crystalline Component T_1 With Structure. *J. Polym. Sci., Part B: Polym. Phys.* **21**(11), 2319–2335 (1983).

[Axelson 86] D. E. Axelson. High Resolution NMR Spectroscopy of Synthetic Polymers in Bulk, Band solid, Chapter 5: Carbon-13 Solid-State NMR of Semicrystalline Polymers, pp 157–226. VCH Publishers Inc. Deefield Beach, FL (1986).

[Banks 51] R. Banks, J. Hogan. Note. Phillips catalysts discovered by R. Banks and J. Hogan at Phillips Petroleum. (1951).

[Bartholdi 73] E. Bartholdi, R. R. Ernst. Fourier Spectroscopy and the Causality Principle. *J. Magn. Reson.* **11**, 9–19 (1973).

[Bax 80] A. Bax, R. Freeman, S. P. Kempsell. Natural abundance ^{13}C–^{13}C coupling observed via double-quantum coherence. *J. Am. Chem. Soc.* **102**, 4849–4851 (1980).

[Bax 81] A. Bax, R. Freeman, T. H. Frenkiel. An NMR technique for tracing out the carbon skeleton of an organic molecule. *J. Am. Chem. Soc.* **103**, 2102–2104 (1981).

[Beckmann 00] P. A. Beckmann, C. Dybowski. A thermometer for nonspinning solid-state NMR spectroscopy. *J. Magn. Reson.* **146**(2), 379–380 (2000).

[Bennett 95] A. E. Bennett, C. M. Rienstra, M. Auger, K. V. Lakshmi, R. G. Griffin. Heteronuclear Decoupling In Rotating Solids. *J. Chem. Phys.* **103**(16), 6951–6958 (1995).

[Bielecki 95] A. Bielecki, D. P. Burum. Temperature-Dependence Of ^{207}Pb MAS Spectra Of Solid Lead Nitrate - An Accurate, Sensitive Thermometer For Variable-Temperature Mas. *J. Magn. Reson., Ser A* **116**(2), 215–220 (1995).

[Blitz 94] J. P. Blitz, D. C. McFaddin. The Characterization Of Short-Chain Branching In Polyethylene Using Fourier-Transform Infrared-Spectroscopy. *J. Appl. Polym. Sci.* **51**(1), 13–20 (1994).

[Bloch 46] F. Bloch. Nuclear Induction. *Phys. Rev.* **70**, 460 (1946).

[Bloembergen 53] N. Bloembergen, T. J. Rowland. On the Nuclear Magnetic Resonance in Metals and Alloys. *Acta Metall.* **1**, 731–746 (1953).

[Bovey 76] F. A. Bovey, F. C. Schilling, F. L. McCrackin, H. L. Wagner. Short-Chain and Long-Chain Branching in Low-Density Polyethylene. *Macromolecules* **9**, 76–80 (1976).

[Bovey 96] F. A. Bovey, P. A. Mirau. NMR of Polymers. Academic Press: San Diego (1996).

[Brant 93] P. Brant, J. A. M. (to Exxon Chemical Patents Inc.) Canich. Ethylene/Longer α-olefin copolymers. U.S. Patent 5,475,075 (1993).

[Bugada 87] D. C. Bugada, A. Rudin. Long Chain Branching Indices of Low Density Polyethylenes from Size Exclusion Chromatography and ^{13}C-NMR Spectroscopy. *Eur. Polym. J.* **23**, 847–850 (1987).

[Busfield 87] W. K. Busfield, J. V. Hanna, J. H. O'Donnel, A. K. Whittaker. A ^{13}C-NMR Study of Radiation-induced Racemization in Isotactic Polypropylene. *Br. Polym. J.* **19**, 223–226 (1987).

[Busfield 91] W. K. Busfield, J. V. Hanna. A ^{13}C NMR-Study Of End Groups And Stereoregularity Changes Induced By Gamma-Irradiation Of Molten Polypropylenes. *Polymer J.* **23**(10), 1253–1263 (1991).

[Busico 01] V. Busico, R. Cipullo. Microstructure of polypropylene. *Prog. Polym. Sci.* **26**(3), 443–533 (2001).

[Busico 02] V. Busico, R. Cipullo, A. L. Segre. Advances in the ^{13}C NMR characterization of ethene/propene copolymers 1, C_2-symmetric ansa-metallocene catalysts. *Macromol. Chem. Phys.* **203**(10-11), 1403–1412 (2002).

[Capacchione 04] C. Capacchione, A. Proto, J. Okuda. Synthesis of Branched Polyethylene by Ethylene Homopolymerization Using Titanium Catalysts that Contain a Bridged Bis(phenolate) Ligand. *J. Polym. Sci., Part A: Polym. Chem.* **42**, 2815–2822 (2004).

[Carney 05a] M. J. Carney. Thermoplastics 1. handouts of course "Chemistry 411-Survey of Industrial Chemistry"(2005).

[Carney 05b] M. J. Carney. Thermoplastics 2. handouts of course "Chemistry 411-Survey of Industrial Chemistry"(2005).

[Cheng 76] H. N. Cheng, F. C. Schilling, F. A. Bovey. ^{13}C Nuclear Magnetic-Resonance Observation Of Oxidation Of Polyethylene. *Macromolecules* **9**(2), 363–365 (1976).

[Claridge 99] T. D. W. Claridge. High-Resolution NMR Techniques in Organic Chemistry, Band 19 (*Tetrahedron Organic Chemistry Series*). Elsevier Science Ltd. (1999).

[Clark 56] A. Clark, J. P. Hogan, R. L. Banks, W. C. Lanning. Marlex Catalyst Systems. *Ind. Eng. Chem.* **48**, 1152 (1956).

[Cooley 65] J. W. Cooley, J. W. Tuckey. An algorithm for the machine calculation of complex fourier series. *Math. Comp.* **19**, 297–301 (1965).

[Crosby 02] B. J. Crosby, M. Mangnus, W. de Groot, R. Daniels, T. C. B. McLeish. Characterization of long chain branching: Dilution rheology of industrial polyethylenes. *J. Rheol.* **46**, 401–426 (2002).

[De Paëpe 03] D. De Paëpe, D. Sakellariou, P. Hodgkinson, S. Hediger, L. Emsley. Heteronuclear Decoupling in NMR of Liquid Crystals Using Continuous Phase Modulation. *Chem. Phys. Lett.* **368**, 511–522 (2003).

[De Pooter 91] M. De Pooter, P.B. Smith, K. K. Dohrer, K. F. Bennett, M. D. Meadows, C. G. Smith, H. P. Schouwenaars, R. A. Geerards. Determination of the Composition of common Linear Low Density Polyethylene Copolymers by ^{13}C NMR Spectroscopy. *J. Appl. Polym. Sci.* **42**, 399–408 (1991).

[Dechter 81] J. J. Dechter, R. A. Komoroski, D. E. Axelson, L. M. Mandelkern. ^{13}C NMR Linewidths of Polyethylenes and Related Polymers. *J. Polym. Sci., Part B: Polym. Phys.* **19**, 631–651 (1981).

[Dixon 82] W. T. Dixon. Spinning-sideband-free and spinning-sideband-only NMR spectra in spinning samples. *J. Chem. Phys.* **77**, 1800–1809 (1982).

[Doddrell 72] D. Doddrell, Allerhan.A, V. Glushko. Theory Of Nuclear Overhauser Enhancement And ^{13}C-^{1}H Dipolar Relaxation In Proton-Decoupled ^{13}C NMR-Spectra Of Macromolecules. *J. Chem. Phys.* **56**(7), 3683 (1972).

[Doddrell 82] D. M. Doddrell, D. T. Pegg, M. R. Bendall. Distortionless Enhancement of NMR Signals by Polarization Transfer. *J. Magn. Reson.* **48**, 323–327 (1982).

[Dorman 72] D. E. Dorman, F. A. Bovey, E. P. Otocka. ^{13}C Observations Of Nature Of Short-Chain Branches In Low-Density Polyethylene. *Macromolecules* **5**(5), 574 (1972).

[Ernst 87] R. R. Ernst, G. Bodenhausen, A. Wokaun. Principles of Nuclear Magnetic Resonance in One and Two Dimensions. Clarendon Press, Oxford (1987).

[Ernst 03] M. Ernst. Heteronuclear spin decoupling in solid-state NMR under magic-angle sample spinning. *J. Magn. Reson.* **162**, 1–34 (2003).

[Fawcett 37] E. W. Fawcett, R. O. Gibson, M. W. Perrin, J. G. Patton, E. G. Williams. Free radical polymerisation of polyethylene. British Patent 471590 (1937).

[Fleury 04] G. Fleury, G. Schlatter, R. Muller. Non linear rheology for long chain branching characterization, comparison of two methodologies: Fourier transform rheology and relaxation. *Rheol. Acta* **44**(2), 174–187 (2004).

[Frey 06] H. Frey, F. Gröhn, A. Kilbinger. Trendbericht Makromolekulare Chemie 2005. *Nachr. Chem.* **54**, 292–300 (2006).

[Gaborieau 05] M. Gaborieau. *Solid-state NMR investigation of spatial and dynamic heterogeneity in acrylic pressure sensitive adhesives (PSAs) compared to model poly(n-alky acrylates) and poly(n-alkyl methacrylates)*. Dissertation, University Louis Pasteur Strasbourg, http://eprints-scd-ulp.u-strasbg.fr:8080/301/01/PhD_thesis_Marianne Gaborieau.pdf (2005).

[Gabriel 98] C. Gabriel, J. Kaschta, H. Munstedt. Influence of molecular structure on rheological properties of polyethylenes I. Creep recovery measurements in shear. *Rheol. Acta* **37**(1), 7–20 (1998).

[Gabriel 99] C. Gabriel, H. Munstedt. Creep recovery behavior of metallocene linear low-density polyethylenes. *Rheol. Acta* **38**(5), 393–403 (1999).

[Gabriel 02] C. Gabriel, H. Munstedt. Influence of long-chain branches in polyethylene on linear viscoelastic flow properties in shear. *Rheol. Acta* **41**, 232–244 (2002).

[Gotsis 04] A. D. Gotsis, L. F. Zeevenhoven. The Effect of Long Chain Branching on the Processability of Polypropylene in Thermoforming. *Polym. Eng. Sci.* **44**(5), 973–982 (2004).

[Grey 93] C. P. Grey, A. K. Cheetham, C. M. Dobson. Temperature-Dependent Solid-State ^{119}Sn MAS NMR Of $Nd_2Sn_2O_7$, $Sm_2Sn_2O_7$, and $Y_{1.8}Sm_{0.2}Sn_2O_7$ - 3 Sensitive Chemical-Shift Thermometers. *J. Magn. Reson., Ser A* **101**(3), 299–306 (1993).

[Grimmer 97] A. R. Grimmer, A. Kretschmer, V. B. Cajipe. Influence of magic angle spinning on sample temperature. *Magn. Reson. Chem.* **35**(2), 86–90 (1997).

[Gugumus 02] F. Gugumus. Physico-chemical aspects of polyethylene processing in an open mixer 8: Various reactions of polyethylene hydroperoxide in the melt. *Polym. Degrad. Stab.* **75**, 131–142 (2002).

[Guo 00] M. Guo, S. Z. D. Cheng, R. P. Quirk. Olefin Polymerization, Emerging Frontiers, Band 749 (*Symposium Book Series*), Chapter 11: Variable temperature, solid-state ^{13}C NMR study of linear low-density polyethylene, pp 163–176. America Chemical Society (2000).

[Gurp 98] M. van Gurp, J. Palmen. Time temperature superposition for polymeric blends. *Rheol. Bull.* **67**, 5–8 (1998).

[Halász 05] L. Halász, O. Vorster, K. Belina. The effect of short chain branching on the rheological and thermal properties of olefin: α-olefin copolymers. *Rheol. Acta* **44**, 427–433 (2005).

[Hansen 97] E. W. Hansen, R. Blom, O. M. Bade. NMR characterization of polyethylene with emphasis on internal consistency of peak intensities and estimation of uncertainties in derived branch distribution numbers. *Polymer* **38**(17), 4295–4304 (1997).

[Hatfield 95] G. R. Hatfield, W. E. Killinger, R. C. Zeigler. MeltlState ^{13}C MAS NMR Determination of Comonomer Type and Content in Ethylene/α-Olefin Copolymers. *Anal. Chem.* **67**, 3082–3085 (1995).

[Hatzikiriakos 00] S. G. Hatzikiriakos. Long chain branching and polydispersity effects on the rheological properties of polyethylenes. *Polym. Eng. Sci.* **40**(11), 2279–2287 (2000).

[Hehn 05] M. Hehn. personal communication. different materials used for high temperature probeheads result commonly in slightly lower sensitivity, however, much higher sensitivity gained by resonance circuit optimisation (2005).

[Hoch 96] J. C. Hoch, A. S. Stern. NMR Data Processing. Wiley-Liss (1996).

[Hogan 58] J. P. Hogan, R. L. Banks. Polymerization of olefins. US Patent 2825721 (1958).

[Izzo 99] L. Izzo, L. Caporaso, G. Senatore, L. Oliva. Branched polyethylene by ethylene homopolymerization with meso-zirconocene catalyst. *Macromolecules* **32**(21), 6913–6916 (1999).

[Janzen 99] J. Janzen, R. E. Colby. Diagnosing long-chain branching in polyethylenes. *J. Mol. Struct.* **486**, 569–584 (1999).

[Jelinski 84] L. W. Jelinski, J. J. Dumais, J. P. Luongo, A. L. Cholli. Thermal-Oxidation And Its Analysis At Low-Levels In Polyethylene. *Macromolecules* **17**(9), 1650–1655 (1984).

[Kaji 91] A. Kaji, Y. Akitomo, M. Murano. NMR-Study Of Microstructure Of Ultra-High-Molecular-Weight Polyethylene. *J. Polym. Sci., Part A: Polym. Chem.* **29**(13), 1987–1990 (1991).

[Kaminsky 83] W. Kaminsky, M. Miri, H. Sinn, R. Woldt. Bis(cyclopentadienyl)-zirkonverbindungen und Aluminoxan als Ziegler-Katalysatoren für die Polymerisation und Copolymerisation von Olefinen. *Macromol. Rapid Commun.* **4**(6), 417 (1983).

[Kaminsky 01] W. Kaminsky. Olefin Polymerization Catalyzed by Metallocenes. *Adv. Catal.* **46**, 89–159 (2001).

[Kaminsky 05] W. Kaminsky, C. Piel, K. Scharlach. Polymerisation of Ethene and Longer Chained Olefins by Metallocene Catalysis. *Macromol. Symp.* **226**, 25–34 (2005).

[Khitrin 03] A. K. Khitrin, Toshimichi Fujiwara, Hideo Akutsu. Phase-modulated Heteronuclear Decoupling in NMR of Solids. *J. Magn. Reson.* **162**, 46–53 (2003).

[Klimke 06] K. Klimke, M. Parkinson, C. Piel, W. Kaminsky, H. W. Spiess, M. Wilhelm. Optimisation and Application of Polyolefin Branch Quantification by Melt-State ^{13}C NMR Spectroscopy. *Macromol. Chem. Phys.* **207**, 382–395 (2006).

[Knuuttila 04] H. Knuuttila, A. Lehtinen, Nummila-Pakarinen A. Advanced Polyethylene Technologies–Controlled Material Properties. In Long-Term Properties of Polyolefins, Band 169 (*Advances in Polymer Science*), pp 13–27. Springer (2004).

[Koerner 02] R. M. Koerner, G. Hsuan. Appendix B Antioxidant Depletion Time in High Density Polyethylene Geomembranes. Rapport technique, United States Environmental Protection Agency (2002).

[Kokko 00a] E. Kokko, P. Lehmus, R. Leino, H. J. G. Luttikhedde, P. Ekholm, J.H. Näsman, J.V. Seppälä. meso- and rac-Diastereomers of 1- and 2-tert-Butyldimethylsiloxy Substituted Ethylenebis(indenyl)zirconium Dichlorides for Formation of Short- and Long-Chain Branched Polyethylene. *Macromolecules* **33**, 9299–9204 (2000).

[Kokko 00b] E. Kokko, A. Malmberg, P. Lehmus, B. Löfgren, J. Seppälä. Influence of the Catalyst and Polymerization Conditions on the Long-Chain Branching of Metallocene-Catalyzed Polyethenes. *J. Polym. Sci., Part A: Polym. Chem.* **38**, 376–388 (2000).

[Kokko 01] E. Kokko, P. Lehmus, A. Malmberg, B. Löfgren, J. Seppälä. Organometallic Catalyst and Olefin Polymerization, Catalysts for a New Millennium, Chapter Long-Chain Branched Polyethene via Metallocene-Catalysis: Comparison of Catalysts., pp 335–345. Springer (2001).

[Kristen 99] M. O. Kristen. Metallocenes - From a Laboratory Curiosity to Industrial Scale Applications. In merging Technology Series: New and Advanced Materials (1999).

[Kuwabara 97] K. Kuwabara, H. Kaji, F. Horii, D. C. Bassett, R. H. Olley. Solid-state ^{13}C NMR analyses of the crystalline-noncrystalline structure for metallocene-catalyzed linear low-density polyethylene. *Macromolecules* **30**(24), 7516–7521 (1997).

[Lagendijk 01] R. P. Lagendijk, A. H. Hogt, A. Buijtenhuijs, A. D. Gotsis. Peroxydicarbonate modification of polypropylene and extensional flow properties. *Polymer* **42**, 10035–10043 (2001).

[Lai 93] S. Y. Lai, J. R. Wilson, G. W. Knight, J. C. Stevens, P. W. S. (to Dow Chemical Co.) Chum. Elastic substantially linear olefin polymers. U.S. Patent 5,272,236 (1993).

[Lamar 71] G. N. Lamar. Effect Of Paramagnetic Metal Ions On Proton-Decoupled ^{13}C NMR Intensities. *Chem. Phys. Lett.* **10**(2), 230 (1971).

[Langer 99] B. Langer, L. Schnell, H. W. Spiess, A. R. Grimmer. Temperature calibration under ultrafast MAS conditions. *J. Magn. Reson.* **138**(1), 182–186 (1999).

[Laupretre 90] F. Laupretre. Applications of high-resolution solid-state ^{13}C NMR to polymers. *Prog. Polym. Sci.* **15**, 425–474 (1990).

[Lehmus 99] P. Lehmus, E. Kokko, O. Harkki, R. Leino, H. J. G. Luttikhedde, J. H. Nasman, J. V. Seppala. Homo- and copolymerization of ethylene and alpha-olefins over 1- and 2-siloxy-substituted ethylenebis(indenyl)zirconium and ethylenebis(tetrahydroindenyl)zirconium dichlorides. *Macromolecules* **32**(11), 3547–3552 (1999).

[Lehmus 00] P. Lehmus, E. Kokko, R. Leino, H. J. G. Luttikhedde, B. Rieger, J. V. Seppala. Chain end isomerization as a side reaction in metallocene- catalyzed ethylene and propylene polymerizations. *Macromolecules* **33**(23), 8534–8540 (2000).

[Levitt 79] M. H. Levitt, R. Freeman. Population Inversion Using a Composite Pulse. *J. Magn. Reson.* **33**, 473 (1979).

[Levitt 01] M. H. Levitt. Spin dynamics. Wiley (2001).

[Levy 75] G. C. Levy, U. Edlund. Quantitative ^{13}C Fourier-Transform Nuclear Magnetic-Resonance - Limitations Of Spin Relaxation Reagents. *J. Am. Chem. Soc.* **97**(16), 4482–4485 (1975).

[Litvinov 02] V. M. Litvinov, V. B. F. Mathot. Partitioning of main and side-chain units between different phases: a solid-state ^{13}C NMR inversion-recovery cross-polarization study on a homogeneous, metallocene-based, ethylene-1-octene copolymer. *Solid State Nucl. Magn. Reson.* **22**, 218–234 (2002).

[Liu 99] W. Liu, D. G. Ray, P. Rinaldi. Resolution of Signals from Long-Chain Branching in Polyethylene by ^{13}C NMR at 188.6 MHz. *Macromolecules* **32**, 3817–3819 (1999).

[Liu 01] W. X. Liu, P. L. Rinaldi, L. H. McIntosh, R. P. Quirk. Poly(ethylene-co-1-octene) characterization by high-temperature multidimensional NMR at 750 MHz. *Macromolecules* **34**(14), 4757–4767 (2001).

[Löfgren 04] B. Löfgren, E. Kokko, J. Seppälä. Specific Structures Enabled by Metallocene Catalysis in Polyethylenes. In Long-Term Properties of Polyolefins, Band 169 (*Advances in Polymer Science*), pp 1–12. Springer (2004).

[Lohse 02] D. J. Lohse, S. T. Milner, L. J. Fetters, M. Xenidou, N. Hadjichristidis, R. A. Mendelson, C. A. Garcia-Franco, M. K. Lyon. Well-defined, model long chain branched polyethylene. 2. Melt rheological behavior. *Macromolecules* **35**(8), 3066–3075 (2002).

[Lowe 59] I. J. Lowe. Free Induction Decays of Rotating Solids. *Phys. Rev. Lett.* **2**, 285–287 (1959).

[Luongo 60] J. P. Luongo. Infrared Study of Oxygenated Groups Formed in Polyethylene During Oxidation. *J. Polym. Sci.* **42**, 139–150 (1960).

[MacNamara 00] E. MacNamara, C. V. Rice, J. Smith, L. J. Smith, D. Raftery. Cross-relaxation dynamics between laser-polarized xenon and a surface species using a simple three-spin model. *Chem. Phys. Lett.* **317**, 165–173 (2000).

[Malmberg 98] A. Malmberg, E. Kokko, P. Lehmus, B. Lofgren, J. V. Seppala. Long-chain branched polyethene polymerized by metallocene catalysts Et[Ind]$_2$ZrCl$_2$/MAO and Et[IndH$_4$]$_2$ZrCl$_2$/MAO. *Macromolecules* **31**(24), 8448–8454 (1998).

[Malmberg 99] A. Malmberg, J. Liimatta, A. Lehtinen, B. Lofgren. Characteristics of long chain branching in ethene polymerization with single site catalysts. *Macromolecules* **32**(20), 6687–6696 (1999).

[Marion 89] Marion, Ikura, A. Bax. Improved solvent suppression in one- and two-dimensional NMR spectra by convolution of time domain data. *J. Magn. Reson.* **84**, 425–430 (1989).

[McCormick 06] M. McCormick. personal communication. High percentage of corporate analytical NMR analysis at 3M (St. Paul, USA) is undertaken in the melt-state. (2006).

[McFaddin 86] D. C. McFaddin, K. E. Russell, E. C. Kelusky. C-13 Nmr Solid-State Studies of Relaxation Behavior of Branches in Homogeneous 1-Alkene-Ethylene Copolymers. *Polymer Commun.* **27**(7), 204–206 (1986).

[Mehring 83] M. Mehring. High Resolution NMR of Solids. Springer-Verlag, Berlin (1983).

[Metz 94] G. Metz, X. L. Wu, S. O. Smith. Ramped-Amplitude Cross-Polarization In Magic-Angle-Spinning NMR. *J. Magn. Reson., Ser A* **110**(2), 219–227 (1994).

[Michalovic 05] M. Michalovic. The Macrogalleria (2005).

[Morris 79] G. A. Morris, R. Freeman. Enhancement of Nuclear Magnetic Resonance Signals by Polarization Transfer. *J. Am. Chem. Soc.* **101**, 760–761 (1979).

[Morris 86] G. A. Morris. Modern NMR Techniques for Structure Elucidation. *Magn. Reson. Chem.* **24**, 371 (1986).

[Mowery 05] D. M. Mowery, Assink R. A., Derzon D. K., Klamo S. B., Clough R. L., Bernstein R. Solid-State ^{13}C NMR Investigation of the Oxidative Degradation of Selectively Labeled Polypropylene by Thermal Aging and γ-Irradiation. *Macromolecules* **38**, 5035–5046 (2005).

[Natta 56] G. Natta. Stereospezifische Katalysen und isotaktische Polymere. *Angew. Chem.* **68**(12), 393–403 (1956).

[Neue 96] G. Neue, C. Dybowski, M. L. Smith, M. A. Hepp, D. L. Perry. Determination of $^{207}Pb^{2+}$ chemical shift tensors from precise powder lineshape analysis. *Solid State Nucl. Magn. Reson.* **6**(3), 241–250 (1996).

[Neue 97] G. Neue, C. Dybowski. Determining temperature in a magic-angle spinning probe using the temperature dependence of the isotropic chemical shift of lead nitrate. *Solid State Nucl. Magn. Reson.* **7**(4), 333–336 (1997).

[Neuhaus 89] D. Neuhaus, M. Williamson. The Nuclear Overhauser Effect in Structural and Conformational Analysis. VCH Publishers (1989).

[Okamoto 92] D. T. Okamoto, S. L. Cooper, T. W. Root. Control of Solid-State Nuclear Overhauser Enhancement in Polyurethane Block Copolymers. *Macromolecules* **25**(12), 3301–3303 (1992).

[Pake 48] G. E. Pake. Nuclear Resonance Absorption in Hydrated Crystals: Fine Structure of the Proton Line. *J. Chem. Phys.* **16**, 327–336 (1948).

[Palza 05] H. Palza, J. M. Lopez-Majada, R. Quijada, R. Benavente, E. Perez, M. L. Cerrada. Metallocenic copolymers of isotactic propylene and 1- octadecene: Crystalline structure and mechanical behavior. *Macromol. Chem. Phys.* **206**(12), 1221–1230 (2005).

[Parkinson 04] M. Parkinson. personal communication. differences between solution-state and melt-state NMR chemical shifts observed by M. Parkinson (2004).

[Piel 05] C. Piel. *Polymerization of Ethene and Ethene-co-α-Olefin: Invetsigations on Short- and Long-Chain Branching and Structure-Property Relationships*. Dissertation, Department of Chemistry, University Hamburg (2005).

[Pigeon 94] M. G. Pigeon, A. Rudin. Branching measurement by analytical TREF: A fully quantitative technique. *J. Appl. Polym. Sci.* **51**(2), 303–311 (1994).

[Pines 72] A. Pines, M. G. Gibby, J. S. Waugh. Proton-Enhanced Nuclear Induction Spectroscopy. A Method for High Resolution NMR of Dilute Spins in Solids. *J. Chem. Phys.* **56**, 1776–1777 (1972).

[Pines 73] A. Pines, M. G. Gibby, J. S. Waugh. Proton-enhanced NMR of Dilute Spins in Solids. *J. Chem. Phys.* **59**, 569–590 (1973).

[PlasticsEurop 04] PlasticsEurope. Consultic (2004).

[PlasticsEurop 05] PlasticsEurope. WG Statistics and Market Research (2005).

[Pollard 04] M. Pollard, K. Klimke, R. Graf, H. W. Spiess, M. Wilhelm, O. Sperber, C. Piel, W. Kaminsky. Observation of Chain Branching in Polyethylene in the Solid State and Melt via ^{13}C NMR Spectroscopy and Melt NMR Relaxation Time Measurements. *Macromolecules* **37**, 813–825 (2004).

[Prasad 91] J. V. Prasad, P. V. C. Rao, V. N. Garg. Quantification Of Branching In Polyethylene By ^{13}C-NMR Using Paramagnetic Relaxation Agents. *Eur. Polym. J.* **27**(3), 251–254 (1991).

[Prosenc 97] M. H. Prosenc, H. H. Brintzinger. Zirconium-alkyl isomerizations in zirconocene-catalyzed olefin polymerization: A density functional study. *Organometallics* **16**(18), 3889–3894 (1997).

[Qiu 00] X. H. Qiu, M. D. Ediger. Branching effects on the segmental dynamics of polyethylene melts. *J. Polym. Sci., Part B: Polym. Phys.* **38**(20), 2634–2643 (2000).

[Quijada 99] R. Quijada, A. Narvaez, R. Rojas, F. M. Rabagliati, G. Barrera-Galland, R. Santos-Mauler, R. Benavente, E. Pérez, J. M. Pereña, A. Bello. Synthesis and characterization of copolymers of ethylene and 1-octadecene using the rac-Et(Ind)$_2$ZrCl$_2$ catalyst system. *Macromol. Chem. Phys.* **200**, 1306–1310 (1999).

[Randall 89] J. C. Randall. A Review of High Resolution Liquid ^{13}C Nuclear Magnetic Resonance Characterizations of Ethylene-Based Polymers. *J. Macromol. Sci., Rev. Macromol. Chem. Phys.* **C29**, 201–317 (1989).

[Rego 04] R. Rego, P. J. Adriaensens, R. A. Carleer, J. A. Gelan. Fully quantitative ^{13}C NMR characterization of resol phenolformaldehyde prepolymer resins. *Polymer* **45**(1), 33–38 (2004).

[Resconi 00] L. Resconi, L. Cavallo, A. Fait, F. Piemontesi. Selectivity in propene polymerization with metallocene catalysts. *Chem. Rev.* **100**(4), 1253–1345 (2000).

[Rohlfing 00] D. C. Rohlfing, J. Janzen. Metallocene-based Polyolefins, Chapter Melt-rheological Characteristics of Metallocene-catalyzed Polyethylenes, pp 419–434. Wiley (2000).

[Sahoo 03] S. K. Sahoo, T. Zhang, D. V. Reddy, P. L. Rinaldi, L. H. McIntosh, R. P. Quirk. Multidimensional NMR studies of poly(ethylene-co-1-butene) microstructures. *Macromolecules* **36**(11), 4017–4028 (2003).

[Samoson 03] A. Samoson, Tiit Tuherm. High performance MAS (2003). Poster contribution at the ENC 2003.

[Savitski 03] E. P. Savitski, G. B. Caflisch, C. M. Killian, M. D. Meadows, J. H. Merkley, B. J. Huff. Influence of the short-chain branch length on the calibration of temperature rising elution fractionation systems. *J. Appl. Polym. Sci.* **90**(3), 722–728 (2003).

[Schaefer 77] J. Schaefer, E. O. Stejskal, R. Buchdahl. Magic-Angle ^{13}C Nmr Analysis Of Motion In Solid Glassy Polymers. *Macromolecules* **10**(2), 384–405 (1977).

[Schilling 78] F. C. Schilling, R. E. Cais, F. A. Bovey. Chain dynamics of poly(but-1-ene) from ^{13}C nuclear magnetic relaxation measurements. *Macromolecules* **11**, 325–328 (1978).

[Schmidt-Rohr 94] K. Schmidt-Rohr, H.W. Spiess. Multidimensional Solid-State NMR and Polymers. Academic Press, London (1994).

[Schmidtrohr 91] K. Schmidtrohr, H. W. Spiess. Chain Diffusion Between Crystalline and Amorphous Regions in Polyethylene Detected By 2D Exchange ^{13}C Nmr. *Macromolecules* **24**(19), 5288–5293 (1991).

[Seger 04] M. R. Seger, G. E. Maciel. Quantitative ^{13}C NMR Analysis of Sequence Distributions in Poly(ethylene-co-1-hexene). *Anal. Chem.* **76**, 5734–5747 (2004).

[Shaka 83a] A. J. Shaka, J. Keeler, R. Freeman. Evaluation of a New Broadband Decoupling Sequence: WALTZ16. *J. Magn. Reson.* **53**, 313–340 (1983).

[Shaka 83b] A. J. Shaka, J. Keeler, T. Frenkiel, R. Freeman. An Improved Sequence for Broadband Decoupling: WALTZ16. *J. Magn. Reson.* **52**, 335–338 (1983).

[Sharma 05] K. G. Sharma. *Easily Processable Ultra High Molecular Weight Polyethylene with Narrow Molecular Weight Distribution*. Dissertation, Technical University Eindhoven (2005).

[Shiono 99] T. Shiono, S. M. Azad, T. Ikeda. Copolymerization of atactic polypropene macromonomer with propene by an isospecific metallocene catalyst. *Macromolecules* **32**(18), 5723–5727 (1999).

[Shroff 96] R. Shroff, A. Prasad, C. Lee. Effect of Molecular Structure on Rheological and Crystallization Properties of Polyethylenes. *J. Polym. Sci., Part B: Polym. Phys.* **34**, 2317–2333 (1996).

[Shroff 99] R. N. Shroff, H. Mavridis. Long-chain-branching index for essentially linear polyethylenes. *Macromolecules* **32**(25), 8454–8464 (1999).

[Shroff 01] R. N. Shroff, H. Mavridis. Assessment of NMR and Rheology for the Characterization of LCB in Essentially Linear Polyethylenes. *Macromolecules* **34**, 7362–7367 (2001).

[Slichter 96] C. P. Slichter. Principles of Magnetic Resonance. Springer-Verlag, Berlin (1996).

[Solomon 55] I. Solomon. Relaxation Processes in a System of two Spins. *Phys. Rev.* **99**(2), 559–565 (1955).

[Sørensen 83] O. W. Sørensen, G. W. Eich, M. H. Levitt, G. Bodenhausen, R. R. Ernst. Product Operator Formalism for the Description of NMR Pulse Experiments. *Prog. Nucl. Magn. Reson. Spectrosc.* **16**, 163–192 (1983).

[Spiess 78] H. W. Spiess. Rotation of Molecules and Nuclear Spin Relaxation. In P. Diehl, E. Fluck, R. Kosfeld (Hrsg.), NMR Basic Principles and Progress, Band 15, pp 55–214. Springer-Verlag, Berlin (1978).

[Stadler 05] F. Stadler, C. Piel, J. Kaschta, S. Rulhoff, W. Kaminsky, H. Münstedt. Dependence of the zero shear-rate viscosity and the viscosity function of linear high-density polyethylenes on the mass-average molar mass and polydispersity. *Rheol. Acta* (2005).

[Stadler 06] F. J. Stadler, C. Piel, K. Klimke, J. Kaschta, M. Parkinson, M. Wilhelm, W. Kaminsky, H. Münstedt. Influence of Type and Content of Various Comonomers on Long-Chain Branching of Ethene/α-Olefin Copolymers. *Macromolecules* (2006).

[Stevens 93] J. Stevens. Low temperature CP MAS. In Proceedings of MetCon. Houston (1993).

[Striegel 00] A. M. Striegel, M. R. Krejsa. Complementarity of universal calibration SEC and ^{13}C NMR in determining the branching state of polyethylene. *J. Polym. Sci., Part B: Polym. Phys.* **38**(23), 3120–3135 (2000).

[Sun 01] T. Sun, P. Brant, R. R. Chance, W. W. Graessley. Effect of short chain branching on the coil dimensions of polyolefins in dilute solution. *Macromolecules* **34**(19), 6812–6820 (2001).

[Takahashi 99] T. Takahashi, H. Kawashima, H. Sugisawa, T. Baba. ^{207}Pb chemical shift thermometer at high temperature for magic angle spinning experiments. *Solid State Nucl. Magn. Reson.* **15**(2), 119–123 (1999).

[Thakur 03] K. Thakur. NMR Spectroscopy of Polymers in Solution and in the Solid State, Band 834 (*America Chemical Society Symposium Book Series*), Chapter 3: High-Temperature Solid-State NMR of Cross-Linked, Insoluble, and Unswellable Polymers, pp 32–42. America Chemical Society (2003).

[Thorshaug 98] K. Thorshaug, J. A. Stovneng, E. Rytter, M. Ystenes. Termination, isomerization, and propagation reactions during ethene polymerization catalyzed by $Cp_2Zr\text{-}R^+$ and $Cp^*Zr_2\text{-}R^+$. An experimental and theoretical investigation. *Macromolecules* **31**(21), 7149–7165 (1998).

[Tice 03] P. Tice. Packaging Materials 4. Polyethylene for Food Packaging Applications. Rapport technique, ILSI Europe Packaging Material Task Force (2003).

[Trinkle 01] S. Trinkle, C. Friedrich. Van Gurp-Palmen-plot: a way to characterize polydispersity of linear polymers. *Rheol. Acta* **40**(4), 322–328 (2001).

[Trinkle 02] S. Trinkle, P. Walter, C. Friedrich. Van Gurp-Palmen Plot II - classification of long chain branched polymers by their topology. *Rheol. Acta* **41**, 103–113 (2002).

[VanderHart 80] D. L. VanderHart. High Resolution NMR in Solids. Presentation at the NATO Advanced Study Institute (1980).

[Vandeveer 04] H. G. Vandeveer. Fine-tuning Ziegler-Natta polymerizations: stereocontrol of polypropylene formation. Rapport technique, Department of Chemistry, University of Illinois (2004).

[Vanmoorsel 95] Gjmp Vanmoorsel, E. R. H. Vaneck, C. P. Grey. $Pr_2Sn_2O_7$ And $Sm_2Sn_2O_7$ As High-Temperature Shift Thermometers In Variable-Temperature ^{119}Sn MAS NMR. *J. Magn. Reson., Ser A* **113**(2), 159–163 (1995).

[Vega 98] J. F. Vega, A. Santamaría, A. Muñoz-Escalona, P. Lafuente. Small-Amplitude Oscillatory Shear Flow Measurements as a Tool To Detect Very Low Amounts of Long Chain Branching in Polyethylenes. *Macromolecules* **31**, 3639–3647 (1998).

[Vitorias 06] I. Vitorias, M. Parkinson, K. Klimke, B. Debbaut, M. Wilhelm. Detection and quantification of industrial polyethylene branching topologies via Fourier-Transform Rheology and simulation using the Pom-pom model and NMR. Accepted Rheologica Acta (2006).

[Völkel 88] R. Völkel. High-Resolution Solid-State ^{13}C-NMR Spectroscopy of Polymers. *Angew. Chem. Int. Ed.* **27**, 1468–1483 (1988).

[Wang 98a] W. Wang, D. Yan, P. A. Charpentier, S. Zhu, A. E. Hamielec, B. G. Sayer. Long chain branching in ethylene polymerization using constrained geometry metallocene catalyst. *Macromol. Chem. Phys.* **199**, 2409–2416 (1998).

[Wang 98b] W. J. Wang, D. J. Yan, S. P. Zhu, A. E. Hamielec. Kinetics of long chain branching in continuous solution polymerization of ethylene using constrained geometry metallocene. *Macromolecules* **31**(25), 8677–8683 (1998).

[Wang 04] W. J. Wang, S. Kharchenko, K. Migler, S. P. Zhu. Triple-detector GPC characterization and processing behavior of long-chain-branched polyethylene prepared by solution polymerization with constrained geometry catalyst. *Polymer* **45**(19), 6495–6505 (2004).

[Weng 02] W. Q. Weng, W. G. Hu, A. H. Dekmezian, C. J. Ruff. Long chain branched isotactic polypropylene. *Macromolecules* **35**(10), 3838–3843 (2002).

[Wood-Adams 00] P. M. Wood-Adams, J. M. Dealy, A. W. deGroot, O. D. Redwine. Effect of Molecular Structure on the Linear Viscoelastic Behavior of Polyethylene. *Macromolecules* **33**, 7489–7499 (2000).

[Wood-Adams 01] P. M. Wood-Adams. The effect of long chain branches on the shear flow behavior of polyethylene. *J. Rheol.* **45**(1), 203–210 (2001).

[Yan 99] D. Yan, W. J. Wang, S. Zhu. Effect of long chain branching on rheological properties of metallocene polyethylene. *Polymer* **40**(7), 1737–1744 (1999).

[Yau 01] W. W. Yau, D. Gillespie. New approaches using MW-sensitive detectors in GPC-TREF for polyolefin characterization. *Polymer* **42**, 8947–8958 (2001).

[Ye 03] Z. B. Ye, S. P. Zhu. Synthesis of branched polypropylene with isotactic backbone and atactic side chains by binary iron and zirconium single-site catalysts. *J. Polym. Sci., Part A: Polym. Chem.* **41**(8), 1152–1159 (2003).

[Ye 04] Z. B. Ye, F. AlObaidi, S. P. Zhu. Synthesis and rheological properties of long-chain-branched isotactic polypropylenes prepared by copolymerization of propylene and nonconjugated dienes. *Ind. Eng. Chem. Res.* **43**(11), 2860–2870 (2004).

[Yefeng 03] Y. Yefeng, R. Graf. Personal communication. The apparent sample temperatures of all 4 mm probeheads used in this work corresponded to the actual sample temperatures (2003).

[Young 91] R. J. Young, P. A. Lovell. Introduction to Polymers. Chapman and Hall (1991).

[Yu 90] T. Yu, M. Guo. Recent developments in ^{13}C solid state high-resolution NMR of polymers. *Prog. Polym. Sci.* **15**, 825–908 (1990).

[Yu 05] Y. Yu, P. J. Deslauriers, Rohlfing D. C. SEC-MALS method for the determination of long-chain branching and long-chain branching distribution in polyethylene. *Polymer* **46**, 5165–5182 (2005).

[Zeigler 94] R. C. Zeigler. Dynamics of polypropylene and propene-ethylene copolymers at temperatures above ambient. *Macromol. Symp.* **86**, 213–227 (1994).

[Zhang 01] Y. D. Zhang, D. T. Lynch, S. E. Wanke. Effect of molecular structure distribution on melting and crystallization behavior of 1-butene/ethylene copolymers. *Polymer* **42**, 3067 (2001).

[Zhang 03] M. Zhang, S. E. Wanke. Quantitative Determination of Short-Chain Branching Content and Distribution in Commercial Polyethylenes by Thermally Fractionated Differential Scanning Calorimetry. *Polym. Eng. Sci.* **43**, 1878–1888 (2003).

[Ziegler 55] K. Ziegler, E. Holzkamp, H. Breil, H. Martin. The Mühlheim low-pressure polyethylene process. *Angew. Chem. Int. Ed.* **67**, 541–547 (1955).

[Zimm 49] B. H. Zimm, W. H. Stockmayer. The Dimensions of Chain Molecules Containing Branches and Rings. *Chem. Phys.* **17**, 1301 (1949).